

**BIOMIMETIC SCAFFOLDS BASED ON
HYDROXYETHYL CELLULOSE FOR
SKIN TISSUE ENGINEERING**

FARAH HANANI BINTI ZULKIFLI

UMP

**DOCTOR OF PHILOSOPHY
(ADVANCED MATERIALS)
UNIVERSITI MALAYSIA PAHANG**

UNIVERSITI MALAYSIA PAHANG

DECLARATION OF THESIS AND COPYRIGHT

Author's full name : Farah Hanani binti Zulkifli

Date of birth : 1st October 1987

Title : Biomimetic scaffolds from chemically modified cellulose for skin tissue engineering

Academic Session : 2014/2015

I declare that this thesis is classified as:

CONFIDENTIAL (Contains confidential information under the Official Secret Act 1972)

RESTRICTED (Contains restricted information as specified by the organization where research was done)

OPEN ACCESS I agree that my thesis to be published as online open access (Full text)

I acknowledge that Universiti Malaysia Pahang reserve the right as follows:

1. The Thesis is the Property of Universiti Malaysia Pahang
2. The Library of Universiti Malaysia Pahang has the right to make copies for the purpose of research only.
3. The Library has the right to make copies of the thesis for academic exchange.

Certified By:

(Student's Signature)

Farah Hanani binti Zulkifli
871001-43-6054
Date:

(Signature of Supervisor)

Dr. Fathima Shahitha Jahir Hussain
Date:

BIOMIMETIC SCAFFOLDS FROM CHEMICALLY
MODIFIED CELLULOSE FOR SKIN TISSUE
ENGINEERING



FARAH HANANI BINTI ZULKIFLI

Thesis submitted in fulfillment of the requirements
for the award of the degree of
Doctor of Philosophy (Advanced Materials)

UMP

Faculty of Industrial Sciences & Technology
UNIVERSITI MALAYSIA PAHANG

SEPTEMBER 2015

SUPERVISOR'S DECLARATION

We hereby declare that we have checked the thesis and in our opinion, this thesis is adequate in terms of scope and quality for the award of the degree of Degree of Philosophy (Advanced Materials).

Signature

Name of Supervisor : DR. FATHIIMA SHAHITHA JAHIR
HUSSAIN

Position : SENIOR LECTURER

Date :

Signature

Name of Co-Supervisor : PROF. MASHITAH BINTI MOHD
YUSOFF

Position : PROFESSOR

Date :

Signature

Name of Co-Supervisor : DR. SYAIFUL BAHARI BIN ABDUL
RASSAD

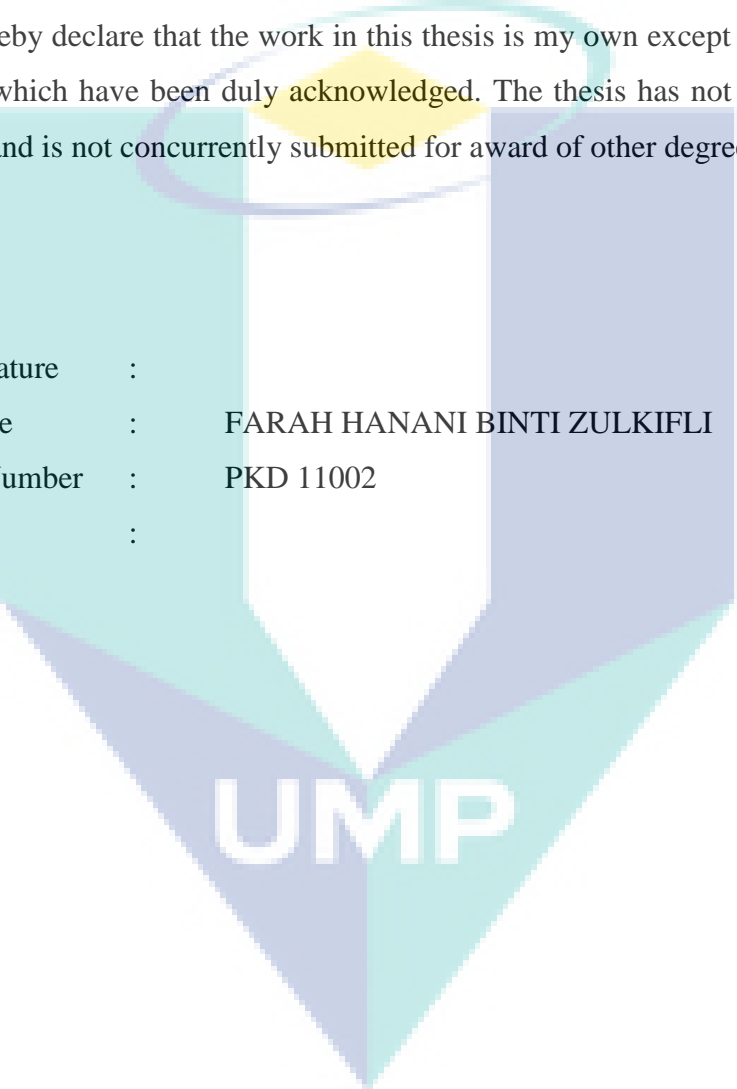
Position : SENIOR LECTURER

Date :

STUDENT'S DECLARATION

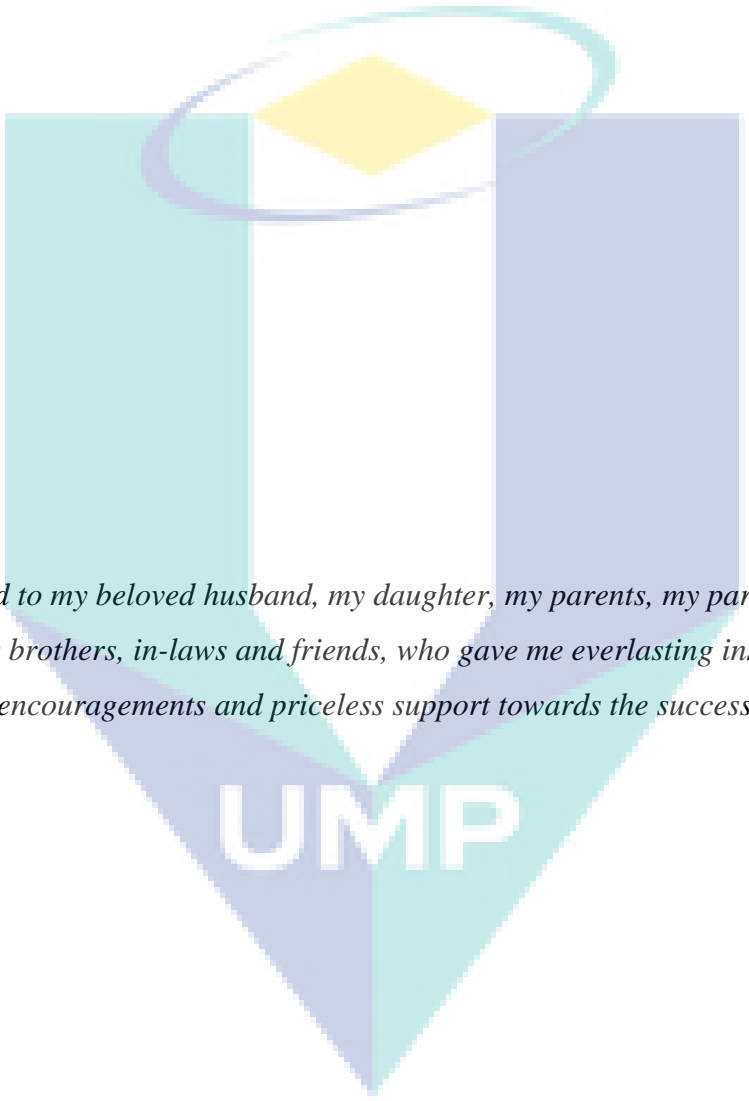
I hereby declare that the work in this thesis is my own except for quotations and summaries which have been duly acknowledged. The thesis has not been accepted for any degree and is not concurrently submitted for award of other degree.

Signature :
Name : FARAH HANANI BINTI ZULKIFLI
ID Number : PKD 11002
Date :

The logo of Universiti Malaysia Perlis (UMP) is a shield-shaped emblem. It features a central white shield with a blue border. The shield is divided into four quadrants by a vertical and a horizontal line. The top-left and bottom-right quadrants are light blue, while the top-right and bottom-left quadrants are light purple. The letters 'UMP' are written in large, bold, white capital letters across the center of the shield.

UMP

DEDICATION



Dedicated to my beloved husband, my daughter, my parents, my parents-in law, my sisters, my brothers, in-laws and friends, who gave me everlasting inspiration, never-ending encouragements and priceless support towards the success of this study.

UMP

ACKNOWLEDGEMENTS

First and foremost, I must thank to Allah SWT for giving me an opportunity to further my study and gain precious knowledge in this world. I am grateful and would like to express my sincere gratitude to my supervisor Dr. Fathima Shahitha Jahir Hussain, for her germinal ideas, invaluable guidance, continuous encouragement, and constant support in making this research possible. I am truly grateful for her progressive vision about my training in science, her tolerance of my naive mistakes, and her commitment to my future career. I would also like to express very special thanks to my co-supervisors Prof. Mashitah binti Mohd Yusoff and Dr. Syaiful Bahari bin Abdul Rassad, for their suggestions and co-operation throughout the study.

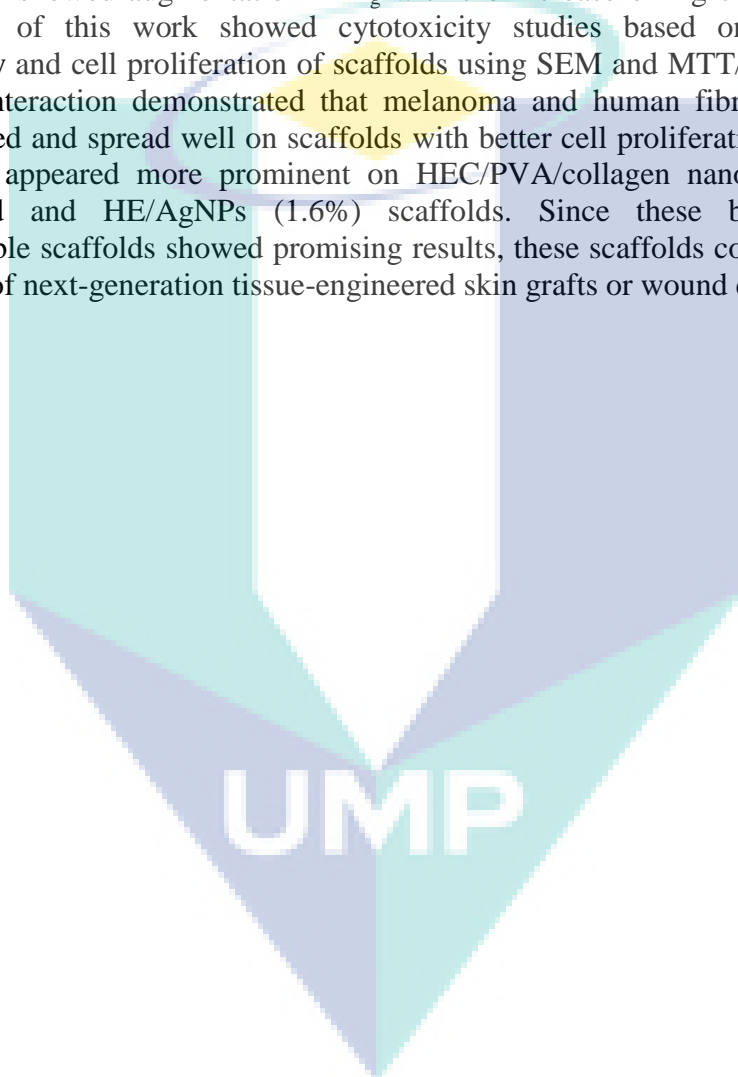
My sincere thanks go to all science officers and laboratory assistant of Faculty of Industrial Science and Technology (FIST) for their invaluable assistance and helps in many ways. Credit also goes to the Dean of FIST, Prof. Jamil bin Ismail and staff of FIST and Institute of Postgraduate Studies (IPS) for their excellent assistance, inspirations and supports throughout this research. Many special thanks go to the Ministry of Education for the financial support of this work *via* the research grant RDU 100106.

I must put on record my sincere indebtedness and gratitude to my beloved husband, Mohd Nawawi bin Abdul Ghani for his sacrifice, patience and understanding that were inevitable to make this work possible. I cannot find the appropriate words that could describe my appreciation for their devotion, support and faith in my ability to attain my goals all these years.

ABSTRACT

Research using biomaterials as scaffolds in skin tissue engineering is tremendously increasing as these biomaterials have been found to mimic the structure of extracellular matrix (ECM) that provides a platform for cell attachment, differentiation and proliferation. Hydroxyethyl cellulose (HEC) is modified cellulose, one of the most abundant natural polymers in the world. The advantage of HEC is its chemical structure, which exactly matches that of glycosaminoglycan (GAG) in the dermis. The focus of this research is to develop scaffolds based on HEC for skin tissue engineering. Two techniques were used to fabricate scaffolds, which are electrospinning and freeze-drying. Electrospinning produces fibers in nanometer scale and interconnected pores that closely resemble the topography features of ECM. Freeze-drying is an easy and convenient technique to produce highly interconnected pores, favourable in tissue engineering. This report comprised of two parts. The first part is about the fabrication and characterization of scaffolds using electrospinning and freeze-drying techniques while the second part is the cell culture studies of nanofibers and freeze-dried scaffolds. In the first part, there are four different studies conducted based on HEC polymers. The first study is on the effect of cross-linking effect on HEC/PVA and HEC/PVA/collagen nanofiber scaffolds prepared by electrospinning method. The concentration of HEC (5%) with PVA (15%) was optimized, blended in different ratios (30-50%) of HEC content and electrospun to obtain smooth nanofibers. The fabrication of HEC/PVA/collagen (0.38%) was also reported. Nanofibers were made water insoluble through chemical cross-links using glutaraldehyde. The microstructure, morphology, mechanical and thermal properties of the HEC/PVA and HEC/PVA/collagen nanofibrous scaffolds was characterized *via* SEM, ATR-FTIR, DSC, UTM and TGA. The second is the *in vitro* degradation study aimed to investigate the behaviour of electrospun HEC/PVA and HEC/PVA/collagen nanofibrous scaffolds in two biologically related media: phosphate buffered solution (PBS) and Dulbecco's modified Eagle's medium (DMEM) for a 12-week incubation period. The results showed that HEC/PVA/collagen scaffolds degraded slower in both media than HEC/PVA scaffolds. All fibers displayed uneven and rough surfaces towards the final week of incubation periods. As degradation time increased, the thermal studies revealed that the melting temperatures and crystallinity of the scaffolds slightly shifted to a lower value. Both HEC/PVA and HEC/PVA/collagen fibers showed a significant decrease in Young's modulus and tensile stress over the 12-week degradation. The third study is fabrication of biopolymeric scaffolds of HEC and PVA using freeze-dry technique and characterized based on their potential for skin tissue engineering. The pore size of HEC/PVA blended scaffolds (2 - 40 μm) showed diameters in the range of both pure HEC (2 - 20 μm) and PVA (14 - 70 μm) scaffolds. All porous scaffolds revealed porosity above 85 %. The water uptake and degradation rate of HEC scaffolds could be controlled by incorporation of PVA in the blends. The ATR-FTIR results exhibit possible interactions between hydroxyl groups of HEC and PVA in the blends. TGA/DrTGA curves clarified different major steps of weight loss involved with different scaffolds. The T_g values of HEC/PVA of the DSC curve occur in the range of

HEC and PVA, which represents the miscibility of HEC/PVA blend polymers. Higher Young's modulus was obtained by increasing the HEC content. The fourth study is the fabrication of novel HEC/silver nanoparticles (AgNPs) formed *via* the freeze-drying using mixture of HEC and AgNO₃ where HEC acts as the reducing agent to silver nanoparticles. Scaffolds from HEC/AgNPs composites were successfully prepared with average pore size ranging from 50 to 150 μm. The surface Plasmon resonance, which shows absorption peaks in the range of 417 – 421 nm, validates the presence of silver nanoparticles in the HEC matrices. The HEC/AgNPs scaffolds showed significant porosity of more than 80 % and a high degree of swelling ratio properties. The DSC thermogram showed augmentation in T_g with the increase of Ag content. The second major part of this work showed cytotoxicity studies based on investigation of morphology and cell proliferation of scaffolds using SEM and MTT/MTS assays. Cell-scaffolds interaction demonstrated that melanoma and human fibroblast (hFB) cells differentiated and spread well on scaffolds with better cell proliferation and attachment with time, appeared more prominent on HEC/PVA/collagen nanofibers, HEC/PVA freeze-dried and HE/AgNPs (1.6%) scaffolds. Since these biocompatible and biodegradable scaffolds showed promising results, these scaffolds could be adopted for the design of next-generation tissue-engineered skin grafts or wound dressing.



ABSTRAK

Penyelidikan menggunakan biobahan sebagai perancah pada kejuruteraan tisu kulit menunjukkan peningkatan yang ketara memandangkan kesamaan biobahan ini dalam struktur ekstrasellular matriks (ECM) serta menyediakan platform untuk perlekatan, percambahan dan perkembangan sel. Hidroksietil selulosa (HEC) adalah selulosa yang diubahsuai, dan merupakan salah satu polimer semulajadi terbanyak di dunia. Kelebihan HEC terletak pada struktur kimianya yang sepadan dengan glikosaminoglikan (GAGs) pada dermis. Fokus kajian ini adalah untuk membangunkan perancah berasaskan HEC untuk kejuruteraan tisu kulit. Terdapat dua teknik digunakan untuk mengfabrikasi perancah ini iaitu elektroputaran dan beku-pengeringan. Elektroputaran adalah teknik bagi menghasilkan gentian pada saiz nanometer dan menunjukkan ciri-ciri topografi poros saling berhubung yang hampir sama dengan ECM. Selain itu, terdapat juga teknik beku-pengeringan, iaitu teknik yang mudah dan sesuai dalam menghasilkan poros saling berhubung yang tinggi, dimana sangat diperlukan dalam bidang kejuruteraan tisu. Terdapat dua bahagian utama dalam kajian ini. Pertama adalah fabrikasi dan pencirian perancah menggunakan teknik elektroputaran dan beku-pengeringan, dan bahagian kedua adalah kajian kultur sel ke atas perancah gentian nano dan beku-pengeringan dalam aplikasi kejuruteraan tisu kulit. Dalam bahagian pertama, terdapat 4 kajian yang berlainan dijalankan berasaskan polimer HEC. Pertama ialah kajian pautan silang ke atas perancah gentian nano HEC/PVA dan HEC/PVA/ kolagen yang disediakan melalui kaedah elektroputaran. Kepekatan HEC (5%) dengan PVA (15%) telah dioptimumkan, dicampur dalam nisbah yang berbeza (30 - 50%) dan dielektroputar untuk mendapatkan gentian nano yang rata. Fabrikasi pada gentian nano HEC/PVA/kolagen (0.38%) juga turut dilaporkan. Gentian nano dijadikan tidak larut air melalui pautan silang secara kimia menggunakan glutaraldehid. Mikrostruktur, morfologi, sifat mekanikal dan haba perancah gentian nano dari campuran HEC/PVA dan HEC/PVA/kolagen telah dicirikan melalui SEM, ATR-FTIR, DSC, UTM dan TGA. Kajian kedua ialah degradasi secara *in vitro*, yang dilakukan untuk menyelidik ciri-ciri perancah gentian nano HEC/PVA dan HEC/PVA/kolagen dalam dua media biologi: larutan tampan fosfat (PBS) dan media DMEM selama 12 minggu tempoh inkubasi. Keputusan menunjukkan bahawa perancah HEC/PVA/kolagen mempamerkan kadar degradasi yang perlahan dalam kedua-dua media berbanding gabungan gentian nano HEC/PVA. Semua gentian menunjukkan permukaan yang tidak rata dan kasar pada minggu-minggu terakhir tempoh inkubasi. Apabila masa inkubasi meningkat, terdapat beberapa perubahan kecil dalam struktur kimia dimana dipaparkan pada spektrum FTIR manakala kajian terma mempamerkan puncak suhu lebur dan penghabluran perancah sedikit beralih kepada nilai yang lebih rendah. Kedua-dua gentian HEC/PVA dan HEC/PVA/kolagen menunjukkan penurunan yang ketara dalam modulus Young dan tegasan tegangan dalam tempoh 12 minggu degradasi. Kajian ketiga ialah perancah biopolimer daripada HEC dan PVA telah disintesis menggunakan teknik beku-pengeringan dan dicirikan berdasarkan potensi mereka dalam kejuruteraan tisu kulit. Saiz liang daripada perancah gabungan HEC/PVA (2-40 μm) menunjukkan diameter dalam lingkungan perancah HEC (2-20 μm) dan PVA

(14-70 μm) tulen. Semua perancah poros menunjukkan nilai porositi lebih daripada 85%. Penyerapan air dan kadar degradasi perancah HEC boleh dikawal dengan penambahan PVA dalam sebatian matriks polimer. Keputusan FTIR pula menunjukkan interaksi-interaksi kimia yang wujud di antara kumpulan hidroksil HEC dan sebatian perancah komposit. Lengkung TGA/DrTGA memaparkan perbezaan tangga penurunan berat bagi setiap perancah yang berkadar dengan suhu. Nilai T_g bagi lengkung DSC pada HEC/PVA berada diantara HEC dan PVA tulen menunjukkan keterlarutcampuran daripada HEC/PVA polimer campuran. Nilai modulus Young yang lebih tinggi telah diperolehi dengan peningkatan nilai HEC. Kajian keempat, novel nanopartikel HEC/perak (AgNPs) yang terdiri daripada pelbagai kepekatan AgNO_3 dibentuk melalui teknik beku-pengeringan. Larutan HEC digunakan sebagai agen penurunan dalam sintesis nanopartikel perak. Perancah dari HEC dengan nanopartikel perak telah berjaya dihasilkan dengan purata saiz liang antara 50-150 μm . Permukaan Plasmon resonans menunjukkan puncak penyerapan dalam lingkungan 417-421 nm, mengesahkan kehadiran nanopartikel perak dalam matriks HEC. HEC/AgNPs perancah menunjukkan keliangan lebih daripada 80% dan mempamerkan sifat nisbah penyerapan yang tinggi. Thermogram DSC menunjukkan peningkatan di T_g bertambah dengan kepekatan AgNO_3 . Dalam bahagian kedua tesis ini, kajian sitotoksiti telah dilakukan, dimana morfologi dan sel pembiakan perancah diuji menggunakan SEM dan MTT/MTS antibiofilem. Interaksi sel-perancah menunjukkan bahawa sel-sel melanoma dan fibroblas manusia (hFB) membiak dan bercambah dengan baik berkadar dengan masa, dimana keputusan lebih jelas diperhatikan pada perancah gentian nano HEC/PVA/kolagen, HEC:PVA (1:2) beku-pengeringan dan HEC/AgNPs (1.6%). Oleh kerana perancah bioserasi dan biodegradasi menunjukkan hasil yang memberangsangkan, perancah ini boleh diguna pakai untuk reka bentuk tisu-kejuruteraan generasi akan datang cantuman kulit atau berpakaian luka.

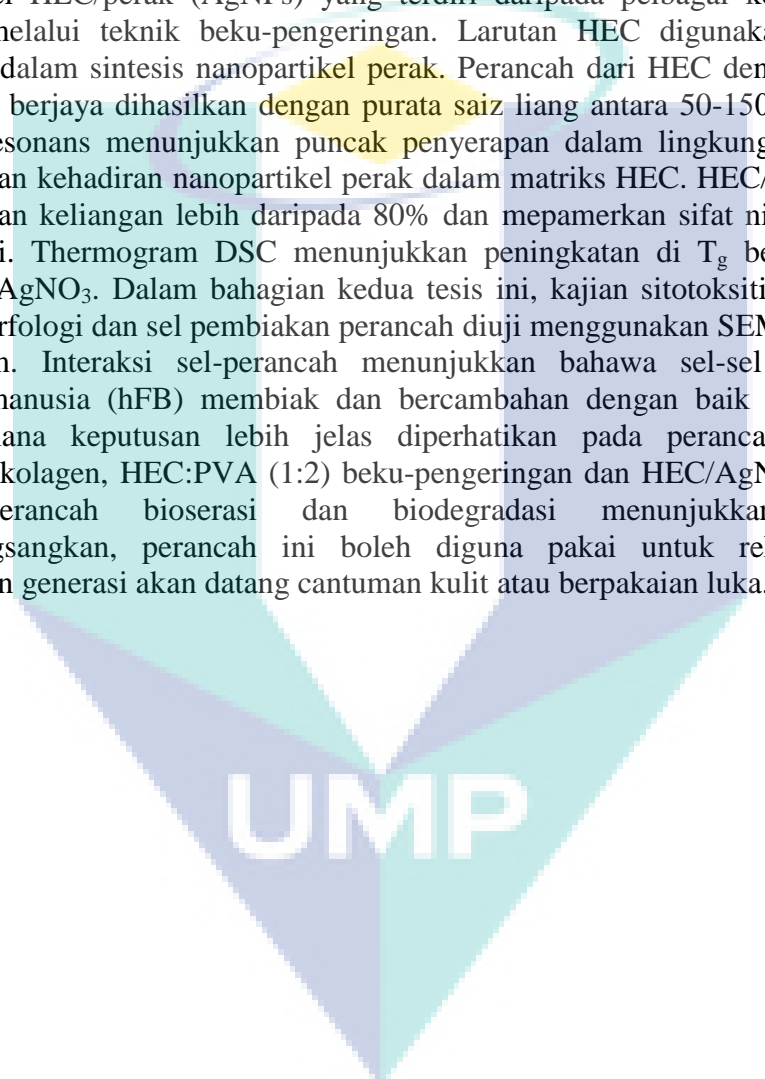
The logo of Universiti Malaysia Perlis (UMP) is a large, stylized letter 'V' shape. The left side of the 'V' is light blue, the right side is light green, and the bottom point is a darker blue. The letters 'UMP' are written in white, bold, sans-serif font across the center of the 'V'.

TABLE OF CONTENTS

	Page
SUPERVISOR'S DECLARATION	II
STUDENT'S DECLARATION	III
DEDICATION	IV
ACKNOWLEDGEMENTS	V
ABSTRACT	VI
ABSTRAK	VIII
TABLE OF CONTENTS	X
LIST OF TABLES	XIV
LIST OF FIGURES	XV
LIST OF SYMBOLS	XX
LIST OF ABBREVIATIONS	XXI
CHAPTER 1 INTRODUCTION	1
1.1 Background	1
1.2 Problem statement	3
1.3 Significance of studies	4
1.4 Research objectives	5
1.5 Research scope	5
1.6 Thesis outline	6
CHAPTER 2 LITERATURE REVIEW	7
2.1 Human skin physiology	7
2.1.1 General function of skin	8
2.1.2 Structural and mechanical properties of skin	9
2.2 Skin tissue engineering	10
2.3 Biomaterials in tissue engineering	18
2.3.1 Evolution of biomaterials	18
2.3.2 Characteristics of biomaterials scaffold	20

2.3.3	Biodegradable scaffolds	21
2.3.4	Classification of biomaterials	22
2.3.5	Hydroxyethyl cellulose	25
2.3.6	Poly (vinyl) alcohol	26
2.3.7	Collagen	28
2.4	Overview of nanoparticle	30
2.4.1	Silver nanoparticles	30
2.5	Summary	32
CHAPTER 3	MATERIALS AND METHODS	34
3.1	Research methodology	34
3.2	Materials preparation	35
3.3	Preparation of electrospinning aqueous polymeric solutions	36
3.3.1	Synthesis of HEC/PVA and HEC/PVA/collagen nanofibers scaffolds	36
3.4	Preparation of freeze-dried aqueous polymeric solutions	37
3.4.1	Synthesis of HEC/PVA freeze-dried scaffolds	37
3.4.2	Synthesis of HEC/silver nanoparticles freeze-dried scaffolds	37
3.5	Fabrication techniques	38
3.5.1	Electrospinning	38
3.5.2	Freeze-drying	41
3.6	Characterization technique	43
3.6.1	Scanning electron microscope	43
3.6.2	Attenuated total reflectance-Fourier Transform Infrared Spectroscopy	45
3.6.3	Thermogravimetric analysis	47
3.6.4	Differential scanning calorimetry	49
3.6.5	Mechanical properties	51
3.6.6	Ultraviolet-visible spectroscopy	53
3.6.7	Porosity study	55
3.6.8	Swelling ratio study	55
3.6.9	pH value measurements	56
3.6.10	Swelling ratio study	56
3.6.11	Weight loss study	56
3.7	Cell culture studies	57
3.7.1	Cell expansion and seeding	58
3.7.2	Cell morphology studies	59
3.7.3	A375 melanoma cell proliferation study	59
3.7.4	hFB cell proliferation study.	60
3.8	Statistical analysis	61

CHAPTER 4	FABRICATION AND CHARACTERIZATION OF SCAFFOLDS USING ELECTROSPINNING AND FREEZE-DRYING TECHNIQUES	62
4.1	CHEMICALLY CROSSLINKED STUDY OF HEC/PVA AND HEC/PVA/COLLAGEN NANOFIBERS SCAFFOLDS	62
4.1.1	Introduction	62
4.1.2	Morphology of HEC/PVA nanofibrous scaffolds	62
4.1.3	ATR-FTIR study	66
4.1.4	TGA measurements	68
4.1.5	DSC study	72
4.1.6	Mechanical properties	75
4.2	<i>IN VITRO</i> DEGRADATION STUDY OF HEC/PVA AND HEC/PVA/COLLAGEN NANOFIBERS SCAFFOLDS	77
4.2.1	Introduction	77
4.2.2	Morphological changes of nanofibers scaffold.	77
4.2.3	Weight loss, swelling ratio and pH value analysis	80
4.2.4	ATR-FTIR spectra analysis	84
4.2.5	DSC study	86
4.2.6	Mechanical characterization	88
4.3	MICROSTRUCTURE STUDY OF HEC/PVA POROUS SCAFFOLDS	90
4.3.1	Introduction	90
4.3.2	Microstructure of scaffolds	90
4.3.3	Porosity of scaffolds	92
4.3.4	Swelling ratio studies	93
4.3.5	<i>In vitro</i> degradation studies	94
4.3.6	ATR-FTIR spectroscopy analysis	95
4.3.7	Thermogravimetric (TGA) studies	97
4.3.8	Differential scanning calorimetry (DSC) study	99
4.3.9	Mechanical properties	101
4.4	STUDY OF HEC/SILVER NANOPARTICLES POROUS SCAFFOLDS	103
4.4.1	Introduction	103
4.4.2	Microstructure of HEC/AgNPs scaffolds	103
4.4.3	Porosity studies	105
4.4.4	Swelling ratio studies	106
4.4.5	<i>In vitro</i> degradation studies	107
4.4.6	UV-Vis absorbance spectroscopy	108
4.4.7	ATR-FTIR studies	109
4.4.8	TGA and DrTGA analysis	111
4.4.9	DSC study	113
4.5	Conclusion	114

CHAPTER 5	CELL CULTURE STUDIES ON NANOFIBERS AND FREEZE-DRIED SCAFFOLDS FOR SKIN TISSUE ENGINEERING APPLICATIONS	115
5.1	Introduction	115
5.2	Cells morphology studies	115
5.2.1	A375 cytotoxicity studies of HEC/PVA nanofibrous scaffolds	115
5.2.2	hFB cytotoxicity studies of HEC/PVA HEC/PVA/collagen electrospun nanofibrous scaffolds	117
5.2.3	hFB cells morphology on HEC/PVA porous scaffolds	118
5.2.4	hFB cells morphology on HEC/silver nanoparticles scaffolds	121
5.3	Cells proliferation studies	123
5.3.1	A375 cells proliferation studies on HEC/PVA nanofibrous scaffolds	123
5.3.2	hFB cells proliferation studies on HEC/PVA and collagen nanofibrous scaffolds	125
5.3.3	hFB cells proliferation studies on HEC/PVA porous scaffolds	126
5.3.4	hFB cells proliferation studies on HEC/silver nanoparticles scaffolds	128
5.4	Conclusion	129
CHAPTER 6	SUMMARY AND RECOMMENDATIONS	130
6.1	Summary	130
6.2	Recommendations for future studies	132
REFERENCES		134
ACHIEVEMENTS		160

LIST OF TABLES

Table No.	Title	Page
2.1	Examples of some commercially available skin substitutes	13
3.1	Summarized of samples prepared and incubation time points for cell culture studies in this work	59
4.1	Electrospinning parameters for HEC/PVA nanofibers and their corresponding average fiber diameter	64
4.2	TGA and DrTGA for polymer blends (CL-crosslinked, NCL- non-crosslinked)	72
4.3	DSC data and the characteristics (CL-crosslinked, NCL- non-crosslinked)	74
4.4	Mechanical data observed for the electrospun nanofibers (CL-crosslinked, NCL-non-crosslinked)	76
4.5	DSC data and the characteristics observed for the electrospun HEC/PVA and HEC/PVA/collagen nanofibers before and after <i>in vitro</i> degradation	86
4.6	Mechanical data of HEC/PVA and HEC/PVA/collagen nanofibers before and after degradation for up to 12 weeks	90
4.7	TGA and DrTGA data for HEC and PVA scaffolds	97
4.8	DSC data and the characteristics observed for the HEC, PVA and HEC/PVA blend samples	101
4.9	Mechanical data observed for the HEC, PVA and HEC/PVA blend samples	102
4.10	TGA and DrTGA data for HEC/AgNPs scaffolds	111
4.11	DSC data and the characteristics of HEC/PVA composites scaffold	114

LIST OF FIGURES

Figure No.	Title	Page
2.1	The structure of human skin	8
2.2	Evolution of biomaterials	19
2.3	Molecular structure of HEC	26
2.4	Molecular structure of PVA	27
2.5	Chemical structure of PVA and glutaraldehyde cross-linking	28
2.6	Triple-helical structure of collagen	29
3.1	Summary of research methodology implemented in this work	35
3.2	HEC/PVA (50:50) blended solution	37
3.3	HEC with 0.8% silver nanoparticles blended solution	38
3.4	Schematic diagram of the basic setup for electrospinning and Taylor cone Formation	40
3.5	Photograph of electrospinning machine, Electroris	40
3.6	Photograph of freeze-dryer machine, Labconco	42
3.7	The (a) HEC/PVA and (b) HEC/AgNPs freeze-dried scaffolds	43
3.8	Schematic diagram of a SEM	44
3.9	Photograph of SEM, Zeiss EVO 50	45
3.10	Graphical representation of multiple ATR reflection	46
3.11	Photograph of ATR-FTIR, Perkin-Elmer	47
3.12	Schematic diagram of TG-DTA system	47
3.13	Photograph of TGA	48
3.14	Schematic diagram of DSC	50

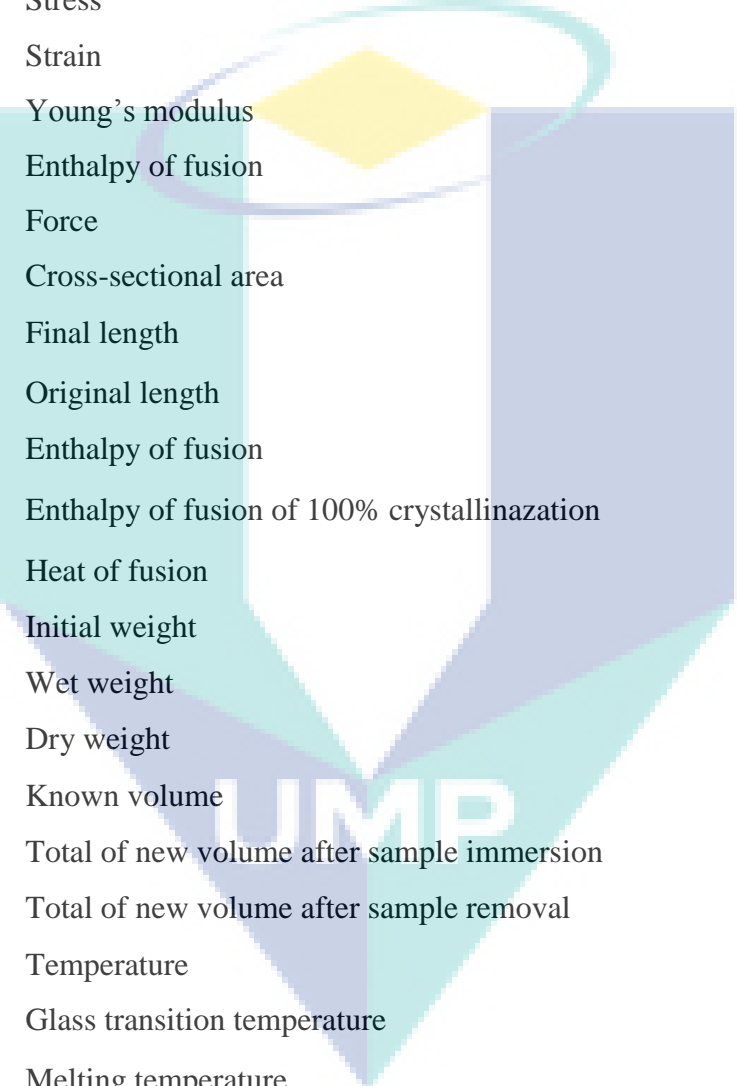
3.15	DSC thermograms	50
3.16	Photographs of DSC, TA instruments	50
3.17	Stress-strain curve diagram	52
3.18	Photograph of universal testing machine, Shimadzu	53
3.19	UV-Vis spectrophotometer, Thermoscientific	54
3.20	Collective oscillations of free electrons due to applied electric field	55
3.21	Summarize of cell culture study	57
3.22	Cell culture studies of HEC/PVA nanofibers scaffolds at different weight ratios	58
3.23	Photograph of ELISA microplate reader, VersaMax™	60
3.24	MTS assay of HEC/PVA nanofibers scaffolds at different weight ratios	61
4.1	Plot of the viscosity of the solution with respect to the wt% of the HEC/PVA (a) 50:50, (b) 40:60, (c) 30:70 in the solution	63
4.2	SEM images of HEC nanofibers mats (white arrow indicates the droplets)	64
4.3	SEM images and diameter distribution of electrospun HEC/PVA nanofibers: (a,b) H50P50, (c,d) H40P60, (e,f) H30P70, (g,h) with collagen	65
4.4	ATR-FTIR spectra of (i) non-crosslinked and (ii) crosslinked electrospun HEC/PVA nanofibers: (a) H50P50, (b) H40P60, (c) H30P70, (d) with collagen	67 - 68
4.5 (a*-d*)	TGA and drTGA curves for non-crosslinked electrospun HEC/PVA nanofibers: (a) H50P50, (b) H40P60, (c) H30P70, (d) with collagen	69
4.5 (a-d)	TGA and drTGA curves for crosslinked electrospun HEC/PVA nanofibers: (a)H50P50, (b) H40P60, (c) H30P70, (d) with collagen	71
4.6	DSC thermograms for (i) non-crosslinked and (ii) crosslinked electrospun HEC/PVA nanofibers:(a) H50P50, (b) H40P60, (c) H30P70, (d) with collagen	74

4.7	Stress-strain curves for (i) non-crosslinked and (ii) crosslinked electrospun HEC/PVA nanofibers: (a) H50P50, (b) H40P60, (c) H30P70, (d) with collagen	76
4.8	SEM micrographs of HEC/PVA and HEC/PVA/collagen nanofibrous scaffolds after degradation in DMEM media at different time	78
4.9	SEM micrographs of HEC/PVA and HEC/PVA/collagen nanofibrous scaffolds after <i>in vitro</i> degradation in PBS media at different time	79
4.10	Weight loss of HEC/PVA and HEC/PVA/collagen nanofibrous scaffolds after degradation in PBS and DMEM media for up to 12 weeks	81
4.11	Swelling ratio of HEC/PVA and HEC/PVA/collagen nanofibrous scaffolds after degradation in PBS and DMEM media for up to 12 weeks	82
4.12	pH value of HEC/PVA and HEC/PVA/collagen nanofibers scaffold after degradation for up to 12 weeks in (a) DMEM and (b) PBS solution	83
4.13	ATR-FTIR analysis before and after degradation for incubation up to 12 weeks. (a) HEC/PVA/collagen nanofibers immersed in DMEM solution; (b) HEC/PVA nanofibers immersed in DMEM solution; (c) HEC/PVA/collagen nanofibers immersed in PBS solution; (d) HEC/PVA nanofibers immersed in PBS solution	85
4.14	DSC thermogram before and after degradation for incubation up to 12 weeks: (a) HEC/PVA/collagen nanofibers immersed in DMEM solution; (b) HEC/PVA nanofibers immersed in DMEM solution; (c) HEC/PVA/collagen nanofibers immersed in PBS solution; (d) HEC/PVA nanofibers immersed in PBS solution	87
4.15	Stress-strain curves (i) before and (ii) after degradation for incubation up to 12 weeks: (a) HEC/PVA/collagen nanofibers immersed in DMEM solution; (b) HEC/PVA nanofibers immersed in DMEM solution; (c) HEC/PVA/collagen nanofibers immersed in PBS solution; (d) HEC/PVA nanofibers immersed in PBS solution.	89
4.16	SEM micrographs of interconnected porous scaffolds (a) pure HEC, (b) HEC/PVA (2:1), (c) HEC/PVA (1:1), (d) HEC/PVA (1:2) and (e) pure PVA	91

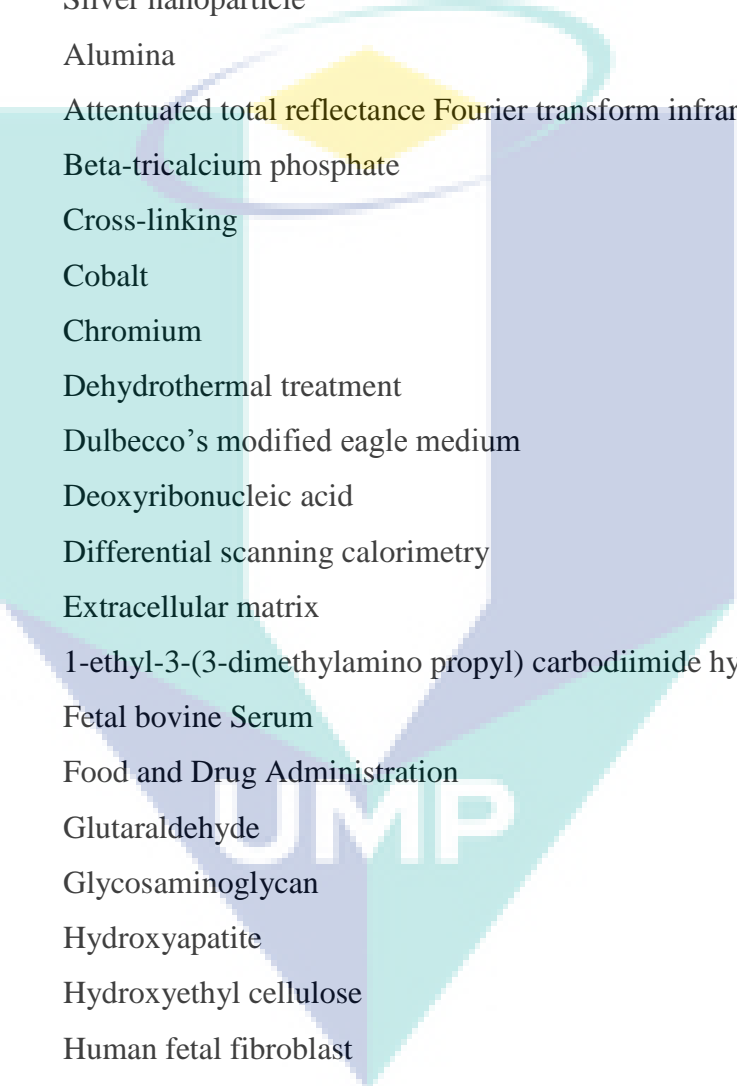
4.17	Porosity of different porous scaffolds	93
4.18	Swelling ratio of pure HEC, HEC/PVA (2:1), HEC/PVA (1:1), HEC/PVA (1:2) and pure PVA porous scaffolds	94
4.19	Percentage of weight loss of pure HEC, HEC/PVA (2:1), HEC/PVA (1:1), HEC/PVA (1:2) and pure PVA porous scaffolds	95
4.20	ATR-FTIR analysis for (a) pure HEC, (b) HEC/PVA (2:1), (c) HEC/PVA (1:1), (d) HEC/PVA (1:2) and (e) pure PVA porous scaffolds	96
4.21	TGA and DrTGA analysis for (a) pure HEC, (b) HEC/PVA (2:1), (c) HEC/PVA (1:1), (d) HEC/PVA (1:2) and (e) pure PVA porous scaffolds	99
4.22	DSC analysis for (a) HEC only, (b) HEC/PVA (2:1), (c) HEC/PVA (1:1), (d) HEC/PVA (1:2) and (e) PVA scaffolds	100
4.23	Stress-strain curves for (a) HEC only, (b) HEC/PVA (2:1), (c) HEC/PVA (1:1), (d) HEC/PVA (1:2) and (e) PVA scaffolds	102
4.24	(i) Photograph of HEC/AgNPs solution obtained at different concentrations of AgNO ₃ , (ii) macroscopic appearance of HEC/AgNPs scaffold, SEM micrograph of HEC/AgNPs scaffold at different concentrations of Ag (a) 0.4%, (b) 0.8%, (c) 1.6 %.	104 - 105
4.25	Porosity of HEC/AgNPs scaffolds with different Ag concentrations at 0.4%, 0.8% and 1.6%	106
4.26	Swelling ratio of HEC/AgNPs scaffolds with different Ag concentrations at 0.4%, 0.8% and 1.6%	107
4.27	Weight loss of degrading HEC/AgNPs scaffolds with different Ag concentrations at 0.4%, 0.8% and 1.6%	108
4.28	UV-Vis absorption spectra of HEC/AgNPs scaffolds	108
4.29	ATR-FTIR studies for HEC with different concentrations of Ag (a) 0.4%, (b) 0.8% and (c) 1.6% porous scaffolds	110
4.30	TGA and DrTGA analysis for HEC with different concentrations of Ag (a) 0.4%, (b) 0.8% and (c) 1.6% porous scaffolds	112
4.31	DSC study for HEC with different concentrations of Ag (a)	114

	0.4%,(b) 0.8% and (c) 1.6% porous scaffolds	
5.1	SEM micrographs of human A375 melanoma cells attached on nanofibrous scaffolds: (a) H50P50, (b) H40P60, (c) H30P70	116
5.2	SEM micrographs of hFB cells attached on HEC/PVA and HEC/PVA/collagen after 2, 4 and 7 days incubation	118
5.3 (i)	SEM micrograph images of hFB cells attached on (a) pure HEC, (b) HEC/PVA (2:1), (c) HEC/PVA (1:1), (d) HEC/PVA (1:2) and (e) pure PVA scaffolds after day 1 cell culture (black arrow indicates the growth cells)	119
5.3 (ii)	SEM micrograph images of hFB cells attached on (a) pure HEC, (b) HEC/PVA (2:1), (c) HEC/PVA (1:1), (d) HEC/PVA (1:2) and (e) pure PVA scaffolds after day 4 cell culture (black arrow indicates the growth cells)	120
5.3 (iii)	SEM micrograph images of hFB cells attached on (a) pure HEC, (b) HEC/PVA (2:1), (c) HEC/PVA (1:1), (d) HEC/PVA (1:2) and (e) pure PVA scaffolds after day 7 cell culture (black arrow indicates the growth cells)	121
5.4	SEM micrograph images of hFB cells attached on HEC with different concentrations of Ag (a) 0.4%, (b) 0.8% and (c) 1.6% scaffolds after 4 h and 24 h incubation period (black arrow indicates the growth cells)	122
5.5	Graph showing human A375 melanoma viability after 1, 3 and 7 days of incubation (1×10^5 cells/well in complete DMEM) at different weight ratios of nanofibrous scaffolds. (<i>H</i> -HEC content, <i>P</i> -PVA content)	124
5.6	Graph showing human fibroblast viability after 2, 4 and 7 days of incubation (1×10^5 cells/well in complete MEM) at different weight ratios of nanofibrous scaffolds	126
5.7	Graph showing human fibroblast viability after 2, 4 and 7 days of incubation (1×10^5 cells/well in complete MEM) at different weight ratios of HEC/PVA scaffolds	127
5.8	Graph showing human fibroblast viability after 4, 12 and 24 h of incubation (1×10^6 cells/well in complete MEM) of HEC in different concentrations of Ag (a) 0.4%, (b) 0.8% and (c) 1.6% scaffolds	128

LIST OF SYMBOLS

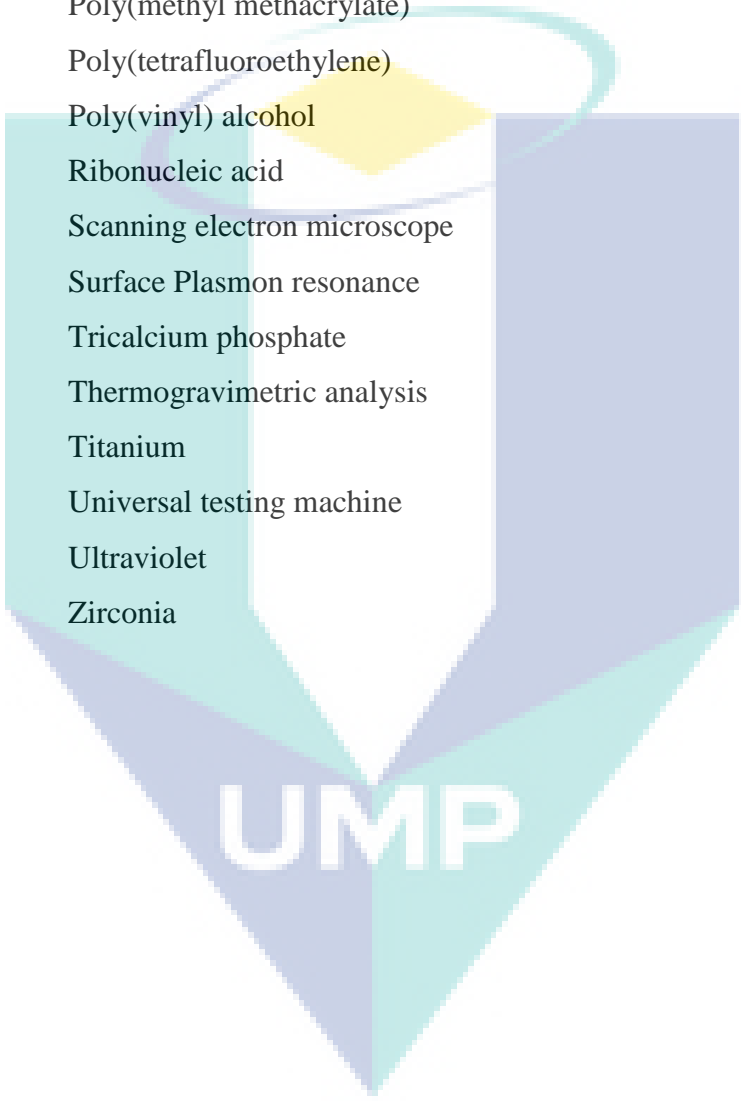


χ_c	Crystallinity
σ	Stress
ε	Strain
E	Young's modulus
ΔH	Enthalpy of fusion
F	Force
A_o	Cross-sectional area
L_f	Final length
L_o	Original length
ΔH_f	Enthalpy of fusion
ΔH_f^o	Enthalpy of fusion of 100% crystallization
ΔH_m	Heat of fusion
W_o	Initial weight
W_t	Wet weight
W_d	Dry weight
V_1	Known volume
V_2	Total of new volume after sample immersion
V_3	Total of new volume after sample removal
T	Temperature
T_g	Glass transition temperature
T_m	Melting temperature
d	Diameter
λ	Wavelength

LIST OF ABBREVIATIONS

AgNO ₃	Silver nitrate
AgNP	Silver nanoparticle
Al ₂ O ₃	Alumina
ATR-FTIR	Attenuated total reflectance Fourier transform infrared spectroscopy
Ca ₃ (PO ₄) ₂	Beta-tricalcium phosphate
CL	Cross-linking
Co	Cobalt
Cr	Chromium
DHT	Dehydrothermal treatment
DMEM	Dulbecco's modified eagle medium
DNA	Deoxyribonucleic acid
DSC	Differential scanning calorimetry
ECM	Extracellular matrix
EDC	1-ethyl-3-(3-dimethylamino propyl) carbodiimide hydrochloride
FBS	Fetal bovine Serum
FDA	Food and Drug Administration
GA	Glutaraldehyde
GAG	Glycosaminoglycan
HA	Hydroxyapatite
HEC	Hydroxyethyl cellulose
hFB	Human fetal fibroblast
HUVECs	Human umbilical vein endothelial cells
MEM	Minimum essential media
NaBH ₄	Sodium borohydride
NCL	Non-cross-linking
PBS	Phosphate buffered saline
PCL	Polycaprolactone
PE	Poly(ethylene)

PET	Poly(ethylene terephthalate)
PFF	Polypropylene fumarate
PGA	Polyglycolic acid
PLA	Poly(lactic) acid
PLGA	Poly(lactic-co-glycolic acid)
PLLA	Poly-L-lactide acid
PMMA	Poly(methyl methacrylate)
PTFE	Poly(tetrafluoroethylene)
PVA	Poly(vinyl) alcohol
RNA	Ribonucleic acid
SEM	Scanning electron microscope
SPR	Surface Plasmon resonance
TCP	Tricalcium phosphate
TGA	Thermogravimetric analysis
Ti	Titanium
UTM	Universal testing machine
UV	Ultraviolet
ZrO ₂	Zirconia



UMP

CHAPTER 1

INTRODUCTION

1.1 BACKGROUND

Skin is the largest organ of the human body. It serves as a barrier against pathogenic microbial agents, UV irradiation, mechanical disturbances, and protects substantial loss of body fluids. Loss of skin integrity arising from acute trauma, chronic wounds and severe burns may result in organ malfunction or even death (Sangur, 2010). Tissue engineering can be defined as a combination of multidisciplinary fields that applies the principles and systematic procedures of engineering and biological sciences that restore, maintain or improve the structure and functions of damaged tissue (Sachlos and Czernuszka, 2003). The emergence of tissue engineered skin replacements have conquered several limitations over conventional tissue transplants of autograft, allograft and xenograft such as preventing additional surgical procedures, eliminating the chance of graft rejection or the transmission of infection diseases (Böttcher-Haberzeth et al., 2010). For these reasons, the use of artificial skin equivalents becomes great and extensively grown in skin tissue markets. Moreover, since skin transplant becomes clinically practicable, the demand for safe, affordable and stable product always exceeds the available supply. In 2009, Medtech Insight reported that the potential US market for tissue engineered skin replacement and substitutions total approximately \$18.9 billion based on target population of approximately 5.0 million people (Medtech Insight, 2014). This target population is expecting to reach 6.4 million people that result in approximately \$24.3 billion by 2019. In skin tissue market, a wide variety of skin substitutes such as Alloderm®, Graftjacket® and Gammagraft® have been clinically tested and approved by Food and Drug Administration (FDA). These commercial products are introduced into the market especially for superficial, partial and deep burn

wounds and chronic ulcers. However, most of these bioengineered skin substitutes necessitate high cost, expertise and experience that might confer difficulty and financial issue to some patients. For instance, the cost of Apligraf® is about \$ 1,000 to \$ 1, 200 per use and at least \$2000 is needed for an 8” x 10” sheet of Integra™ skin. In other cases, the price of Epicel™ including operation procedure can range from \$ 6,000 to \$10,000 per 1% total body area surface.

The basic concepts of tissue engineering are to harvest a small biopsy of the specific cells from the donor site and expand the cells in a Petri dish. After confluence, the cells are seeded on a polymeric scaffold for *in vitro* cell culture study and consequently transplanted into the defect area of a patient’s body (Arya et al., 2009). Three main factors that contribute to the success of tissue engineering are cells, scaffolds and cell-scaffold interactions that play a major role in organizing and assembling subsequent function into particular tissues. Nowadays, research using nano biomaterials as scaffolds in skin tissue engineering is tremendously increasing as these biomaterials mimic the structure of extracellular matrices and provide a platform for cell attachment, differentiation and proliferation. Biopolymer used to construct three-dimensional scaffolds should be biocompatible, biodegradable, highly porous in structure, and possessing adequate mechanical strength and stability. The nanoscale biomaterials are produced *via* several methods including self-assembly, template assisted synthesis, drawing, phase separation and electrospinning (Kumbar et al., 2008). However, electrospinning gains most interest among researchers because of the capability to fabricate a variety of polymeric nanofibers (Huang et al., 2003). Electrospinning is a technique that produces fibers in nanometer length and interconnected pores that closely resemble the topography features of ECM. It is a versatile technique to produce nano and microfibers from polymer solutions or melts in the range of 30-200 nm through the action of high electric fields (Taylor et al., 2006; Reneker and Chun, 1996 and Yarin et al., 2001). The morphology and properties of the nanofibers can be varied by changing the process parameters such as solution viscosity and conductivity, applied voltage, average molecular weight of the polymer and the distance between the needle and the collector plate (Zong et al., 2002 and Shin et al., 2001). The main attractions of the electrospun nanofibers are their unique properties such as high surface area-to-volume ratio, high porosity, and their diameter, which is in

the nanometer range. Scaffold fabrication by lyophilization or freeze-drying is another convenient technique to produce highly interconnected micropore structures. Freeze-drying removes most of the water from the sample under vacuum to obtain highly porous architecture scaffolds. Porous microstructures are very important especially for nutritional support and removal of metabolic waste produced by the populated cells in the injured site (Xiao et al., 2011). The microstructure of the design scaffolds have to mimic the native structure of the extracellular matrix (ECM) to support and enhance the growth of new tissue during the recovery period.

Although current skin engineered constructs seem to increase healing rates of burn or chronic injuries, the dire demands on less complex tissue-engineered construct that are relatively cost-effective with minimal risk of infection still remain as great challenges. Until this day, no ideal skin substitute is successfully achieved, thus consequently leading to continuous studies in finding the optimal criteria for suitable skin substitute equivalent. In regard to this, it is vital to understand the influence of polymer scaffolds on cellular function and behaviour. Therefore, further research should be executed to compare and characterize different types of skin substitutes and evaluate the substrates' biological response for skin tissue engineering applications.

1.2 PROBLEM STATEMENT

Skin tissue engineering using scaffolds overcomes the limitations from several wound healing processes like autografts, allografts and xenografts (Groeber et al., 2011 and Macneil, 2008). The advent of skin tissue substitutes revolutionized the therapeutic potential for critical wounds and wounds that are not amenable to primary closure. Although conventional transplant revealed efficient performance, they still present several limitations such as double surgery site, immune rejection, risk of infection and viral transmission. At worst, most organ recipients need to take drugs for suppression of natural immune responses, which may lead to immunological imbalances or even tumor growth in the long term (Zhang and Michniack-Khon, 2012).

In previous research, scaffolds that have suitable surface chemistry and excellent mechanical strength have been fabricated from several natural and synthetic polymers,

which includes chitin, chitosan, polyurethane (PU), nylon, polyglycolic acid/poly(lactic acid) (PGA/PLA), poly(L-lactide) (PLLA), polycaprolactone (PCL), and copolymer poly(ethyleneglycolterephthalate)-poly(butylene terephthalate) (Dai et al., 2004 and Beumer et al., 1993). Fabrication of nanomaterials from most of these polymers require harmful or organic acid solvents like acrylic acid, acetic acid, chloroform, trifluoroacetic acid and 1,1,1,3,3,3-hexafluoro-2-propanol, give difficulties to researchers to handle the toxic solvents (Zhang et al., 2006, Liu et al., 2011 and Huang et al., 2003). In addition, although there are a number of commercially bioengineered skin substitutes available in the market- as will be outlined in Chapter 2 of this thesis- due to high prices, poor vascularization and toxicity issues during synthesis process, there are tremendous demands for tissue engineered biopolymer scaffolds, which are comparably cost-effective, better cell-tissue interaction and constructed in an environmentally friendly way. As a key to address these issues, designation and fabrication of scaffolds that possess as accurate as possible the characteristics of native ECM with no adverse effects on the damaged skin are immensely favourable.

1.3 SIGNIFICANCE OF STUDIES

In this work, HEC nanomaterials were prepared using a 'green' chemistry approach in a straightforward procedure. The HEC solutions were prepared using water as the only solvent. The HEC scaffolds were synthesized using two simple techniques, which are electrospinning and freeze-drying. This research aims to develop non-toxic, biocompatible, and biodegradable scaffolds that can potentially be commercialized as skin substitute equivalents. Since a small amount of HEC powder can be processed to produce scaffolds in large scale, this novel material will be of high demand in tissue engineering markets that lack superior healing rate scaffolds with affordable prices. The findings of this work will merit the medical community especially those who work in skin tissue engineering as well as low and middle-class patients who bear acute burn injuries, ulcers, and venous stasis that prerequisite cost-effective scaffolds with rapid healing response.

1.4 RESEARCH OBJECTIVES

The main objectives of this thesis are:

- i. To fabricate scaffolds based on HEC/PVA, HEC/PVA/collagen and HEC/Ag nanoparticles using an aqueous polymeric-solution-based electrospinning and freeze-drying techniques.
- ii. To evaluate the physical, chemical, thermal and mechanical properties of all scaffolds produced.
- iii. To investigate the potential of the produced scaffolds as substrates for skin tissue engineering applications.

1.5 RESEARCH SCOPE

The following research scopes are essential to achieve the first objective:

- i. To optimize the viscosity of the electrospun polymer solution for developing uniform, beadless and continuous nanofibers.
- ii. To optimize the electrospinning parameters such as high applied-voltage, feed rate, tips-to-collector distance and rotation speed that tailor the diameter of nanofibers.
- iii. To find the effect of different weight ratios of HEC/PVA scaffolds that offer the best performance as skin tissue engineered scaffolds.
- iv. To optimize the concentration of HEC as a reducing agent in the formation of silver nanoparticles and also the concentration of AgNO_3 that would generate an ideal HEC/silver nanoparticle based scaffold.

The following research scopes are necessary to achieve the second objective:

- i. To identify surface morphology *via* SEM images and to measure the diameter of the fiber and the pore size of all scaffolds using ImageJ software.
- ii. To recognize the functional groups of all scaffolds using ATR-FTIR spectra.
- iii. To examine the thermal stability and decomposition behaviour of scaffolds using TGA and DSC.

- iv. To study the strength of scaffolds by analyzing the stress-strain curves using UTM.
- v. To identify the pore size and porosity of the freeze-dried scaffolds.
- vi. To investigate the degradation behaviour of electrospun polymer scaffolds in PBS and DMEM at different time points. The analysis will involve pH changes of the solutions, weight loss and swelling ratio.

Finally, the following research scopes are necessary to achieve the third objective:

- i. To investigate the cellular biocompatibility by carrying out *in vitro* cell culture studies and measure the absorbance value using MTT and MTS assays.
- ii. To determine the adherence, differentiation and proliferation of skin melanoma and fibroblast cells on the scaffolds and observe surface morphological changes by SEM.
- iii. To configure the potential incorporation of collagen with HEC/PVA electrospun mats that might display positive response towards skin cells.
- iv. To compare the effect of different weight ratios of HEC/PVA and HEC with different concentrations of AgNO_3 as potential substrates for skin tissue engineering applications.

1.6 THESIS OUTLINE

The following is a brief aspect of the contents in this thesis. Chapter 2 provides a comprehensive overview of former and recent research on skin tissue engineering and details of polymeric materials involved in the research. Chapter 3 presents the experimental method used in this work and the working principle of the instruments used for characterization. Chapter 4 discusses the synthesis and characterization of HEC/PVA, HEC/PVA/collagen and HEC/AgNPs scaffolds. Chapter 5 outlines the cell culture studies on the scaffolds for skin tissue engineering application. Finally, the summary of this work and the recommendations for future work are given in Chapter 6.

CHAPTER 2

LITERATURE REVIEW

2.1 HUMAN SKIN PHYSIOLOGY

Human skin represents approximately one-tenth of body mass. Skin consists of different cell types found in three layers that are epidermis, dermis, and hypodermis (subcutaneous layer) as illustrated in Figure 2.1. Keratinocytes are the basic cell type in the epidermis. It contains 90 – 95 % epidermal cells originated from the basal layer. On the other hand, melanocytes are initiated in the lower layer of the epidermis. The epidermal layer is thin and entirely cellular but can still suffice in thickness to provide vital barrier function and protects the body against pathogens and microorganisms (Groeber et al., 2011).

The dermis is built by a dense and irregular connective tissue that protects blood vessels, hair follicles, sweat glands and other structures. It composes of two layers that are the papillary and the reticular layers. The outer papillary layer has a loose connective tissue comprising of anchoring fibrils and plenty of dermal cells. The dermis is secured to the epidermis *via* the basement membrane zone by anchoring fibrils. The reticular layer has a compact connective tissue consisting of massive bundles of collagen and elastic fibers. The structure and organization of these fibers provide the dermis with strength and resilience. The reticular dermis is connected to the hypodermis by a network of fibers.

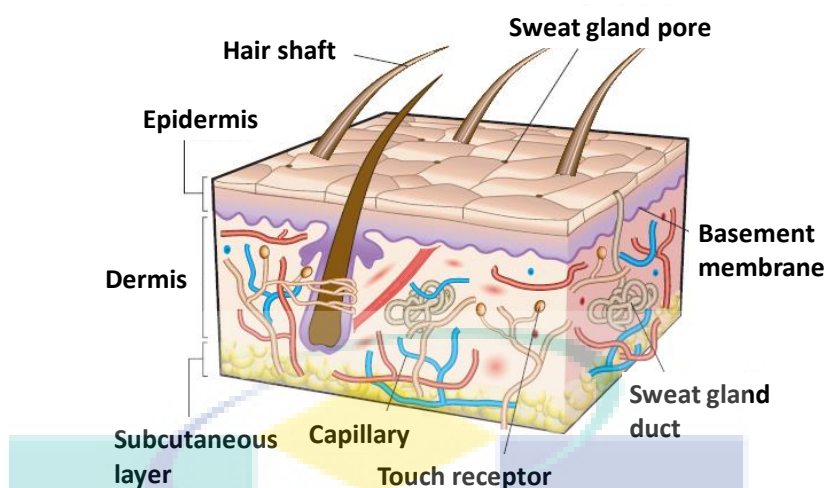


Figure 2.1: The structure of human skin (Millington & Wilkinson, 2009)

2.1.1 General function of skin

Skin consists of three consecutive layers, which are epidermis, dermis and hypodermis. They work together to protect the body through body temperature regulation, provide sensation and excretion, as a blood reservoir and synthesizes vitamin D (Tortora and Bryan, 2012).

The epidermis' function is to prevent water loss *via* evaporation. In the epidermis, melanocytes play a critical role as a protective barrier for the underlying tissues. The presence of melanocyte cells in releasing pigmentation act as a shield towards harmful sun rays, which is essential for human skin in order to avoid numerous injurious effects including skin cancer. In addition, the melanocytes are also responsible for the synthesis of vitamin D (Freinkel and Woodley, 2001). It is well-known that the epidermis contains keratin- a tough, fibrous protein- and has no blood supply. Hence, the epidermis will gain nutrients from the papillary layer of the dermis.

The dermis is a layer of connective tissue consisting of blood vessels, fibers, cells, and gelatinous materials that support and nourish the epidermis (Maceo, 2011). It also serves as a blood reserve and is responsible for sensory reception and temperature regulation. The papillary layer, which provides oxygen and nutrients to the epidermis

and the reticular layer, is critical to maintain skin integrity and to protect the body from external stimuli. Fibroblasts that form the lower dermal layer provide strength and resilience. It is also capable of producing remodelling enzymes such as proteases and collagenases. Both enzymes play an important role in the wound healing process (Metcalf and Ferguson, 2007). The dermis is vascularized and contains receptors for touch, temperature and pain as well as hair follicles and sweat ducts in which the latter are lined with keratinocytes that contribute to epidermal regeneration. Below that lies the reticular or deep dermis, which has dense collagen fibers and overlies the subcutaneous fat layer (Watt and Fujiwara, 2011). Below the dermis, there is a layer of fat that helps to insulate the body from heat and cold and serves as an energy storage area (MacNeal, 2014).

The epidermal-dermal junction is an interface between the epidermis and the dermis, i.e. the basement membrane. It has three major functions. First, it provides a permeable barrier between the vascular dermis and avascular dermis. Second, it is thought to influence the epidermal cells during their differentiation, growth and repair. Lastly, it provides adherence to the underlying tissues. In addition, the structure of the epidermal-dermal junction may significantly affect the tissue integrity. The skin capillaries are situated just under the reticulation sheet of the papillary layer of the dermis, providing oxygen and nutrients to the epidermis. Thus, if the junction becomes flattened, capillary density becomes less and consequently compromises tissue viability.

2.1.2 Structural and mechanical properties of skin

Skin is a multi-layered material with well-defined anatomic regions (Smith et al., 1982 and Ramshaw, 1986). The superficial epidermis forms an uninterrupted barrier that ranges in thickness from 0.07 mm to 0.12 mm over most of the body surface (Silver, 1987) and contributes little to the mechanical properties (Silver et al., 1992). The dermis has thickness in the range of 1 mm to 4 mm (Smith et al., 1982). The papillary dermis forms the upper layer, which comprises about 10 % of the full dermal thickness. It contains thin collagen fibrils, 20 – 40 nm (Smith et al., 1982) in diameter that are bound to thicker collagen fibers of 0.3 – 3.0 μm in diameter (Brown, 1972). Below the papillary layer is the reticular layer, which contains collagen fibrils 60 – 100

μm in diameter. Reticular collagen fibrils are composed primarily of type I collagen and have fiber diameters between 10 μm and 40 μm (Smith et al., 1982). Type III collagen accounts for only approximately 15 % of the dermal collagen, most of it is in the papillary layer (Smith et al., 1982).

The skin has important protective functions against mechanical trauma such as friction, impact, pressure, cutting, and shear. It must be an active or adaptable barrier between physiological conditions within the body and the varying ambient environment. The skin must also help regulate the internal environment by dissipating or conserving heat. The strength of the skin depends on proteoglycans as well as the structure and properties of collagen and elastic fibers that are found in the skin. Results from *in vitro* tests done by Edwards and Marks have estimated the skin properties from fundamental mechanical studies of strength and elasticity in the architecture of human skin (Edwards & Marks, 1995). The reports claimed that the tensile strength of skin ranges from 5 to 30 N/mm^2 , with the mean of about 21 N/mm^2 at 8 years, declining to about 17 N/mm^2 at 95 years. The ultimate modulus of elasticity calculated from the end portion of the stress-strain curves ranges from approximately 15 to 150 N/mm^2 . The mean shows a maximum value of about 70 N/mm^2 at age 11, with a shallow decline to about 60 N/mm^2 at 95 years. The ultimate strain varies from about 35 to 115%. The mean value decreases in a linear fashion from 75% from birth to 60% at 90 years. The study of mechanical behaviour in skin tissue engineering is crucial to ensure the stiffness of the material meets the requirements of an ideal scaffold for skin tissue regeneration.

2.2 SKIN TISSUE ENGINEERING

Tissue-engineered skin has been practiced clinically for the last 30 years and is known as the most advanced wound management technology. The first written report on skin xenograft was found in 15th century BC in the medical document of Ebers Papyrus while the first clinical use of human skin allograft was originally described in the manuscript of Branca of Sicily in 1503 (Halim et al., 2010).

Generally, tissue-engineered skin covers situations in which: (i) cells delivered on their own, (ii) cells delivered within two or three dimensional biomaterials, (iii)

biomaterials for replacement skin's dermal layer (with and without cells), and (iv) biomaterials to support the replacement of both epidermis and dermis (Macneil, 2008). Skin defects caused by skin or cutaneous wounds may interrupt skin functions at various stages leading to permanent disability or even death depending on the severity of the injury. Skin wounds that emerge from burns, aging, mechanical trauma, surgical procedures and reduced blood circulations may be capable of healing itself (Zhong et al., 2010). However, any loss of full-thickness skin of more than 4 cm in diameter will not heal without surgical intervention (Herndon et al., 1989). Additional surgery involving skin substitutes might be required to repair and regenerate large scale skin defects. These skin substitutes will provide a temporary scaffold for skin regeneration and allow early wound excision as well as help to improve other functional and aesthetic qualities.

Skin substitutes are defined as various groups of wound coverage materials that aid in wound closure and replace the functions of the skin, either temporarily or permanently, depending on the product characteristics (Halim et al., 2010). The initial inclination of bioengineered skin substitute technology is to replace autograft, allograft and xenograft, which are also recognized as biological substitutes (Eisenbud et al., 2004). The biological skin substitute experiments started with the introduction of skin grafting by Reverdin in 1871 (Horch et al., 2005). However, skin grafts face many limitations including donor site availability especially in the case of extensive skin loss or immune rejection in allogeneic skin grafts, pain, scarring, slow healing and infection (Yannas et al., 1989).

Therefore, through the advancement and progress of biotechnology and tissue engineering, researchers have conducted research on a broad range of skin substitutes to overcome the limits for the treatment of wounds and burn injuries. Both Zhang and Michniak-Kohn reported that clinical skin replacements and grafts are in high demand for the treatment of skin injuries with approximately 50% of tissue engineering and regenerative medicine market revenues (Zhang and Michniak-Kohn, 2012). Commercially bioengineered skin substitutes that are available in today's market can be classified into the following types and some of them are summarized in Table 2.1

(Synder et al., 2012; UCare, 2013; Blue Cross Blue Shield Association, 2002; Harding et al., 2010 and Arbor Health Plan, 2014):

- a) Cultured epithelial autografts
- b) Human skin allografts derived from donated human cadaver tissue
- c) Allogenic matrices derived from human neonatal fibroblasts
- d) Composite matrices derived from human keratinocytes, fibroblasts, and bovine or porcine collagen
- e) Acellular matrices derived from porcine or bovine collagen

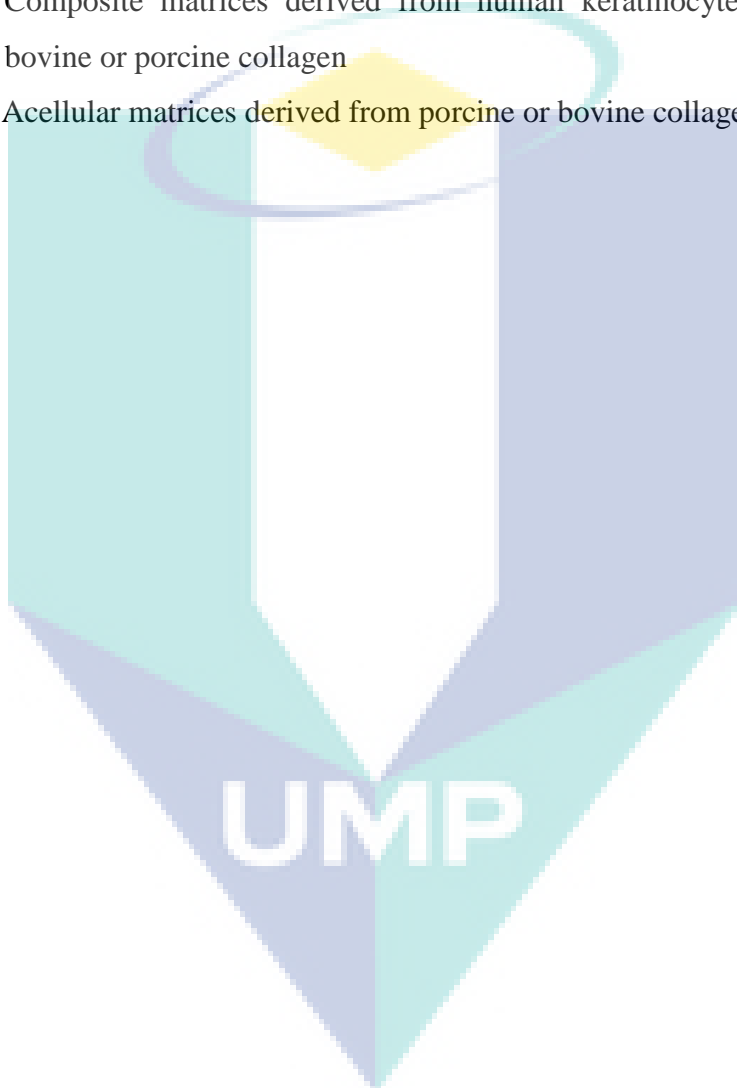


Table 2.1: Examples of some commercially available skin substitutes

Product	Manufacturer	Description	Indication/uses	Disadvantages
(a) Cultured epithelial autografts				
Epicel tm	Genzyme Tissue Repair; Cambridge, MA	Cultured epidermal autograft.	Severe deep dermal, full thickness burns.	Expensive. 2-3 week lag period between biopsy and obtaining epidermis. Lacks dermal component.
Epidex tm	Euroderm AG (Baden-Dättwil, Switzerland)	Generated from patients hair follicles.	Treatment of chronic leg ulcers.	2-3 week lag period between biopsy and obtaining epidermis. Lacks dermal component. Not suitable for deep burns or infected wounds. No FDA approved
Hyalomatrix [®]	Fidia Advanced Biopolymers; Abano Terme, Italy.	Bioresorbable dermal substitute made of long-derivative hyaluronic acid.	Partial and full thickness wounds, ulcers, surgical and traumatic wounds, burns.	Expensive. Not suitable for infectious wounds. On jellifying, it takes on a greenish colour which can be misinterpreted as a symptom of infection.
(b) Human skin allografts derived from donated human cadaver tissue				
Alloderm [®]	Life Cell Corp.; The Woodlands, TX.	Processed from human cadaver skin with acellular dermal matrix and intact basement membrane.	Hernia repair, breast reconstruction postmastectomy, reconstructive, micro, gastrointestinal and cardiovascular surgical.	May necessitate removal after 2-3 week. Autograft is needed for epithelial cover. Not suitable for infected wounds.

Table 2.1: Continued

Product	Manufacturer	Description	Indication/uses	Disadvantages
Alloskin™	Allosource Inc.; Centennial, CO.	Derived from epidermal and dermal cadaveric.	For traumatic and chronic wounds.	May causing visible rippling and contour irregularities. No immune response is elicited after replacement.
Gammagraft™	Promethean Lifesciences, Inc.; Pittsburgh, PA.	Derived from a γ -irradiated cadaveric allograft.	Treating wounds including venous stasis ulcers, diabetic foot ulcers, and full-thickness wounds.	Temporary dressing that may require multiple applications.
Graftjacket®	Wright Medical Technology; Arlington, TN.	Originates from cadaveric skin.	Deep and superficial wounds.	History of unsuccessful treatment that consisted of two failed.
Theraskin®	Soluble Solutions, Newport News, VA.	Composed of living cells; fibroblasts, and keratinocytes, and a fully developed extracellular matrix.	Diabetic foot ulcers, venous stasis ulcers, and pressure ulcers.	Not suitable for patients with a known history of hypersensitivity to collagen or bovine products.
(c) Allogenic matrices derived from human neonatal fibroblasts				
Allomax™	Bard Davol, Incooperation.	Regenerate from human collagen matrix.	Soft tissue repair including hernia and abdominal wall reconstruction, and	Lack of tensile strength.

Table 2.1: Continued

Product	Manufacturer	Description	Indication/uses	Disadvantages
			post-mastectomy breast reconstruction.	
Celaderm®	Advanced Biohealing; Westport, CT.	Contains metabolically active human foreskin derived from allogeneic keratinocytes.	Partial and full thickness burns, venous wounds.	No FDA approved.
Dermagraft®	Advanced Biohealing; Westport, CT / Smith & Nephew, Inc.; La Jolla, CA.	Living dermal replacement that employs human neonatal foreskin fibroblasts.	Diabetic foot ulcers (ulcers secondary to epidermolysis bullosa)	Difficult logistics of ordering and application and short shelf life (unless stored cryopreserved).
(d) Composite matrices derived from human keratinocytes, fibroblasts and bovine or porcine collagen				
Apligraf®	Organogenesis, Inc.; Canton, MA.	The epidermal layer consists of live keratinocytes, while the dermal layer contains living fibroblasts.	Venous/ diabetic ulcers.	Expensive. Additional applications beyond five in a one year period.
Orcel™	Ortec International, Inc.; New York.	Human epidermal keratinocytes and dermal fibroblasts	Venous and diabetic wounds.	Requires cryopreserved storage.

Table 2.1: Continued

Product	Manufacturer	Description	Indication/uses	Disadvantages
		that are cultured into two separate layers on a bovine collagen sponge.		
Transcyte™	Advanced biohealing; Westport, CT.	Consist of polymer membrane and neonatal human fibroblast cells cultured.	Full and partial-thickness burns.	Silicone membrane must be removed.
(e) Acellular matrices derived from porcine or bovine collagen				
Biobrane®	UDL Laboratories Inc.; Rockford, IL.	Constructed using collagen (porcine type 1) that is incorporated with both silicone and nylon.	To cover partial thickness burns and skin graft donor site.	Temporary. Not suitable for infected wounds.
Ez derm™	Brennen Medical, Inc.; St. Paul, MN.	Porcine derived xenograft in which the collagen has been chemically cross-linked with aldehyde.	Partial-thickness burns, venous ulcers, diabetic ulcers, pressure ulcers.	Not suitable for deep burns. Not suitable for infected wounds.
Integra® dermal regeneration template	Integra Lifesciences Corp.,	ECM fibers of cross-linked bovine collagen and	Deep partial-thickness and full-thickness burns.	Expensive. Operative removal of silicone layer required.

Table 2.1: Continued

Product	Manufacturer	Description	Indication/uses	Disadvantages
	Plainsboro, NJ.	chondroitin-6-sulfate with silicone backing.		
Matristem® wound matrix	Acell inc. Jessup, MD.	Derived from porcine in single or multi-layer of ECM sheet.	Diabetic foot ulcers, venous leg ulcers, pressure ulcers and second degree burns.	Scar tissue would be expected.
Oasis burn matrix™	Cook Biotech Incorporated; West Lafayette, IN, USA.	Derived from porcine small intestinal submucosa (sis).	Partial and full-thickness pressure, venous and diabetic wounds or burns.	Requires reapplication every 5-7 days.
Primatrix™ Dermal Repair Scaffold	TEI Biosciences Inc.; Boston, MA.	ECM created from the submucosal layer of porcine small intestine.	Diabetic ulcers, venous static ulcers, partial thickness wounds, surgical wounds, trauma wounds.	Not suitable for patients with a known history of hypersensitivity to collagen or bovine products. Not indicated for third-degree burns.

2.3 BIOMATERIALS IN TISSUE ENGINEERING

2.3.1 Evolution of biomaterials

Biomaterials are defined as a substance, other than drugs, or a combination of substances, derived from natural or synthetic origins to be used in any period of time, as a whole or as a part of the system that treats, augments or replaces any tissue, organ, or function of the body (Williams, 1987). Later, biomaterial had been defined by Black et al. as a natural or manmade origin, which is used to direct, supplement, or replace the functions of living tissues of the human body (Black, 1992). The use of biomaterials were first reported around 2000 BC where the Egyptians applied elephant's tusks, walrus teeth and linen to replace bone, missing teeth or wound closure (Williams and Cunningham, 1979).

The twentieth century is a milestone for most currently used biomaterials and surgical implants with the first metallic bone plate made of vanadium steel introduced in 1912 by Sherman. However, due to mechanical failure, corrosion and poor biocompatibility, in the 1920s, several less steel alloys were developed with superior strength and notable corrosion resistance. In 1947, the use of titanium and its alloys into surgical applications was successfully introduced by Cotton with improved biocompatibility, strength, corrosion resistance and wear resistance. Back then, the use of polymethyl methacrylate (PMMA) was mentioned as the first synthetic polymer used for denture bases in 1939 followed by corneal replacement in the 1940s.

In 1963, alumina (Al_2O_3) was the first ceramic material used mainly for orthopedic and dental implants followed by zirconia (ZrO_2) in the 1980s. Both of these ceramics were popular owing to its excellent biocompatibility, hardness, strength to resist fatigue and corrosion resistance. However, chemical inertness of these materials gave no chance of tissue-implant interactions leading to implant loosening within a short time. Therefore, in the 1970s, a new bioactive ceramic such as hydroxyapatite (HA) was introduced in dentistry and orthopedic as a result of its structural and compositional similarity to minerals of calcified tissue. Ducheyne et al. once reported

that ceramic-coated metallic implants (HA-coated metallic) increased the bonding strength and bone volume compared to uncoated metals (Ducheyne et al., 1980).

It is worth to mention that as a result of various contributions from expertise and researchers to the new processing methodologies, design principles and surgical techniques in the last 50 years, today, we gain the benefit of some excellent biomaterials and surgical implants that improved the quality of lives of many people each year around the world. In recent years, nanotechnology, biomimetics and tissue engineering concepts are generating a new phase of challenges in the development of biomaterials at nanoscale levels. As per the literature survey, each year, we noticed the increase in the number of published studies detailing on potential nano biomaterials intended for hard and soft tissues. Some of the developments of biomaterials over the last few decades are illustrated in Figure 2.2. This evolution trend clearly indicates the potential of nano biomaterials as processing methodologies to face the medical challenges in daily life.

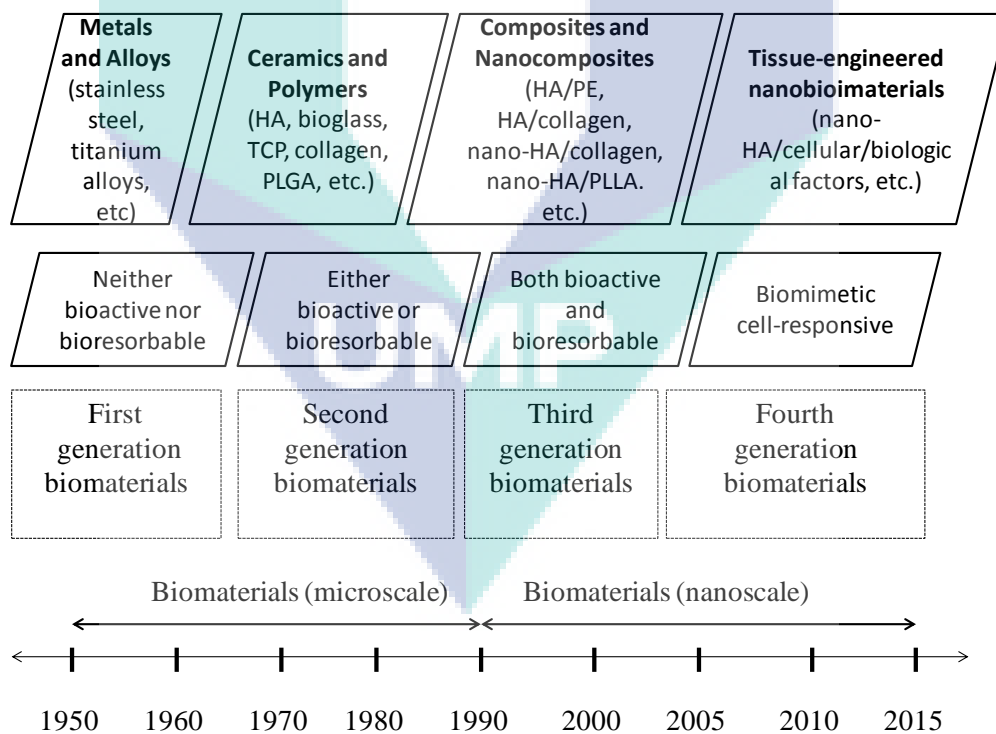


Figure 2.2: Evolution of biomaterials (Ramakrishna, 2011)

2.3.2 Characteristics of biomaterials scaffold

The structural and behaviour characteristics of tissue scaffold including physical, mechanical, chemical and biological are critical to ensure normal cell activities and performance during cell cultivation (Karp et al., 2003). The ideal scaffold should meet the physiological demands of native extracellular matrix (ECM) in order to promote excellent host-cell mediated healing (Barnes et al., 2007). The characteristics of biomaterial scaffolds vary depending on the types of materials and the tissue types where the scaffold is to be applied (Chua, 2001).

First of all, scaffolds should be biocompatible, whereby neither the biomaterials nor its degradation by-products should provoke any rejection, inflammation or immune responses (Chen et al., 2002). The scaffold should provide three-dimensional structures with interconnected porous architecture to assist cellular ingrowth and facilitate nutrients and oxygen delivery (Deluzi et al., 2013 and Leukers et al., 2005). The three-dimensional scaffolds should be able to initiate cell attachment and subsequent tissue formation to ensure the cell adheres and proliferates into the structure. The biomaterial scaffolds should also be biodegradable upon implantation at a rate matching that of new tissue regeneration (Chan and Leong, 2008).

In addition, the scaffold should provide adequate mechanical properties consistent with the site into which it is to be implanted and bear strong enough biological forces to allow surgical handling during implantation (O'Brien, 2011). The biomaterial scaffolds should exhibit high surface area to support better cell adhesion, promote cell growth and allow the retention of differentiated cell functions (Chen et al., 2002). The scaffold should also have surface roughness similar to native tissues for enhanced tissue-scaffold interaction (Zhao et al., 2012). Furthermore, the scaffold should be vascular supportive to provide channels for adequate blood supply for rapid and healthy tissue regeneration (Zhang and Michniak-Kohn, 2012). Finally, the biomaterial should be stable during storage and must be sterilizable in order to avoid any contaminations, without compromising any structural or other related properties (Ramakrishna, 2011). Despite the above discussed properties, it should be noted that the

success of biomaterial scaffolds also depends on many other factors such as implant design, surgical techniques, health conditions and activities of the patient.

2.3.3 Biodegradable scaffolds

Biopolymeric scaffold degradability is one of the main key factors for designation and fabrication of biomimetic scaffolds in skin tissue engineering applications. Scaffolds should mimic the structure and biological functions of natural extracellular matrix (ECM) as closely as possible to create conducive living substrates that will induce cells to function naturally. The construction of new scaffolds does not only depend on material selection, but also the capability of perceiving its potential behaviour once implanted and endures the recovery time (Peña et al., 2006). In tissue engineering, biodegradable scaffolds must be able to maintain their physical, chemical and mechanical properties to support the growth of new tissues at an injured site till full regeneration, without any reverse effects on the repair of neighboring tissues and organs (Zhu et al., 2013). The stability of biopolymers developed as a substrate for tissue engineering with particular prominence of durability during their service life is crucial in tissue engineering fields. Indeed, it is important to ensure that the rate of degradation coincides with the rate of new tissue formation. If the rate of polymer degradation is too slow, the new tissue formation will be obstructed; however, if the rate of degradation is too fast, the mechanical stability of the scaffold and developing tissue will be compromised. To achieve this behaviour, an *in vitro* degradation study examining the rate of hydrolysis can be used as an initial estimate of the degradation rate as well as to predict its *in vivo* degradation behaviour.

Biodegradable polymers intended for tissue engineering are mostly tailored to decompose *via* hydrolytic and enzymatic degradable polymers (Eglin et al., 2009). There are many factors that may affect polymer degradation kinetics such as type of chemical bond, polymer molecular weight, crystallinity and the presence of cross links, fillers, additives, etc. (Göpferich, 1996). In order to more accurately mimic the natural ECM, former researchers had also investigated the potential of natural materials such as collagen, chitosan, gelatine, alginate, and silk fibroin (Pereira and Bártolo, 2013 and Armentano et al., 2010). However, these materials often lack the desired physical

properties when operating in a single network. This unavailability leads to the development of hybrid materials that consist of a blend of synthetic and natural materials. Niget et al. found that the use of hybrid blend PLLA and chitosan showed decrease in the degradation rate after an 8-week incubation period compared with pure PLLA scaffolds (Zhu et al., 2013). Thus, incorporation of natural materials with synthetic polymers can be effectively applied to control the degradation rates of polymeric scaffolds used for biomedical applications.

2.3.4 Classification of biomaterials

A variety of biomaterials have been investigated as scaffolding materials for tissue engineering applications. This includes metallic, ceramics, polymeric and composite biomaterials. Biomaterials can be classified based on its applications, for instance, skin substitute materials, dental materials, orthopedic materials and vascular graft materials. Generally, in most of the cases, based on their mechanical properties, metals and ceramics are used in hard-tissue applications while polymers are used in soft-tissue applications. Further details will be described in the following sections.

a) Metals.

For more than 100 years ago, metallic biomaterials have been widely used for replacing failed hard tissues; Lane first introduced metal plates for bone fracture fixation in 1895 (Lane, 1895). In its early development, metal implants faced corrosion and insufficient strength problems (Lambotte, 1909 and Sherman, 1912). Although metallic implants such as Co-Cr alloys and Ti with its alloys have successfully been used for hard-tissue applications, there remains a mismatch of mechanical consistency with hard-tissues like bone (Liu, 2007). Furthermore, metallic biomaterials are bioinert by which they do not have the ability to interact with the host tissues either chemically or biologically, like blood compatibility, bone conductivity and bioactivity (Hermawan et al., 2011). Hence, surface modifications are required to improve hard-tissues such as bone conductivity by coating with bioactive ceramics like hydroxyapatite (Habibovic

et al., 2004) or blood compatibility by coating with biopolymers (Lahann et al., 1999).

b) Ceramic and glass.

In the late 1960's, ceramics have been widely used in biomedical applications due to its superior biocompatibility in the replacement of metal (Roohani-Esfahani and Zreiqat, 2012). Bioceramics have been extensively used as implant materials for the treatment of bone defects in the hips, knees, and teeth, as well as maxillofacial reconstruction, augmentation and stabilization of the jawbone, and spinal fusion and bone fillers after tumour surgery (Davis, 2003 and Park and Bronzino, 2003). Based on tissue response, bioceramics can be classified into three types, (i) nearly bioinert in which tissue forms a non-adherent fibrous capsule around the implant surface (e.g., alumina and zirconia), (ii) bioactive in which tissue chemically bonds with the implant surface (e.g., HA and bioglass) and (iii) bioresorbable in which the implant surface dissolves and allows tissues to refill the space previously occupied by the implant (e.g. TCP, and $\text{Ca}_3(\text{PO}_4)_2$) (Hermansson, 2014). Bioceramics show ultimate results with optimal surface properties and surface features when the grain size is less than 100 nm. This feature leads to active formation and enhancement of osteoblasts and osteoclasts that are suitable for orthopedic and dental implantation *in vivo* (Ramakrishna, 2011).

c) Polymers biomaterials.

Polymers are the largest class of biomaterials broadly used in biomedical applications owing to their functional properties, design flexibility and surface modifiability. Polymers are made up of repeated, small and simple chemical units called monomers. Polymeric biomaterials used in tissue engineering could be classified into two types: (i) naturally derived such as proteins (e.g., collagen, fibrin and silk), polysaccharides (e.g., starch, alginate, cellulose and agarose) and nucleic acid of nucleotides (e.g., DNA and RNA) and (ii) synthetic polymers including biodegradable (e.g., poly(lactic acid) (PLA), poly(glycolic

acid) (PGA) and poly(lactic-co-glycolic) acid (PLGA)) or nonbiodegradable (e.g., poly(ethylene) (PE), poly(ethylene terephthalate) (PET) and poly(tetrafluoroethylene) (PTFE).

Naturally derived polymers or also called biopolymers are usually biodegradable and the rate of degradation depends on the molecular weight, composition and crystallinity of the respective polymers. Natural polymers are the best options due to its biocompatibility, biodegradability and non-toxicity. Meanwhile, synthetic polymers offer many advantages over naturally derived biopolymers such as free from concerns of immunogenicity, easily processed, surface modifiable and sterilizable. However, only few biodegradable polymers are often used in tissue engineering applications if compared to nonbiodegradable polymers. The main reason is that nonbiodegradable polymers always induce chronic inflammation, known as foreign body response, whereas biodegradable polymers allow formation of temporary scaffolding to provide sufficient mechanical and biochemical support until new tissue regeneration.

Cellulose is the most abundant natural polymer consisting of $\beta(1-4)$ -D-glucose linkages majorly found in plant cell walls (Roohani et al., 2008). The remarkable physical properties associated with cellulose polymers accumulate from their water and organic solvent solubility, thermal plasticity, thickening and colloid stabilizing abilities (Kamide, 2005). Recently, cellulose derivatives have been extensively utilized in medicine and pharmaceutical applications (Dugan et al., 2013). This renewable material is very popular due to their advantages over synthetic polymers such as low-toxicity, biodegradable, water soluble, cost-effective, and chemically resembles the glycosaminoglycan (GAG) molecules as one of the components in the ECM of mammalian tissues (Malafay et al., 2007 and Trombino et al., 2009).

Recently, cellulose derivatives have been extensively utilized in medicine and pharmaceutical applications. This renewable material is very popular due to their advantages over synthetic polymers for instance low-toxicity, biodegradable, water soluble, cost effective, and chemically resembles

the glycosaminoglycan (GAG) molecules in which the ECM of mammalian tissues is composed of (Malafaya, Silva and Reis, 2007; Trombino et al., 2009)

2.3.5 Hydroxyethyl cellulose

Hydroxyethyl cellulose (HEC) is a hydrophilic polysaccharide biopolymers with $\beta(1\rightarrow4)$ glycosidic linkage. HEC is an important derivative of cellulose, in which ethyl group replaces one or more of three hydroxyl groups, which are present in each glucopyranoside. This is used as a soluble intermediate for processing of cellulose into sponge, fiber and film forms. The degree of substitution and their relative distribution in C_1 , C_2 and C_6 positions strongly affect the properties and behaviour of these polymers (Sannino et al., 2003). It is a non-ionic water soluble derivative of cellulose ethers with low charge density, particularly used as stabilizers and thickeners in paint formulations, hair and eye-care solutions, as protective colloids in polymerization processes and as thickeners in water based paints (Kfistner et al., 1996; Akiyama et al., 2005 and Arfin and Bohidar, 2012).

HEC has large amounts of hydroxyl units that can be attached by numbers of functional groups (Erkselius and Karlsson, 2005). Strong hydrogen bonding among the hydroxyl groups of HEC makes it available to be employed in extensive utilizations due to its water solution properties and chemical compositions (Erkselius and Karlsson, 2005; Liedermann and Lapc, 2000 and Sun et al., 2007). Indeed, the remarkable physical properties associated with cellulose polymers accumulate from their water and organic solvent solubility, thermal plasticity, thickening and colloid stabilizing abilities. The chemical composition of HEC will allow the occupation of large amounts of relatively easily accessible hydroxyl units that can be attached by a number of functional groups (Erkselius and Karlsson, 2005; Liedermann and Lapc, 2000 and Sun et al., 2007). Moreover, the chemical structure of HEC exactly matches that of glycosaminoglycans (GAGs) in the dermis (Figure 2.3) whereby specific GAGs of physiological significance are hyaluronic acid, dermatan sulphate and heparin. Although each of these GAGs has a predominant disaccharide component, heterogeneity does exist in the sugars present in the formation of any given class of GAG, thus having particularly promising applications in the growing field of tissue engineering.

In this work, HECs are used as the main polymer for potential substrates in skin tissue engineering. To the best of our knowledge, this is the first report where HEC-based scaffolds are used for skin tissue engineering. The study on cell-scaffold interactions was carried out to assess the growth, proliferation and biocompatibility of the test scaffold.

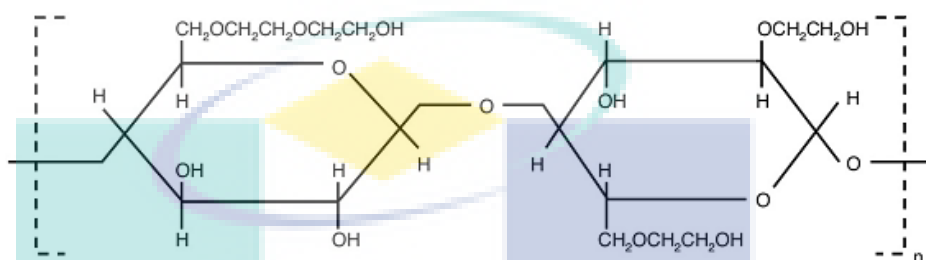


Figure 2.3: Molecular structure of HEC (Abdel-Halim, 2013)

2.3.6 Poly (vinyl) alcohol

Poly (vinyl) alcohol (PVA), a water soluble hydrophilic synthetic polymers, has been widely used in biomedical fields due to its excellent chemical and physical properties such as in contact lenses, lining for artificial hearts, wound dressing and drug delivery applications (Peresin et al., 2010). This biodegradable and biocompatible polymer has piqued the interest of researchers in tissue engineering fields as well as in regenerative medicine due to its non-toxic, non-carcinogenic, bioadhesive characteristics; easy processing technique, and proven mechanical strength (Georgieva et al., 2012 and Song et al., 2012b).

Surface modified PVA hydrogels have been previously used for numerous biomedical and pharmaceutical applications (Tanigami et al., 1995). PVA has a simple chemical structure (Figure 2.4) thereby chemical modifications are possible using simple reactions as well. PVA can form polymeric blends with other water-soluble polymers. For example, PVA blended with starch can be used as a new material in packaging (Parvin et al., 2010) whereas PVA blended with collagen can be used in biomedical applications (Song et al., 2012b). PVA blended with poly (acrylic acid) are

attractive materials for the use of polymer electrolytes (Wu et al., 2006). Moreover, PVA is widely used in preparation of composites containing inorganic particles like perlite, montmorillonite and graphite (Greve and Richards, 1979; Yoon et al., 2009 and Chandrasekhar et al., 2012).

PVA gels also possess high degrees of swelling in water or biological fluids aside from being elastic or rubbery in nature. PVA is capable of simulating natural tissues and can be completely accepted into the body (Peppas and Merrill, 1977). Generally, the cross-linking process achieved by PVA polymers can be performed *via* several methods including physical cross-linking such as dehydrothermal treatment (DHT), plasma treatment and ultraviolet (UV) treatment; and chemical cross-linking by using cross-linking agents such as glutaraldehyde (GA) and 1-ethyl-3-(3-dimethylamino propyl) carbodiimide hydrochloride (EDC), polyglycidyl ether and polyepoxide resins (Osborne et al., 1999; Courtman et al., 2001; Khor, 1997; Zeeman et al., 1999; Sung, et al., 1996 and Ratanavaraporn et al., 2010). Cross-linking this hydrogel by various chemical bonds and physical interactions can significantly improve their mechanical, thermal and chemical properties (Mansur et al., 2004). A preferable example of chemical cross-linking of PVA is carried out with the aid of glutaraldehyde (GA) in a manner represented in Figure 2.5.

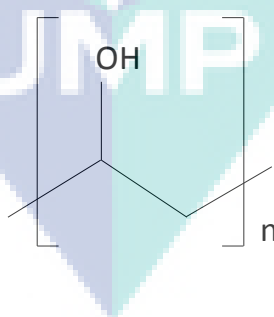


Figure 2.4: Molecular structure of PVA

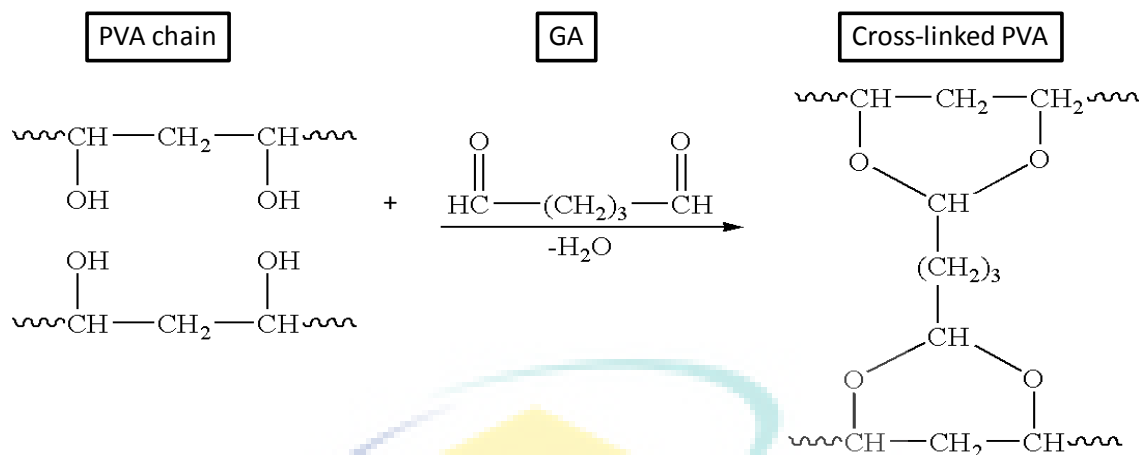


Figure 2.5: Chemical structure of PVA and glutaraldehyde cross-linking (Reis et al., 2006)

2.3.7 Collagen

Collagens are the most abundant protein in natural ECM that provides the principal structure and mechanical support as well as biological signals to adjacent cells for tissue regeneration (Sionkowska et al., 2004). Collagens have been used in a variety of tissue engineering applications owing to its biocompatibility and biodegradability (Tangsadthakun et al., 2006). Although many types of collagens exist in living organisms, type I and type III are the most abundant in native tissues. Collagen type I consists of two α_1 chains and one α_2 chain with a fiber diameter of about 50 nm, presented in bone, skin, dentin, cornea, fibrocartilage, tendon and blood vessels (Sell et al., 2009). Collagen type III is composed of three α_1 chains with fibers ranging from 30 to 130 nm in diameter (Ramshaw, 1986). The main amino acids in collagen are glycine, proline and hydroxyproline (Figure 2.6). The triple helical structure of collagen is stabilized by both interchain hydrogen bonds and structural water molecules (van der Rest and Garrone, 1991; Paul and Bailey, 2003 and Matthews et al., 2002). Generally, the direct use of collagen extracted from natural tissues is limited due to its capability to elicit immunogenic response upon implantation (Habermehl et al., 2005). Hence, better treatments using reconstituted collagen (a purified form of collagen) produced by various biochemical methods with relatively less immunogenic response are commercially available for a variety of biomedical applications (Danielsen, 1984).

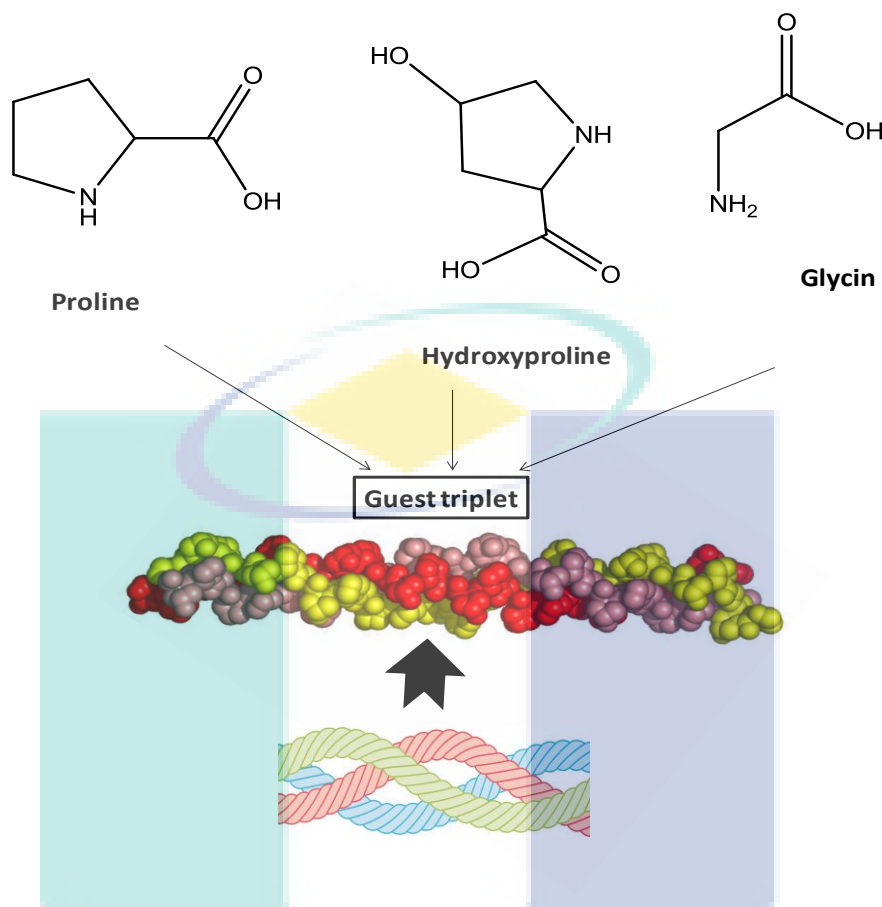


Figure 2.6: Triple-helical structure of collagen (Petsko & Ringe, 2004)

Collagens present in skin are mainly synthesized by fibroblast and myofibroblast. In tissue engineering, collagen blended with biodegradable synthetic polymers are often used as cell culture substrates due to its natural ECM properties and complex signalling capabilities (Asran et al., 2010 and Song et al., 2012b). Based on previous reports, the blends of collagen with poly (vinyl) alcohol (PVA) are extensively used in biomedical applications owing to its non-toxicity, water solubility, biocompatibility and biodegradability with excellent mechanical properties (Lee et al., 2009 and Georgieva et al., 2012). In this present work, collagen added to HEC/PVA scaffolds does not just improve the biocompatibility and mechanical properties but also enables manipulation of bioactive molecule release from the scaffolds.

2.4 OVERVIEW OF NANOPARTICLE

Nanoparticles are clusters of atoms in the size range of 1–100 nm (Rai et al, 2009). In nanotechnology, a particle is defined as a small object that behaves as a whole unit with respect to its transport and properties. The prefix ‘nano’ is used to indicate one billionth or 10^{-9} meters (El-Nour et al., 2010). Currently, the use of nanoparticles have initiated intense research interests as they possess defined chemical, optical and mechanical properties compared to their macro scaled counterparts due to high surface-to-volume ratio (El-Nour et al., 2010 and Sharma et al., 2009).

Synthesis of noble metal nanoparticles and their polymer composites represent an important field for fundamental studies particularly in biological and biomedical applications. The metallic nanoparticles such as gold, silver and copper are most promising as they show good antibacterial properties due to their large surface area to volume ratio, which piqued interests among researchers due to the limitations of antibiotic treatments for the prevention of periprosthetic infections; the growing microbial resistance against metal ions, antibiotics; and the development of resistant strains (Marsich et al., 2013 and Abdo et al., 2014).

2.4.1 Silver nanoparticles

Silver nanoparticles (AgNPs), silver oxide and its salts have great advantages in the medical arena owing to its remarkable antimicrobial activity and non-toxicity (Prabhakar et al., 2011 and Song et al., 2012). Currently, nanosilver materials are widely used to treat severe burn (Chen et al., 2006) and chronic ulcers (Gunasekaran et al., 2011) and is extensively used as an additive in many fields including prostheses (Ferreri et al., 2014), catheters (Antonelli et al., 2012 and Stevens et al., 2009), dental materials (Espinosa-Cristóbal et al., 2013 and Zhang et al., 2012), coating stainless steel materials (Liu et al., 2012), textile fabrics (Kwak et al., 2014 and Zhang et al., 2013), human skin (Larese et al., 2009 and Mukherjee et al., 2012), and water treatment (Lv et al., 2009 and Viet et al., 2013).

In tissue-engineered skin substitutes, the moisture environment impregnated by the dressing has been investigated to promote healing of ulcers and reduce the suffering of patients (Czaja et al., 2006). Although silver is relatively inert, its interaction with moisture from the surface of the skin as well as fluids in the wound bed leads to the release of silver ions. Silver ions, which are highly reactive, bind to bacterial DNA and RNA, denaturing them and inhibit the growth of bacteria (Rai et al., 2009). However, the very small size of the nanoparticles enables their penetrations into the stratum corneum of the skin and thereby interferes with a variety of cellular mechanism (Mohiti-Asli et al., 2014). Hence, the design of tissue engineered skin should be optimized by controlling the concentration, synthesis route, size and distribution of silver nanoparticles to prevent the wound from microorganism contaminations and also further physical damage with a rapid healing process and minimum scarring.

Generally, silver nanoparticles can be prepared and stabilized by physical and chemical methods. Physical methods using laser ablation (Siljanovska et al., 2014), radiolysis (Biswal et al., 2013) or aerosol techniques (Paur et al., 2011), although effective, require expensive instruments and consume large amounts of energy. These methods typically make use of agents that are both toxic and environmentally polluting (Lim & Hudson, 2004). Chemical approaches such as chemical reduction (Mukherjee and Mahapatra, 2009), electrochemical techniques (Szymanski and Porter, 2013; Batchelor-McAuley et al., 2014), NaBH_4 and UV irradiation photoreduction (Pinto et al., 2009) and photochemical reduction (Mathew and Kuriakose, 2013) are most widely used. Among them, the most frequently applied method for the preparation of AgNPs is the chemical reduction of silver salt solutions in water or organic solvents to produce a colloidal suspension.

Methods based on chemical reduction offer the best chance of being both low cost and environmentally friendly. Environmentally friendly (green) approach to prepare AgNPs depend on three important parameters, which are solvent medium, reducing and stabilizing or capping agents for AgNPs (Abdel-Mohsen et al., 2012, 2013). Natural polymers such as sodium hyaluronate, chitosan and/or chitosan derivatives and cellulose are all important macromolecular materials that are increasingly used as reducing agents due to their inherent biodegradability with

degradation products, which is also non-toxic for the cells. Previous reports mentioned that AgNPs have been synthesized using water as solvent and starch as a capping agent and these were shown to have advantages over conventional methods involving chemical agents that are associated with environmental toxicity (Sharma et al., 2009). The synthesis of AgNPs using chitosan as both a reducing and a capping agent has also been developed (Sanpui et al., 2008). In addition, synthesis of starch-AgNPs has been carried out with starch as a capping agent and β -D-glucose as a reducing agent in a gently heated system (Raveendran et al., 2003). The starch in the solution mixture avoids the use of relatively toxic organic solvents (Amanullah and Yu, 2005).

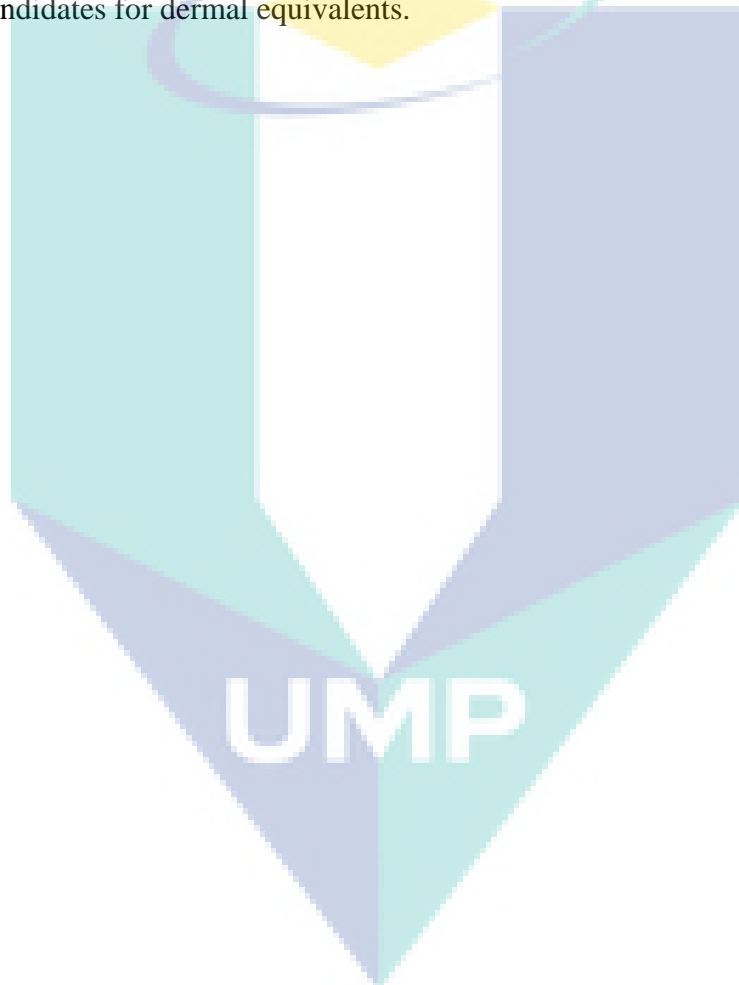
In this study, biocompatible polymers, HEC are used as a reducing agent of AgNPs and its cell biocompatibility is investigated. The HEC/AgNPs scaffolds are fabricated by using freeze-drying or lyophilization technique. The advantage of using HEC is that the silver ions are reduced to silver nanoparticles in a few minutes at room temperature by heat treatment without any external reducing agents. Preliminary results of the application of these scaffolds in the cytotoxicity effects against hFB cells are also explored.

2.5 SUMMARY

To summarize, an amount of research has been undertaken to find the ideal scaffolds for skin tissue engineering applications. Although many products are commercially available in the market, there are still limitations in several criteria such as high costs, history of unsuccessful treatments, weak tensile properties, toxicity and instability during storage. In addition, most biomaterial polymers as mentioned in Section 2.34(c) are using organic solvents such as hexafluoroisopropanol, acetic acid and chloroform to dissolve the polymers. Regular or high exposures to organic solvents may induce environmental contamination as well as toxicity and general hazards to the workers.

This research aims to fabricate HEC nanomaterials using water as the only solvent and then investigate their potential as scaffolds in skin tissue engineering applications. By using extremely simple methods, HEC based scaffolds produced *via* a

'green' environmentally friendly approach are easy and capable of processing in a large scale. To the best of our knowledge, this is the first report where HEC is synthesized and fabricated *via* electrospinning and freeze-dried methods and then followed by characterization and application in skin tissue regeneration. In this study, the PVA, collagen and silver nanoparticle are chosen as additive polymers due to their biocompatibility, biodegradability and non-toxicity properties that offer better cell adherence, differentiation and proliferation on the scaffold's surfaces. All scaffolds will undergo an *in vitro* cell culture study by using human melanoma and fibroblast cells as potential candidates for dermal equivalents.



CHAPTER 3

MATERIALS AND METHODS

This chapter discusses in detail the research methodology, which comprise of various methods and materials being employed in the present research. The steps include the synthesis and fabrication of nanofibers and porous freeze-dried scaffolds, the tools and techniques used for the characterization of the material, the procedures involved in the cell-culture experiment, and the techniques used to measure cell proliferation on the scaffolds.

3.1 RESEARCH METHODOLOGY

Flowchart 3.1 pointed out the research methodology being practiced in this work. The materials were synthesized by electrospinning and freeze-drying techniques using aqueous polymeric solution; the parameters for both techniques were optimized to obtain fibers in nanoscale and highly porous freeze-dried scaffolds. The scaffolds were further characterized based on their physical, chemical, thermal and mechanical properties. All scaffolds underwent cell culture studies to check their cell responses and compatibility along incubation periods. The techniques used for synthesis, fabrication, characterization, and testing are further discussed in this chapter.

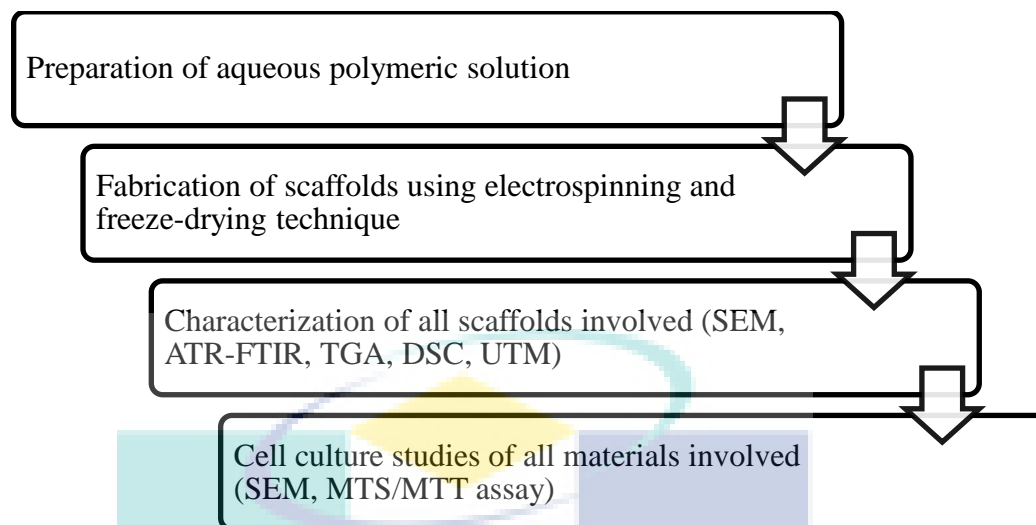


Figure 3.1: Summary of research methodology implemented in this work

3.2 MATERIALS PREPARATION

All materials used in this work are commercially available. Hydroxyethyl cellulose (CAS number: 9004-62-0) was purchased from Merck-Schucardt, Germany. Hydroxyethyl cellulose ($M_w = 250,000$) and silver nitrate (AgNO_3) were purchased from Sigma-Aldrich, USA. Poly (vinyl) alcohol ($M_w = 95,000$) was purchased from ACROS, New Jersey, USA. Collagen type I, liquid rat tendon excised from tail (0.02N acetic acid, pH 3.67) was purchased from Merck-Millipore Corporation, Billerica, MA, USA. Analytical reagent grade glutaraldehyde (GA) solution (25% aqueous solution) was purchased from Merck-Schucardt, Germany. Phosphoric acid was purchased from Merck.KGaA-Darmstadt, Germany. Acetone was purchased from R&M Marketing, Essex, UK. Phosphate buffer saline (PBS) was purchased from Gibco Life Technologies, USA. Dulbecco's Modified Eagle Medium (DMEM) was purchased from Life Technologies, USA. All the chemicals were of highest purity and used without further purification. All the solutions were prepared using Millipore water.

3.3 PREPARATION OF ELECTROSPINNING AQUEOUS POLYMERIC SOLUTIONS

Biomaterial scaffolds with a large amount of water diffused in three dimensional polymeric networks are highly needed in biomedical and health applications (Deligkaris et al., 2010). Many water soluble synthetic polymers such as poly (vinyl) alcohol (PVA) (Zhou et al., 2010), poly (vinyl pyrrolidone) (PVP) (Elashmawi and Abdel Baieth, 2012 and Shi et al., 2014) and poly ethylene glycol (PEG) (El-Ghalbzouri et al., 2004) are combined with natural polymers to improve cell-recognition moieties, mechanical properties and high processability (Arya et al., 2009). Combination of natural polymer with synthetic polymers like PVA, a biodegradable, non-toxic and non-carcinogenic hydrogel, improves the spinnability and mechanical properties such as elasticity and elongation (Mansur and Mansur, 2007). In addition, blending of synthetic and natural biopolymers from three or more components reveal tremendous results in cell-scaffold behaviour (Sionkowska, 2011). In this research, HEC was blended with PVA and collagen to improve their spinnability as well as the cell response towards skin cells.

3.3.1 Synthesis of HEC/PVA and HEC/PVA/collagen nanofibers scaffolds

The HEC solution with a concentration of 5 wt% was prepared by dissolving 5 g of HEC powder in 100 ml of Millipore water for 2 h at room temperature until a clear solution was obtained with a slight increase in viscosity. PVA solution of 15 wt% was prepared by dissolving 15 g of PVA granules in 100 ml of Millipore water and stirring at 80 °C for 2 h. Both solutions were stirred continuously for 12 h at room temperature to ensure complete mixing and eventually obtain a homogeneous solution. HEC was then blended in PVA solution with 3 different weight ratios of HEC/PVA, which are 50:50, 40:60 and 30:70 and stirred overnight to get a homogeneous mixture for electrospinning. The HEC/PVA (50:50) blended aqueous polymeric solution is shown in Figure 3.2. For ternary blend system, collagen solution with concentration of 0.38 % was added into the HEC/PVA solution in the ratio of 1:1:1 and stirred continuously to get homogenous blend solution.



Figure 3.2: HEC/PVA (50:50) blended solution

3.4 PREPARATION OF FREEZE-DRIED AQUEOUS POLYMERIC SOLUTIONS

3.4.1 Synthesis of HEC/PVA freeze-dried scaffolds

The HEC solution with concentration of 5 wt% and PVA solution of 15 wt% was prepared as described in Section 3.3.1. HEC was blended in PVA solution at 3 different weight ratios of HEC/PVA, which are 2:1, 1:1 and 1:2. The blend solutions were stirred overnight to get homogeneous solutions.

3.4.2 Synthesis of HEC/silver nanoparticles freeze-dried scaffolds

The HEC solution with concentration of 10 wt% was prepared by dissolving 10 g of HEC powder ($M_w = 250,000$) in 100 ml of Millipore water for 2 h at room temperature. 200 to 800 μL of 0.05M AgNO_3 in water was added to the HEC solution with constant stirring at 75°C for 2 h, in a dark environment. The HEC solution acquired light yellow colour, indicating the reduction of Ag^+ to Ag^0 . This interaction can be schematically represented as shown in Scheme 4.1. 2.5 % GA was added to the solution for cross-linking purpose. The HEC with 0.8% AgNPs blended solution is shown in Figure 3.3.



Figure 3.3: HEC with 0.8% silver nanoparticles blended solution

3.5 FABRICATION TECHNIQUES

A well-designed three-dimensional scaffold is one of the fundamental tools to guide tissue formation *in vitro* and *in vivo*. Therefore, the selection of fabrication techniques is important to enable the cells to behave in the desired manner to generate tissues and organs of the desired shape and size in the body. To engineer these functional tissue and organs, scaffolds need to be fabricated by different methodology to facilitate the cell distribution and guide their growth into three-dimensional space. There are several techniques to produce scaffold like phase separation, freeze-drying, melt-moulding, self-assembly, sol-gel and electrospinning. The main techniques for scaffolds fabrication used in this work are described as follows:

3.5.1 Electrospinning

Electrospinning is a simple, cost-effective and unique technique to produce non-woven polymer fibers ranging from a few microns down to tens of nanometers. This technique was first observed in 1897 by Rayleigh, studied in detail by Zeleny in 1914 on electro spraying (Zeleny, 1914) and obtained several patents by Formhals from 1934 to 1944 (Anton, 1934). Since the 1980s and especially in recent years, the electrospinning process has gained more interest probably due to a surging awareness in nanotechnology as ultrafine fibers or fibrous structures of various polymers with diameters down to submicrons or nanometers can be easily fabricated with this process (Huang et al., 2003).

The basic configuration of electrospinning apparatus, as shown in Figure 3.4, consists of three major components: (i) spinneret, (ii) a fiber collector and (iii) a high-voltage power system to facilitate the conversion of polymer solution into a charged polymer jet ejected from the spinneret tip towards the surface of the fiber collector. In the electrospinning process, a polymer solution is pumped at a controllable feed rate through a syringe with varied size of metal needle connected to a high-voltage power supply. When the voltage source is applied, an electric field is created between the needle and the collector plate. A polymer solution at the tip of the needle becomes electrified and forms a droplet. As the applied voltage increases, the charge accumulated at the surface of the droplet will be induced and allows the droplet to deform into a conical structure, known as Taylor's cone. Once the applied electric field reaches the threshold value, the electrostatic force tends to exceed the surface tension of the polymer droplet and subsequently, a fine charged polymer jet is forced to eject from the tip of Taylor's cone and collected on a grounded metal plate.

A variety of naturally derived polymer including collagen, chitosan, gelatine, silk fibroin and fibrinogen and synthetic polymers such as PGA, PLLA, PLGA and PCL have been electrospun into nanofibers for tissue engineering scaffolds (Ghasemi-Mobarakeh et al., 2010; Dong et al., 2010; Asran et al., 2010; Liu et al., 2011 and Fang et al., 2011). A variety of cells, which include mesenchymal stem cells, muscle cells, fibroblasts and osteoblasts are seeded onto the scaffolds, which help to attach, proliferate, and differentiate the cells and forms bio-matrix composites for various tissue repairs and replacements (Ma, 2008; Panzavolta et al., 2011; Shao et al., 2011 and Sahoo et al., 2010).

In this study, electrospinning was carried out at room temperature for all concentrations of HEC/PVA and HEC/PVA/collagen. The electrospinning machine is as displayed in Figure 3.5. The polymer solution was filled in a 5 ml syringe fitted with a blunt steel needle of 0.8 mm inner diameter and flow rate of 1 ml/h. The applied voltage was varied from 20 to 25 kV. The electrospun nanofibers were collected using a rotating drum collector wrapped with aluminium foil at the distance of 90 to 110 cm from tip-to-collector at a rotation speed of 1000-1500 rpm. A humidity of 50 % was preserved (Dri-

Tech HT-180) in the room. The collected electrospun nanofibers were stored in desiccators for further use.

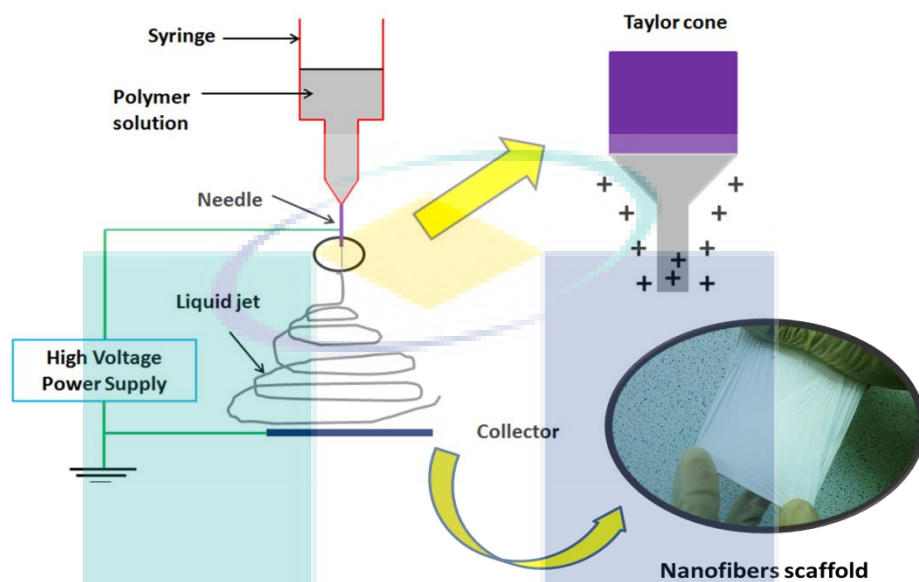


Figure 3.4: Schematic diagram of the basic setup for electrospinning and Taylor cone formation



Figure 3.5: Photograph of electrospinning machine, Electroris

(i) Cross-linking and dissolution studies

The nanofibrous scaffolds were peeled and cut into 4 cm² pieces and allowed to be kept in a Petri dish with diameter of (90 mm). GA solution in acetone followed by phosphoric acid was put in the Petri dish containing the nanofibers for 24 h. The nanofibrous mats were rinsed with water three times to remove excess GA. Water resistance of the scaffolds was evaluated by immersing it in distilled water and dried in a vacuum oven for 1 h for further use.

(ii) *In vitro* degradation study

For nanofiber scaffolds, the *in vitro* degradation study was completed for HEC/PVA (1:1) and HEC/PVA/collagen (1:1:1) nanofiber scaffolds only. The nanofiber scaffolds (15 mm x 15 mm) were cut into rectangular shapes and carried out in two different media which are PBS solution and DMEM media. The scaffolds were sterilized under UV irradiation for 2 hours, placed in 24-well plate containing 3 ml of PBS or DMEM solution and incubated at 37°C in a humidified atmosphere containing 5% CO₂ and 95% humidity respectively for 12 weeks. The incubation media were replaced by fresh solution every four weeks.

3.5.2 Freeze-drying

Freeze-drying, also known as lyophilization has been utilized since 1250 BC as a method for preserving food. In the early 1980s, Altman once reported the use of freeze-drying method in the preparation of histological sections (Meryman, 1976). Nowadays, freeze-drying is one of the techniques used to fabricate porous scaffolds and has been widely investigated for the last two decades in tissue engineering fields (Subia et al., 2010). It is a common method for producing large and highly interconnected porous 3D scaffolds that can be performed with dissolved synthetic and natural polymers including silk, collagen, PGA, PLLA, PLGA, PLGA/PPF blends (Schoof et al., 2001; Vepari and Kaplan, 2007 and Altman et al., 2003).

Basically, freeze-drying involves three major steps; firstly, the solution is frozen at a low temperature usually in the range of -50°C to -80°C , and then, the frozen sample will undergo the primary drying process in which the sample is located in a chamber through a partial vacuum with the pressure lowered to a few millibars (Lu et al., 2013). During this process the ice in the material is removed by direct sublimation while the final stage, which is secondary drying process, showed removal of most of the unfrozen water in the material by desorption (Lu et al., 2013). The main advantage of this technique is that it neither requires high temperature nor separate leaching steps (Subia et al., 2010). Meanwhile, the drawback of this technique is its long processing time, low mechanical stability and sensitivity of the technique where the processing parameters have to be very well controlled (Hutmacher, 2000 and Yang et al., 2001).

In the present study, the scaffolds were fabricated by pouring the aqueous polymeric solutions into the flasks and kept in a deep freezer at -80°C for 24 h. These frozen samples were lyophilized in a freeze-dryer (FreeZone 6 Liter Benchtop Freeze Dry System, Labconco) as shown in Figure 3.6, at -50°C for 72 h. Thereafter, the samples were further kept in a chamber saturated with GA vapor for 72 h for cross-linking formation, underwent heat treatment at 140°C for 10 minutes and dried in a vacuum oven for a day. The samples of HEC/PVA and HEC/AgNPs freeze-dried scaffolds are shown in Figure 3.7.



Figure 3.6: Photograph of freeze-dryer machine, Labconco

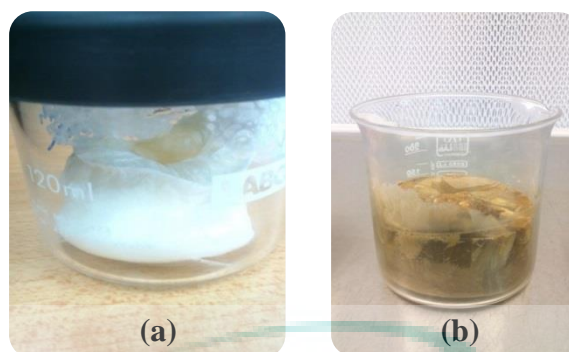


Figure 3.7: The (a) HEC/PVA and (b) HEC/AgNPs freeze-dried scaffolds

3.6 CHARACTERIZATION TECHNIQUE

Before characterize, all scaffolds were dried in an oven for 1 h to eliminate the excessive water. Scaffolds were cut in a particular manner based on the requirements of each characterization conducted - SEM, ATR-FTIR, TGA, DSC and UTM. The details of working principle and operation parameters for respectively instruments are as follows:

3.6.1 Scanning electron microscope

The scanning electron microscope (SEM) is one of the most versatile instruments available for examining and analysis of microstructure morphology and chemical composition characterizations. The SEM is an instrument that produces a largely magnified image by using electrons instead of light to form an image. A beam of electrons is produced at the top of the microscope by an electron gun. The electron beam follows a vertical path through the microscope, which is held within a vacuum. The beam travels through electromagnetic fields and lenses, which focus the beam down towards the sample. The beam is scanned across the surface of the sample by electromagnetic deflection coils, as illustrated in Figure 3.8. Once the beam hits the sample, electrons and X-rays are ejected from the sample. Detection of the electron signals is done either through solid state silicon-based detectors or *via* photomultiplier-type detector involving double-conversion of a

signal through light photons. Detectors collect and convert these electrons into a signal that is sent to a screen, producing the final image.

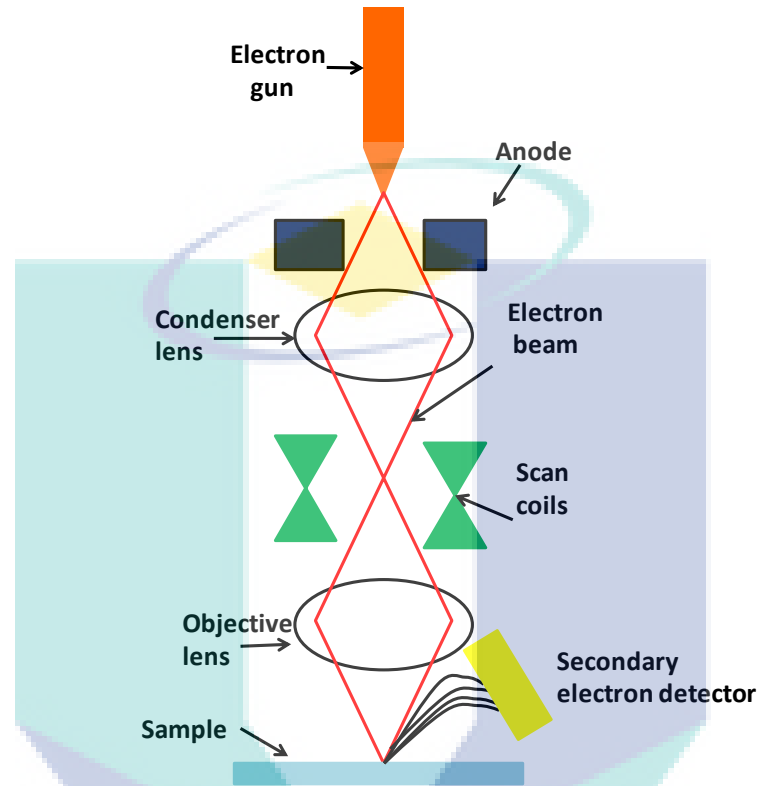


Figure 3.8: Schematic diagram of a SEM (Kopeliovich, 2012)

Since the SEM utilizes vacuum conditions and uses electrons to form an image, special preparations must be done to the sample. Samples must be thoroughly degreased and dried to eliminate any outgassing from organic contamination and water. Conductive metals require no preparation before the scanning process, however all non-metals should be made conductive by coating the sample with a thin layer of gold, silver or platinum by using a sputter coater.

In skin tissue engineering, study on the surface of scaffolds is important to observe the actual morphology, pore structure and adherence of cells, as initial indications of potential tissue scaffolds. In this present study, the surface morphologies of all scaffolds were observed by using a Scanning Electron Microscopy (SEM) (ZEISS EVO 50) as

shown in Figure 3.9 at an accelerating voltage of 15 kV. The samples were sputter coated with a thin layer of platinum in double 30 s consecutive cycles at 45 mA to reduce charging and produce conductive surfaces (BALTEC SCD 005 Sputter Coater – BALTEC). Based on the SEM images, diameters of the scaffolds' fibers/pores were analyzed using an image visualization software ImageJ, developed by Upper Austria University of Applied Science (Zhang et al., 2006).



Figure 3.9: Photograph of SEM, Zeiss EVO 50

3.6.2 Attenuated total reflectance-Fourier Transform Infrared Spectroscopy

Attenuated total reflectance (ATR) is a most widely used Fourier transform infrared (FTIR) sampling tool that greatly expedites sample analysis. This technique requires little or no sample preparation, which enables the samples to be examined directly in the solid or liquid state by transmitting infrared radiation directly through the sample. The main advantages of ATR sampling are the very thin sampling path length and the depth of penetration of the IR beam into the sample. This is in contrast to traditional FTIR sampling by transmission where the sample must be diluted with IR transparent salts and pressed into a pellet to prevent totally absorbing bands in the infrared spectrum.

An ATR operates by measuring the change in the total internally reflected IR beam directed on the surface of an optical dense crystal of relatively higher refractive index. This internal reflectance creates an evanescent wave that projects orthogonally into the sample which is held in contact with the crystal, as shown in Figure 3.10. In regions of the infrared spectrum where the sample absorbs energy, the evanescent wave will be attenuated or altered. The attenuated energy from each evanescent wave is passed back to the IR beam, which then exits the opposite end of the crystal and is passed to the detector in the IR spectrometer. The system then generates an infrared spectrum.

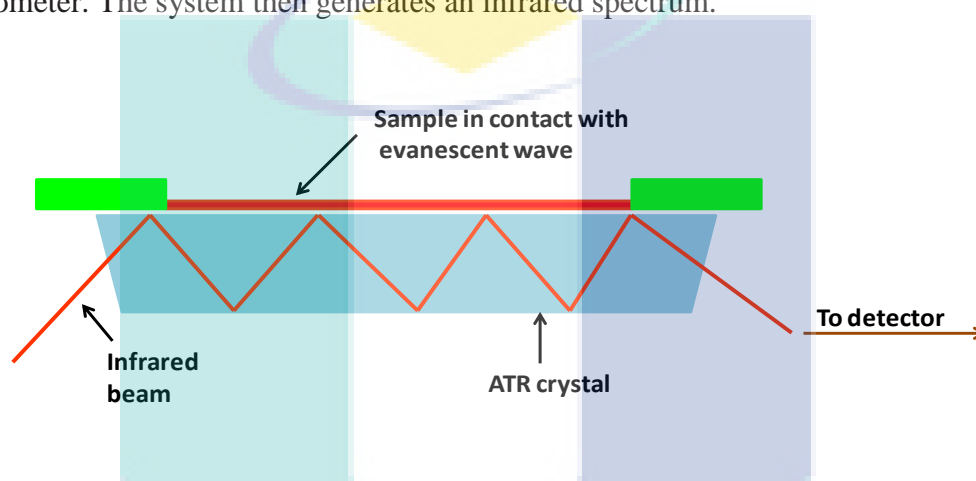


Figure 3.10: Graphical representation of multiple ATR reflection (PerkinElmer, 2005)

In this study, ATR-FTIR spectroscopic analysis of scaffolds was performed on Spectrum One (Perkin–Elmer, USA) spectrophotometer, as shown in Figure 3.11, over a range of 500 to 4000 cm^{-1} at a resolution of 2 cm^{-1} with 100 scans per sample. This characterization was important to ensure the functional group of individual and the effect of blended HEC, PVA, collagen and AgNPs on their intensities and peaks in the ATR-FTIR spectrum.



Figure 3.11: Photograph of ATR-FTIR, Perkin-Elmer

3.6.3 Thermogravimetric analysis

Thermal analysis is a group of physical-chemical methods to study the properties of materials as they change with temperature. Thermal analysis includes several different methods such as thermogravimetric analysis (TGA) and differential scanning calorimetry (DSC). The TGA technique provides quantitative information on the change in mass of a sample as a function of time as it is heated, cooled or held at constant temperature. This technique is effective for quantitative analysis of thermal reactions that are accompanied by mass changes such as evaporation, decomposition, gas absorption, desorption and dehydration.

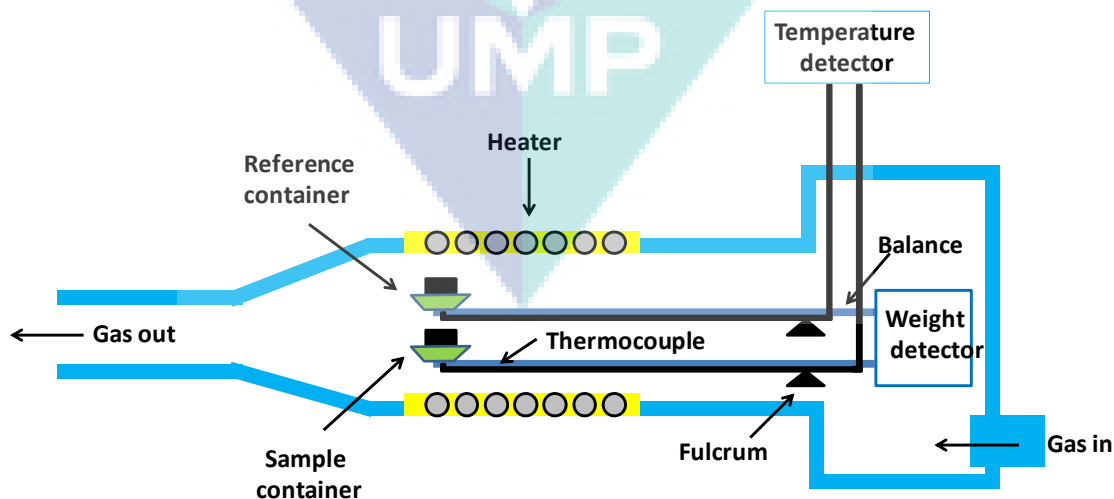


Figure 3.12: Schematic diagram of TG-DTA system (Murasawa et al., 2012)

The schematic diagram of TGA-DTA system was shown in Figure 3.12. The microbalance plays an important role to measure the change of sample mass. Disturbance on the equilibrium balance beam will change the shutter position followed by current development in the photodiode resulting from the upcoming light from the lamp. This imbalance induces a current in the magnetic foil, which generates additional electromagnetic force to recover equilibrium. As the photodiode current is amplified, the amount of additional electromagnetic force is proportional to the mass change.

Differential thermal analysis (DTA) is usually incorporated with TGA to measure the temperature difference between a sample and a reference material as a function of temperature as they are heated or cooled or kept at a constant temperature. This differential temperature is then plotted against time or temperature. Changes in the sample, either exothermic or endothermic, can be detected relative to the inert reference. Consequently, the DTA curve may provide data on the transformations that have occurred such as glass transitions, crystallization, melting and sublimation.

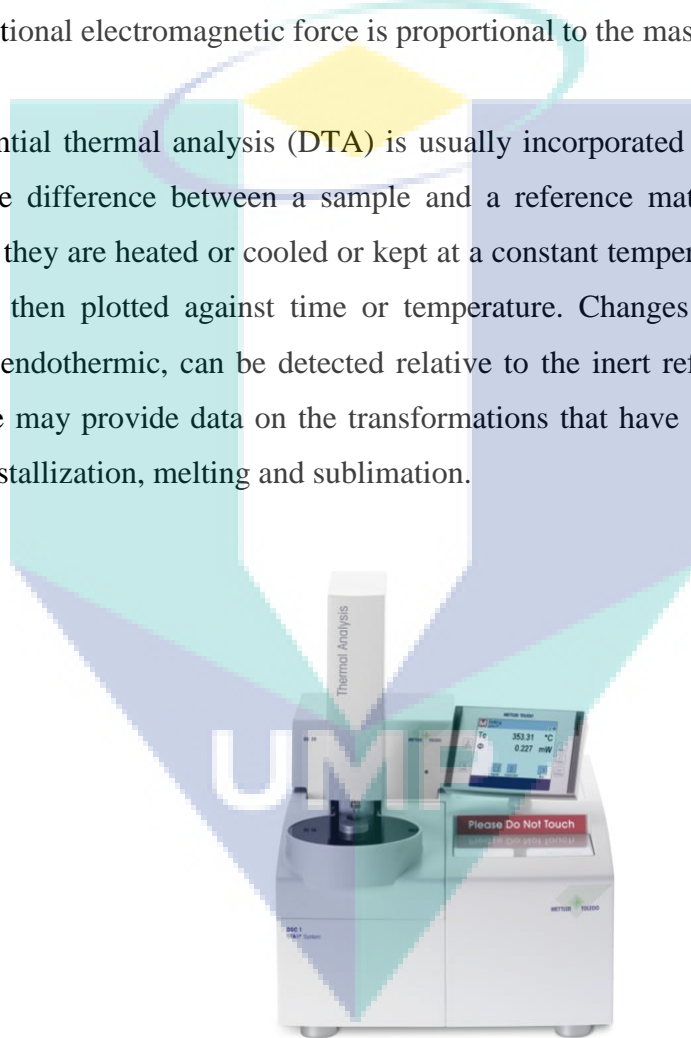


Figure 3.13: Photograph of TGA, Mettler-Toledo

In this present work, TGA was performed using Toledo STAR-1 (Mettler; Switzerland) as exhibited in Figure 3.13. About 5 mg of sample was heat treated from 30 to 750 °C at a heating rate of 10 °C/min with nitrogen as purge gas.

3.6.4 Differential scanning calorimetry

Differential scanning calorimetry (DSC) is a thermodynamic technique used to measure enthalpy changes in samples due to changes in their physical and chemical properties as a function of temperature or time. DSC can be used to obtain thermal critical points like the temperatures of melting point (T_m), crystallization (T_c), or glass transition (T_g), of the sample. When the sample and an empty reference crucible are heated at constant heat flow, the temperature difference of both crucibles caused by the thermal critical points of the sample and the reference can be detected. The reference crucible is generally identical with the sample used. The schematic diagram of a DSC system is shown in Figure 3.14.

Glass transitions may occur as the temperature of an amorphous solid is increased. These transitions appear as a step in the baseline of the recorded DSC signal. This is due to the sample undergoing a change in heat capacity; no formal phase change occurs. As the temperature increases, an amorphous solid will become less viscous. At some point the molecules may obtain enough freedom of motion to spontaneously arrange themselves into a crystalline form. This is known as the cold crystallization temperature. This transition from amorphous solid to crystalline solid is an exothermic process and results in a peak in the DSC signal. As the temperature increases the sample eventually reaches its melting temperature. The melting process results in an endothermic peak in the DSC curve. The ability to determine transition temperatures and enthalpies makes DSC a valuable tool in producing phase diagrams for various chemical systems. The output data displays a thermogram of heat flow (dQ/dt) against temperature as shown in Figure 3.15; ΔH is the estimated area of the DSC peak.

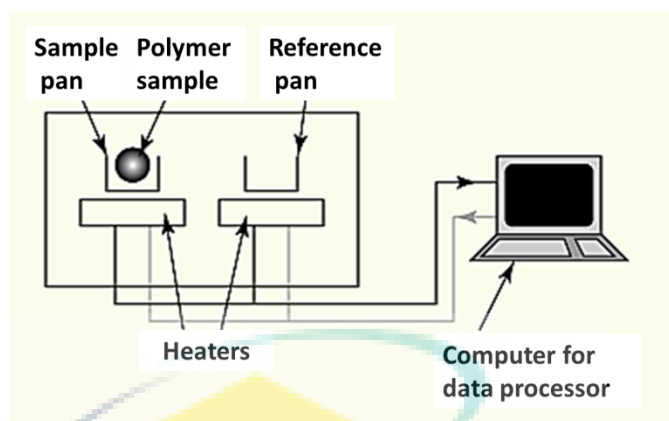


Figure 3.14: Schematic diagram of DSC

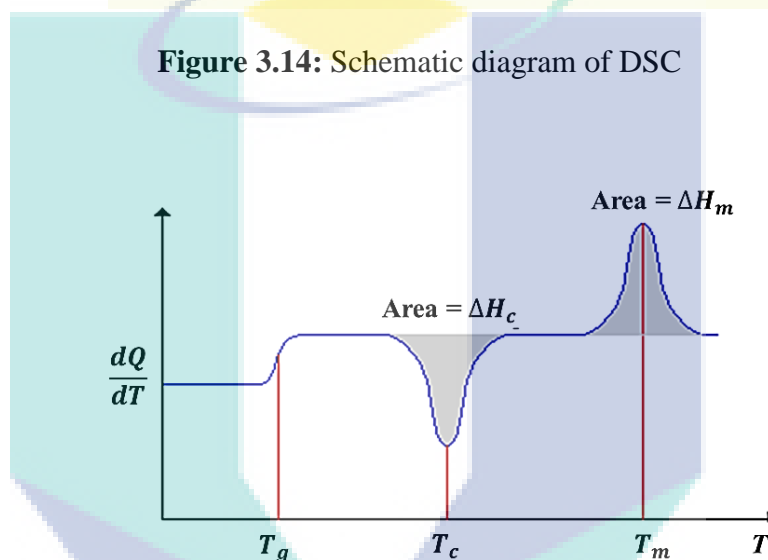


Figure 3.15: DSC thermograms



Figure 3.16: Photographs of DSC, TA instruments

In this work, DSC was performed with a Q500 (TA instruments, New Castle, USA) as shown in Figure 3.16. About 5 mg of sample was heat-treated from 50 to 250 °C at a heating rate of 10 °C/min, under atmospheric conditions. The degree of relative crystallinity, χ_c can be expected from the endothermic area by the following equation:

$$\chi_c = \Delta H_f / \Delta H_f^0 \quad (3.1)$$

where, ΔH_f = measured enthalpy of fusion from DSC thermograms and ΔH_f^0 = enthalpy of fusion for 100 % crystalline polymer, which in this case is PVA=138.6 J/g (Peppas and Merrill, 1976).

3.6.5 Mechanical properties

Tensile testing or strip extensimetry methods have been extensively used to study the mechanical behaviour of various biopolymers scaffold (Silver, 1987; Molladavoodi et al., 2013 and Meyers et al., 2008). The technique involves applying a tensile force to a sample with known dimensions, held between two clamps and stretched. The force exerted by the instrument and length of the sample are measured and used to obtain a stress-strain curve as illustrated in Figure 3.17. This chart can be used to derive several mechanical properties including Young's modulus, ultimate tensile strain and ultimate tensile strength (Chan et al., 1999). Stress-strain diagrams are typically based upon the original cross sectional area and the initial gage length even though these quantities change continuously during the test. Stress, σ can be expressed as in Eq. (3.2) (Brinson and Brinson, 2008):

$$\sigma = \frac{F}{A_0} \quad (3.2)$$

where; F is applied force (N) and A_0 is original cross-sectional area of the sample (m^2).

The unit of the engineering stress is Pascal (Pa) or N/m^2 as it is referred to in the SI Metric Unit. Strain, ε is defined as "deformation of a solid due to stress" can be expressed as Eq. (3.3) (Brinson and Brinson, 2008):

$$\varepsilon = \frac{L_f - L_o}{L_o} \quad (3.3)$$

where; L_o is the original length of the sample and L_f is the final length of the sample.

The slope of the straight-line portion of the stress-strain diagram as shown in Figure 3.17 is called the Young's Modulus, E and can be represented as in Eq. (3.4) (Brinson and Brinson, 2008):

$$E = \frac{\sigma}{\varepsilon} \quad (3.4)$$

The modulus of elasticity may also be characterized as the "stiffness" or ability of a material to resist deformation behaviour within the linear range.

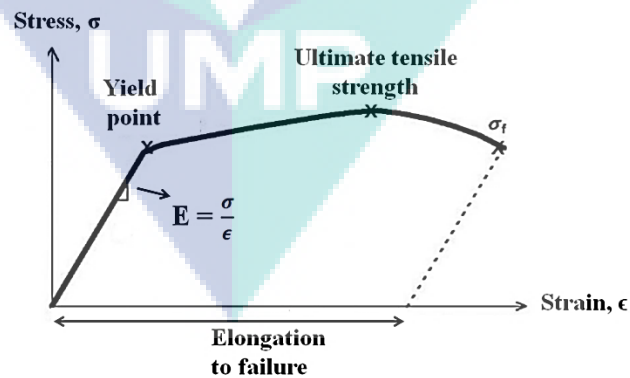


Figure 3.17: Stress-strain curve diagram

The mechanical properties of the scaffolds were measured using a universal testing machine (EZ-X series Tabletop Materials Testers, Shimadzu) as shown in Figure 3.18, with a cross-head speed of 10 mm/min. These properties were important to test the tensile

strength and compressive strength of the scaffolds. Rectangular specimens with dimensions of 10 mm x 20 mm were used for testing. The room conditions were controlled at 25 °C and 34% humidity. The tensile stress and strain at break were calculated based on the obtained tensile stress-strain curve.

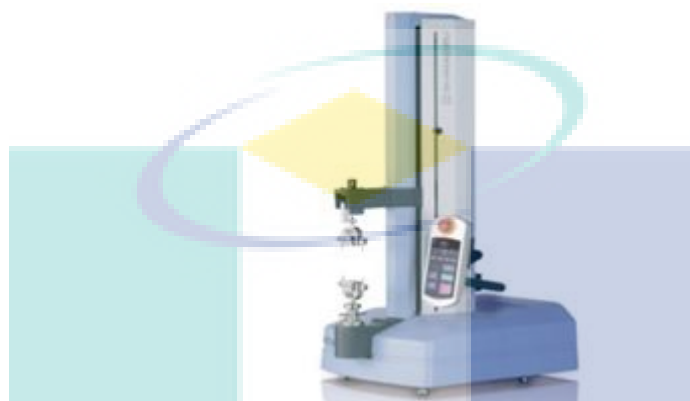


Figure 3.18: Photograph of universal testing machine, Shimadzu

3.6.6 Ultraviolet-visible spectroscopy

Ultraviolet-visible (UV-Vis) spectroscopy is used to measure the attenuation of a beam light after it passes through a sample or after reflection from a sample surface specifically in the ultraviolet-visible spectral region. In this electromagnetic spectrum, molecules undergo electronic transitions. A close relationship exists between the color of a substance and its electronic structure. A molecule or ion will exhibit absorption in the visible or ultraviolet region when radiation causes an electronic transition within its structure. Thus, the absorption of light by a sample in the ultraviolet or visible region is accompanied by a change in the electronic state of the molecules in the sample. The energy supplied by the light will promote electrons from their ground state orbitals to higher energy, i.e. excited state orbitals or antibonding orbitals. A spectrometer records the degree of absorption by a sample at different wavelengths to plot a spectrum of absorbance against wavelength. In this work, UV-visible analysis was carried out with a Thermo Scientific GENESYS 10S UV-Vis spectrophotometer (Figure 3.19), operated using quartz cuvettes in

the range of 250-700 nm. This characterization was done to ensure the occurrence of silver nanoparticles due to the plasmon resonance absorption in the UV-Vis region.



Figure 3.19: UV-Vis spectrophotometer, Thermo Scientific

(i) Surface Plasmon Resonance

The surface plasmon resonance (SPR) plays a major role in retrieving information on optical properties of metal nanoparticles. Basically, the free electrons in metal travel freely through the material (El-Nour et al., 2010). The surface plasmon is generated when the diameter of the metal is smaller than the wavelength of incident radiation ($d \ll \lambda$). The weakly bound conduction electrons on the metal surface will undergo collective oscillation when excited by light at specific wavelengths as shown in Figure 3.20. The electric field of an incoming light induces a polarization of the free electrons relative to the cationic lattice (Abdul Kareem and Anu Kaliani, 2011). Light will be absorbed when the incident light frequency matches the intrinsic electron oscillation frequency resulting in the surface plasmon absorption. The resonance condition of plasmon absorption bands in the absorption spectrum are determined by particle size, shape, dielectric constant, composition, and dielectric constant of the surrounding material (Vodnik et al., 2008).

A unique characteristic of these synthesized metal particles is that a change in the absorbance or wavelength in the UV-Vis region gives a measure of the particle size, shape, and interparticle properties (Sharma et al., 2009). For instance, a single SPR band in the

visible region indicates that the particles are spherical in shape whereas the absorption spectra consisting of more than one SPR bands is classified as nonspherical particles (Mathew and Kuriakose, 2013).

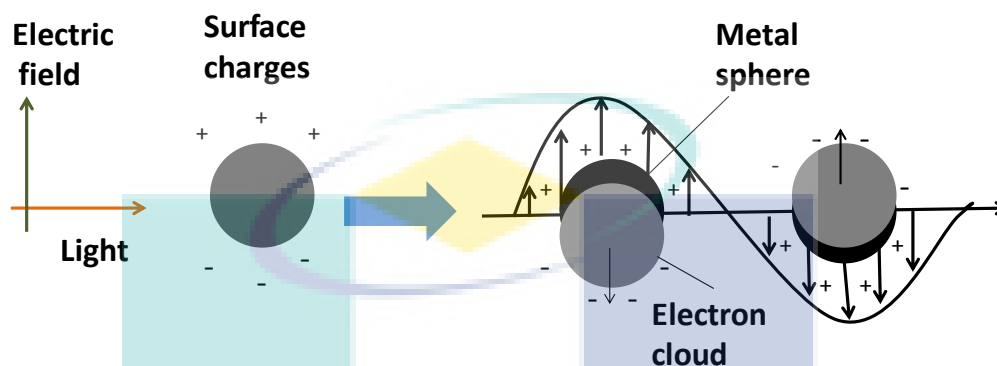


Figure 3.20: Collective oscillations of free electrons due to applied electric field (Kelly et al., 2003)

3.6.7 Porosity study

The porosity of the freeze-dried scaffolds was measured using water displacement method. The scaffolds were cut in 1 cm x 1 cm x 1cm sizes and immersed in a known volume (V_1) of water in a Falcon tube for 30 min. The total volume of water and the water impregnated scaffold were recorded as V_2 . The water-impregnated scaffolds were then removed from the Falcon tube and the residual water volume was recorded as V_3 . Experiments were carried out in six replicates for all types of scaffolds. The porosity of the scaffolds was obtained by Eq. (3.5) (Bhardwaj and Kundu, 2011):

$$\text{Porosity (\%)} = \frac{V_1 - V_3}{V_2 - V_3} \times 100\% \quad (3.5)$$

3.6.8 Swelling ratio study (freeze-dried scaffolds)

The water uptake or swelling analysis was analyzed for 7 days. The lyophilized scaffolds were cut into 1 cm x 1cm x 1cm and placed in 24-well plate. The scaffolds were

weighed (W_d) before submerged in PBS (pH 7.4) and kept in 37°C incubator. The wet weight of the samples (W_t) was determined after 1, 3 and 7 days by gently blotting them on filter paper (Sankar et al., 2012 and Ninan et al., 2013). Experiments were carried out in triplicates for all types of scaffolds. Swelling ratio was calculated according to Eq. (3.6) (Yang et al., 2012):

$$\text{Swelling ratio (\%)} = \frac{W_t - W_d}{W_d} \times 100\% \quad (3.6)$$

3.6.9 pH value measurements

The pH value measurement was done for nanofiber scaffolds only of PBS and DMEM solutions after the degradations at each time point were obtained by using a pH meter (Mettler Toledo FE20 FiveEasy™ pH meter). Each value was averaged from three specimens.

3.6.10 Swelling ratio study (nanofibers scaffolds)

All degraded nanofiber scaffolds were taken out from the media and directly eliminated of the excess water at the surface. The scaffolds were immediately weighted by an electrical balance with a resolution of 0.1 mg to obtain the weights of the samples at the swollen states, W_t . The scaffolds were then dried in a vacuum desiccator for 24 h. The dried mass was exemplified as W_d . Swelling ratio of nanofibrous scaffolds were calculated according to Eq. (3.6).

3.6.11 Weight loss study

Weight loss percentages were calculated from the dried weight obtained before and after degradation using a gravimetric method (Peña et al., 2006). The percentage of weight loss was determined after drying the samples in vacuum by comparing the dry weight, W_d at a certain time point with the initial weight, W_o according to Eq. (3.7) (Zhu et al., 2013):

$$\text{Weight loss (\%)} = \frac{W_o - W_d}{W_o} \times 100\% \quad (3.7)$$

For the lyophilized scaffolds, the samples were cut into 1 cm x 1cm x 1cm and sterilized under UV irradiation for 2 hours. The scaffolds were placed in 24-well plate containing 3 ml of PBS incubated at 37°C for 1, 3 and 7 days. Meanwhile, for nanofibrous scaffolds, the steps were as explained in 3.5.1 (ii). Both nanofibers and freeze-dried scaffolds (six and three replicates respectively) were taken out at different periods of time, washed with distilled water and kept dry in a desiccator for further use.

3.7 CELL CULTURE STUDIES

In order to achieve objective 3, cell culture studies were done to ensure the cell-scaffold interaction as potential substrates for tissue engineering applications. Initially, the primary cells were expanded in tissue culture flask, underwent subculture and seeded on the polymeric 3D scaffolds. The steps are summarized in Figure 3.21 while the details were further elaborated in next sections.

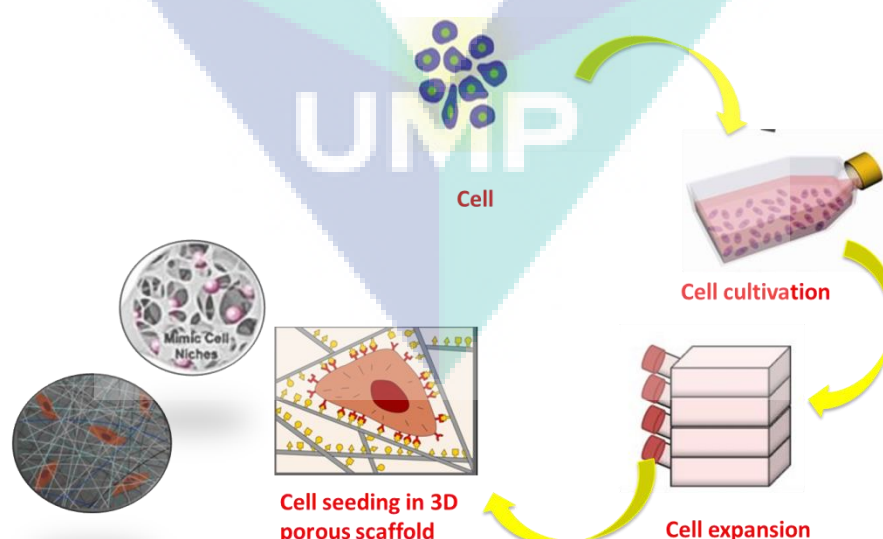


Figure 3.21: Summarize of cell culture study

3.7.1 Cell expansion and seeding

Firstly, the scaffolds were cut into small disks with 10 mm diameter, soaked in 100 % ethanol for 24 h, and then sterilized under UV light for 3 h and subsequently immersed in cell culture medium overnight. The scaffolds were washed thrice with sterile PBS and transferred into a 96-well tissue culture plate.

There are two types of cells used in the current study, which are the A375 melanoma and human fibroblast (hFB) cells. Both the A375 melanoma and hFB cells were cultured in DMEM and MEM respectively containing 10 % FBS and 1 % penicillin streptomycin solution in 75 cm² cell culture flasks. These skin cells were incubated at 37 °C in a humidified atmosphere containing 5 % CO₂ and 95% humidity. Thereafter, both cells grown in 75 cm² cell culture flasks were detached on confluency by adding 1 ml of trypleETM Express (animal origin-free). Detached cells were centrifuged and counted by Trypan blue using a haemocytometer, seeded on the relative scaffolds at a density of (1 x 10⁵) cells/cm² and incubated to facilitate cell growth. The example of cell-scaffold incubated in 96-well plate is shown in Figure 3.22. The medium was refreshed every 3 days. Different scaffolds were incubated at different time points as stated in Table 3.1.

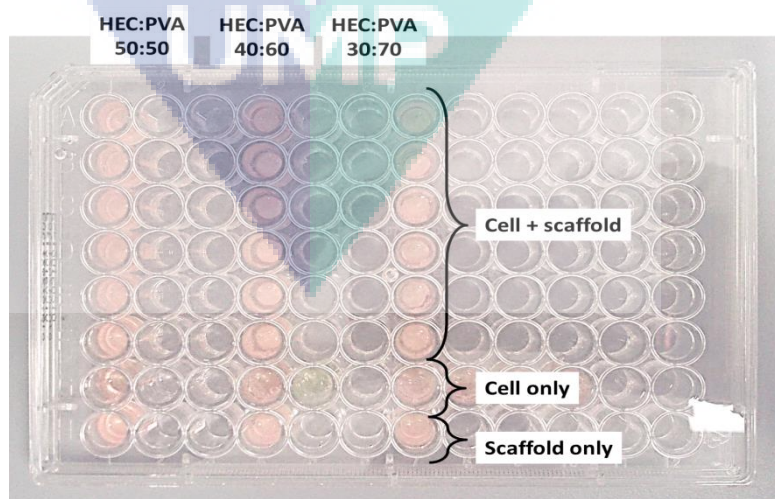


Figure 3.22: Cell culture studies of HEC/PVA nanofibers scaffolds at different weight ratios

Table 3.1: Summarized of samples prepared and incubation time points for cell culture studies in this work

Techniques	Samples	Ratios	Times
Electrospinning	HEC/PVA nanofibers	50:50	1, 4 and 7 days (A375 melanoma cells)
		40:60	
30:70			
	HEC/PVA/collagen nanofibers	50:50:50	2, 4 and 7 days (hFB cells)
Freeze-dried	HEC	1	1, 4, and 7 days (hFB cells)
		2:1	
	HEC/PVA	1:1	
		1:2	
	PVA	1	
	HEC/Silver nanoparticles	0.4 %	
0.8 %			
1.6 %			

3.7.2 Cell morphology studies

After reaching particular time point, the cells grown on scaffolds were rinsed twice with PBS and fixed in 3 % GA for 60 min. Thereafter, the scaffolds were dehydrated with increasing concentrations of alcohol (20, 40, 60, 80 and 100%) for 10 min each. The samples were air dried by keeping the samples in a fume hood. Lastly, the scaffolds were sputter coated with platinum and observed using SEM at an accelerating voltage of 10 kV.

3.7.3 A375 melanoma cell proliferation study

The cell proliferation of A375 melanoma cells were analysed by MTT assay. Initially, 10 μ l of MTT solution (5mg/ml) was added into the 96-well plate that contained the cells and scaffold, and then incubated at 37 °C for 4 h. The MTT solution was removed from each well and 100 μ l of dimethyl sulfoxide DMSO were added to each well to dissolve the MTT formazan crystals. The absorbance was recorded at 570 nm with background 630 nm by an ELISA micro plate reader (VersaMax™) as shown in Figure

3.23. Since the absorbance at 570 nm is proportional to cell viability, the cell viability was calculated as in the following formula (Barnes et al., 2007):

$$\text{Cell viability} = A_{\text{sample}}/A_{\text{control}} \times 100 \quad (3.8)$$

where; A_{sample} = absorbance at 570 nm of the sample and A_{control} = absorbance at 570 nm of the positive control in which the cells are in complete medium, incubated in the absence of the scaffolds. All data were presented as the mean and standard deviation of six measurements.

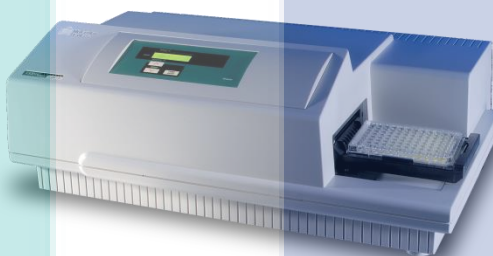


Figure 3.23: Photograph of ELISA microplate reader, VersaMax™

3.7.4 hFB cell proliferation study.

The cell adhesion and proliferation of hFB cells on the scaffolds were determined using the colorimetric MTS assay (CellTiter 96 A_{Queous} One Solution Promega, Madison, WI). The reduction of yellow tetrazolium in MTS (3-(4,5-dimethylthiazol-2-yl)-5-(3-carboxymethoxyphenyl)-2(4-sulfophenyl)-2H-tetrazolium) to form purple formazan crystals by the dehydrogenizing enzymes secreted by the mitochondria of metabolically active cells forms the basis of this assay as observed in Figure 3.24 for HEC/PVA nanofibers scaffolds at different weight ratios. The formazan dye shows absorbance at 492 nm and the amount of formazan crystals formed is directly proportional to the number of living cells. After culturing the cells for a period of time, they were rinsed with PBS to remove unattached cells and incubated with 20% MTS reagent in serum-free MEM for 4 h at 37 °C (Jin et al., 2011 and Cui et al., 2009).

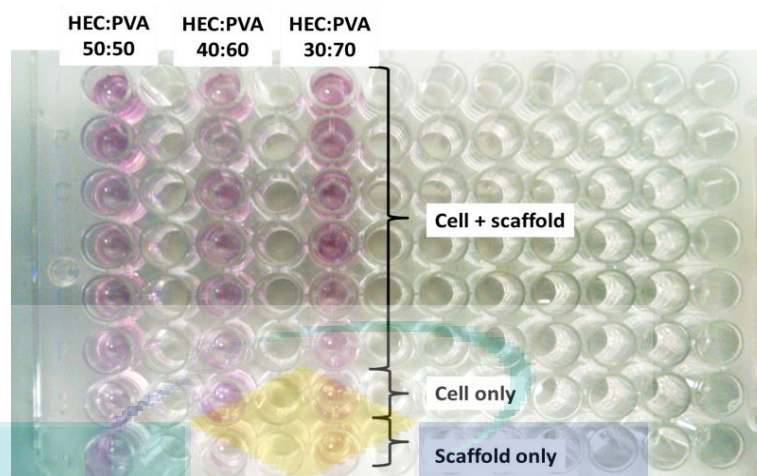


Figure 3.24: MTS assay of HEC/PVA nanofibers scaffolds at different weight ratios

3.8 STATISTICAL ANALYSIS

All data were presented as mean \pm standard deviation and analyzed using Student's t-test to calculate the significance level of the data. Probability values of $p < 0.05$ were interpreted as denoting statistical significance.

CHAPTER 4

FABRICATION AND CHARACTERIZATION OF SCAFFOLDS USING ELECTROSPINNING AND FREEZE-DRYING TECHNIQUES

4.1 CHEMICALLY CROSSLINKED STUDY OF HEC/PVA AND HEC/PVA/COLLAGEN NANOFIBERS SCAFFOLDS

4.1.1 Introduction

The main objective of this part is to develop nanofiber scaffolds from HEC, PVA and collagen *via* electrospinning technique at different weight ratios as summarized in Table 3.1. Nanofibrous scaffolds were made water insoluble by chemical cross-linking using glutaraldehyde. The microstructure, morphology, mechanical and thermal properties of the blended HEC/PVA and HEC/PVA/collagen nanofibrous scaffolds before and after cross-linking were characterized by using SEM, ATR-FTIR, DSC, TGA and UTM.

4.1.2 Morphology of HEC/PVA nanofibrous scaffolds

Viscosity is one of the important parameters in the spinning process of nanofibers. The solution viscosity of HEC (5 wt%) was 2555 cp and that of PVA (15wt%) was 395 cp. Since the aqueous solution of HEC is highly viscous, the increase in HEC content contributed to increased viscosity of the spinning solution. Hence, the added amount of HEC in the HEC/PVA blend from 30% to 50% encountered significant increase from 1504 cp to 2550 cp as depicted in Figure 4.1 (*H*-HEC content, *P*-PVA content). On the other

hand, HEC/PVA with diluted collagen (0.38 wt%) ternary blended solution acquired the lowest viscosity at 1208 cp.

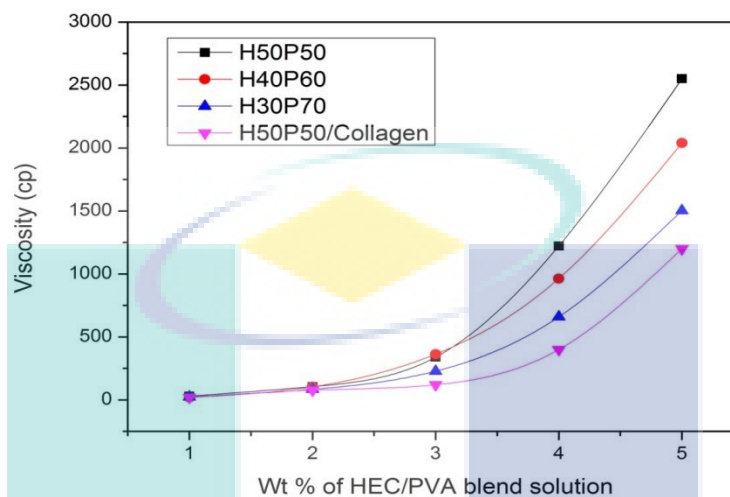


Figure 4.1: Plot of the viscosity of the solution with respect to the wt% of the HEC/PVA (a) 50:50, (b) 40:60, (c) 30:70 in the solution

Although the viscosity of HEC is high, nanofibers from HEC were difficult to obtain. It gives a drop-like deposition in solution phase on the collecting target as shown in Figure 4.2. This is because properties of the polymer solution such as surface tension, electrical conductivity and polymer concentrations influence the electrospinning process (Huang et al., 2003). For HEC with concentration lower than 5 wt%, drops were formed whereas with high concentrations i.e. >5 wt%, the flow of the solution out of the needle is low. When solution viscosity is high, the jets from the needle are stable and would not break up while travelling, split into filaments and form fibers with increased diameters. In contrast, for low viscosity solutions, the jets would likely to break up and form beads on fiber surface, which in turn will increase the difficulty to obtain continuous nanofibers on the rotating collector, thus resulting in a decrease in fiber diameter. Figure 4.3 (a-h) shows the SEM images of nanofibrous scaffolds at different weight ratios of HEC/PVA, with and without collagen, before and after chemically cross-linking with GA. The images revealed uniform, porous, beadless and nano-scaled fibrous structures formed under optimized parameters as summarized in Table 4.1.

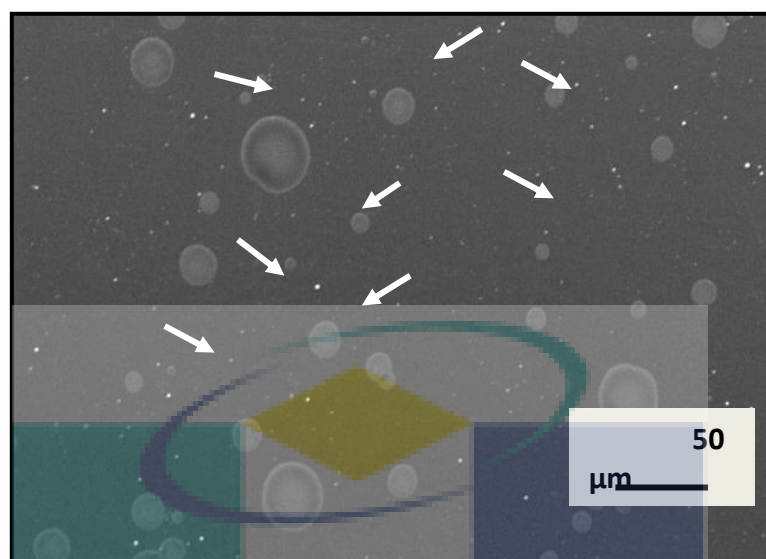


Figure 4.2: SEM images of HEC nanofibers mats (white arrow indicates the droplets)

Table 4.1: Electrospinning parameters for HEC/PVA nanofibers and their corresponding average fiber diameter

Sample Code	Electrospinning parameters.					
	Rotation speed (rpm)	Tips-to-collector distance (mm)	Flow rate (ml/h)	Applied voltage (kV)	Average non-crosslinked fiber diameter (nm)	Average crosslinked fiber diameter (nm)
H50P50	1000	110	1	20	373.08 ± 76.24	280.51 ± 10.56
H40P60	1000	100	1	20	461.38 ± 87.75	303.66 ± 73.86
H30P70	1000	90	1	20	325.10 ± 65.96	204.47 ± 53.61
With collagen	1500	100	1	22	220.14 ± 8.26	188.34 ± 37.30

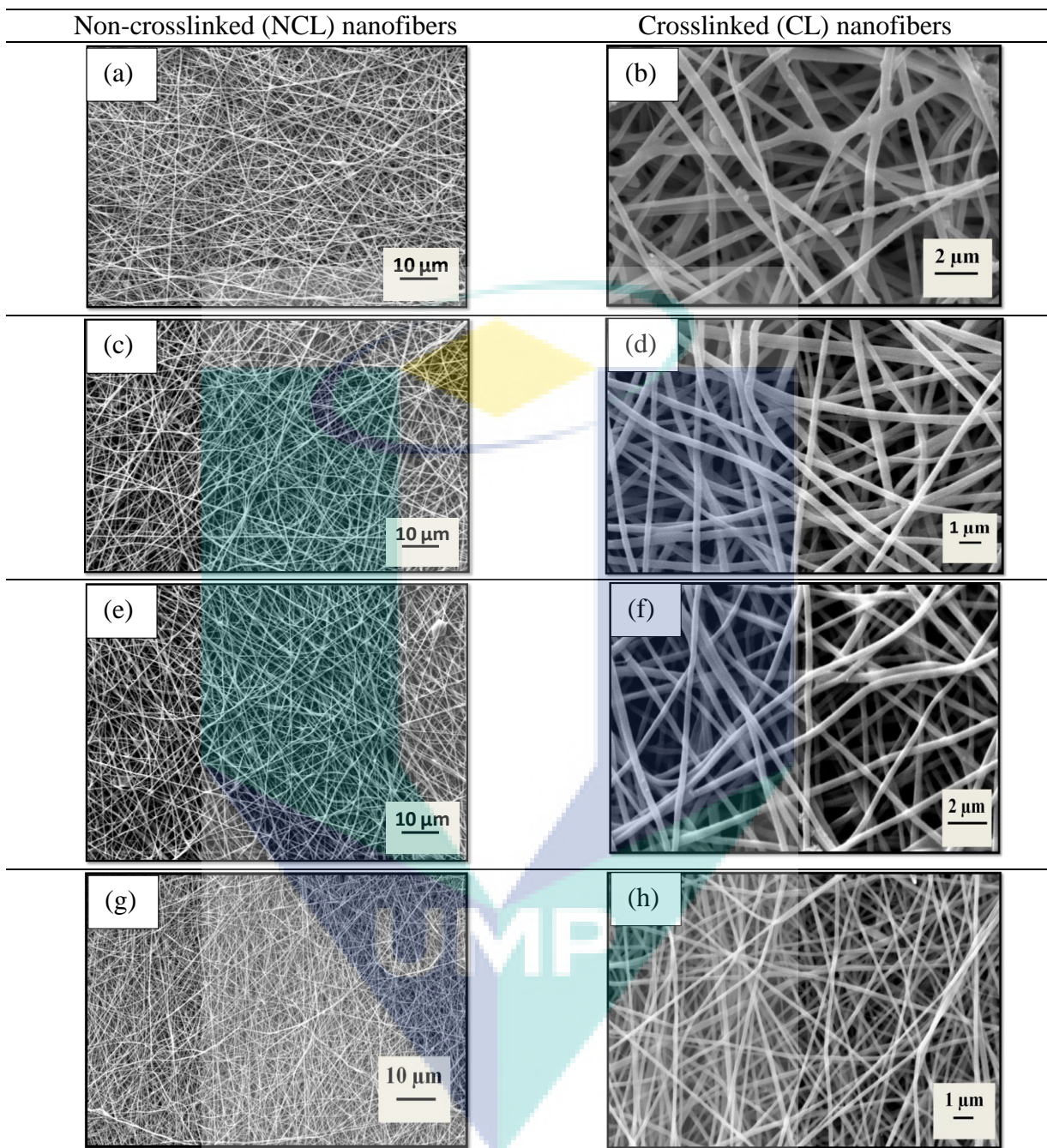


Figure 4.3: SEM images and diameter distribution of electrospun HEC/PVA nanofibers: (a,b) H50P50, (c,d) H40P60, (e,f) H30P70, (g,h) with collagen

The SEM images confirmed the three-dimensionality of the HEC/PVA and HEC/PVA/collagen scaffolds, which also portrays large voids. The nanofibrous mats possess interstitial spaces between the fibers. No pores were observed on the fiber surface,

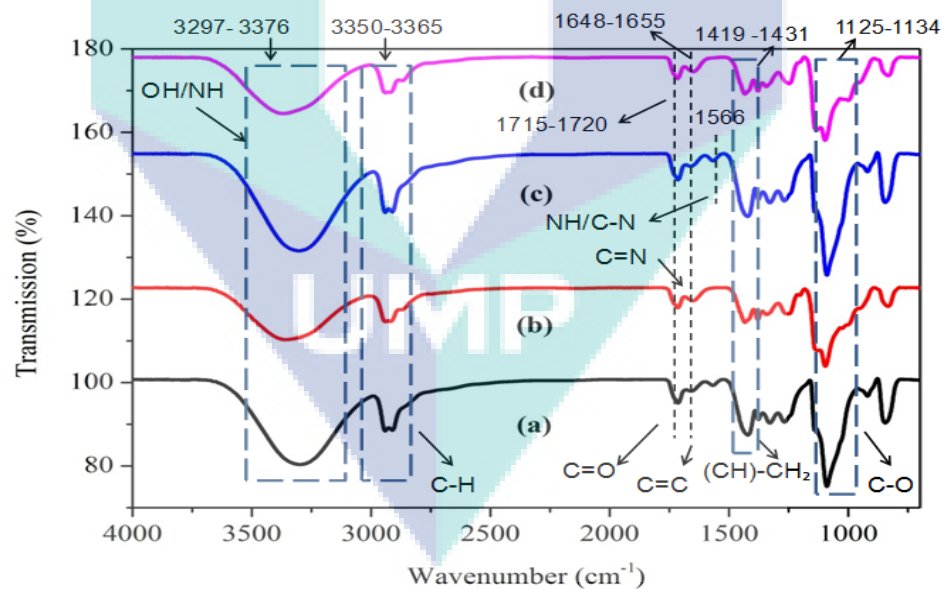
but were instead present between the fibers on the electrospun mats. After cross-linking, there were no significant morphology changes except that the diameters were slightly increased from the range of 188-280 nm to 220-373 nm for non-cross-linked and cross-linked nanofibers respectively as shown in Figure 4.3 (b, d, f and h). The morphological similarity of electrospun nanofibers to native ECM consists of various interwoven protein fibers with diameters ranging from tens to hundreds of nanometers, thus signifying the application of these scaffolds as a supportive matrix for stem cell attachment and differentiations (Prabhakaran, 2012). Nanofiber scaffolds that mimic the fibrous ECM molecules in the native skins could provide mechanical, biological and chemical cues to the cells for tissue morphogenesis, differentiation and homeostasis (Frantz et al., 2010). The determination of fiber diameters is very important as it corresponds not only to molecular level orientation but also affects the cellular behaviour (Eglin et al., 2009).

4.1.3 ATR-FTIR study

The attenuated total reflection-Fourier transform reflection (ATR-FTIR) spectra of HEC/PVA and HEC/PVA/collagen for non-cross-linked and cross-linked electrospun nanofibers are shown in Figure 4.4 (i) and (ii) respectively. FTIR spectra analysis was carried out to elucidate the presence of HEC and PVA in the blended nanocomposite and to analyze the interaction (hydrogen bonding) between them.

As displayed in Figure 4.4 (i), the broad peaks at 3297 to 3376 cm^{-1} indicates stretching vibrations of the hydroxyl groups due to the intramolecular and intermolecular hydrogen bands of the OH groups of PVA and HEC. It was also seen that these peaks become broader with the increase of HEC content. The peaks at 2920 to 2929 cm^{-1} are due to CH_2 stretching vibrations. The presence of two peaks at 1720 to 1715 cm^{-1} indicates stretching of C=O while at 1655 to 1648 cm^{-1} indicates presence of C=C chains. The interaction between natural and synthetic polymers show a moderate peak at 1566 cm^{-1} for NH (amide II, N-H bending and C-N stretching and at 1655 cm^{-1} for C=O stretching (amide I) (Sugantha Kumari, et al., 2011).

After cross-linking the fiber mats with glutaraldehyde, slight changes on the peaks of the absorption band were observed as shown in Figure 4.4 (ii). The peaks of O-H stretching vibrations become broader as well as shifted to the left, which is from 3343 to 3368 cm^{-1} . On the other hand, the C-O stretching peak at 1125-1134 cm^{-1} became stronger compared with that of the non-cross-linked nanofiber. This suggests that the hydroxyl group of the PVA had reacted with GA to form acetal group. In addition, C=O band at 1711 to 1722 cm^{-1} decreased in comparison to the non-cross-linked nanofibers due to reaction of GA with the blend polymer hydroxyl group (Tanyolaç and Sönmezşık, 2005). Further cross-linking with GA showed that the absorption peak at 1650 cm^{-1} is ascribed to C=N stretched peak (imine linkage) as explained by the Schiff base formation from the reaction of aldehyde functional group of GA and amino group of collagen (Angadi et al., 2010 and Costa-Júnior et al., 2009). The imine group was formed by the nucleophilic reaction of the amide from collagen with the aldehyde (Costa-Júnior et al., 2009).



(i)

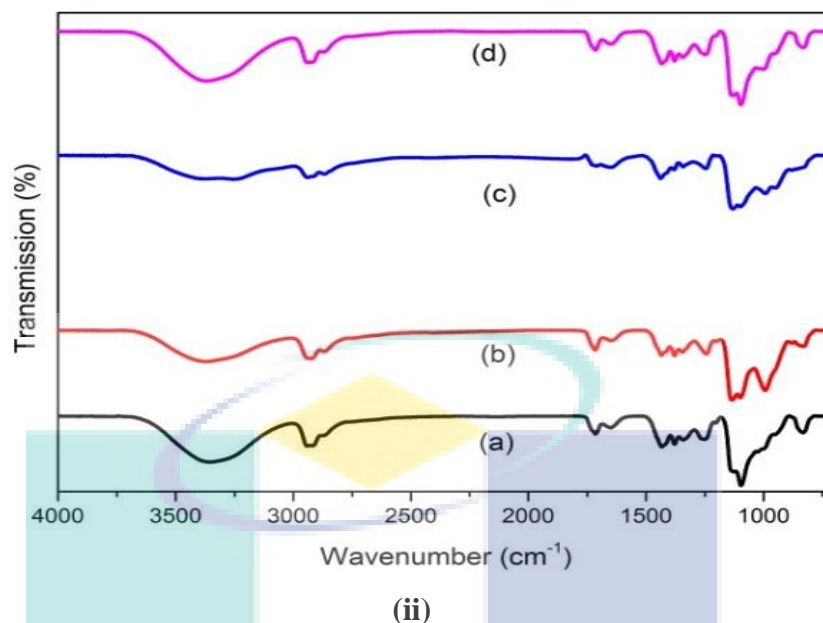


Figure 4.4: ATR-FTIR spectra of (i) non-crosslinked and (ii) crosslinked electrospun HEC/PVA nanofibers: (a) H50P50, (b) H40P60, (c) H30P70, (d) with collagen

4.1.4 TGA measurements

Thermal stability of HEC/PVA and HEC/PVA/collagen electrospun nanofibers was studied using TGA. The thermograms and its derivatives (drTGA) before and after cross-linking are illustrated in Figure 4.5(a*-d*) and (a-d) respectively. All curves exhibited three major weight losses. These steps were distinguishable in the diagram of mass loss (TGA %) during heating as well as more clearly in the diagram of derivative mass loss (drTGA %). The details of the decomposition step and percentage mass loss for HEC/PVA and HEC/PVA/collagen nanofibers are summarized in detail as shown in Table 4.2.

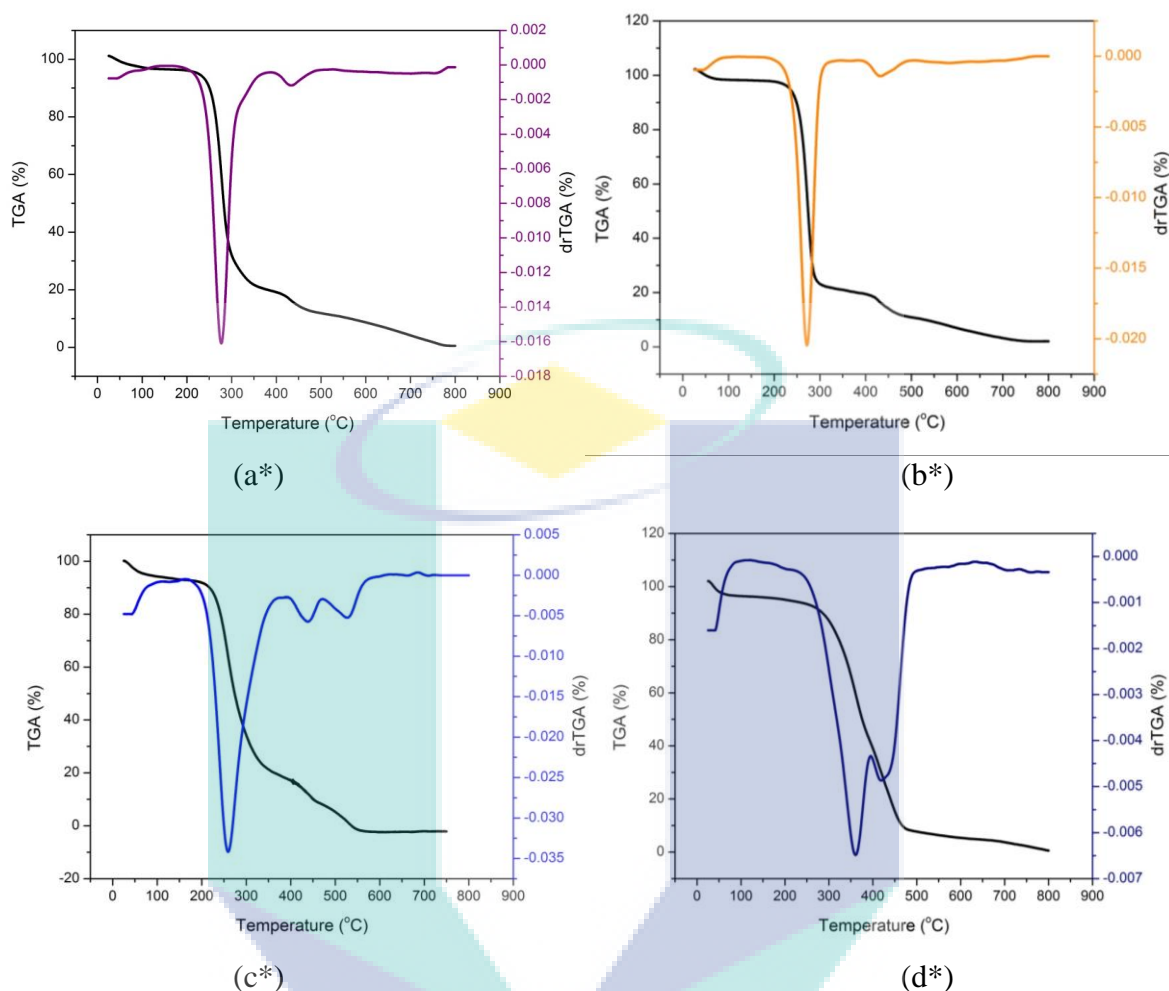
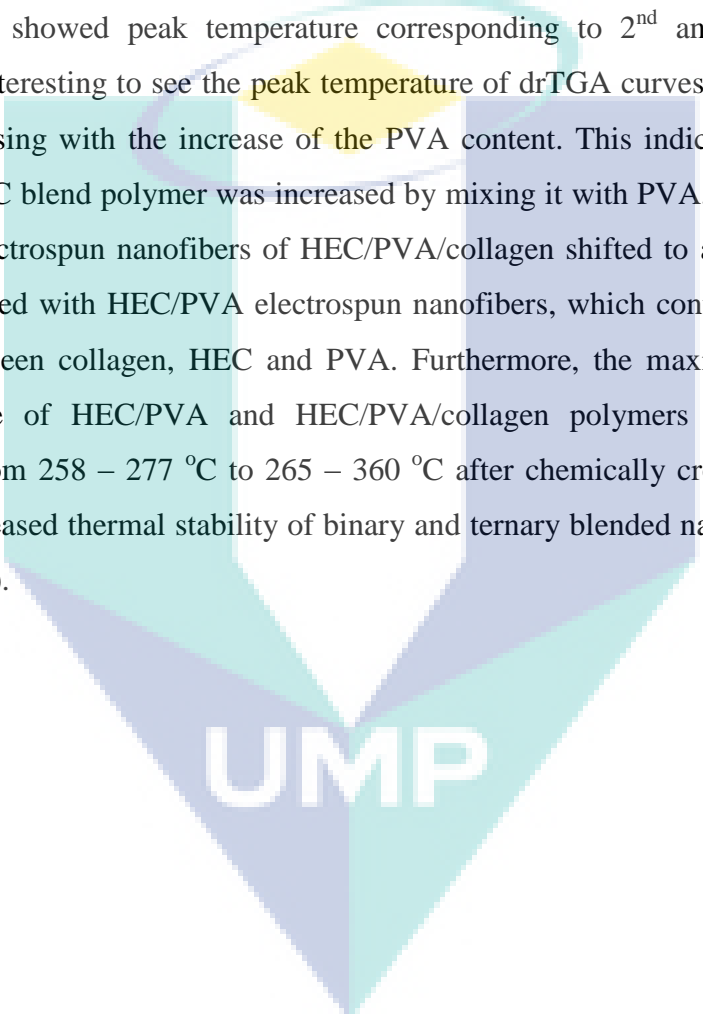


Figure 4.5 (a*-d*): TGA and drTGA curves for non-crosslinked electrospun HEC/PVA nanofibers: (a) H50P50, (b) H40P60, (c) H30P70, (d) with collagen

The lower values of weight loss percentage, varied from 3.2 to 12.7 % in the 1st stage starting from 23^o to 275 °C, affirmed the presence of a thermal process due to moisture evaporation or weak physisorption of water. This could be due to splitting or volatilization of small molecules from the samples, which in this case refers to monosaccharides or disaccharides through constituent monomers of HEC biopolymer (Tripathy et al., 2009). There were more significant weight loss (50 – 76 %) in the range of 275 to 419 °C at the 2nd decomposition stage, proving the existence of a chemical degradation process resulting from bond scissions (carbon-carbon bonds) in the polymeric bone as well as the degradation of side chain of PVA molecule, degradation of collagen

molecule and loss of CO₂ in the case of HEC (El-Sayed et al. 2011). The third weight loss at 420 – 530 °C was due to the by-products generated by PVA during thermal degradation process attributed to decomposition of the main chain of PVA (Holland and Hay, 2001).

The difference in thermal decomposition behaviour of HEC/PVA and HEC/PVA/collagen blend samples can be seen more clearly from drTGA curves. The drTGA curves showed peak temperature corresponding to 2nd and 3rd decomposition regions. It is interesting to see the peak temperature of drTGA curves for HEC/PVA blend samples increasing with the increase of the PVA content. This indicates that the thermal stability of HEC blend polymer was increased by mixing it with PVA. The maximum mass loss rate of electrospun nanofibers of HEC/PVA/collagen shifted to a higher temperature, 360 °C compared with HEC/PVA electrospun nanofibers, which contributed to the strong H₂ bonds between collagen, HEC and PVA. Furthermore, the maximum decomposition mass loss rate of HEC/PVA and HEC/PVA/collagen polymers increased to higher temperature from 258 – 277 °C to 265 – 360 °C after chemically cross-linking with GA, indicating increased thermal stability of binary and ternary blended nanofibers as shown in Figure 4.5 (a-d).

The logo for UMP (Universiti Malaysia Perlis) is a large, stylized shield shape. It is divided into four quadrants by a white cross. The top-left quadrant is light blue, the top-right is light green, the bottom-left is light purple, and the bottom-right is light teal. The letters 'UMP' are written in a bold, white, sans-serif font across the center of the shield.

UMP

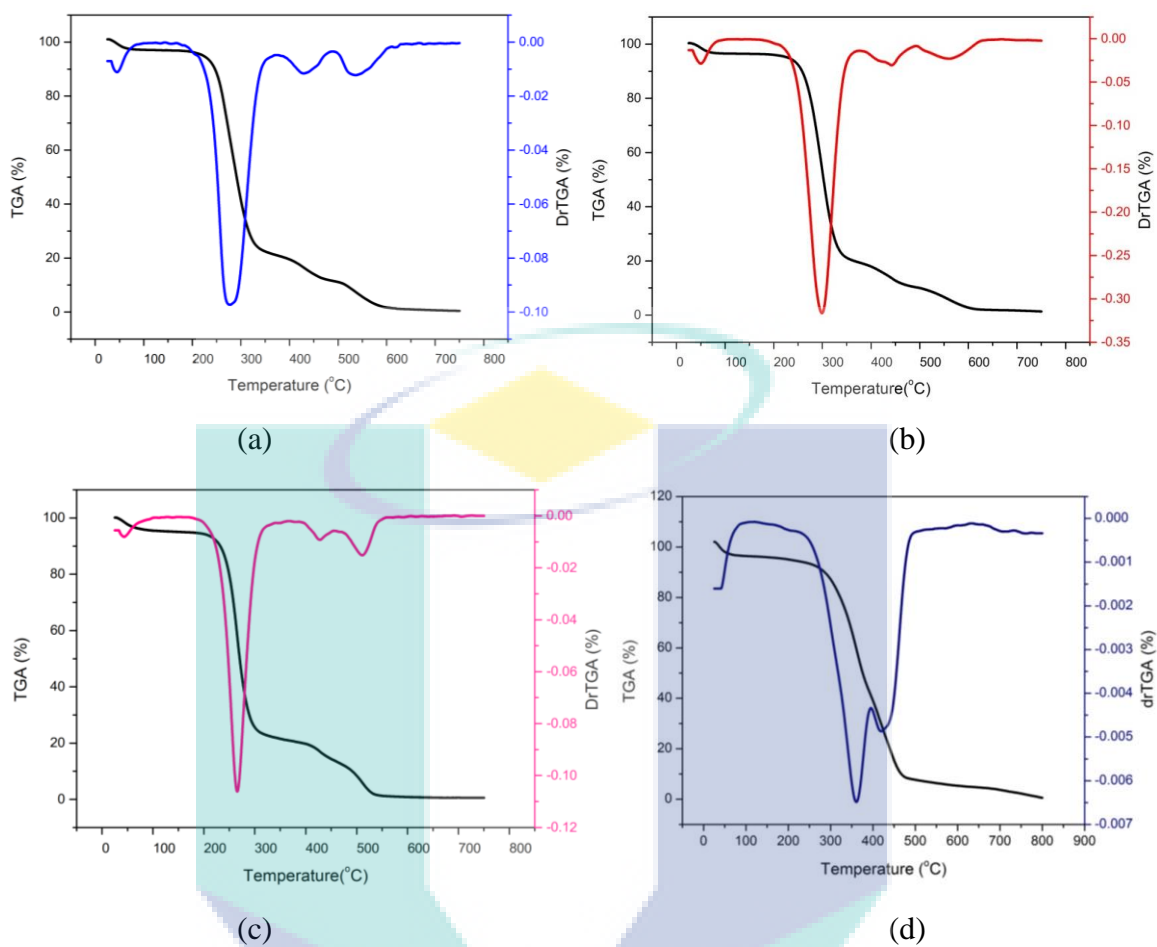


Figure 4.5 (a-d): TGA and drTGA curves for crosslinked electrospun HEC/PVA nanofibers: (a)H50P50, (b) H40P60, (c) H30P70, (d) with collagen

Table 4.2: TGA and DrTGA for polymer blends (CL-crosslinked, NCL- non- crosslinked)

Sample	Modifi- cation	Region of decomposition	Temperature (°C)			Weight loss (%)	
			T _{start}	T _{end}	T _{peak}	Partial	Total
H50P50	CL	1 st	25	196	45	3.2	89.3
		2 nd	196	373	276	76.01	
		3 rd	373	492	429	10.09	
	NCL	1 st	39	197	106	4.1	89.34
		2 nd	197	419	277	77.24	
		3 rd	419	529	434	8	
H40P60	CL	1 st	25	233	49	5.5	88.7
		2 nd	233	404	298	76.3	
		3 rd	404	490	439	6.9	
	NCL	1 st	28	195	132	4.4	89.83
		2 nd	195	371	269	74.8	
		3 rd	371	542	429	10.63	
H30P70	CL	1 st	24	217	45	12.7	84.8
		2 nd	217	373	265	67.1	
		3 rd	373	466	426	5	
	NCL	1 st	23	176	101	6.6	92
		2 nd	176	392	258	75.7	
		3 rd	392	470	436	9.7	
H50P50/ collagen	CL	1 st	23	275	162	8.67	92.26
		2 nd	275	395	360	50.88	
		3 rd	395	512	425	32.71	
	NCL	1 st	25	197	145	3.9	90.3
		2 nd	197	350	277	76.5	
		3 rd	350	529	436	9.9	

4.1.5 DSC study

DSC measurement was carried out to investigate the thermal behaviour of electrospun nanofibers such as melting (T_m) and glass transition (T_g) temperatures phenomena. The results from DSC and the characterization observed for electrospun nanofibers are shown in Figure 4.6 (i) and (ii) and summarized in Table 3.3.

DSC thermograms showed changes in heat capacity of HEV/PVA and HEC/PVA/collagen electrospun nanofiber mats associated with endothermic glass

transition of PVA from 55.3 – 67.9 °C and 62.6 – 72.0 °C before and after cross-linked respectively. The broad glass transition peak may be due to the overlapping transitions of two polymer blend samples (Shalumon et al., 2009). The T_g value as well as enthalpy that are associated with endotherm melting transition exhibited a slightly positive shift in temperature with the increase of PVA content. This increment could be attributed to the segmental motions of polymer chains, which are greatly constricted by the strong interactions between them through hydrogen bonds.

The change in heat capacity was followed by single melting peak resulting from a partial crystallization at 209.9 - 212 °C before cross-linked. Melting point is a physical parameter used to identify the nature of the substance and its degree of purity. The value of melting point depends on the degree of crystallinity phase and water amount in blend polymers (Sionkowska et al., 2009). It was observed that the T_m for HEC/PVA and HEC/PVA/collagen blend polymers is almost the same except the T_m shifted slightly to a higher value with the increase of PVA content. The increment in enthalpy of fusion, ΔH_m and T_m suggests that the crystallinity and perfection of the crystal structure was increased by the addition of PVA content.

Meanwhile, after cross-linking, the decrease in heat of fusion was enlarged in T_m as observed in Figure 4.6 (ii), suggesting that the crystallinity and perfection of the crystal structure had been reduced. Cross-linking causes ‘dehydration’ of fibers (loss of water molecule) and it is the reduced hydration that caused the higher peaks of T_g temperature (Miles et al., 2005). The dehydration was brought about by the cross-linking drawing the collagen as well as HEC and PVA molecules together. For HEC/PVA/collagen nanofibers, the endothermal peak of T_g shifted to a higher temperature, which indicates replacement of amino groups in collagen by aldehyde groups due to the cross-linking of GA, consequently (Pawar and Yadav, 2014). All samples exhibited lower value of T_m due to the involvement of hydrophilic hydroxyl side groups into the cross-linking reaction that reduces their ability to bind water molecules, consequently evaporating a low amount of water from the blend polymers within the same heating rate. It was also observed that the peak of T_m from DSC curves almost diminishes after cross-linking, indicating that the blend polymers act as a

single network with different transition temperature than an individual polymer (Gorgieva and Kokol, 2011). In other words, there were insufficient volumes necessary to make free movements between pendant groups of the cross-linking network due to the reduced molecular space present in the blend polymers (Rivas-Orta et al., 2006). It is thus concluded that the reduced crystallinity reinforced the effect of GA cross-linking in making the HEC/PVA blend system more homogenous and amorphous.

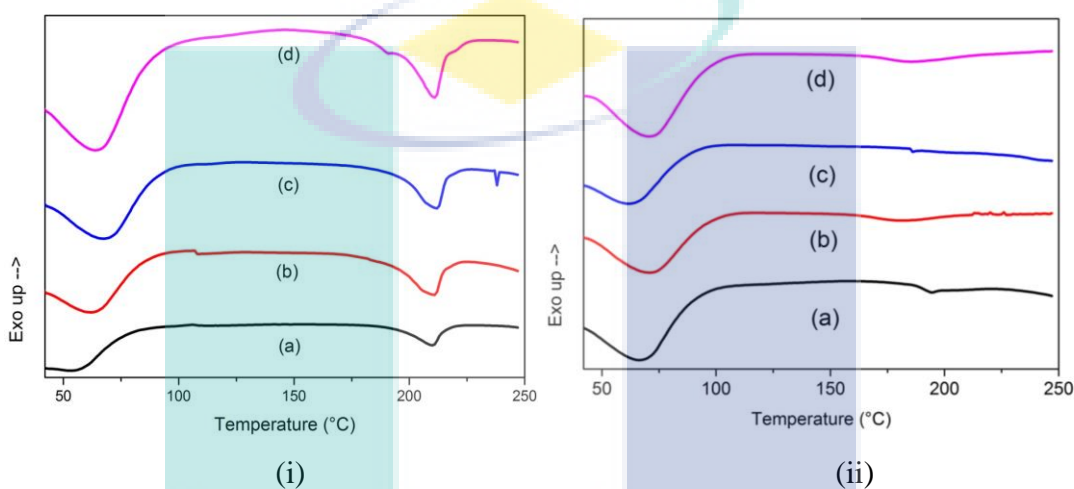


Figure 4.6: DSC thermograms for (i) non-crosslinked and (ii) crosslinked electrospun HEC/PVA nanofibers: (a) H50P50, (b) H40P60, (c) H30P70, (d) with collagen

Table 4.3: DSC data and the characteristics (CL-crosslinked, NCL- non-crosslinked)

Sample code	Modification	T_g (°C)	T_m (°C)	ΔH_m (J/g)	Crystallinity (%)
H50P50	NCL	55.28	209.90	19.10	13.78
	CL	67.38	194.35	10.01	7.22
H40P60	NCL	62.12	210.64	39.14	28.24
	CL	71.81	181.67	13.80	9.96
H30P70	NCL	62.55	211.95	60.66	43.77
	CL	67.85	185.20	14.92	10.76
H50P50/ collagen	NCL	66.25	211.17	34.91	25.19
	CL	72.02	185.82	8.09	5.84

In addition, the data in Table 4.3 also pointed out that the melting point, T_m for polymer blend samples are nearly around the value of pure crystalline PVA, which is 200

°C, which is same as reported by Sudhamani et al. (Sudhamani et al., 2003). It is well known that the heat required for 100 % melting of PVA is 138.6 J/g (Peppas and Merrill, 1976). By calculating the degree of crystallinity, χ_c using Eq. 3.1, it was found that the χ_c of HEC/PVA polymer blend samples increases parallel to PVA content. From data displayed in Table 4.3, it is interesting to observe that the degree of crystallinity for HEC/PVA/collagen was reduced to 25 %. This decrement is attributed to the effect of polymer-polymer interactions in the amorphous phase leading to disorder of the crystals, thus reducing the change of enthalpy (Sugantha Kumari et al., 2011 and Tanyolaç and Sönmezışık, 2005).

4.1.6 Mechanical properties

Mechanical properties such as tensile strength and elongation at break of different nanofibrous scaffolds were evaluated in this study. Figure 4.7 (i) and (ii) show typical nonlinear stress-strain curves of electrospun scaffolds at different ratios for non-cross-linked and cross-linked fiber mats. The mechanical properties such as the data of Young's modulus, ultimate tensile stress and strain are summarized in Table 4.4. Compared with the nanofibrous scaffolds after cross-linking, the Young's modulus and tensile stress significantly increased from 17.37 - 29.0 MPa to 106.1 - 234.25 MPa and 0.57 - 1.03 MPa to 2.31 - 4.04 MPa respectively. In contrast, the ultimate tensile strain was gradually decreased from the range of 15.22 - 33.53 % to 12.43 - 20.35 % indicating an increase of brittleness after cross-linking with GA. This can be explained *via* the formation of covalent bonding of the polymer chains in the cross-linked nanofibers resulting in higher tensile strength and lower elongation (Liao et al., 2011). Higher Young's modulus was obtained with the increase of PVA value. This increment signified the strong influence of amorphous fractions of chains within the fibers due to the cross-linking action that is contributed by the PVA component. Electrospinning showed such impacts in terms of molecular orientation and also alterations in crystallinity, which in turn, impart the physical uniqueness of the materials that leads to physical deformation of the fibers (Goonoo et al., 2014). The presence of collagen into HEC/PVA fibers improve the Young's modulus and tensile stress

of H50P50 from scaffolds due to the increase of rigidity and elongation at break of all scaffolds which imply the ductile properties of the HEC/PVA/collagen scaffolds.

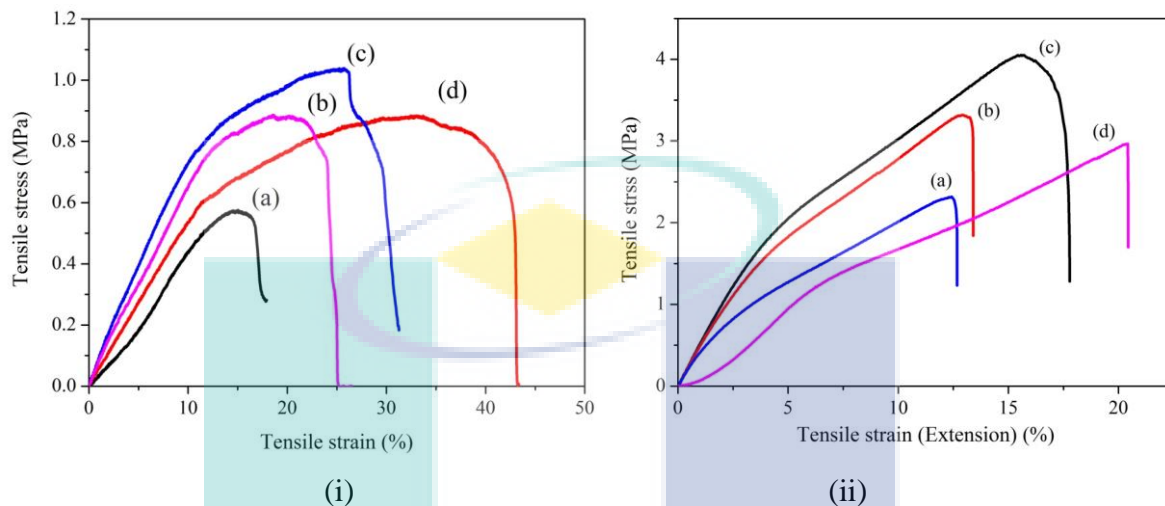


Figure 4.7: Stress-strain curves for (i) non-crosslinked and (ii) crosslinked electrospun HEC/PVA nanofibers: (a) H50P50, (b) H40P60, (c) H30P70, (d) with collagen

Table 4.4: Mechanical data observed for the electrospun nanofibers (CL-crosslinked, NCL-non-crosslinked)

Sample code	Modification	Young's modulus (MPa)	Ultimate tensile stress (MPa)	Ultimate tensile strain (%)
H50P50	NCL	17.37	0.57	15.22
	CL	183.75	2.31	12.43
H40P60	NCL	26.1	0.88	33.53
	CL	223.1	3.3	13.18
H30P70	NCL	36.54	1.03	26.17
	CL	234.25	4.04	15.73
H50P50/ collagen	NCL	29.0	0.97	28.74
	CL	106.1	2.95	20.35

The calculated Young's modulus based on slope in the elastic region is comparable to the tensile modulus of human skin, which lies in the range of 15 to 150 MPa (Edwards and Marks, 1995a). The ultimate tensile strength (MPa) and strain (%) value of blended nanofibrous scaffold are low compared to that of human skin, which is in the range of 5 -

30 MPa and 35 - 115 % respectively (Edwards and Marks, 1995a). However, previous reports have found that tensile strength of electrospun fiber mats range from 0.8 to 18.0 MPa is sufficiently durable for dermal cell culture (He et al., 2005 and Barnes et al., 2007). In addition, fibrous scaffolds as potential skin grafts are seldom under high tensile force when immobilized at a wound site and it is not necessary for the scaffolds to act as permanent replacements for native tissue and replicate the host's environment (Jin et al., 2011 and Cui et al., 2009). In essence, these scaffolds are mechanically stable and could serve as temporary constructs for skin tissue engineering.

4.2 IN VITRO DEGRADATION STUDY OF HEC/PVA AND HEC/PVA/COLLAGEN NANOFIBERS SCAFFOLDS

4.2.1 Introduction

In this part, the study focuses on the degradation behaviour of HEC/PVA incorporated with and without collagen nanofibers in two different biological media for 12 weeks. The study of the degradation after a 12 week incubation period immersed in DMEM and its comparison to the results obtained in PBS should be adequate tools to preview its possible behaviour *in vivo*. The nanofibers were evaluated under physiological conditions of pH ~7.4 and body temperature of 37° C. These nanofiber scaffolds were experimented through a series of degradation process based on swelling ratio, weight loss, chemical bonding, mechanical properties, thermal stability and crystallinity test. These properties will be helpful to presume the biological features of composite scaffolds in the presence of cells during recovery period.

4.2.2 Morphological changes of nanofibers scaffold.

Figures 4.8 and 4.9 show the morphology changes of HEC/PVA and HEC/PVA/collagen nanofiber scaffolds after degradation in different biological media at various time points. PBS solutions have osmolarity and ion concentrations that match with those of the human body. DMEM is used in mammalian cell cultures to increase media

stability, minimize toxic ammonia build up and maximize cell performance. DMEM is a basal medium for supporting the growth of many different mammalian cells including primary fibroblasts, neurons, glial cells, HUVECs and smooth muscle cells (Life Technologies, 2014).

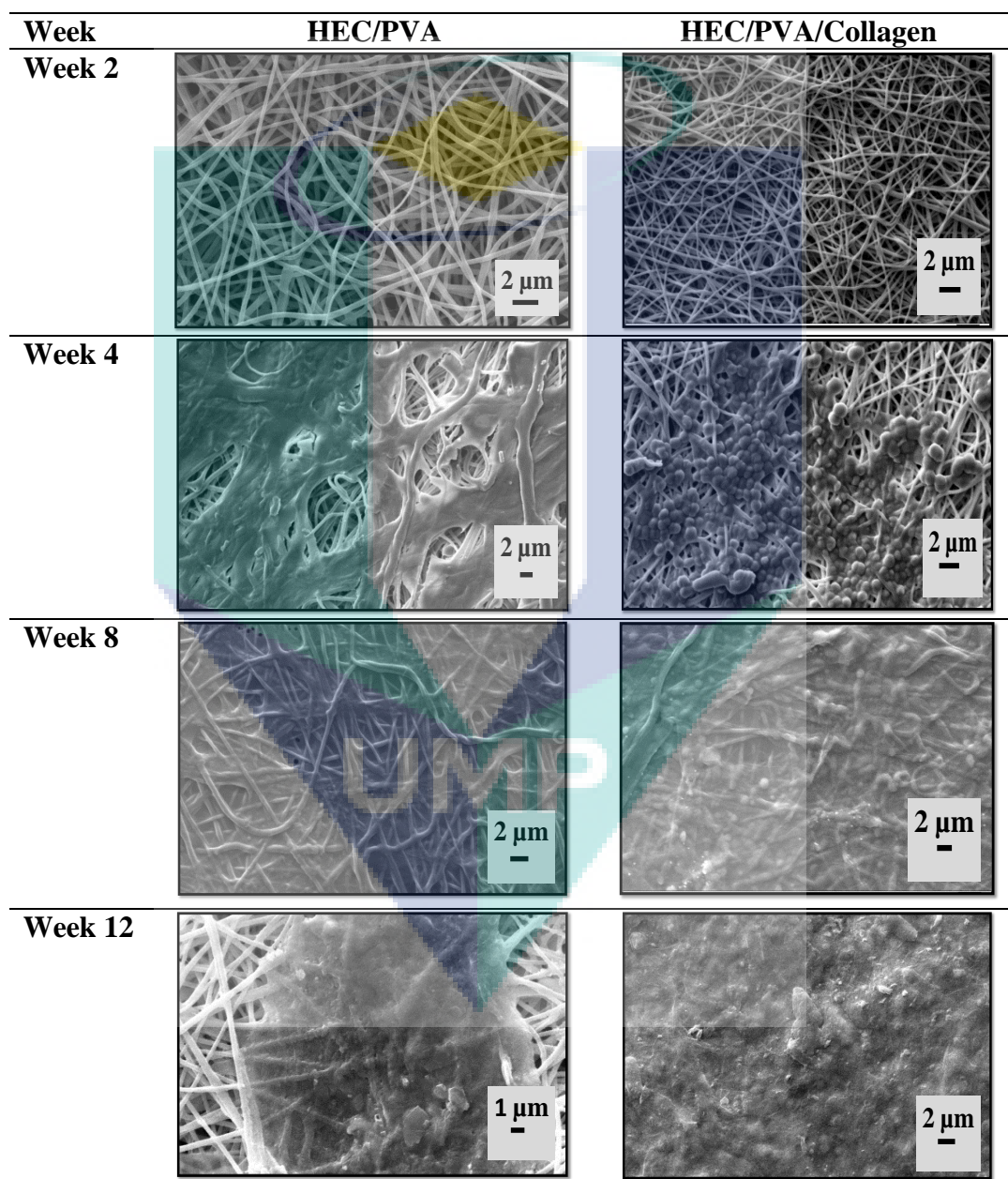


Figure 4.8: SEM micrographs of HEC/PVA and HEC/PVA/collagen nanofibrous scaffolds after degradation in DMEM media at different time

After 2 weeks of degradation, all electrospun fibers exhibited no difference with their original physical structure except for slight swelling properties. After 4 weeks of degradation, HEC/PVA and HEC/PVA/collagen blended nanofibers immersed in DMEM and PBS media presented distinct swelling and the fibers started to connect with each other while still no morphology changes were observed on the surface of HEC/PVA/collagen nanofibers incubated in the PBS solution. In addition, some fibers started to show breakage and fracture with the increase of the degradation period. After degradation for 8 weeks, almost all pores of all the fiber surfaces were covered due to the swelling effect. The internal nanofibers were further visible and ‘fused’ together after 12 weeks of degradation presented uneven and rough surfaces to the fibers. The highly porous three-dimensionally interconnected fiber structure collapsed and adhered together during degradation.

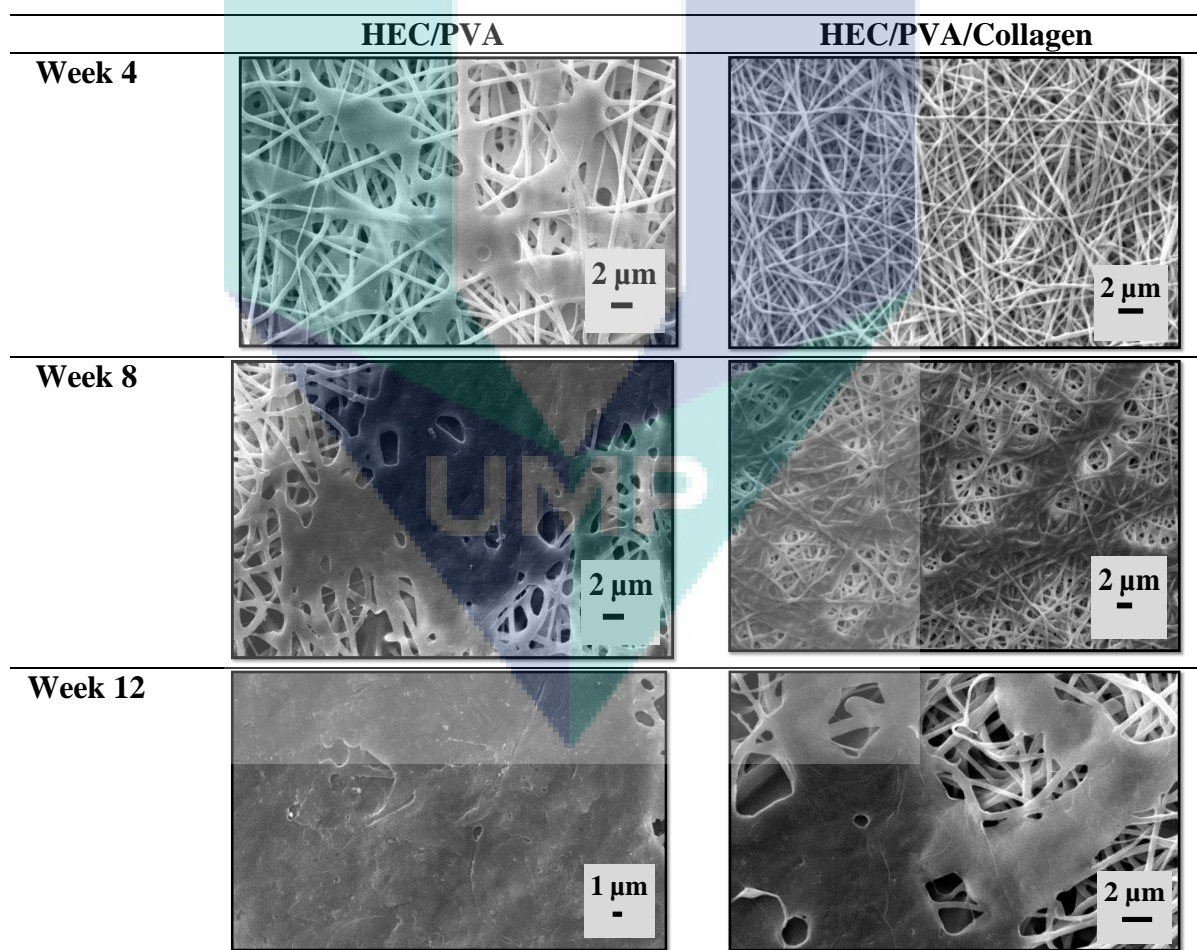


Figure 4.9: SEM micrographs of HEC/PVA and HEC/PVA/collagen nanofibrous scaffolds after *in vitro* degradation in PBS media at different time

Furthermore, it was found that the nanofiber scaffolds are likely to degrade faster in DMEM media than PBS buffer solution. This dissimilarity could be due to different chemical reactions of the scaffold with the media that affect the polymer backbone in a different manner. The nanofibrous scaffolds showed better hydrolysis rates in DMEM comprised of 110.3 mM NaCl inorganic salts, which is less than the NaCl composition in PBS of 137 mM. Although PBS contained higher salt concentration, the hydrolysis activity seems to present an increment in DMEM due to the concentration of salt that fell within the scaffolds' hydrolytic functional threshold, thus affecting the hydrolysis reaction by increasing. Apart from that, all blended nanofibers appeared to be 'melting' during the degradation process. Same results were also reported by K. Zhang et al. where the electrospun silk fibroin/P(LLA-CL) and P(LLA-CL) nanofibers emerged as melted instead of breaking during degradation study (Zhang et al., 2011). This degradation behaviour may be caused by the gradual decrease in the molecular weight of blended polymers associated with the increase in plasticization effect of the fibers (Liu et al., 2008). Moreover, the rigid and immobilized polymer chains in the crystalline region that affected the breakage of fibers along the fiber axis during 'weak' point of degradation, implied that the broken ends were more vulnerable to hydrolytic effect due to higher exposure of degradation medium during degradation (Dong et al., 2010). In skin tissue-engineering, the onset of the maturation phase may vary extensively, depending on the size and type of the wound ranging from approximately 3 days to 3 weeks or may even last for a year or longer. The unmatched degradable rate may deteriorate wound healing progress and leaves inappropriate activity at wound sites.

4.2.3 Weight loss, swelling ratio and pH value analysis

The efficiency of HEC/PVA and HEC/PVA/collagen cross-linked nanofibers were evaluated by measuring the weight change of the fibers incubated in PBS and DMEM solutions for up to 12 weeks as illustrated in Figure 4.10. The HEC/PVA/collagen nanofiber scaffolds exhibited slower degradation rates in both media as compared to HEC/PVA nanofibers. The hydrolysis of protein will mainly result in the fracture of peptide bonds. Thus, the slower rate of collagen incorporated HEC/PVA in PBS buffer

solution might be due to the difficulty of hydrolyzing the peptide bond ($-\text{NH}_2$) in neutral media and inhibited the degradation rate of HEC/PVA/collagen. Meanwhile, the slow rate of HEC/PVA/collagen fibers degraded in DMEM media was probably caused by the presence of various chemicals such as amino acids, vitamins, glucose and inorganic salts, which limited the amount of water molecules with the polymer matrices, thus decreased the breakage of backbone. The HEC/PVA/collagen nanofibers exhibited high weight loss in earlier weeks, which might be due to high surface area of fiber matrices and resulted in faster diffusion rate. In the meantime, the HEC/PVA nanofibers exhibited minor weight loss at earlier stages ($\sim 4\%$) caused by the reaction between aldehyde group and ($-\text{OH}$) during cross-linking process, which retarded the penetration of water molecules into polymer chain segments during the initial degradation process. During this reaction, the polymer chains were retained within the matrix until the chains reached a critical molecular weight and become water soluble. Subsequently, when the chains exit the matrix the weight will slowly decrease by time

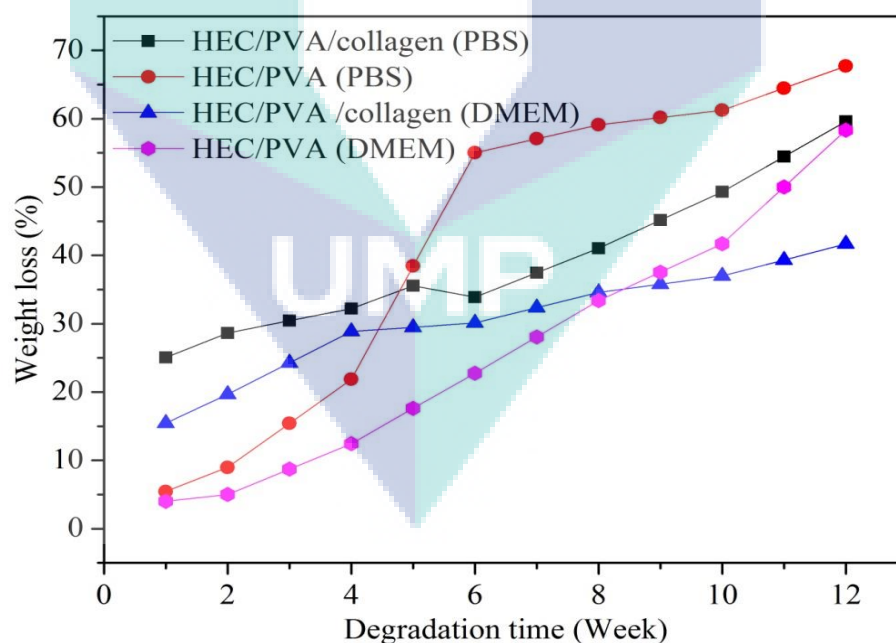


Figure 4.10: Weight loss of HEC/PVA and HEC/PVA/collagen nanofibrous scaffolds after degradation in PBS and DMEM media for up to 12 weeks

Figure 4.11 shows the result of the swelling ratio of HEC/PVA and HEC/PVA/collagen immersed in PBS and DMEM for up to 12 weeks of incubation. Swelling ratio property plays a main role due to the fact that when the scaffolds are capable of swelling, they will somehow allow their pore size to increase in diameter in order to swell thus facilitating the cells not only just to attach but also to allow them to penetrate inside the interpolymer network to grow in a three-dimensional fashion during *in vitro* culture studies (Shanmugasundaram et al., 2001). The cells will then avail the maximum internal surface area of the scaffold. The scaffolds water uptake in PBS increased from 0 to (140 – 238 %) after 2 weeks and slowly increased until maximum of 270% and 251% for HEC/PVA and HEC/PVA/collagen nanofibers respectively. The water uptake of the scaffolds exposed to DMEM media varied from 0 to 150% and 110% after 2 weeks degradation and increased up to 259% and 356% for HEC/PVA and HEC/PVA/collagen respectively towards the end of the degradation study.

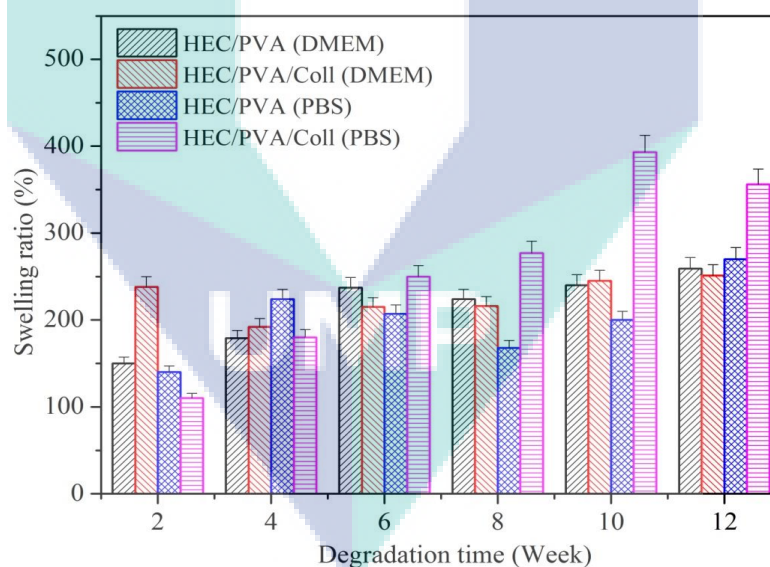


Figure 4.11: Swelling ratio of HEC/PVA and HEC/PVA/collagen nanofibrous scaffolds after degradation in PBS and DMEM media for up to 12 weeks

The swelling ratio was expected to be initially high since the first mechanism during the degradation is the absorption of water. After a certain time point, the chains of the polymer would start to shorten due to cleavage of the polymer backbone. Once the chain

became small enough to exit the matrix, the scaffold would start disintegrating thus leading to the drop in water uptake. The graph illustrated that the total water absorption of HEC/PVA/collagen immersed in PBS solution after 12 weeks was at the highest percentage of approximately 400%. This can be explained in terms of density of the polymer network as the HEC group ($-\text{[CH}_2\text{CH}_2\text{O]}_4\text{H}$) of HEC polymer is bigger than the amino group ($-\text{NH}_2$) of collagen. The addition of collagen in HEC/PVA substrate will decrease the free volume for liquid absorption. Overall, longer degradation period should be considered to indicate the saturated points in which the water absorption of the scaffolds was stabilized.

The pH changes of PBS and DMEM solution at pH 7.4 and 7.2 respectively are illustrated in Figure 4.12 (a and b) correspondingly. It depicted that fibers immersed in DMEM remained at pH ~ 7.2 along 4 weeks of degradation as compared to PBS buffer solution as the pH was decreased to 6.74 from its original pH, which was 7.4. The HEC/PVA nanofiber scaffolds incubated in both media exhibited higher pH value changes compared to HEC/PVA/collagen. The formation of interpenetrating polymer network from HEC/PVA with and without collagen is believed to involve electrostatic interaction, hydrophilic association and hydrogen bonding (Angadi et al., 2010). The cationic collagen and HEC in the presence of GA retain the stability of polymers in the dissolution media, thus limiting the release of acidic products and slows the degradation rate of the scaffolds.

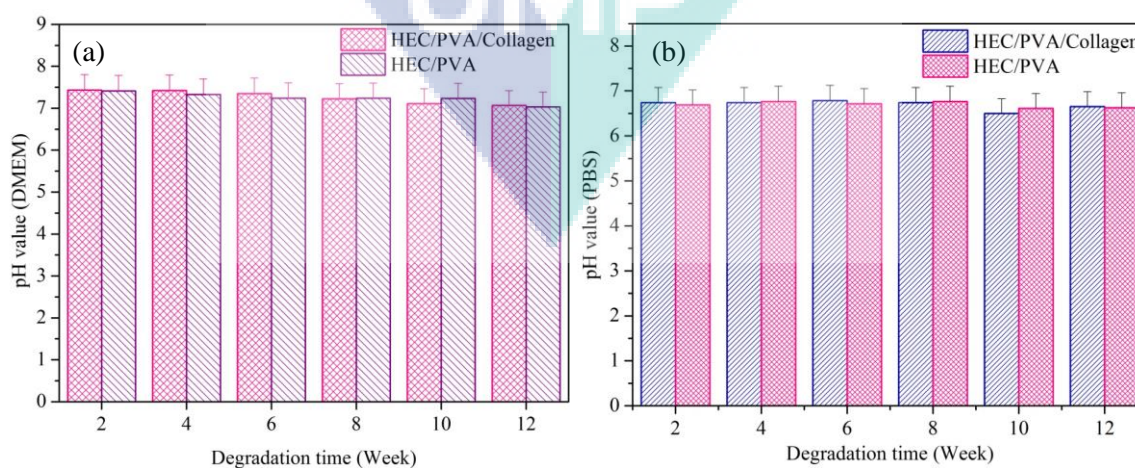


Figure 4.12: pH value of HEC/PVA and HEC/PVA/collagen nanofibers scaffold after degradation for up to 12 weeks in (a) DMEM and (b) PBS solution

4.2.4 ATR-FTIR spectra analysis

The attenuated total reflection-Fourier transform reflection (ATR-FTIR) spectra of HEC/PVA and HEC/PVA/collagen electrospun nanofibers in different degradation media before and after degradation for 12 weeks are shown in Figure 4.13 (a, b, c and d).

The broad peak at 3326 to 3398 cm^{-1} indicates stretching vibrations of the hydroxyl groups due to the intramolecular and intermolecular hydrogen bond of the OH groups of PVA and HEC. The absorption peak was found to have increased and decreased for both types of fibers after 12 weeks of degradation in PBS and DMEM media respectively. The intensity of absorption indicates a stronger hydrogen bond held within the molecular chain of HEC/PVA blend nanofibers that contributes to slower degradation rate in DMEM solution. The intensity of the bands around 2927 – 2942 cm^{-1} corresponded to CH_2 stretching vibrations were almost diminished after the 12-week degradation in PBS media. This result suggested the hydrolysis process of polymer segment chains to soluble oligomers were diffused into the degradation medium. The blend of collagen and HEC/PVA nanofiber scaffolds showed no obvious difference before and after degradation. Collagen is a homo-oligomers protein composed from identical protein chains. This protein has the characteristic absorption band at 1642 cm^{-1} to 1647 cm^{-1} (amide I, for C=O stretching), 1558 cm^{-1} (amide II, for –NH deformation) and 1246 cm^{-1} (amide III, for C-N stretching) attributed to the collagen. As shown in Figure 4.13 (c), the amide I band became weak in PBS media due to reduced stretching vibrations of peptide carbonyl groups (C=O bond) along the polypeptide backbone. The N-H peak that contributed to amide II showed no severe changes in DMEM media as exhibited in Figure 4.13 (a). On the other hand, this peak was almost diminished after degradation in PBS media due to weak intramolecular hydrogen bonding within collagen molecules. In addition, it might be likely due to the breaking of N-H \cdots O=C interchain hydrogen bonds accompanied by the release of the water bound in collagen (Pielesz, 2014). The relative strong hydrogen bond would effectively lengthen the C=O double bond and thus reducing the energy required to displace the oxygen atom from the carbon (Payne and Veis, 1988). This in turn requires a shifted to lower energy band, which translates to an absorption peak at lower frequency in the

infrared spectrum of the scaffolds. The highly reduced absorption peaks in PBS media showed that the occurrence of hydrolysis of PVA has led to hydrolytic cleavage of the polymer backbone.

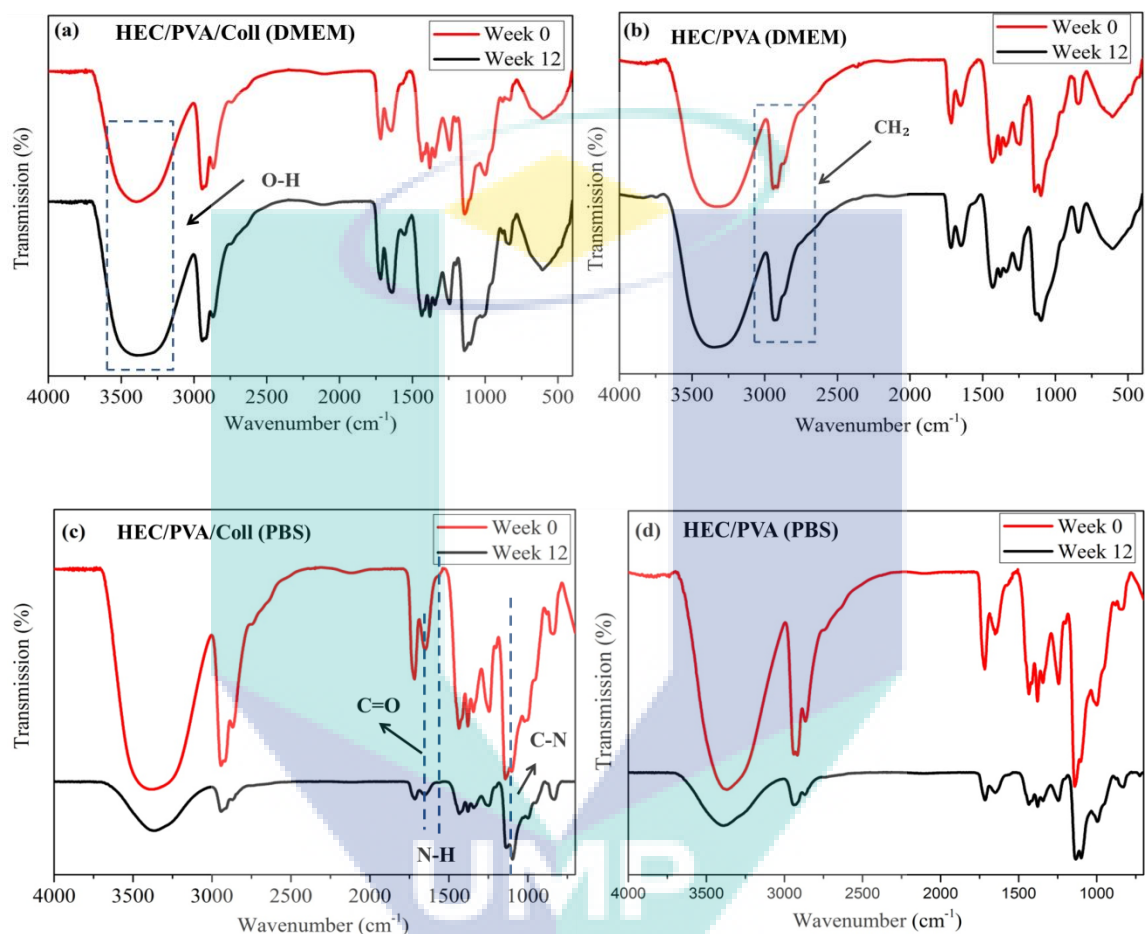


Figure 4.13: ATR-FTIR analysis before and after degradation for incubation up to 12 weeks. (a) HEC/PVA/collagen nanofibers immersed in DMEM solution; (b) HEC/PVA nanofibers immersed in DMEM solution; (c) HEC/PVA/collagen nanofibers immersed in PBS solution; (d) HEC/PVA nanofibers immersed in PBS solution

4.2.5 DSC study

The DSC measurements were conducted to further describe the degradation behaviour of electrospun HEC/PVA and HEC/PVA/collagen nanofibrous scaffolds. In Table 4.5, the crystallinity, χ_c of HEC/PVA incorporated with and without collagen of nanofibers scaffold were calculated based on the melting enthalpy, ΔH_m from DSC thermograms by using Eq. 3.1.

Table 4.5: DSC data and the characteristics observed for the electrospun HEC/PVA and HEC/PVA/collagen nanofibers before and after *in vitro* degradation

Sample	Weeks	T _g (°C)	T _m (°C)	ΔH _m (J/g)	χ _c (%)
HEC/PVA (in DMEM)	0	67.38	194.35	19.10	13.78
	4	85.73	200.88	2.62	1.89
	8	103.55	179.35	17.71	12.78
	12	113.10	178.88	7.26	5.24
HEC/PVA/collagen (in DMEM)	0	72.02	185.82	8.09	5.84
	4	99.21	201.85	9.42	6.80
	8	103.34	200.37	1.75	1.26
	12	105.67	187.28	4.98	3.59
HEC/PVA (in PBS)	0	67.38	194.35	19.10	13.78
	4	72.38	213.48	6.39	4.61
	8	106.70	202.60	11.59	8.36
	12	110.03	195.96	7.97	5.75
HEC/PVA/collagen (in PBS)	0	72.02	185.82	8.09	5.84
	4	122.15	202.01	5.34	3.85
	8	107.62	201.86	6.16	4.44
	12	101.74	194.34	4.25	3.07

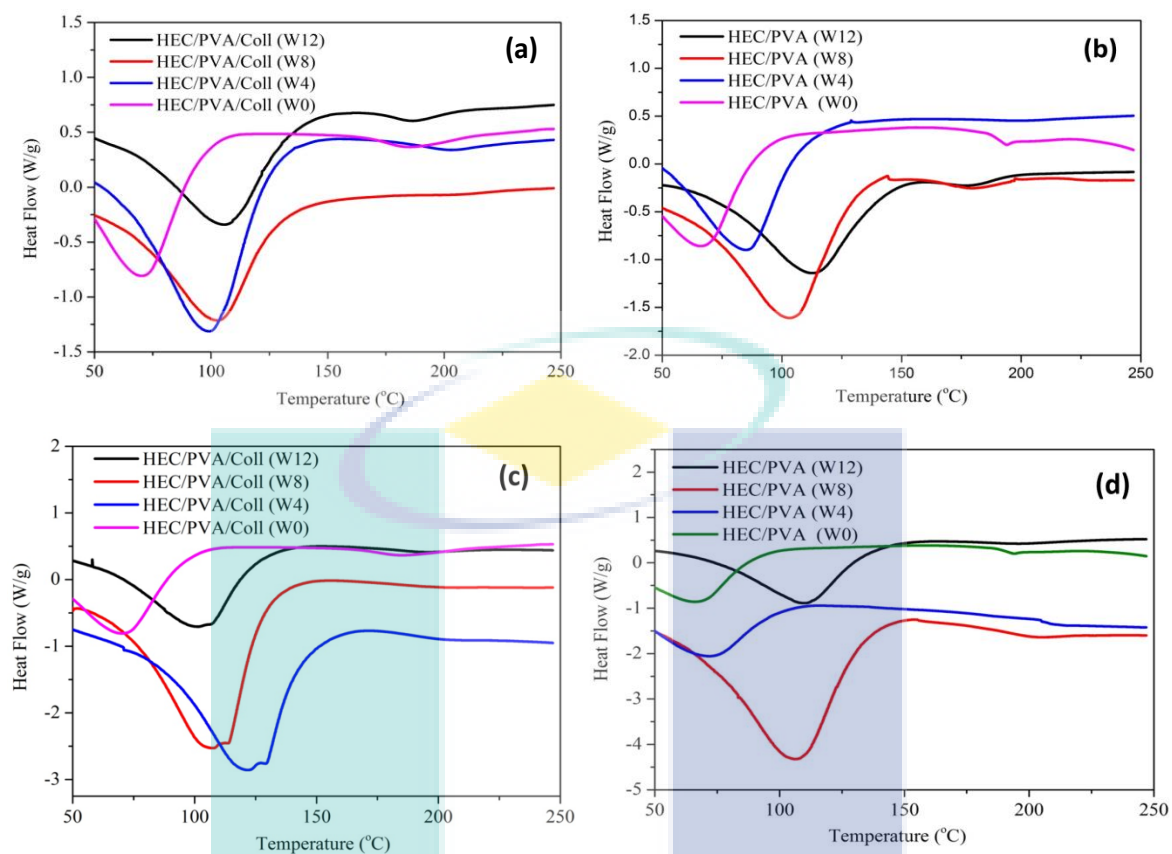


Figure 4.14: DSC thermogram before and after degradation for incubation up to 12 weeks: (a) HEC/PVA/collagen nanofibers immersed in DMEM solution; (b) HEC/PVA nanofibers immersed in DMEM solution ; (c) HEC/PVA/collagen nanofibers immersed in PBS solution; (d) HEC/PVA nanofibers immersed in PBS solution

Thermal studies *via* DSC as illustrated in Figure 4.14 (a, b, c, and d) shows a decrease in melting temperature during *in vitro* degradation. The T_g values of both samples immersed in DMEM media showed an increment after 12 weeks incubation, which indicated a slow degradation process occurred on the samples. This might be due to more crystalline nature than amorphous phase, which has been lost during early degradation process. In contrast, both electrospun nanofiber scaffolds immersed in PBS exhibited a reduction in T_g values and could be attributed to the decrease in molecular weight of the samples. The decrease in T_g values were associated with the increase in the mobility of the polymer chains as a consequence of hydrolytic process (Burgos et al., 2013).

From data summarized in Table 4.5, it can be seen that the data cannot recognize explainable 'trends'. The χ_c demonstrated relatively lower value after 4 weeks degradation time, which is 1.89, 9.42, 6.39 and 5.34 for HEC/PVA (in DMEM), HEC/PVA/collagen (in DMEM), HEC/PVA (in PBS) and HEC/PVA/collagen (in PBS) respectively. However, the degree of crystallinity γ of these nanofibrous scaffolds show augmented significance for up to 8 weeks degradation in the range of 6.16 to 17.71 % and seem to be reduced after 12 weeks of hydrolyzing process, which is from 3.07 to 5.75 % except for HEC/PVA/collagen (in DMEM) that demonstrated a decrease in crystallinity through prolongation time of degradation. This degradation pattern could be elucidated by the fact that initial stage of degradation happened in the amorphous region where the molecular chains are less dense and characteristically disordered in nature (Shum and Mak, 2003). This amorphous nature may enhance the degradation due to the irregularity in the side chain arrangement contributed to the diffusion of water molecules into the polymer network (Salaam et al., 2006). The cleavage of the side chains as well as chain-stripping of PVA will then promote higher molecular chain mobility (Beyler and Hirschler, 2001). The arrangement of polymer chains will facilitate the crystallization process resulting from selective hydrolysis and removal of the chains in case of the amorphous state occurs first through degradation (Fischer et al., 1973). Due to the faster erosion of amorphous regions compared to crystalline polymer regions, the overall crystallinity of the samples increases. After 12 weeks of degradation, the smaller value of crystallinity explained the fact that the perfection of the crystallinities in HEC/PVA and HEC/PVA/collagen fibrous scaffolds could deteriorate with degradation. In addition, it can be seen that the T_m of all fibers decreased after 12 weeks of degradation which further proved that the damage of crystalline structure was achieved during the degradation process.

4.2.6 Mechanical characterization

The stress-strain curves of HEC/PVA and HEC/PVA/collagen nanofibrous scaffolds before and after degradation are shown in Figure 4.15 and the data are summarized in Table 4.6. The Young's modulus of the fibrous exhibited significant decrease after degradation time from 97.8 – 106.1 MPa at week 0 to 11.04 – 36.35 MPa at

week 12. After 12 weeks of incubation, significant drop of tensile stress from 2.95 MPa to the lowest value of 0.60 MPa clearly displayed that the degraded scaffolds lost their structural properties over prolongation incubation time (Shum and Mak, 2003). In addition, this decrement might be caused by the reduction of molecular weight with degradation time resulting in the rapid reduction of modulus and tensile stress (Yang et al., 2008b). The tensile stress (MPa) was found to be less than Young's modulus, which showed that the degraded scaffolds could still bear pressure instead of bear loads indicating that the scaffolds can still remain cell-scaffold interactions during the recovery period. In contrast, the tensile strain of fibrous scaffolds demonstrated the increase in value from 12.43 – 20.35 % at week 0 to 28.58 – 58.45 % at week 12. The decrease in Young's modulus (MPa) and increase in tensile strain (%) revealed that the plasticizing effect was obtained after the degradation period. This effect keeps the polymer chains further apart, which reduces the forces of attraction between them and makes the material more flexible. The scaffolds will probably have reduced strength and stiffness but the material will be more useful where flexibility is required; suitable for tissue engineering applications.

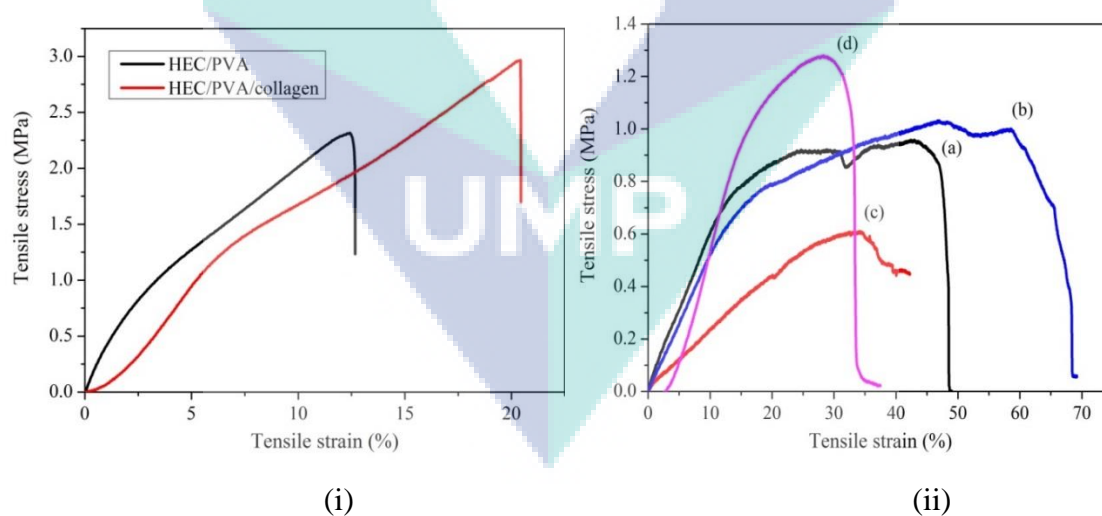


Figure 4.15: Stress-strain curves (i) before and (ii) after degradation for incubation up to 12 weeks. (a) HEC/PVA/collagen nanofibers immersed in DMEM solution; (b) HEC/PVA nanofibers immersed in DMEM solution; (c) HEC/PVA/collagen nanofibers immersed PBS solution; (d) HEC/PVA nanofibers immersed PBS solution

Table 4.6: Mechanical data of HEC/PVA and HEC/PVA/collagen nanofibers before and after degradation for up to 12 weeks.

Time	Sample	Young's modulus (MPa)	Ultimate tensile stress (MPa)	Ultimate tensile strain (%)
Before degradation	HEC/PVA	97.8	2.31	12.43
	HEC/PVA/collagen	106.1	2.95	20.35
After degradation for up to 12 weeks	HEC/PVA/collagen (DMEM)	28.7	0.95	43.24
	HEC/PVA (DMEM)	24.76	0.99	58.45
	HEC/PVA/collagen (PBS)	11.04	0.60	34.19
	HEC/PVA (PBS)	36.35	1.27	28.58

4.3 MICROSTRUCTURE STUDY OF HEC/PVA POROUS SCAFFOLDS

4.3.1 Introduction

In this part, five different samples consisting of HEC, HEC/PVA (2:1, 1:1 and 1:2) and PVA aqueous polymeric solutions were fabricated through freeze-drying technique. This study focuses on the performances of these cross-linked scaffolds based on its morphology, porosity, swelling ratio, *in vitro* degradation loss, chemical bonding, mechanical properties and thermal stability that could present the most significant environment for cell-scaffold interactions.

4.3.2 Microstructure of scaffolds

The microstructures of pure HEC, blended HEC/PVA and pure PVA are illustrated as in Figure 4.16. The microstructures of scaffolds such as pore size, porosity as well as pore shape have great influences in terms of cell intrusion, proliferation and function in tissue engineering (Ma, 2003). The SEM images confirmed the distribution of pore structures of cross-linked three-dimensional scaffolds. High interconnectivities between pores were vastly desirable for uniform cell seeding distributions as well as diffusion of

nutrients to and from the cell/scaffold substrates (Liu et al., 2009). By varying the ratios of HEC/PVA, a controllable pore size with particular wall structure could be obtained.

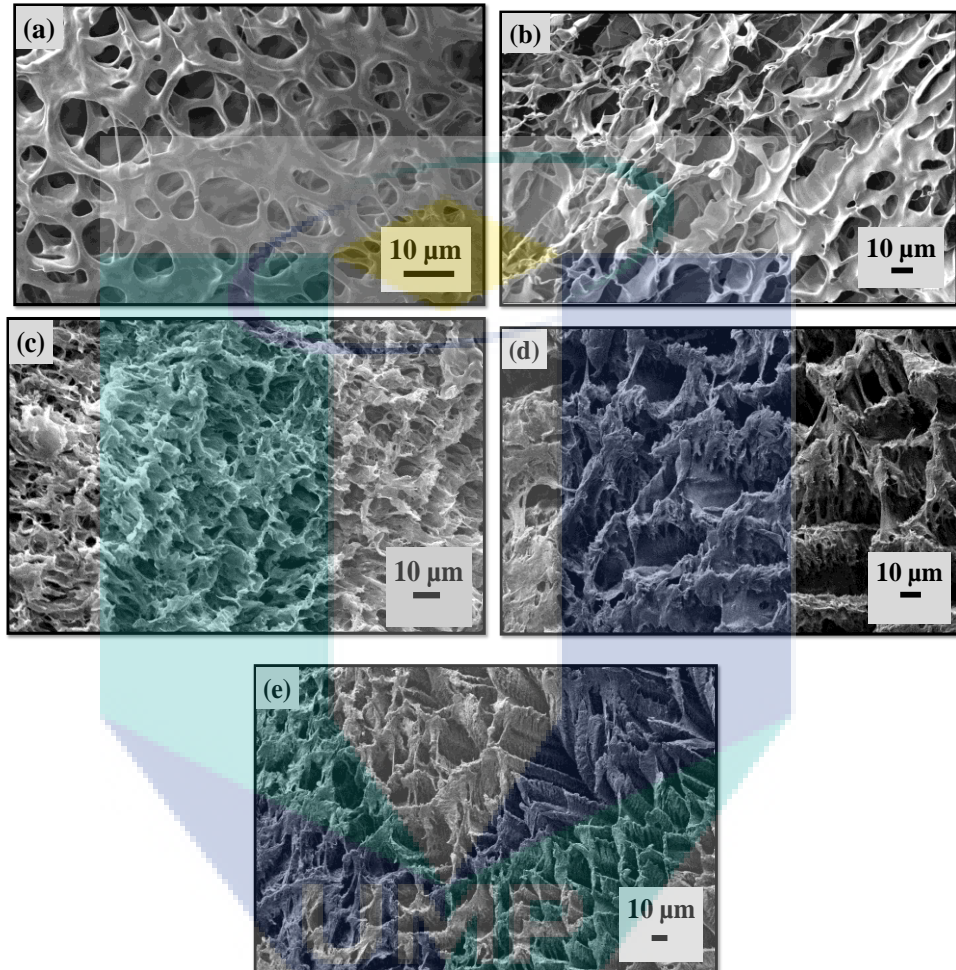


Figure 4.16: SEM micrographs of interconnected porous scaffolds (a) pure HEC, (b) HEC/PVA (2:1), (c) HEC/PVA (1:1), (d) HEC/PVA (1:2) and (e) pure PVA

The HEC scaffolds displayed large porous structure with pore sizes ranging from 2 μm to 20 μm while pure PVA showed a ladder-oval shape in aligned and open microstructure with interspacing pore sizes ranging from 14 μm to 70 μm. On the other hand, blended HEC/PVA scaffolds showed higher pore sizes in the range of 2 μm to 40 μm as compared to pure HEC but relatively lower compared to PVA scaffolds. The pore size was found decreased with slightly increased HEC content. This is attributed to the

additional amount of HEC, which initiates a rise of higher polymer volume in the solution and consequently smaller pore dimensions (Frydrych and Chen, 2013). Morphology of HEC/PVA (2:1) and (1:2) scaffolds revealed a porous structure with a three-dimensionally interconnection throughout the scaffolds in all compositions. The shrink-like structure appeared in blended scaffolds and might be caused by the effect of high GA treatment, which disturbed the round pores formation. The HEC/PVA blend scaffold with equal composition values (1:1) exposed rough surfaces with no well-defined pores. Some micropores less than 10 μm were also observed at higher magnification. These micropores could have been the result from the rapid sublimation by reduced surrounding pressure during freeze-drying. The existence of micropores is favourable since it might increase the interconnectivity and interface area of the porous scaffolds. Overall, these results indicate the scaffolds could be effective scaffolds for skin tissue engineering as keratinocytes are found to grow well in scaffolds with pore sizes as low as 20 μm to 50 μm (Wang et al., 2006).

4.3.3 Porosity of scaffolds

Scaffold porosity is one of the important features to evaluate the biomaterial properties for tissue engineering. It is well-known that both HEC and PVA are water-soluble biopolymers, which are not favourable for cell culture studies. Therefore, cross-linking these materials is a must to decrease their solubility as well as to give mechanical strength for cell culture studies. In this report, porosity measurements of cross-linking scaffolds were completed by using liquid displacement method with deionized water as the displacement liquid.

As illustrated in Figure 4.17, all porous scaffolds show high porosity with percentage value above 85% at a maximum of 99.4 % for pure HEC freeze-dried scaffolds. The results pointed that scaffold porosity decreases with the continuous addition of PVA content, which coincides that scaffold porosity becomes less with the increase of polymer pore size. Meanwhile, the HEC/PVA (2:1) exhibited significantly higher porosity (98.3 %) than other HEC/PVA blends, i.e. (1:1) and (1:2), which is 97% and 90.4 % respectively.

This might be caused by a decrease of PVA content that contributes to the decrease of the total volume occupied from the blend polymer system itself (Bhardwaj and Kundu, 2011). Overall, these results suggested that high porosity of these scaffolds could be suitable for cell cultivation and transplantation in skin tissue bioengineering.

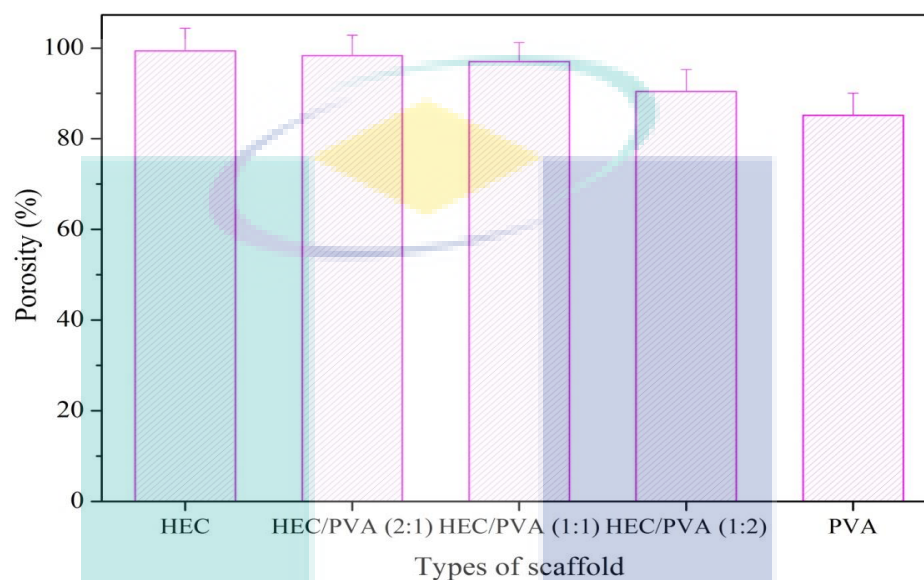


Figure 4.17: Porosity of different porous scaffolds

4.3.4 Swelling ratio studies

The amount of water in hydrogel enables the determination of absorption or/and diffusion of solutes through the hydrogel. The equilibrium swelling ratios of the prepared pure HEC, blended HEC/PVA and pure PVA scaffolds are illustrated in Figure 4.18, as a function of polymer composition. After the day 1 experiment, all scaffolds showed high degree of swelling ratio, reflecting the hydrophilic properties of the scaffolds; i.e., highly porous network enables the absorption of an amount of bulky water. The values of swelling ratio of all scaffolds increased parallel throughout the 7 days of experiment. It is worth to note that after 7 days, at some time point, the swelling capability of the scaffolds will achieve maximum swelling capacity and will ultimately start to degrade due to the breaking of polymer chains (Erol et al., 2012). This behaviour will be further discussed in the following.

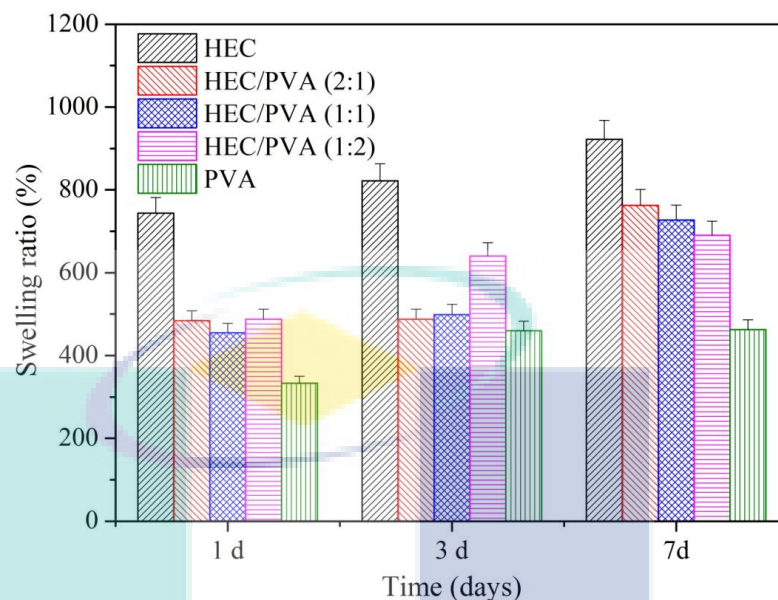


Figure 4.18: Swelling ratio of pure HEC, HEC/PVA (2:1), HEC/PVA (1:1), HEC/PVA (1:2) and pure PVA porous scaffolds

4.3.5 *In vitro* degradation studies

In tissue engineering, porous biodegradable scaffolds are said to facilitate and provide sufficient spaces for cell growths and tissue formation. The degradation of scaffolds in PBS at 37 °C over 7-day incubation was evaluated as shown in Figure 4.19. All scaffolds exhibited increment in percentage of degradation with time. Pure HEC showed higher degradation rates compared with blended HEC/PVA and pure PVA scaffolds, with maximum value at 52 %. HEC scaffolds exhibited high weight loss at primary weeks which might be due to high surface area of porous scaffolds resulting in faster diffusion rates to the medium. On the other hand, PVA showed minor weight loss after 24 h (~7 %) and tend to degrade faster after 3-day incubation. This slow degradation might be caused by the reaction between aldehyde group and (-OH) during cross-linking process, which formed acetal bridges between PVA hydroxyl groups and the aldehyde molecule, thus reducing the penetration of water molecules into the polymer chain segments of the scaffolds during the initial degradation process. During this reaction, the polymer chains were retained within the matrix until the chains reach a critical molecular weight and become water soluble. For

all blended scaffolds, the higher the PVA composition, the lower the percentage of weight loss. After 7 days of degradation, the scaffolds with the ratio of HEC to PVA (2:1), (1:1) and (1:2) had a percentage weight loss at 43 %, 40.3 % and 34.4 % respectively. As scaffolds degrade over time, the ruptures of chain scissions will consequently facilitate the diffusion of more aqueous solution inside the scaffolds. Thus, the increase of swelling ratio of the hydrogel indicates that their degradation properties could be adjusted by varying the blended scaffold compositions; proving the capability of the scaffolds in retaining their physical integrity.

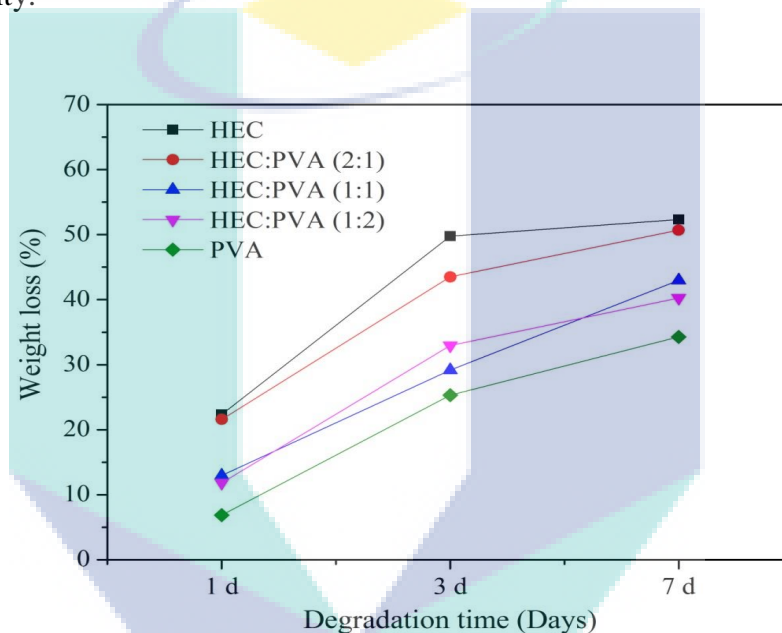


Figure 4.19: Percentage of weight loss of pure HEC, HEC/PVA (2:1), HEC/PVA (1:1), HEC/PVA (1:2) and pure PVA porous scaffolds

4.3.6 ATR-FTIR spectroscopy analysis

The attenuated total reflection-Fourier transform reflection (ATR-FTIR) spectra of HEC, PVA and HEC/PVA blend cross-linked porous scaffolds is illustrated in Figure 4.20. FTIR spectra analysis was carried out to determine the possible interactions between hydroxyl groups of HEC and in the blended composite scaffolds.

Pure HEC showed a broad peak at 3376 cm^{-1} assigned to O-H stretching vibrations and 2929 cm^{-1} assigned to C-H aliphatic stretching vibrations. The absorption spectra of

HEC presented specific bands in 1463, 1354, 1310 and 932 cm^{-1} (Zhbankov, 1966), which corresponded to a characteristic of amorphous region and possible heterogeneity on the distribution of the replaced groups in the polymer chains (Kumar et al., 2012). For pure PVA, a large band appeared at 3303 cm^{-1} , representing the O-H stretching from the intermolecular and intramolecular hydrogen bonds while the vibrational bond at 2944 cm^{-1} contributed to the stretching of C-H from alkyl groups of PVA. Strong peaks emerged at 1709 cm^{-1} and 1655 cm^{-1} referring to the stretching of C-O from acetate groups remaining in PVA, while peaks for 1429 cm^{-1} were related to the bending vibrations of CH_2 .

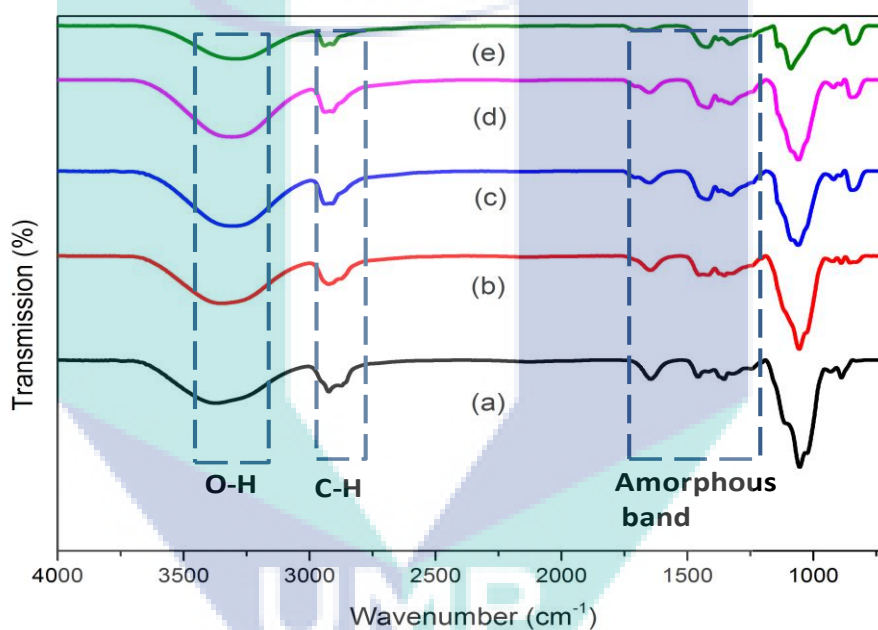


Figure 4.20: ATR-FTIR analysis for (a) pure HEC, (b) HEC/PVA (2:1), (c) HEC/PVA (1:1), (d) HEC/PVA (1:2) and (e) pure PVA porous scaffolds

Meanwhile, the FTIR spectra for HEC/PVA blended scaffolds showed the combination of major peaks of HEC and PVA. It was found that the ratio of absorption intensities of C-H and O-H stretching increased with the addition of HEC content. The broad pattern of blend scaffolds observed at O-H region (3313 – 3337 cm^{-1}) and peak of C-H varied from 2870 to 2939 cm^{-1} , which might be due to the rise in swelling ratio of the samples. The strong peaks observed from 829 to 937 cm^{-1} exhibited the C-H and CH_2

bending vibrations while peaks varied from 1055 to 1059 cm^{-1} were assigned to C-O stretching, showing peaks with slight shift to the left with the increase of HEC polymers. These results suggest that the H₂ bonding becomes increased due to increased number of OH groups.

4.3.7 Thermogravimetric (TGA) studies

Thermal degradation behaviours of pure HEC, pure PVA and blended HEC/PVA were examined *via* thermogravimetric analysis (TGA) as shown in Figure 4.21. There were two major steps observed for pure HEC (Figure 4.21(a)) and HEC/PVA (2:1) (Figure 4.21(b)) and three major steps for pure PVA and other blends of HEC/PVA scaffolds (Figure 4.21(c-d)). These steps were distinguishable in the diagram of mass loss (TGA %) during heating and more clearly in the diagram of derivative mass loss (drTGA %). Table 4.7 shows the decomposition step and percentage mass loss for the scaffolds. HEC and PVA homopolymers showed 4.73 % and 3.5 % weight loss respectively in the first stage beginning from 23.6 °C to 198.6 °C. More significant loss around 72.43 % and 75.38 % were observed in the second stage starting from 158.4 to 449.7 °C for HEC and PVA correspondingly. PVA showed third weight loss by about 16.9 % in the temperature range of 417.9 °C to 532 °C.

Table 4.7: TGA and DrTGA data for HEC and PVA scaffolds

Sample	Region of decomposition	Temperature			Weight loss	
		T _{start}	T _{end}	T _{peak}	Partial	Total
HEC	1	23.6	158.4	66.6	4.73	77.16
	2	158.4	449.7	346.5	72.43	
HEC/PVA (2:1)	1	22.2	186.9	119.7	3.84	85.9
	2	186.9	525.5	350.6	82.06	
HEC/PVA (1:1)	1	23.6	155.6	63.8	4.5	88.9
	2	155.6	407.9	354.8	78.5	
	3	407.9	512.5	439.5	5.9	
HEC/PVA (1:2)	1	22.19	162.72	62.4	5.9	91.73
	2	162.7	407.9	353.4	75.09	
	3	407.9	522.7	433.5	10.74	
PVA	1	23.6	198.6	56.5	3.5	95.78
	2	198.6	417.9	371.9	75.38	
	3	417.9	532	436.6	16.9	

The TGA curves for HEC/PVA blends showed three degradation regions, which suggested the existence of more than one degradation process (Guirguis and Moselhey, 2012). This is however excluding the HEC/PVA (2:1) sample, which displayed two significant weight losses during heating process that might be attributed to the high content of HEC in its blend solution. Overall, all HEC/PVA samples showed lower values of percentage weight loss varying from (3.84 – 5.9 %) in the first stage beginning from 22.19 °C to 186.99 °C, affirming the presence of thermal process due to moisture evaporation or weakly physisorption of water. This is also might be due to splitting or volatilization of small molecules from the samples (Tripathy et al., 2009). There were more significant weight loss (75.09 – 82.06 %) in the range of 155.58 °C to 525.5 °C, which includes the melting point such as physical transition and the degradation temperature of polymers. Therefore, the higher value of weight loss at second decomposition stage verified the existence of a chemical degradation process resulting from bond scission (carbon-carbon bonds) in the polymeric bone, which in this case refers to the degradation of the side chain of PVA and loss of CO₂ in the case of HEC (Guirguis and Moselhey, 2012) . The second weight loss is the most important both in the rate of weight loss and in total loss. The difference in thermal decomposition behaviour of different HEC/PVA blend samples can be seen more clearly from derivative thermogravimetric (DrTGA) curves. All blended scaffolds demonstrated intermediate degradation behaviour between that of pure HEC (T_p = 346.5 °C) and PVA (T_p = 377.9 °C) as the peak temperature of blend scaffolds varied from 350.6 °C – 354.8 °C. The DrTGA curve also implied that HEC/PVA (1:2) exhibited slower degradation rates than those of the other two blended scaffolds. This indicated that the thermal stability of HEC was increased by mixing it with PVA. The third weight loss at 407.9 °C – 522.7 °C was due to the by-products generated by PVA during thermal degradation process attributed to the decomposition of the main chain of PVA (Holland and Hay, 2001).

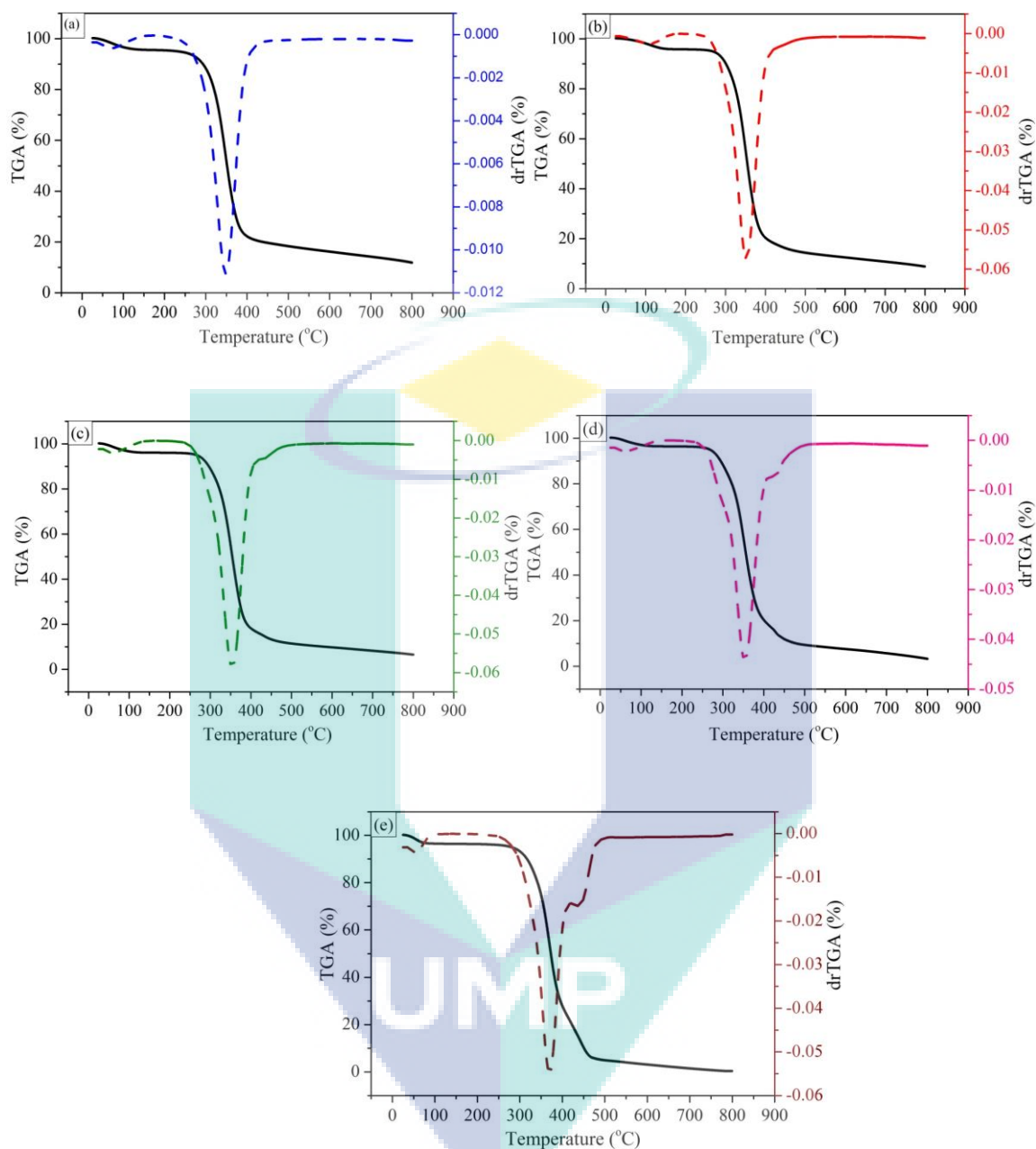


Figure 4.21: TGA and DrTGA analysis for (a) pure HEC, (b) HEC/PVA (2:1), (c) HEC/PVA (1:1), (d) HEC/PVA (1:2) and (e) pure PVA porous scaffolds

4.3.8 Differential scanning calorimetry (DSC) study

DSC measurement technique could provide thermal behaviour of the first and second thermal transitions such as melting (T_m) and glass transition (T_g) phenomena. The results from DSC thermograms and the temperature of the phase transitions as well as

change of enthalpies, ΔH_m are shown in Figure 4.22 and summarized in Table 4.8. Figure 4.22 depicts the heating run of HEC (a), PVA (e) and HEC/PVA (b, c, d) blend solutions up to 250 °C. DSC thermogram of pure HEC scaffolds showed a relatively broad endothermic glass transition temperature at ~92.48 °C associated with an enthalpy 181.7 J/g. Meanwhile, the pure PVA (e) represented two endothermic peaks at 104.72 °C and 222.26 °C corresponding to the glass transition and melting temperature respectively. The relatively wide and broadened glass transitions corresponded to semi-crystalline nature of the materials. As the heat required to melt 100 % crystalline PVA was 138.6 J/g, the sharp endothermic melting transitions of PVA with an enthalpy 52.94 J/g showed a nominal value of crystallinity at about 38.20 %.

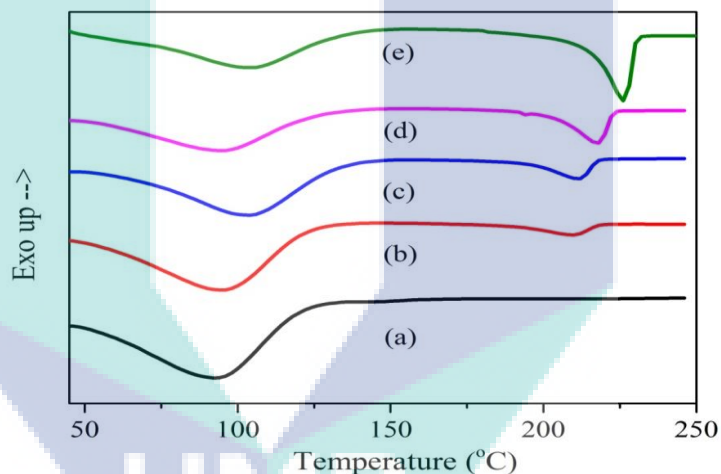


Figure 4.22: DSC analysis for (a) HEC only, (b) HEC/PVA (2:1), (c) HEC/PVA (1:1), (d) HEC/PVA (1:2) and (e) PVA scaffolds

For all blended scaffolds, it was observed that the DSC thermograms of HEC/PVA (b, c and d) showed one single broad glass transition in the range of 95.27 °C – 102.95 °C, which intensifies with the increasing of PVA content up to 50 wt%. Meanwhile, a decrease in T_g value was identified for HEC/PVA (1:2) blend samples. Overall, these observations might indicate the compatibility between HEC and PVA because of the presence of large hydroxyl groups of PVA with highly interconnected hydrogen bonding, leading to high glass transition temperature (El-Sayed et al., 2011). The broad glass transition peak of

HEC/PVA blended samples might also be due to overlapping T_g transitions of the two polymer blend samples. Furthermore, the T_g values were found to be in the range of pure HEC and PVA, ($T_{g(\text{HEC})} < T_{g(\text{HEC/PVA})} < T_{g(\text{PVA})}$), indicating the miscibility of both polymers, affected from well dispersed blend polymers and less free volume. It was also noted that the melting transition temperature showed augmentation from 210.22 °C to 218.19 °C with the increase of PVA content. The tendency of a proportional increment in enthalpy with an increase of PVA content implies the improved degree of crystallinity of PVA in the blends with decreasing HEC content.

Table 4.8: DSC data and the characteristics observed for the HEC, PVA and HEC/PVA blend samples

Sample	T_g (°C)	T_m (°C)	ΔH_m (J/g)	χ_c (%)
HEC	92.48	-	-	-
HEC/PVA (2:1)	95.27	210.22	9.37	6.76
HEC:PVA (1:1)	102.95	212.14	18.64	13.45
HEC:PVA (2:1)	96.32	218.19	28.81	20.79
PVA	104.72	222.26	52.94	38.20

4.3.9 Mechanical properties

One of the most important characteristics of a scaffold to be used in tissue engineering is that it needs to have particular strength to maintain integrity while maintaining their shape for cell ingrowths and matrix production until later neo-tissue formation. Figure 4.23 illustrates the typical non-linear stress-strain curves of freeze-dried scaffolds and their characteristic data are summarized in Table 4.9. The HEC demonstrated highest Young's modulus and tensile stress of 28.56 MPa and 0.99 MPa, respectively, while PVA scaffolds exhibited the parameters in the order of 2.99 MPa and 0.33 MPa respectively. On the other hand, HEC/PVA blend samples showed elastic modulus in range of 14.67 – 22.46 MPa with tensile stress varying from 0.43 to 0.64 MPa. Higher Young's modulus was obtained with the increase in HEC value and might be due to high molecular weight of HEC, which contributed to the enhancement of intrinsic properties of polymer. The addition of PVA into HEC reduced the strength and increased the strain of the blending

scaffolds up to 13.65 %. Higher strength obtained from blending scaffolds compared with pure PVA is due to formation of compact structures, which probably leads to the increase in modulus and strength of blended scaffolds. Overall, low tensile strength for all samples is probably due to the reduced dimensional stability of non-cross-linked scaffolds, resulting in low degree of orientation (Liu et al., 2012).

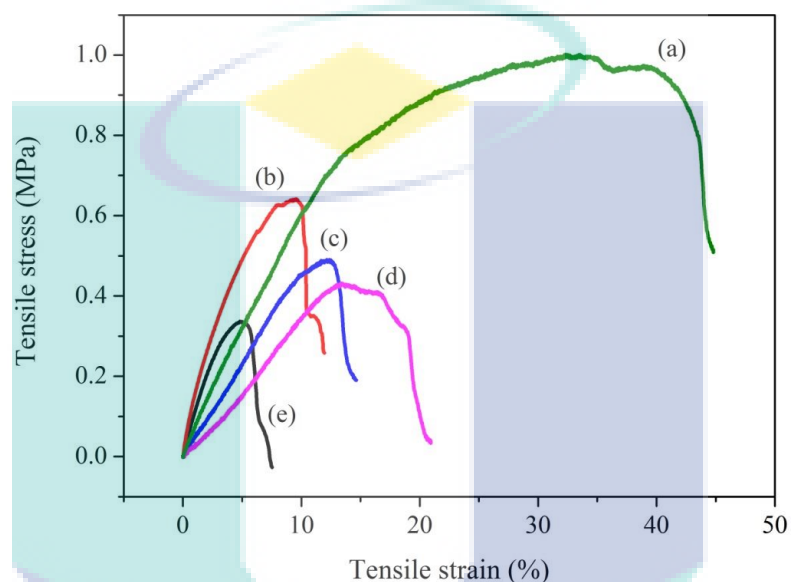


Figure 4.23: Stress-strain curves for (a) HEC only, (b) HEC/PVA (2:1), (c) HEC/PVA (1:1), (d) HEC/PVA (1:2) and (e) PVA scaffolds

Table 4.9: Mechanical data observed for the HEC, PVA and HEC/PVA blend samples.

Sample	Young's modulus (MPa)	Ultimate tensile stress (MPa)	Ultimate tensile strain (%)
HEC	28.56	0.99	34.83
HEC/PVA (2:1)	22.46	0.64	9.63
HEC/PVA (1:1)	17.77	0.49	12.4
HEC/PVA (1:2)	14.67	0.43	13.65
PVA	2.99	0.33	4.96

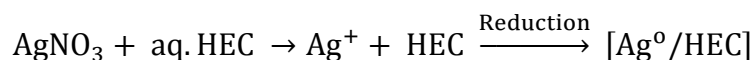
4.4 STUDY OF HEC/SILVER NANOPARTICLES POROUS SCAFFOLDS

4.4.1 Introduction

The aim of this work is to investigate the characteristic behaviour of HEC/silver nanoparticles as potential scaffolds for skin tissue engineering applications. The composite substrates which contained varied concentrations of AgNO₃ (0.4, 0.8 and 1.6%) were formed in the presence of a biocompatible polymer, HEC in a single step in water. Those solutions were fabricated *via* freeze-drying technique. All HEC/AgNPs scaffolds were studied based on their porosity, swelling ratio, *in vitro* degradation loss and characterized by using SEM, UV-Vis, ATR-FTIR, TGA and DSC.

4.4.2 Microstructure of HEC/AgNPs scaffolds

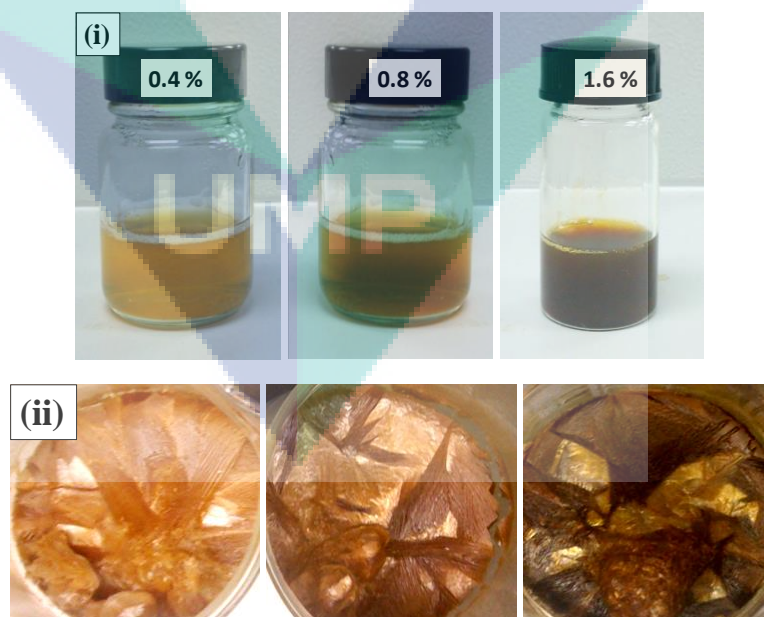
The morphology of three-dimensional scaffold structure should possess high porosity and adequate pore size distribution to allow vascularisation and colonization by the cells (Marsich et al., 2013). HEC was dissolved in deionized water to achieve concentration of 10 wt% and different amounts of 0.05M AgNO₃ (0.4%, 0.8% and 1.6%) were added to the HEC solution. The silver nanoparticles were formed upon heating the aqueous solution of HEC and AgNO₃ in an oil bath with gentle stirring at 75°C for 2 h. As illustrated in Figure 4.24 (i), the presence of silver nanoparticles was confirmed by the colour changes of the reaction mixture from colourless to pale yellow within 5 minutes from the start of the reaction. As the time increased, colour was changed from bright yellow (as displayed for 0.4% AgNP) to light brown for 0.8% AgNP and to dark brown for 1.6% AgNP at the end of 2 h. In this process, it was expected that the hydroxyl group on the HEC backbones reduces the Ag⁺ ions to Ag nanoparticles. The reduction of silver ions by HEC is schematically illustrated in Scheme 4.1.



Scheme 4.1: Reduction of silver ion by HEC

Same results of color changes were obtained for freeze-dried scaffolds in sponge-based like properties as shown in Figure 4.24 (ii). As the concentration of AgNO_3 increased, the scaffolds became darker.

The SEM images displaying the morphology of the scaffolds after the lyophilization process are shown in Figure 4.24 (a - c). Previous studies reported that collagen-GAGs scaffold for skin tissue regeneration required the vascularization *via* an interconnected pore size in the range of 20 to 120 μm (Yannas et al., 1989) while fibroblasts preferably bind to larger pores ($>90 \mu\text{m}$) (O'Brien et al., 2005). In this work, the HEC/AgNPs scaffolds possess interconnected open-pore microstructure with average pore size ranging from 50 to 150 μm , thus, suitable for tissue engineering applications. The shrink-like structure as well as layered surfaces that appeared in HEC/AgNPs scaffolds might be caused by the effect of high GA treatment, which retarded the formation of round pores during the lyophilization process. Uneven pore size and distribution might be due to the fast formation of ice crystals during freezing that leaves holes in the structure when the sample is dried.



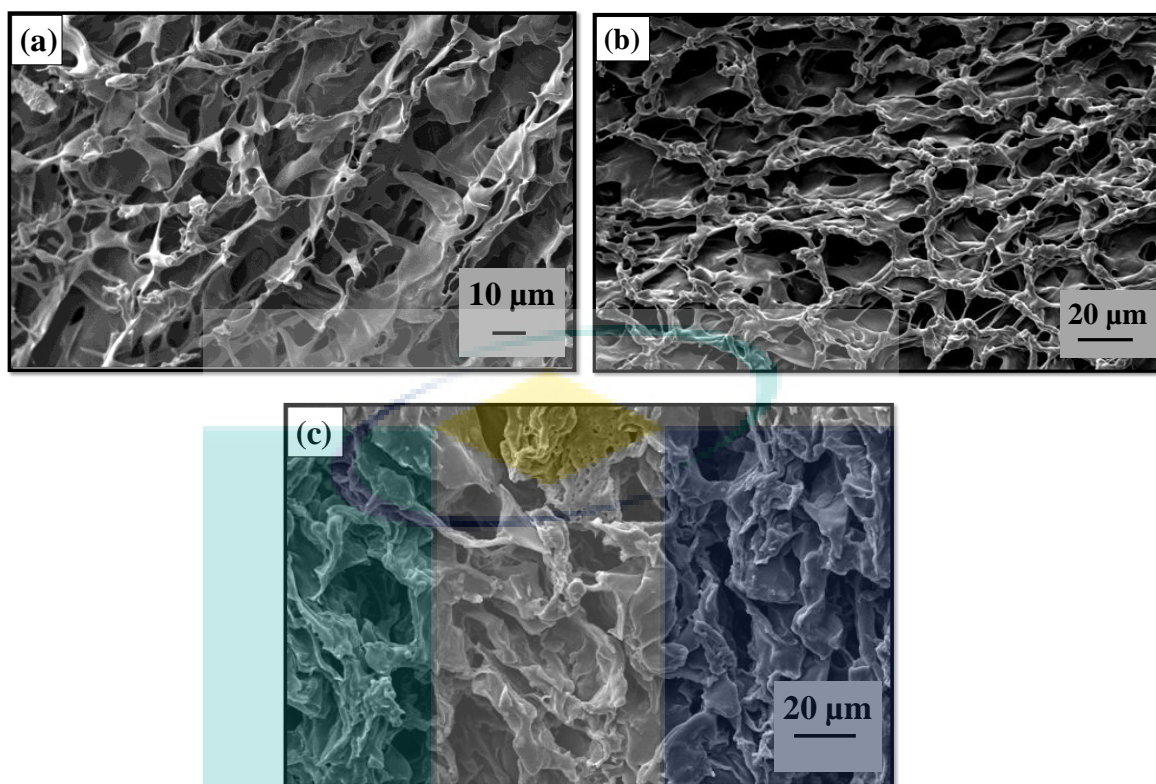


Figure 4.24: (i) Photograph of HEC/AgNPs solution obtained at different concentrations of AgNO_3 , (ii) macroscopic appearance of HEC/AgNPs scaffold, SEM micrograph of HEC/AgNPs scaffold at different concentrations of Ag (a) 0.4%, (b) 0.8%, (c) 1.6 %.

4.4.3 Porosity studies

Porosity of the scaffolds is a very important feature to evaluate biomaterial properties for tissue engineering especially to encourage fluid absorption and healing process. It is well-known that HEC is water soluble and not favourable for cell culture studies. Therefore, cross-linking the HEC/AgNPs was desired to decrease their solubility as well as giving adequate mechanical strength for cell culture studies. In this report, porosity measurements of cross-linking scaffolds were completed by using liquid displacement method with deionized water as a displacement liquid. Figure 4.25 portrays the porosity of HEC/AgNPs scaffolds made using various AgNO_3 concentrations. All porous scaffolds showed high porosity with percentages above 87.1 % up to 89.5 %. The porosity of

HEC/AgNPs scaffolds decreased significantly with the increase of AgNO_3 concentrations. Overall, all cross-linked HEC/AgNPs freeze-dry scaffolds had high porosity that was suitable for transplanting cells and materials for cell cultivation in skin tissue engineering.

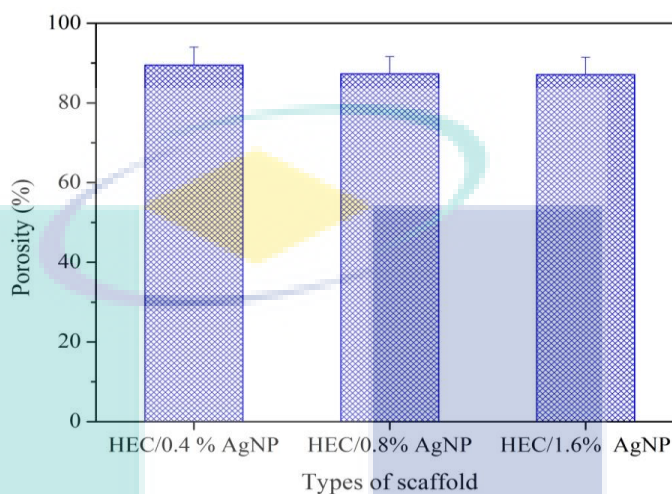


Figure 4.25: Porosity of HEC/AgNPs scaffolds with different Ag concentrations at 0.4%, 0.8% and 1.6%

4.4.4 Swelling ratio studies

The swelling of polymer matrix strongly depends on the rate of penetration solvent into the scaffold's matrix (Sinha Roy and Rohera, 2002). The equilibrium swelling ratios of the prepared HEC/AgNPs scaffolds are illustrated in Figure 4.26, as a function of AgNO_3 concentration. The swelling behaviour observed for HEC incorporated with silver nanoparticles indicated the rate at which these scaffolds absorb water and swell. After the first day of the experiment, all scaffolds showed high degree of swelling ratio due to the porous polymer network that enables the absorption of the amount of bulky water *via* hydrogen bonds. The water uptake showed higher swelling with the increase of AgNO_3 concentration except for 1.6% AgNO_3 . This could be caused by its porosity, which is lower than 0.4% and 0.8% AgNO_3 scaffolds. However, due to the heterogeneous nature of HEC sponge and the existence of free water that fills the space of macropores (> 60%), the results obtained cannot be interpreted unambiguously (Stoyneva et al., 2014). All HEC/AgNPs blended scaffolds obtained at the present study were visually sponge-like

materials, which easily absorbed water due to their porous structure. The high swelling ratio of HEC/AgNPs blended scaffolds was ascribed to the strong hydrogen bonding and Van der Waals interactions between polymer chains. These strong interactions offered huge capacity to absorb large amounts of water and swell to a great extent without being dissolved in the aqueous solution (Wu et al., 2010). After 7 days, the swelling ratio was increased to a maximum 849 %, 1163 % and 987 % for HEC with 0.4 %, 0.8 % and 1.6 % AgNO₃ porous scaffolds respectively. The percentage of swelling ratio was found to upsurge with prolonged time. Overall, this property is very important in inducing the uptake of nutrients to the interior of porous polymer scaffolds.

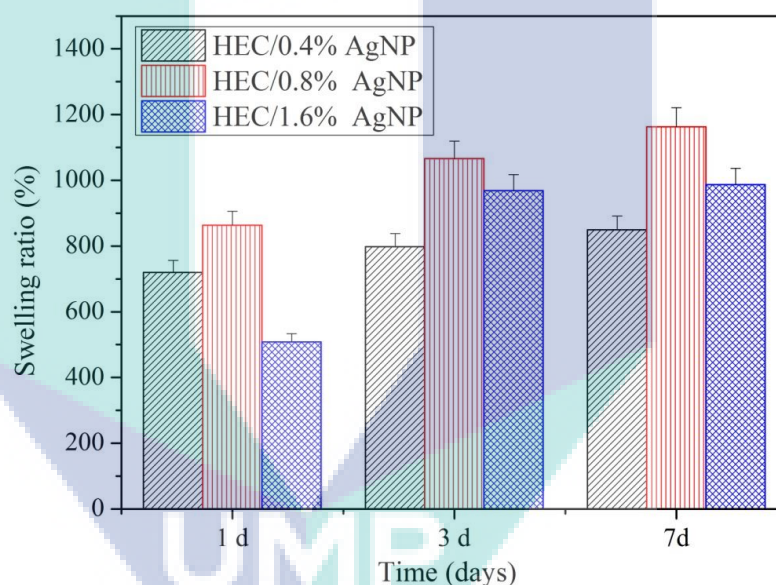


Figure 4.26: Swelling ratio of HEC/AgNPs scaffolds with different Ag concentrations at 0.4%, 0.8% and 1.6%

4.4.5 *In vitro* degradation studies

Degradation behaviour of porous scaffolds plays a vital role in the engineering process of a new tissue. The degradation rate of porous scaffolds could affect the cell vitality, cell growth and even host response (Freier et al., 2002). The degradation of HEC/AgNPs scaffolds in PBS at 37 °C over 7 days was evaluated as shown in Figure 4.27. All scaffolds demonstrated augmentation in percentage of weight loss as a function of

incubation time. Initially, all materials showed that high reduction of weight loss at maximum of approximately 24% might be due to the sidechain breakage of polymer backbone during immersion in the PBS solution. After 3 days of incubation, the scaffolds began to disintegrate, which leads to the increase in weight loss simultaneously. The larger weight loss might be due to the formation of micro holes and cracks in the bulk of the specimen during degradation of polymer matrix (Fortunati et al., 2011). After 7 days of degradation, HEC/AgNPs at 0.4 %, 0.8 % and 1.6 % AgNPs concentration showed further increase of percentage weight loss at 35.6 %, 43 % and 45.4 % respectively, implying biodegradable behaviour which is favourable in skin tissue engineering applications.

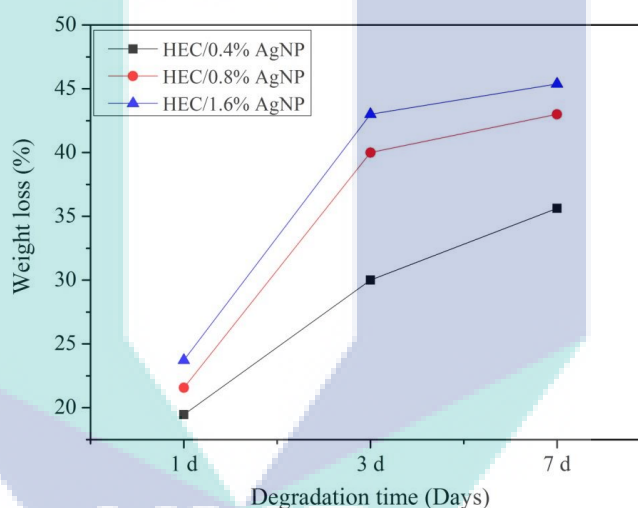


Figure 4.27: Weight loss of degrading HEC/AgNPs scaffolds with different Ag concentrations at 0.4%, 0.8% and 1.6%

4.4.6 UV-Vis absorbance spectroscopy

UV- Vis absorption was performed to verify the presence of silver nanoparticles in the prepared sample of HEC-stabilized silver composites. The surface plasmon resonance of the silver nanoparticles arises due to the free oscillating electron on the metal nanoparticles absorbing the electromagnetic radiation from particular energy levels. The surface plasmon resonance simply generates when the size of a metal nanocrystal is smaller than the wavelength of the incident radiation (Jana et al., 1999). The particle size, shape of particle, refractive index of surrounding medium and dielectric properties are most likely to

affect the peak of surface plasmon resonance (Huang et al., 1996; Elechiguerra et al., 2005). As reported in the previous literatures, silver nanoparticles have surface plasmon absorption between 400 nm and 450 nm (Fortunati et al., 2011; Mani et al., 2013 and Faghihi and Shabaniyan, 2011). From Figure 4.28, the silver nanoparticles demonstrated plasmon absorption at 417.72 nm, 420.73 nm and 421.93 nm for the 0.4 wt%, 0.8 wt% and 1.6 wt% of AgNO_3 respectively, which is consistent with the surface of plasmon resonance of Ag nanoparticles. The slight shift in the absorption peak might be due to the change in the number and size of particles embedded on the HEC scaffolds (Sumitha et al., 2012). Essentially, as the particles become larger, the maximum absorption shifts to longer wavelengths and the peaks will become broader.

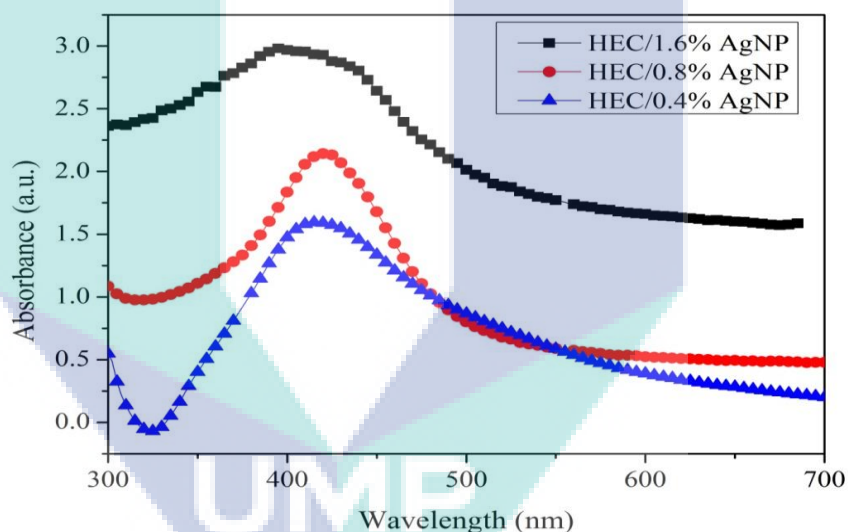


Figure 4.28: UV-Vis absorption spectra of HEC/AgNPs scaffolds

4.4.7 ATR-FTIR studies

The ATR-FTIR spectra of HEC/AgNPs cross-linked porous scaffolds are illustrated in Figure 4.29. FTIR spectra analysis was carried out to determine the possible interactions between hydroxyl groups of HEC due to the addition of AgNO_3 into the composite scaffolds.

The broad peak at 3389 to 3393 cm^{-1} indicated stretching vibrations of the hydroxyl groups due to the intramolecular and intermolecular hydrogen bands of the OH groups HEC. The vibrational band observed between 2876 and 2940 cm^{-1} , in reference to the stretching C-H from alkyl groups. The absorption peaks at 1706 – 1721 cm^{-1} in FTIR spectra of HEC/AgNPs composite materials indicated the existence of carboxylate groups due to the C=O stretching vibration. The same results were obtained by J. Wu et al., who explained the fact that there were new peaks in the range of 1720 – 1760 cm^{-1} for AgNPs-bacterial cellulose as compared with purified bacterial cellulose (Wu et al., 2014). These new peaks implied the oxidation of hydroxyethyl cellulose that supports the reaction of $\text{Ag}(\text{NH}_3)_2\text{OH}$ with hydroxyl in C_6 , the most reactive position of this cellulose derivatives (Salmoria et al., 2009). It was found that the ratio of absorption intensities of C=O stretching slightly shifted to the left with the increase of AgNPs content. The intensity of bands that varied from 1055 to 1059 cm^{-1} were assigned to C-O stretching vibrations, which showed weak peaks with slight shift to the left with the increase of AgNPs content. Lastly, the absorption peaks observed from 1455 to 1248 cm^{-1} exhibited the C-H and CH_2 bending vibrations in the C_6 of the HEC chains.

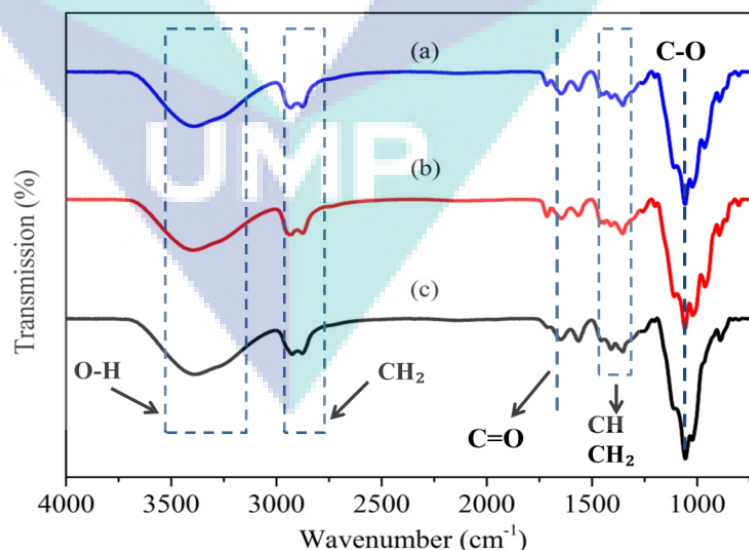


Figure 4.29: ATR-FTIR studies for HEC with different concentrations of Ag (a) 0.4%, (b) 0.8% and (c) 1.6% porous scaffolds

4.4.8 TGA and DrTGA analysis

TGA is an analytical technique used to determine a material's thermal stability and its fraction of volatile components by monitoring the weight change that occurs as a specimen is being heated. Table 4.10 summarizes the decomposition step and percentage mass loss for the HEC/AgNPs composite scaffolds.

The relation between temperature and weight loss of the samples was illustrated in TGA and DrTGA curves as exemplified in Figure 4.30. The TGA curves for HEC/AgNPs blends showed three degradation regions, which suggested the existence of more than one degradation process (Guirguis and Moselhey, 2012). These steps were distinguishable in the diagram of mass loss (TGA %) during heating and more clearly in the diagram of derivative mass loss (drTGA %).

Table 4.10: TGA and DrTGA data for HEC/AgNPs scaffolds

Sample	Region of decomposition	Temperature (°C)			Weight Loss (%)	
		T _{start}	T _{end}	T _{peak}	Partial	Total
HEC+ 0.4% AgNO ₃	1 st	25	89.1	53.6	1.9	70.8
	2 nd	89.1	168.4	108.1	4.5	
	3 rd	168.4	526.8	285.9	64.4	
HEC+ 0.8% AgNO ₃	1 st	25.1	149.7	102.4	13.7	72.36
	2 nd	149.7	195.6	169.9	3.2	
	3 rd	195.6	512.5	290.2	55.46	
HEC+ 1.6% AgNO ₃	1 st	25.1	95.2	60.7	4.6	73.4
	2 nd	95.2	162.5	119.7	2.2	
	3 rd	162.5	529.6	283.1	66.6	

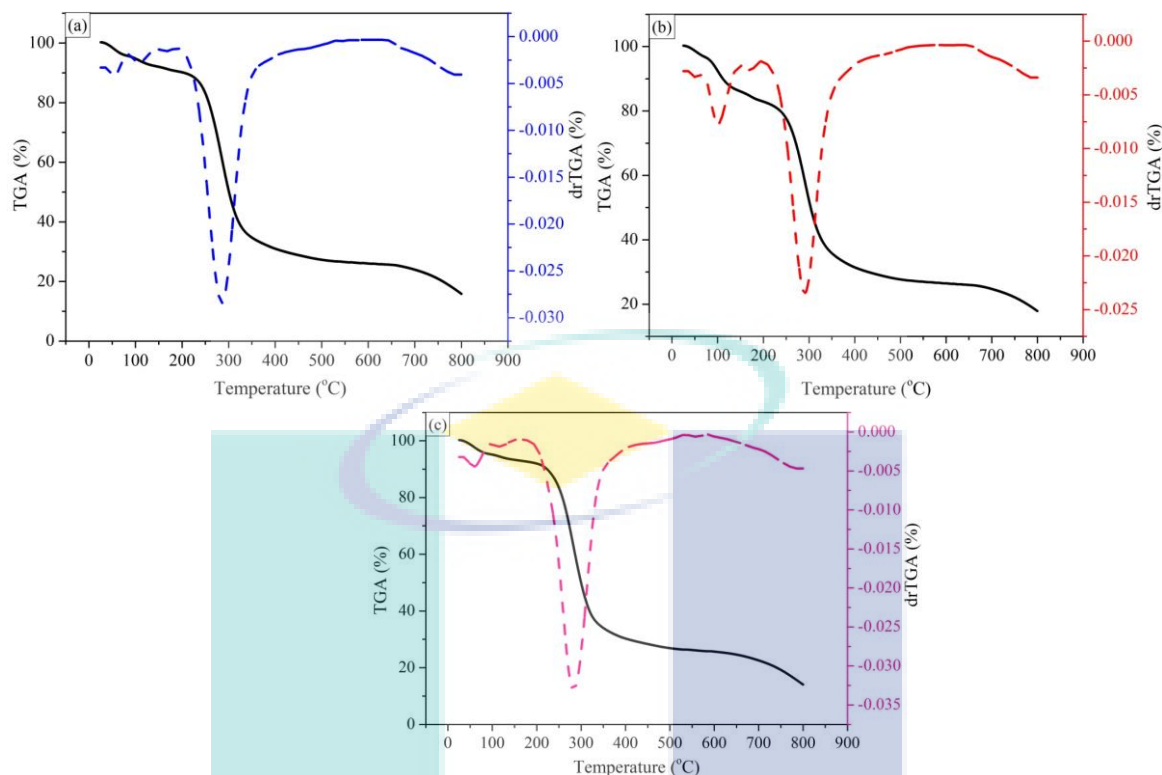


Figure 4.30: TGA and DrTGA analysis for HEC with different concentrations of Ag (a) 0.4%, (b) 0.8% and (c) 1.6% porous scaffolds

There are two initial small peaks emerge on the TGA curve with the initial weight loss in the range of 1.9% to 13.7 % at temperatures of 25 °C to 150 °C. These first small peaks were attributed to moisture absorption or vaporization of water within scaffold matrices. Meanwhile, the second small peaks that appeared between 89.1 °C and 195.6 °C with weight loss up to ~ 5% could be due to residual solvent loss from the Ag nanoparticles, which is the same as reported by previous research on thermal study of silver nanoparticles and PVA (Abdul kareem and Anu kaliani, 2011). Further weight losses were observed in third decomposition region varying from 162.5 °C to 529.6 °C with maximum weight loss up to 66.6 %. The higher value of weight loss at the third decomposition stage verified the existence of a chemical degradation process resulting from bond scission (carbon-carbon bonds) in the polymeric bone, which in this case refers to the loss of CO₂ in HEC (Guirguis and Moselhey, 2012). The difference in thermal decomposition behaviours of different HEC/AgNPs composite scaffolds can be seen more clearly from derivative thermogravimetric (DrTGA) curves. The occurrence of double peak at early stages

indicates that the weight loss could be due to weakly or strongly chemisorbed encapsulates on the silver surface (Nishida et al., 1996 and Dong et al., 2009). The DrTGA plot clearly displayed an intense exothermic peak varying from 283.1 °C – 293.8 °C and exhibited slower degradation rate despite the thermal stability of HEC/AgNPs scaffolds.

4.4.9 DSC study

DSC is a high sensitivity instrument to measure the thermodynamic properties of thermally induced transitions. DSC monitors heat effects associated with phase transitions and chemical reactions as a function of temperature. The results from DSC and the temperature of the phase transitions as well as change of enthalpies, ΔH are shown in Figure 4.31 and characterized in Table 4.11.

Figure 4.31 depicts the heating run of HEC/AgNPs blend samples up to 250 °C. The DSC thermograms demonstrates relatively broad endotherm glass transition temperature, T_g at 106.8 °C, 104.4 °C and 105.8 °C for HEC blended with 0.4 %, 0.8% and 1.6 % AgNO_3 respectively. The value of T_g corresponds to the temperature at which amorphous solids of HEC biopolymers become fragile on cooling or soft on heating. In addition, the decomposition temperature exhibited by the TGA curve and the study done *via* DSC showed good agreement since the value of enthalpy of HEC/AgNPs scaffolds displayed almost the same value with the second stage decomposition of the composite, as obtained from the TGA curve (Figure 4.31). Furthermore, DSC thermograms show an increase in T_g with the increase of AgNO_3 concentration, thus predicting the stability of the sample with the addition of AgNO_3 wt%.

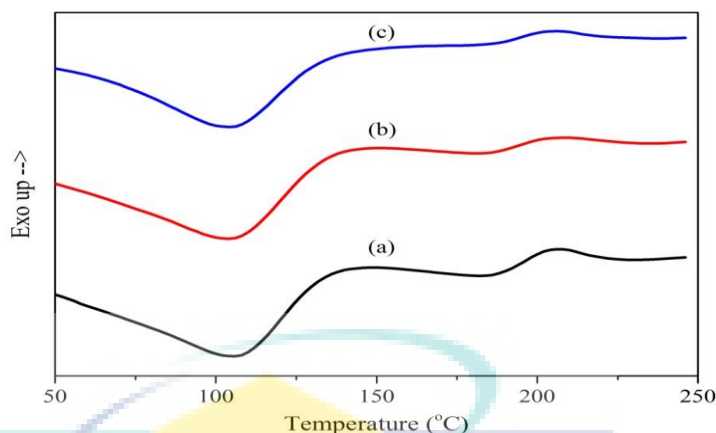


Figure 4.31: DSC study for HEC with different concentrations of Ag (a) 0.4%, (b) 0.8% and (c) 1.6% porous scaffolds

Table 4.11: DSC data and the characteristics of HEC/PVA composites scaffold.

Sample	T_g (°C)	T_m (°C)	ΔH (J/g)
HEC+ 0.4% AgNO ₃	104.4	205.7	18.6
HEC+ 0.8% AgNO ₃	105.8	205.7	22.5
HEC+ 1.6% AgNO ₃	106.8	205.7	31.5

4.5 CONCLUSION

To conclude, HEC/PVA, HEV/PVA/collagen and HEC/silver nanoparticles scaffolds have been characterized based on 4 different studies. The characterization includes porosity, swelling ratio, in vitro degradation study, morphological, chemical, thermal and mechanical properties studies. Both nanofibers and freeze-dried scaffolds showed diameter of fibers and pores in the range of (188 - 461 nm) and (2 - 150 μ m) respectively. For nanofibers scaffolds, HEC/PVA/collagen exhibited higher surface-to-volume ratio, slower degradation rate, higher thermal stability and better strength compared to HEC/PVA scaffolds. Meanwhile, for freeze-dried scaffolds, HEC/silver nanoparticles show lower porosity, slower degradation rate and lower thermal stability compared to HEC/PVA freeze-dried scaffolds.

CHAPTER 5

CELL CULTURE STUDIES ON NANOFIBERS AND FREEZE-DRIED SCAFFOLDS FOR SKIN TISSUE ENGINEERING APPLICATIONS

5.1 INTRODUCTION

In this chapter, a cell culture experiment is conducted to test the toxicity and biocompatibility of the materials towards the living cells. Generally, good biocompatibility requires the cells to attach and grow well internally and externally of the scaffolds. The toxicity of the materials towards the culture environment could be indicated through the morphological and quantitative changes of the cells. Hence, the results obtained from the *in vitro* culture are feasible to predict the cell-construct reaction *in vivo*. In this work, cell morphology and proliferation studies on nanofibrous and freeze-dried scaffolds are carried out using human melanoma and fibroblast cells. The surface morphology is observed using SEM and the utilization of scaffolds for skin tissue engineering application is studied with the MTT/MTS assay.

5.2 CELLS MORPHOLOGY STUDIES

5.2.1 A375 cytotoxicity studies of HEC/PVA nanofibrous scaffolds

Figure 5.1 shows the morphology of human A375 melanoma cells on different ratios of HEC/PVA on day 3 and 7 as observed by SEM. The image clearly shows the cells attachment and adherence on the HEC/PVA blend substrates with PVA contents up to 70%.

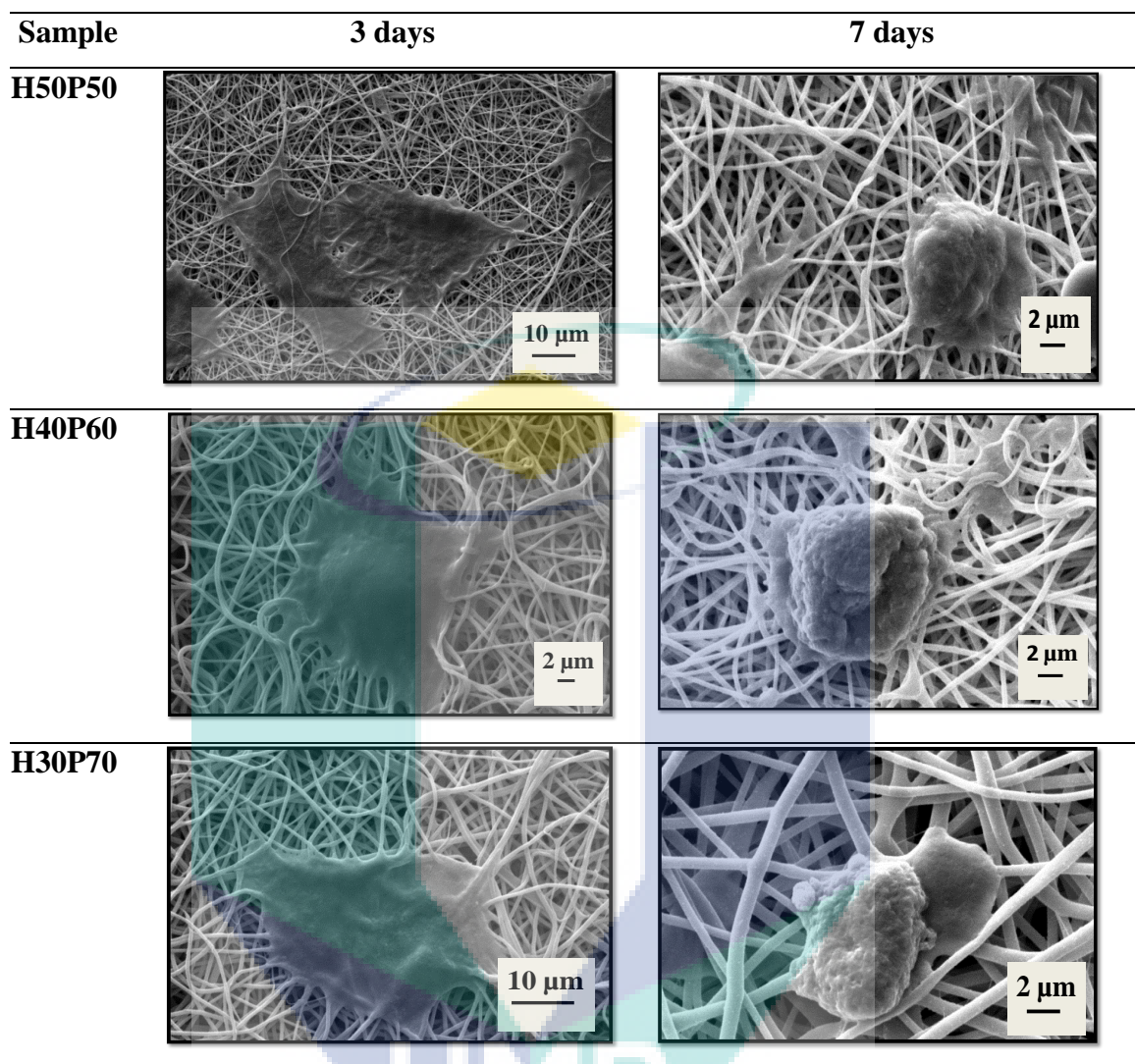


Figure 5.1: SEM micrographs of human A375 melanoma cells attached on nanofibrous scaffolds: (a) H50P50, (b) H40P60, (c) H30P70

On day 3, the cells started to spread on the surface of nanofibers scaffolds in a flat morphology. The cells bridged the nanofiber filaments and were thoroughly hybridized within the nanofiber network. The fibroblastic morphology of A375 melanoma cells gradually progressed towards rounded and globular morphology of epidermal-like cells in a time-dependent manner and became apparent after 7 days of induction in complete media (Mei et al., 2012). More cells were found to be clustered around HEC/PVA nanofibers scaffolds. In addition, it was observed that there was a greater tendency of cell spreading with increased PVA contents. This could be explained by the fact that the electrospun

nanofibers of H30P70 has a smaller average diameter compared to the remaining electrospun mats, hence having higher porosity, which favoured cell migration and infiltration into the nanofiber scaffolds. It also showed that the cells were intimately hybridized with the nanofiber network, being likely to migrate into the mesh holes and grow within fibrous networks (Cui et al., 2009). These cells were grown with effective spreading, indicating that HEC/PVA scaffolds exhibited excellent biocompatibility and supported cell attachment and proliferation.

5.2.2 hFB cytotoxicity studies of HEC/PVA HEC/PVA/collagen electrospun nanofibrous scaffolds

Cell morphology of hFB cells on the HEC/PVA and HEC/PVA/collagen composite scaffolds was observed under SEM as shown in Figure 5.2. As expected, all cross-linking nanofibrous scaffolds maintained their 3D and porous structure after incubated into the medium. After 2 days of cell seeding, the cells started stretching and spreading in a spindle-shaped morphology over the surface of nanofibrous scaffolds. After 4 days, HEC/PVA and HEC/PVA/collagen scaffolds started to cover some parts by cells and form an intact layer thus indicating that the scaffolds supported the cell attachment and proliferation. On day 7, both HEC/PVA and HEC/PVA/collagen composite nanofibers exhibited more cells attaching and spreading on the surfaces. Good attachment between the cells and nanofibers were clearly visible through the edge of the adhered cells. From the cell-scaffold constructs, it is clear that cells comply well with nanofiber surfaces and are capable to migrate inside the scaffolds. Multiple layers of cells were observed on the HEC/PVA/collagen nanofibers scaffold which signified that the substrates were preferred for cell proliferation.

The presence of an ECM protein, collagen in the HEC/PVA scaffolds enhances the possibility of cell-scaffold transplantation of a construct with differentiated keratinocytes to enhance skin regeneration process (Gattazzo et al., 2014). Overall, it indicates good adhesion, high cell proliferation rate, migration and penetration of hFB cells on HEC/PVA/collagen electrospun nanofibrous scaffolds compared with HEC/PVA nanofibers.

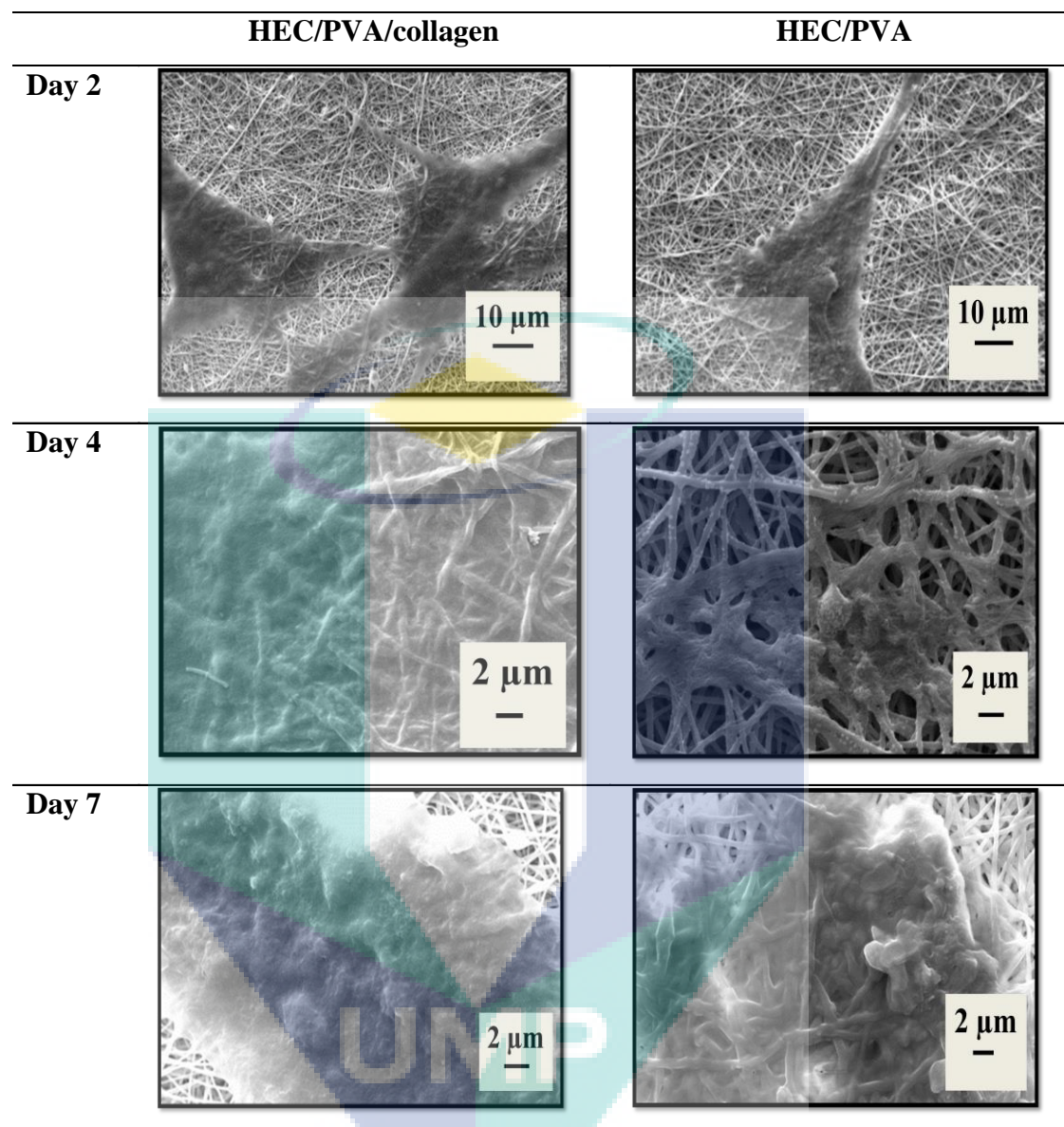


Figure 5.2: SEM micrographs of hFB cells attached on HEC/PVA and HEC/PVA/collagen after 2, 4 and 7 days incubation

5.2.3 hFB cells morphology on HEC/PVA porous scaffolds

Figure 5.3 (i, ii, iii) shows the SEM micrographs of cell cultures for 1, 4 and 7 days on the outer and inner surfaces of the scaffolds. After 1 day of cell culture, round shape morphology of fibroblast cells adhered on the surface of the scaffolds. The cells exhibited smooth surface for pure HEC while slightly rough surface for blended HEC/PVA scaffolds.

Bundle of cells were proliferated on the HEC/PVA (2:1) scaffolds whereas the cell of spindle-shaped morphology was observed on the pure PVA scaffolds.

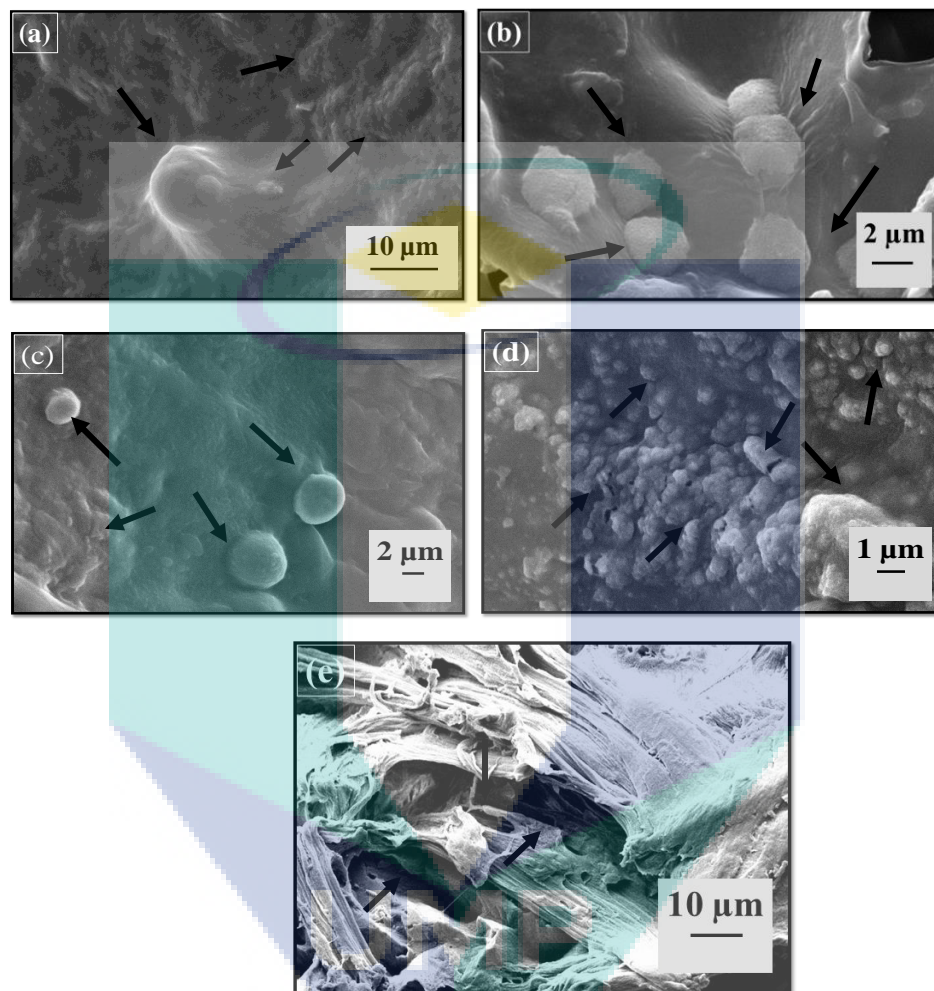


Figure 5.3(i): SEM micrograph images of hFB cells attached on (a) pure HEC, (b) HEC/PVA (2:1), (c) HEC/PVA (1:1), (d) HEC/PVA (1:2) and (e) pure PVA scaffolds after day 1 cell culture (black arrow indicates the growth cells)

After 4 days of cell culture, hFB cells elongated and spread well to a vast area of the scaffold surface. Some confluent layer of fibroblast cells with slight filopodial extension were seen across the valley of the inner and formed multiple points of attachments from the surface. Large flat fibroblast cells were produced indicating that the fibroblast cell proliferation had begun.

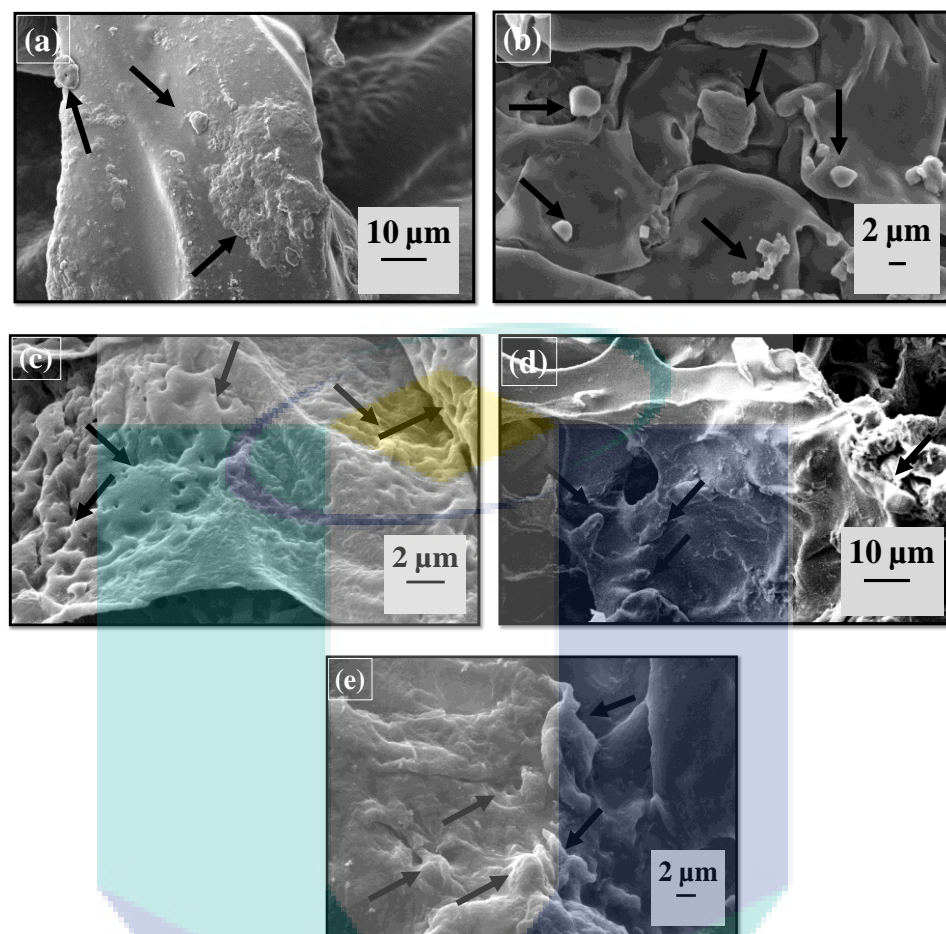


Figure 5.3(ii): SEM micrograph images of hFB cells attached on (a) pure HEC, (b) HEC/PVA (2:1), (c) HEC/PVA (1:1), (d) HEC/PVA (1:2) and (e) pure PVA scaffolds after day 4 cell culture (black arrow indicates the growth cells)

In reference to Figure 5.3 (iii), after 7 days of cell attachment, the cells regenerated its filopodia which indicated good cell adhesion property of the scaffolds. More surfaces were merely covered with the cells internally and externally. The cells were grown in groups and converged to form large areas in the culture medium. As a result, the number of fibroblast cells obviously increased with the prolongation time without significant difference between pure HEC and PVA with blended HEC/PVA scaffolds. The favorable environment provided by HEC/PVA encouraged cell affinity and cell differentiation. All scaffolds showed low toxicity and supported the growth of hFB cells. This observation will be further proven by the following statistics analysis of cellular proliferation and viability

of cell growth. Great cell attachment, adherence and proliferation are suitable remarks for *in vivo* culture.

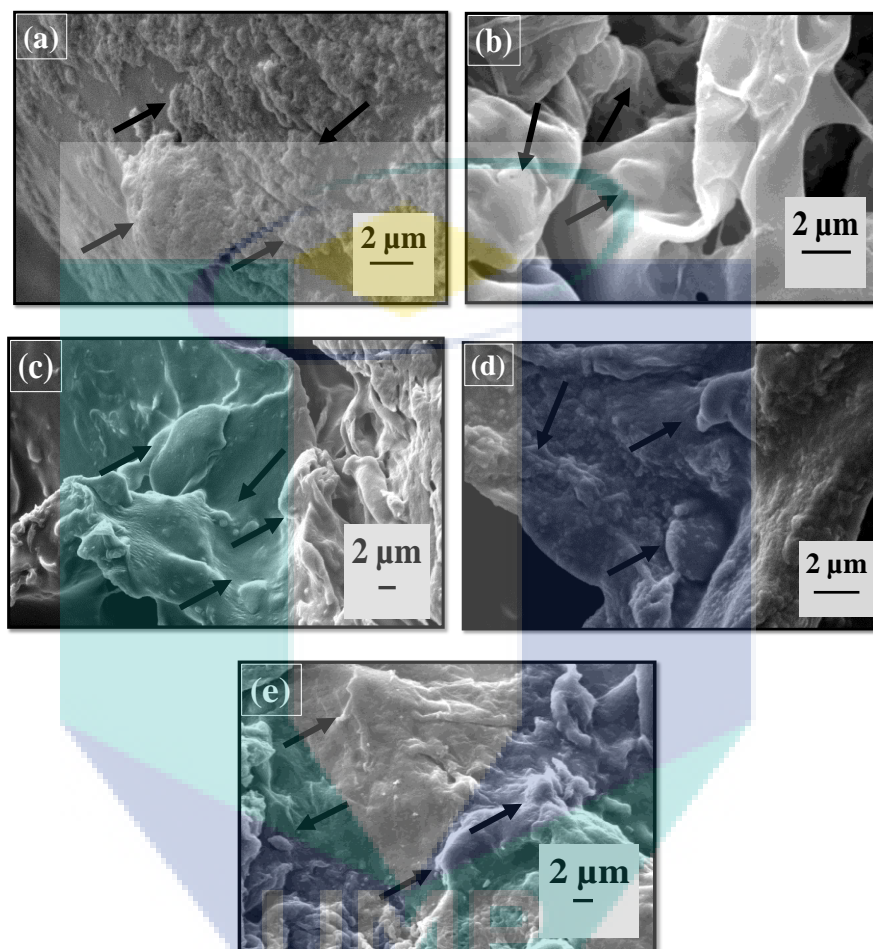


Figure 5.3(iii): SEM micrograph images of hFB cells attached on (a) pure HEC, (b) HEC/PVA (2:1), (c) HEC/PVA (1:1), (d) HEC/PVA (1:2) and (e) pure PVA scaffolds after day 7 cell culture (black arrow indicates the growth cells)

5.2.4 hFB cells morphology on HEC/silver nanoparticles scaffolds

In tissue engineering, silver nanoparticle based-scaffolds received high concerns regarding their potential cytotoxicity to host mammalian cells. Silver in the form of nanoparticles has gained increasing access to tissues, cells and biological molecules within the human body. However, one must consider that certain nanoscale materials do exhibit significant toxicity to mammalian cells even if they are biochemically inert and

biocompatible in bulk size, e.g. carbon (Magrez et al., 2006 and Shvedova et al., 2005). Previous reports mentioned the cytotoxic effects of silver depends on dose, exposure time and cell line tested (Mukherjee et al., 2012). Furthermore, since silver nanoparticles are known as antibacterial agents, it is essential to prove that nanosilver does not bring any toxicity to mammalian cells. The biocompatibility of HEC containing different concentrations of porous silver nanoparticle scaffolds was evaluated by culturing with hFB cells for 4 and 24 hours. The morphology changes are shown in Figure 5.4.

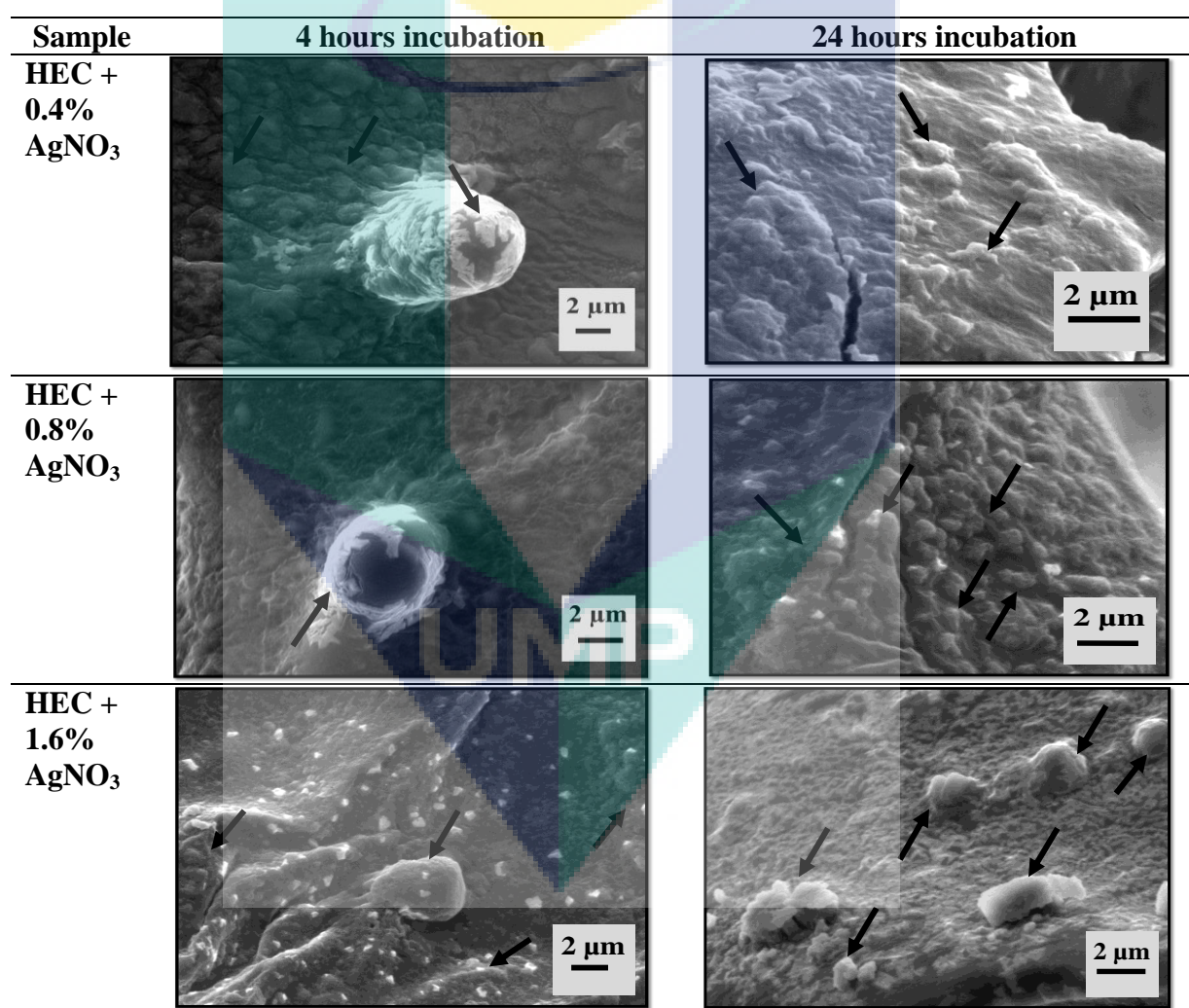


Figure 5.4: SEM micrograph images of hFB cells attached on HEC with different concentrations of AgNO₃ (a) 0.4%, (b) 0.8% and (c) 1.6% scaffolds after 4 h and 24 h incubation period (black arrow indicates the growth cells)

After 4 hours of cultivation, spherical shape fibroblast cells formed on the surface of the scaffolds. The cells exhibit slightly uneven and rough surfaces for all scaffolds indicating adhesion and interaction between the media and cells-scaffold construct. After 24 hours, the cells grew and spread well to a vast area of the scaffold surface with enhanced granular shape observed for 1.6 % AgNO₃. This observation indicated that HEC-silver nanoparticles possess good biocompatibility and support the growth of fibroblast cells.

5.3 CELLS PROLIFERATION STUDIES

5.3.1 A375 cells proliferation studies on HEC/PVA nanofibrous scaffolds

Biomaterials projected for *in vivo* applications should not exhibit toxicity to mammalian cells. Thus, the prepared HEC/PVA electrospun scaffolds were subjected to cytotoxicity analysis using MTT assay to human A375 melanoma cells. MTT assay is a calorimetric study based on the ability of cellular mitochondrial dehydrogenase in reducing the yellow coloured tetrazolium salt to blue coloured formazan crystals. The proliferation of human A375 melanoma cells on the nanofiber scaffolds was studied by examining cell viability on days 1, 3 and 7. By using cells in a complete media without the presence of scaffolds as a positive control, the relative cell viability on each scaffold was calculated and exemplified in Figure 5.5. As shown in Figure 5.5, all nanofiber scaffolds showed significant increase ($p \leq 0.05$) from day 1 to day 7 due to the increase in the number of cell attachment and penetration through the porous fibers. After day 1 and 3, the HEC/PVA nanofibers showed a significant level of slow increase in cell proliferation rates which might be due to the shrinkage and hydrophobic surfaces of electrospun mats. These scaffolds shrank, and their pore size as well as porosity, decrease dramatically during the incubation process, which hindered cell migration into the nanofibers mats (Pham et al., 2006). The results on day 7 showed better cell infiltrations and proliferation with the highest MTT absorbance index reaching 0.58. Comparing the effect of PVA contents in HEC/PVA nanofibers scaffolds, there is no significant difference among them. However, H50P0 demonstrated higher cell proliferation compared to other scaffolds. These increments are due to a higher cell density (proved by the MTT assay) around the

nanofibers, contributing to a more conducive environment for A375 cells differentiation on HEC/PVA nanofibers.

The nanofibrous structure produced by electrospinning has a high surface area to volume ratio, providing more substrates for cell attachment (and therefore a higher cell density per unit of space) compared with other structures (Li et al., 2002). He et al. also found that a high surface area to volume ratio facilitates more growth factor and cytokine binding by fibers from the serum in the culture medium (He et al., 2010). Moreover, HEC/PVA nanofibers with high hydrophilicity can bind more differentiation-inducing factors from the medium, thereby enabling close contact and intimate interaction between the cells and growth factors. From the results of this study, we infer that the electrospun nanofibrous substrates can serve as a tissue engineering scaffold.

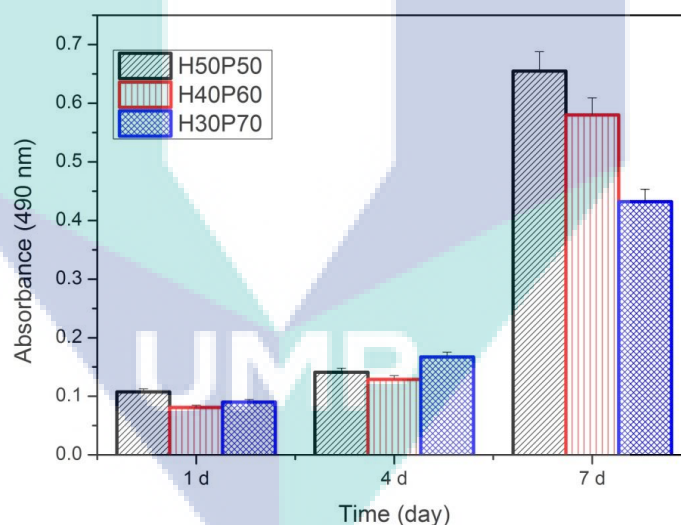


Figure 5.5: Graph showing human A375 melanoma viability after 1, 3 and 7 days of incubation (1×10^5 cells/well in complete DMEM) at different weight ratios of nanofibrous scaffolds. (*H*-HEC content, *P*-PVA content)

5.3.2 hFB cells proliferation studies on HEC/PVA and HEC/PVA/collagen nanofibrous scaffolds

Fibroblasts exist widely in the dermal layer and play key roles in the wound healing process (El Ghalbzouri et al., 2009). In order to evaluate the effect of collagen on the cytotoxicity of the scaffold, the morphology and viability of the fibroblast seeded on the scaffolds were compared. Cell proliferation assay of hFB cells on the HEC/PVA and HEC/PVA/collagen nanofibrous scaffolds has been carried out for the period of 2, 4 and 7 days. As shown in Figure 5.6, all nanofibers show high MTS absorbance indices from 1.2 to 1.5 after 2 days of incubation period but after 4 and 7 days of cell seeding, the rates of cell proliferation decreased vividly. This condition might be explained by the reason that after 2 days of cell seeding, the nanostructured microenvironment suited best to the cells and promoted high confluency of the cells on the nanofibrous scaffolds. In addition, the confluency of cells over the scaffolds produced space stress on the cells and depletions in nutrients supply (Gautam et al., 2013). Overall, HEC/PVA/collagen nanofiber scaffolds showed higher cell proliferation compared to HEC/PVA composite nanofibers. Although there was no significant difference between HEC/PVA electrospun nanofibers with and without collagen, HEC/PVA/collagen exhibited a slightly better value than HEC/PVA alone. Thus, compared with pure HEC/PVA, collagen incorporated with HEC/PVA nanofibers could provide better growth condition for cell proliferation. In our study, HEC/PVA/collagen electrospun nanofibers scaffold might pose as the most suitable candidate for skin tissue engineering applications.

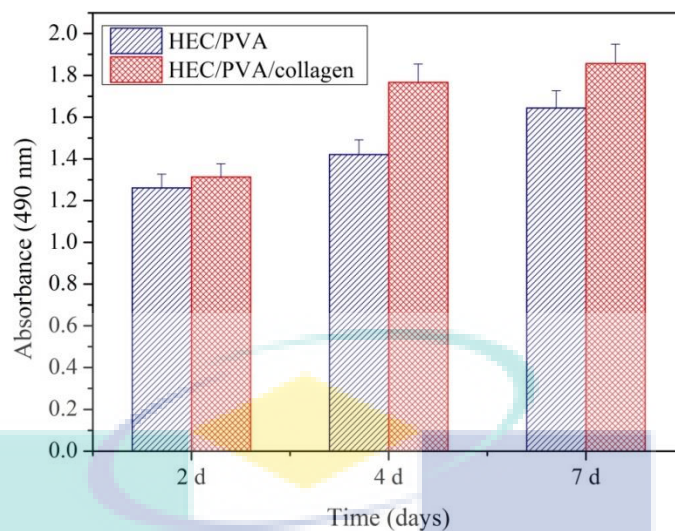


Figure 5.6: Graph showing human fibroblast viability after 2, 4 and 7 days of incubation (1×10^5 cells/well in complete MEM) at different weight ratios of nanofibrous scaffolds

5.3.3 hFB cells proliferation studies on HEC/PVA porous scaffolds

The proliferation of human fibroblast cells on the freeze-dry scaffolds was studied by examining cell viability on days 1, 4 and 7. The quantitative measurement of cell proliferation was analyzed by MTS assay. By using cells in a complete media without the presence of scaffolds as a positive control, the relative cell viability on each scaffold was calculated and exemplified in Figure 5.7. As shown in Figure 5.7, all scaffolds show significant increase ($p \leq 0.05$) from day 1 to day 7 due to the increase in the number of cell attachment and penetration through the porous scaffolds.

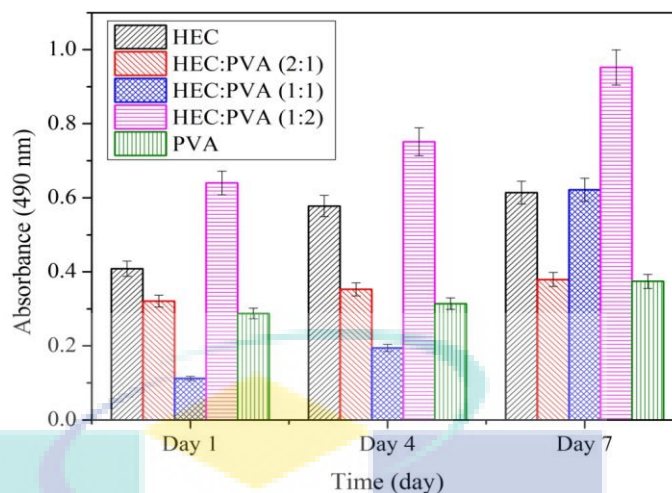


Figure 5.7: Graph showing human fibroblast viability after 2, 4 and 7 days of incubation (1×10^5 cells/well in complete MEM) at different weight ratios of HEC/PVA scaffolds

On day 1, HEC/PVA (1:1) (abs. index at 0.11) exhibited slowest proliferation rate than HEC/PVA (2:1) and (1:1) with abs. index 0.32 and 0.64 respectively. This might be due to the lack of cell-scaffold interactions required to induce signal proliferation of cells based on this equal HEC and PVA weight ratio. However, HEC/PVA (1:1) showed rapid cell growth after 4 days of culture with absorbance index achieving 0.62 on day 7 of cultivation. Pure HEC demonstrated higher absorbance index with prolongation time than pure PVA with maximum absorbance index 0.61 and 0.37 correspondingly. This was due to the high porosity of HEC scaffolds that enabled the high quantity of cells to infiltrate the scaffold pore structure. However, it is important to note that pore geometry and pore size do not necessarily effect the adhesion, spreading and proliferation of cells (Vlierberghe et al., 2007). The absorbance index corresponding to greater cell number of scaffolds HEC/PVA (2:1) showed significantly higher value than the others for 1, 4 and 7 days of culture time. Although this type of scaffold represented lower porosity (~ 90%) than other scaffolds, the high absorbance index might be due to optimum conditions provided by the scaffolds, which produced a conducive environment for cell inhibition. Overall, it can be concluded that HEC/PVA has good biocompatibility, non-toxic and suitable for *in vivo* investigation.

5.3.4 hFB cells proliferation studies on HEC/silver nanoparticles scaffolds

The MTS assay data demonstrated the relative viability of epidermal cells growing on HEC with different concentrations of AgNO₃. Figure 5.8 represents the viability of hFB cells on the scaffolds after 4, 12 and 24 h of culture period. By using cells in a complete media without the presence of scaffolds as a positive control, the relative cell viability on each scaffold was calculated.

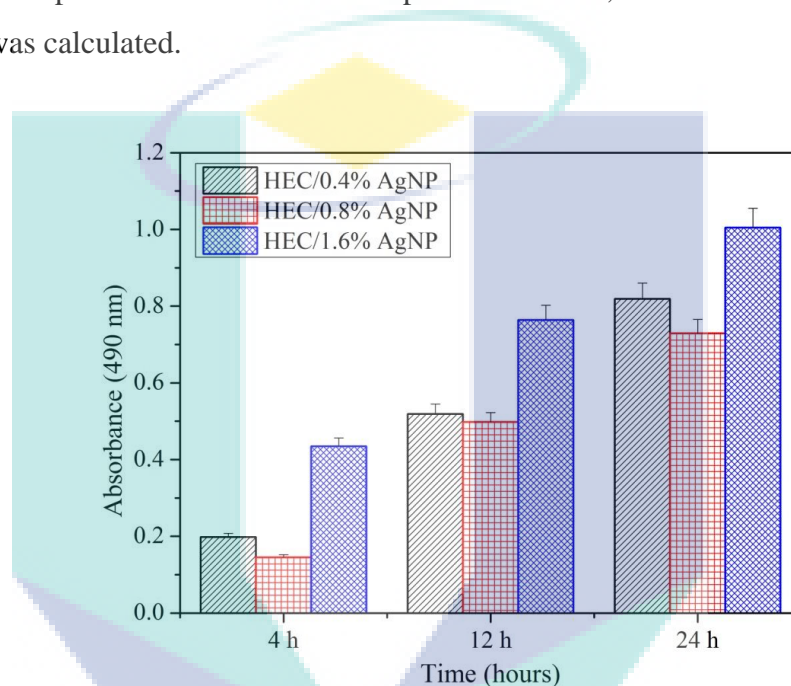


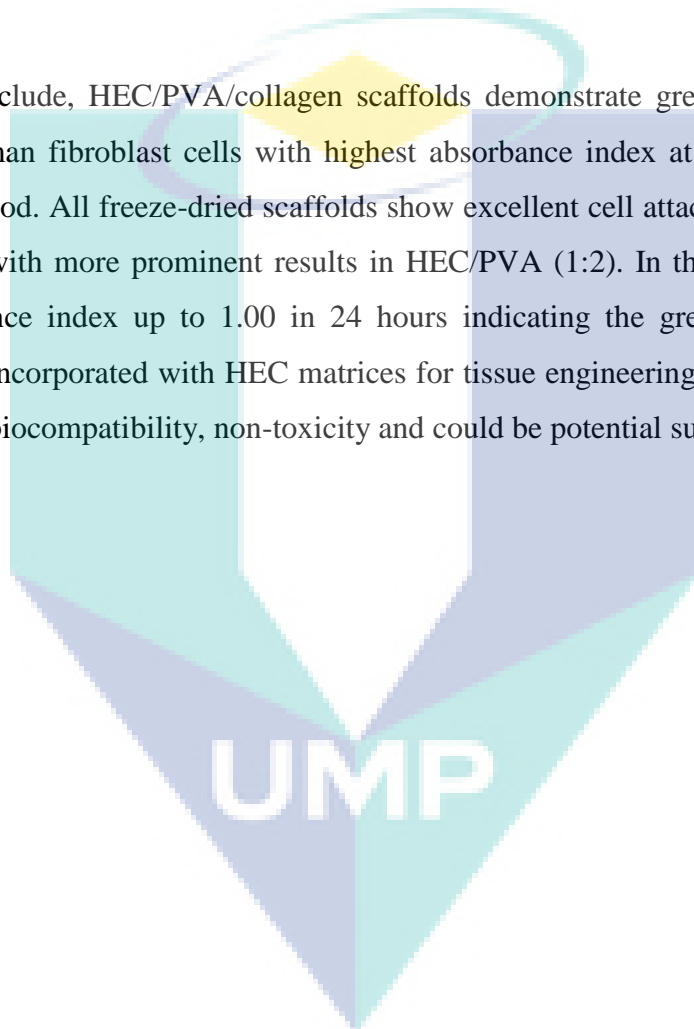
Figure 5.8: Graph showing human fibroblast viability after 4, 12 and 24 h of incubation (1×10^6 cells/well in complete MEM) of HEC in different concentrations of Ag (a) 0.4%, (b) 0.8% and (c) 1.6% scaffolds

All scaffolds showed significant increase ($p \leq 0.05$) in viability with incubation time due to enhanced number of cell attachment, population and penetration through the porous scaffolds. HEC with 0.8% silver nitrate exhibited slowest proliferation rate than other samples with maximum absorbance index up to 0.73. HEC with 1.6% silver nitrate demonstrated higher absorbance index with time at maximum absorbance index 1.00. This might be due to higher concentrations of AgNO₃ that triggered many cellular pathways, which could lead to cellular proliferation. However, it is important to note that high concentrations of silver nanoparticles might also point to cell damages with the increase of incubation time as nanoparticles can undergo a series of processes like binding and reacting

with proteins, phagocytosis, deposition, clearance and translocation (Mukherjee et al., 2012). Therefore, further studies should be done to determine an exact and optimal concentration of HEC incorporated silver nanoparticles that gives the most positive sensitivities and vice versa towards living cells.

5.4 CONCLUSION

To conclude, HEC/PVA/collagen scaffolds demonstrate greater response towards A375 and human fibroblast cells with highest absorbance index at ~ 1.9 after 7 days of incubation period. All freeze-dried scaffolds show excellent cell attachment, adherence and proliferation, with more prominent results in HEC/PVA (1:2). In this study, HEC/AgNPs show absorbance index up to 1.00 in 24 hours indicating the great influence of silver nanoparticles incorporated with HEC matrices for tissue engineering. Overall, all scaffolds endorse good biocompatibility, non-toxicity and could be potential substrates for skin tissue engineering.



CHAPTER 6

SUMMARY AND RECOMMENDATIONS

6.1 SUMMARY

The research and development of work during this doctoral research brought in important results, which would eventually help the industry to develop new biocompatible scaffolds that offer rapid healing response for tissue engineering applications. In this research, HEC as the main biopolymer has been fabricated using two different techniques, which are electrospinning and freeze-dried methods. Cell culture studies have been performed to demonstrate the scaffolds as potential substrates for skin tissue engineering. This chapter briefly outlines the major conclusions of this doctoral research and recommendations for further improvements.

1. The HEC/PVA and HEC/PVA/collagen nanofibers fabricated *via* electrospinning technique. The HEC/PVA cross-linked nanofibers showed diameter in the range of 204-283 nm. The HEC/PVA cross-linked nanofibers displayed Young's modulus, ultimate tensile strength and ultimate tensile strain at 183.75 – 234.25 MPa, 2.30 – 4.04 MPa and 12.43-15.73 % respectively. Meanwhile, the HEC/PVA/collagen fibers displayed fiber diameter at 188.34 nm and Young's modulus, ultimate tensile strength and ultimate tensile strain at 106.1 MPa, 2.95 MPa and 20.35 % correspondingly. The cross-linked fibers have a maximum decomposition mass loss occurring at the second decomposition region of the TGA curve at 265 – 360 °C. The T_g and T_m value

exhibited a single peak in DSC thermograms indicating the miscibility of the blend polymers.

2. The *in vitro* degradation study has been carried out to examine the degradation rate of both HEC/PVA and HEC/PVA/collagen nanofibers. The polymer nanofibers were immersed in PBS and DMEM solution for 12 weeks and measured of its swelling ratio, pH changes and mass loss at each time point. By SEM observation, all fibers exhibited uneven and rough surfaces while some fibers started to show signs of breakage and fracture with time. Faster degradation behaviour was observed in PBS compared to that determined in DMEM. This effect is more prominent in HEC/PVA samples compared to HEC/PVA/collagen. The mechanical studies showed significant decrease in Young's modulus from 97.8 – 106.1 MPa at week 0 to 11.04 – 36.35 MPa at week 12. All scaffolds showed a decrease in T_g , T_m and crystallinity value after 12 weeks of degradation period. In tissue-engineered skin, the maturation phase point may vary extensively depending on the size and type of the wound ranging from approximately three days to three weeks or may last for even a year or longer. These preliminary studies could be used as an initial estimate of the degradation rate as well as to predict the skin *in vivo* degradation behaviour of HEC/PVA blend system.
3. In the porous HEC, PVA and HEC/PVA blend polymer scaffolds, the polymer solutions have been fabricated using a freeze-dried method. The SEM images displayed interconnected porous structure ranging from 50 to 150 μm . All scaffolds exhibited porosity above 85 % and high swelling ratio after 7 days of incubation period, which revealed their suitability in cell-scaffold environment. The T_g values were found in the range of both HEC and PVA pure scaffolds, emphasizing the miscibility of both polymers. The Young's modulus of HEC/PVA which varied from 14.7 - 22.46 MPa indicated better mechanical properties of blend polymers compared to single polymer.

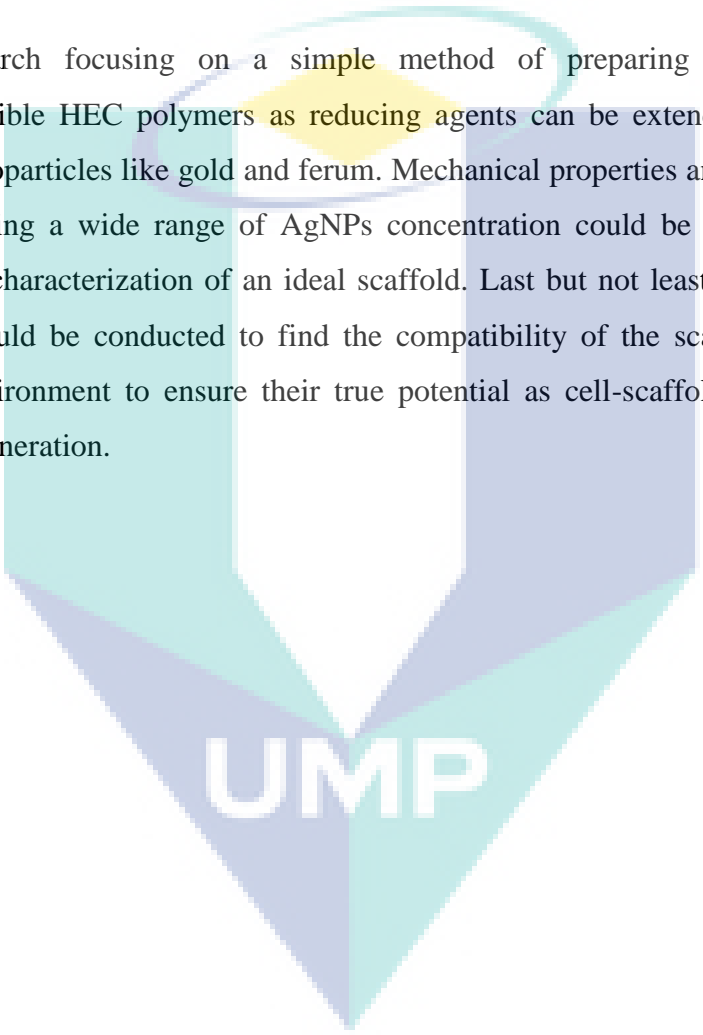
4. The HEC with silver nanoparticles at varied concentrations have been fabricated by a freeze-drying technique. The presence of silver nanoparticles was confirmed by the colour changes of the reaction mixture from bright yellow to light brown and finally to dark brown at the end of a 2 h heat treatment. The presence of AgNPs was further confirmed using UV-Vis where the surface plasmon absorption observed is in the range of 417.72 nm to 421.93 nm. All scaffolds showed high porosity up to ~ 90 % and the percentage of swelling ratio was found to increase with time. The HEC/AgNPs also demonstrated good degradation mechanisms which indicated their biodegradable properties and the occurrence of hydrolysis process.
5. In cell culture studies, different weight ratios of HEC/PVA fibers showed good cell adhesion and growth during cell-scaffold *in vitro* study of human melanoma cells with more prominent results in HEC:PVA (50:50) nanofibers scaffold. HEC/PVA/collagen scaffolds also demonstrated enhanced response towards human fibroblast cells with highest absorbance index at ~ 1.9 after 7 days of incubation period. All freeze-dried scaffolds showed excellent cell attachment, adherence and proliferation, with more prominent results in HEC/PVA (1:2) with 0.95 of absorbance index. The HEC/AgNPs scaffolds showed the most positive response towards skin cells with the value of absorbance index at 1.00 after only 24 hours of incubation period.

6.2 RECOMMENDATIONS FOR FUTURE STUDIES

1. In further research, the studies using HEC/PVA nanofibers as scaffolds can be extended to different cell growth works such as mesenchymal stem cells, endothelial and osteoblast cells. In addition, multiple types of proteins like chitosan, gelatine or silk fibroin incorporated with HEC could be explored as potential scaffolds for tissue engineering.
2. For *in vitro* degradation studies, the critical time point where the scaffolds started losing its strength and integrity was not achieved completely. Longer incubation time

could be considered to understand the full effect of the polymer degradation material towards physical, chemical, thermal and mechanical properties. In addition, determination on the molecular weight distribution could be done to understand the difference in chemical reactions of the scaffolds with the medium. In further research, different types of media such as complete medium of DMEM, FBS and Pen Strep or immersion in cell line could be used as test degradation media.

3. The research focusing on a simple method of preparing nanoparticles using biocompatible HEC polymers as reducing agents can be extended to prepare other metal nanoparticles like gold and ferum. Mechanical properties and longer cell culture studies using a wide range of AgNPs concentration could be explored to find the optimum characterization of an ideal scaffold. Last but not least, *in vivo* cell culture studies could be conducted to find the compatibility of the scaffolds with the real tissue environment to ensure their true potential as cell-scaffold constructs in skin tissue regeneration.

The logo for UMP (Universitas Muhammadiyah Purwokerto) is a large, downward-pointing arrow shape. It is composed of four triangular sections meeting at a central point: a light blue section on the top-left, a light purple section on the top-right, a teal section on the bottom-left, and a light blue section on the bottom-right. The letters 'UMP' are printed in white, bold, sans-serif font across the center of the arrow's shaft.

UMP

REFERENCES

- Abdel-Halim, E.S. 2013. Chemical modification of cellulose extracted from sugarcane bagasse: Preparation of hydroxyethyl cellulose. *Arabian Journal of Chemistry*. **7**(3): 362-371.
- Abdel-Mohsen, A.M., Hrdina, R., Burgert, L., Abdel-Rahman, R.M., Hašová, M., Šmejkalová, D., Kolář, M., Pekar, M. and Aly, A.S. 2013. Antibacterial activity and cell viability of hyaluronan fiber with silver nanoparticles. *Carbohydrate polymers*. **92**(2): 1177–1187.
- Abdel-Mohsen, A.M., Hrdina, R., Burgert, L., Krylová, G., Abdel-Rahman, R.M., Krejčová, A., Steinhart, M. and Beneš, L. 2012. Green synthesis of hyaluronan fibers with silver nanoparticles. *Carbohydrate polymers*. **89**(2): 411–422.
- Abdo, H.S., Khalil, K.A., Al-Deyab, S.S., Altaieb, H. and Sherif, E.-S.M. 2014. Antibacterial effect of carbon nanofibers containing Ag nanoparticles. *Fibers and Polymers*. **14**(12): 1985–1992.
- Abdul Kareem, T. and Anu Kaliani, A. 2011. Synthesis and thermal study of octahedral silver nano-plates in polyvinyl alcohol (PVA). *Arabian Journal of Chemistry*. **4**(3): 325–331.
- Abou El-Nour, K.M.M., Eftaiha, A., Al-Warthan, A. and Ammar, R. A.A. 2010. Synthesis and applications of silver nanoparticles. *Arabian Journal of Chemistry*. **3**(3): 135–140.
- Aguzzi, C., Sandri, G., Bonferoni, C., Cerezo, P., Rossi, S., Ferrari, F., Caramella, C. and Viseras, C. 2014. Solid state characterisation of silver sulfadiazine loaded on montmorillonite / chitosan nanocomposite for wound healing. *Colloids and Surfaces B: Biointerfaces*. **113**: 152–157.
- Akiyama, E., Kashimoto, A., Fukuda, K., Hotta, H., Suzuki, T. and Kitsuki, T., 2005. Thickening properties and emulsification mechanisms of new derivatives of polysaccharides in aqueous solution. *Journal of colloid and interface science*. **282**(2): 448–457.
- Ali, I.O. 2013. Aspects Synthesis and characterization of Ag⁰ / PVA nanoparticles via photo- and chemical reduction methods for antibacterial study. *Colloids and Surfaces A: Physicochemical and Engineering*. **436**: 922–929.
- Al-Sabagh, A. M. and Abdeen, Z. 2010. Preparation and Characterization of Hydrogel Based on Poly(vinyl alcohol) Cross-Linked by Different Cross-Linkers Used to Dry Organic Solvents. *Journal of Polymers and the Environment*. **18**(4): 576–583.

- Altman, G.H., Diaz, F., Jakuba, C., Calabro, T., Horan, R.L., Chen, J., Lu, H., Richmond, J. and Kaplan, D.L. 2003. Silk-based biomaterials. *Biomaterials*. **24**(3): 401–416.
- Amanullah, M. and Yu, L. 2005. Environment friendly fluid loss additives to protect the marine environment from the detrimental effect of mud additives. *Journal of Petroleum Science and Engineering*. **48**: 199–208.
- Angadi, S.C., Manjeshwar, L.S. and Aminabhavi, T.M. 2010. Interpenetrating polymer network blend microspheres of chitosan and hydroxyethyl cellulose for controlled release of isoniazid. *International journal of biological macromolecules*. **47**(2), 171–179.
- Anton, F. 1934. *Process and apparatus for preparing artificial threads*. U.S. Patent No. 1, 975, 504.
- Antonelli, M., De Pascale, G., Ranieri, V.M., Pelaia, P., Tufano, R., Piazza, O., Zangrillo, A., Ferrario, A., De Gaetano, A., Guaglianone, E. and Donelli, G. 2012. Comparison of triple-lumen central venous catheters impregnated with silver nanoparticles (AgTive®) vs conventional catheters in intensive care unit patients. *The Journal of hospital infection*. **82**(2):101–107.
- Arbor Health Plan. 2014. *Clinical Policy Title : Bioengineered Skin Substitutes for Ulcers and Wound Care*. Clinical Policy Number (931), 2013.
- Arfin, N. and Bohidar, H.B. 2012. Concentration selective hydration and phase states of hydroxyethyl cellulose (HEC) in aqueous solutions. *International journal of biological macromolecules*. **50**(3): 759–767.
- Armentano, I., Dottori, M., Fortunati, E., Mattioli, S. and Kenny, J.M. 2010. Biodegradable polymer matrix nanocomposites for tissue engineering: A review. *Polymer Degradation and Stability*. **95**(11): 2126–2146.
- Arya, N., Sharma, P. and Katti, D.S. 2009. *Advanced Biomaterials: Fundamentals, Processing, and Applications*. New York: John Wiley and Sons. Inc.
- Asran, A.S., Henning, S. and Michler, G.H. 2010. Polyvinyl alcohol–collagen–hydroxyapatite biocomposite nanofibrous scaffold: Mimicking the key features of natural bone at the nanoscale level. *Polymer*. **51**(4): 868–876.
- Atala, A., Bauer, S.B., Soker, S., Yoo, J.J. and Retik, A.B. 2006. Tissue-engineered autologous bladders for patients needing cystoplasty. *Lancet*, **367**(9518):1241–1246.

- Barnes, C.P., Sell, S.A., Boland, E.D., Simpson, D.G. and Bowlin, G.L. 2007. Nanofiber technology: designing the next generation of tissue engineering scaffolds. *Advanced drug delivery reviews*. **59**(14): 1413–1433.
- Batchelor-McAuley, C., Martinez-Marrades, A., Tschulik, K., Patel, A.N., Combellas, C., Kanoufi, F., Tessier, G. and Compton, R.G. 2014. Simultaneous electrochemical and 3D optical imaging of silver nanoparticle oxidation. *Chemical Physics Letters*. **597**: 20–25.
- Beumer, G.J., Van Blitterswijk, C.A., Bakker, D. and Ponec, M. 1993. Cell-seeding and *in vitro* biocompatibility evaluation of polymeric matrices of PEO/PBT copolymers and PLLA. *Biomaterials*. **14**(8), 598–604.
- Beyler, C.L. and Hirschler, M.M. 2001. *Thermal Decomposition of Polymers: SPFE Handbook of Fire Protection Engineering*. 3rd ed. NFPA, Quincy, MA.
- Bhardwaj, N. and Kundu, S.C. 2011. Silk fibroin protein and chitosan polyelectrolyte complex porous scaffolds for tissue engineering applications. *Carbohydrate Polymers*. **85**(2): 325–333.
- Biswal, J., Misra, N., Borde, L.C. and Sabharwal, S. 2013. Synthesis of silver nanoparticles in methacrylic acid solution by gamma radiolysis and their application for estimation of dopamine at low concentrations. *Radiation Physics and Chemistry*. **83**: 67–73.
- Black, J. 1992. *Biological Performance of Materials: Fundamentals of Biocompatibility*. 2nd ed. CRC Press. New York: Marcel Dekker.
- BlueCross BlueShield Association. 2002. *Bioengineered tissue products for wound treatment and surgical interventions*. Policy number: 7.01.35, 2002
- Böttcher-Haberzeth, S., Biedermann, T. and Reichmann, E., 2010. Tissue engineering of skin. *Burns*. **36**(4): 450–60.
- Brinson, H.F. and Brinson, L.C. 2008. *Polymer engineering science and viscoelasticity*. Heidelberg: Springer-Verlag GmbH.
- Brown, I. A. 1972. Scanning electron microscopy of human dermal fibrous tissue. *Journal of anatomy*. **113**:159–168.
- Burgos, N., Martino, V.P. and Jiménez, A. 2013. Characterization and ageing study of poly(lactic acid) films plasticized with oligomeric lactic acid. *Polymer Degradation and Stability*. **98**: 651-658.

- Chan, B.P. and Leong, K.W. 2008. Scaffolding in tissue engineering: general approaches and tissue-specific considerations. *European spine journal*. **17**(4): 467–479.
- Chan, L.W., Hao, J.S. and Heng, P.W.S. 1999. Evaluation of permeability and mechanical properties of composite polyvinyl alcohol films. *Chemical and Pharmaceutical Bulletin*. **47**(10): 1412–1416.
- Chandrasekhar, K.B., Ramachandriah, M.H., Sudarshana, P.P. and Valiavalappil, S. 2012. *Formation of High Electrical Conductivity Polymer Composites with Multiple Fillers*. U.S. Patent No.13/398,300.
- Chang, M.C. and Tanaka, J. 2002. FT-IR study for hydroxyapatite/collagen nanocomposite cross-linked by glutaraldehyde. *Biomaterials*. **23**(24): 4811–4818.
- Chen, G., Ushida, T. and Tateishi, T. 2002. Scaffold Design for Tissue Engineering. *Macromolecular Bioscience*. **2**: 67–77.
- Chen, J., Han, C., Lin, X., Tang, Z. and Su, S. 2006. Effect of silver nanoparticle dressing on second degree burn wound. *Chinese journal of surgery*. **44**(1): 50–52.
- Chua, C. 2001. Review The Design of Scaffolds for Use in Tissue Engineering. Part I. Traditional Factors. *Tissue engineering*. **7**(6): 679–689.
- Cifra, P., Karasz, F.E. and MacKnight, W.J. 1992. Expansion of polymer coils in miscible polymer blends of asymmetric composition. *Macromolecules*. **25**(1):192–194.
- Costa-Júnior, E.S., Barbosa-Stancioli, E.F., Mansur, A. a. P., Vasconcelos, W.L. and Mansur, H.S. 2009. Preparation and characterization of chitosan/poly(vinyl alcohol) chemically crosslinked blends for biomedical applications. *Carbohydrate Polymers*. **76**(3): 472–481.
- Courtman, D.W., Errett, B.F. and Wilson, G.J. 2001. The role of cross-linking in modification of the immune response elicited against xenogenic vascular acellular matrices. *Journal of biomedical materials research*. **55**(4): 576–586.
- Cui, W., Zhu, X., Yang, Y., Li, X. and Jin, Y., 2009. Evaluation of electrospun fibrous scaffolds of poly(dl-lactide) and poly(ethylene glycol) for skin tissue engineering. *Materials Science and Engineering: C*. **29**(6): 1869–1876.
- Czaja, W., Krystynowicz, A., Bielecki, S. and Brown, R.M., 2006. Microbial cellulose-the natural power to heal wounds. *Biomaterials*. **27**(2): 145–151.

- Dai, N.-T., Williamson, M.R., Khammo, N., Adams, E.F. and Coombes, A.G.A. 2004. Composite cell support membranes based on collagen and polycaprolactone for tissue engineering of skin. *Biomaterials*. **25**(18): 4263–4271.
- Danielsen, C.C. 1984. Reconstituted collagen fibrils. Fibrillar and molecular stability of the collagen upon maturation *in vitro*. *The Biochemical journal*. **222**(3): 663–668.
- Davis, J.R. 2003. *Handbook of Materials for Medical Devices*. Netherlands: ASM Internationals.
- Deligkaris, K., Tadele, T.S., Olthuis, W. and van den Berg, A. 2010. Hydrogel-based devices for biomedical applications. *Sensors and Actuators B: Chemical*, **147**(2): 765–774.
- Deluzio, T.G., Seifu, D.G. and Mequanint, K. 2013. 3D scaffolds in tissue engineering and regenerative medicine: beyond structural templates?. *Pharmaceutical Bioprocessing*. **1**(3): 267–281.
- Ding, C.-M., Zhou, Y., He, Y.-N. and Tan, W.-S. 2008. Perfusion seeding of collagen–chitosan sponges for dermal tissue engineering. *Process Biochemistry*. **43**(3): 287–296.
- Dong, T.-Y., Chen, W.-T., Wang, C.-W., Chen, C.-P., Chen, C.-N., Lin, M.-C., Song, J.-M., Chen, I.-G. and Kao, T.-H. 2009. One-step synthesis of uniform silver nanoparticles capped by saturated decanoate: direct spray printing ink to form metallic silver films. *Physical chemistry chemical physics*. **11**(29): 6269–6275.
- Dong Y.X , Yong T, Liao S, Chan CK, Ramakrishna, S. 2010. Distinctive degradation behaviours of electrospun PGA, PLGA and P(LLA-CL) nanofibers cultured with/without cell culture. *Tissue Engineering: Part A*. **16**(1): 283-298.
- Ducheyne, P., Hench, L.L., Kagan, A., Martens, M., Bursens, A. and Mulier, J.C. 1980. Effect of hydroxyapatite impregnation on skeletal bonding of porous coated implants. *Journal of biomedical materials research*. **14**(3): 225–237.
- Dugan, J.M., Gough, J.E. and Eichhorn, S.J. 2013. Bacterial cellulose scaffolds and cellulose nanowhiskers for tissue engineering. *Nanomedicine*. **8**(2): 287–98.
- Edwards, C. and Marks, R. 1995. Evaluation of biomechanical properties of human skin. *Clinics in dermatology*. **13**(4): 375–380.
- Eglin, D., Mortisen, D. and Alini, M. 2009. Degradation of synthetic polymeric scaffolds for bone and cartilage tissue repairs. *Soft Matter*. **5**(5): 938-947.

- Eisenbud, D., Huang, N.F., Luke, S. and Silberklang, M. 2004. Skin Substitutes and Wound Healing: Current Status and Challenges. *Wound*. (online). <http://www.medscape.com/viewarticle/470251>.
- Elashmawi, I.S. and Abdel Baieth, H.E. 2012. Spectroscopic studies of hydroxyapatite in PVP/PVA polymeric matrix as biomaterial. *Current Applied Physics*. **12**(1): 141–146.
- Elechiguerra, J.L., Larios-Lopez, L., Liu, C., Garcia-Gutierrez, D., Camacho-Bragado, A. and Yacaman, M.J. 2005. Corrosion at the Nanoscale: The Case of Silver Nanowires and Nanoparticles. *Chemistry of Materials*. **17**(24): 6042–6052.
- El-Ghalbzouri, A., Lamme, E.N., van Blitterswijk, C., Koopman, J. and Ponec, M. 2004. The use of PEGT/PBT as a dermal scaffold for skin tissue engineering. *Biomaterials*. **25**(15): 2987–2996.
- El-Ghalbzouri, A., Commandeur, S., Rietveld, M.H., Mulder, A.A. and Willemze, R. 2009. Replacement of animal-derived collagen matrix by human fibroblast-derived dermal matrix for human skin equivalent products. *Biomaterials*. **30**(1): 71–78.
- El-Sayed, S., Mahmoud, K.H., Fatah, A.A. and Hassen, A. 2011. DSC, TGA and dielectric properties of carboxymethyl cellulose/polyvinyl alcohol blends. *Physica B: Condensed Matter*. **406**(21): 4068–4076.
- El-Zaher, N.A. and Osiris, W.G. 2005. Thermal and structural properties of poly(vinyl alcohol) doped with hydroxypropyl cellulose. *Journal of Applied Polymer Science*. **96**(5): 1914–1923.
- Erkselius, S. and Karlsson, O. 2005. Free radical degradation of hydroxyethyl cellulose. *Carbohydrate Polymers*. **62**(4): 344–356.
- Erol, M.M., Mouriño, V., Newby, P., Chatzistavrou, X., Roether, J.A., Hupa, L., and Boccaccini, A.R. 2012. Copper-releasing, boron-containing bioactive glass-based scaffolds coated with alginate for bone tissue engineering. *Acta biomaterialia*. **8**(2): 792–801.
- Espinosa-Cristóbal, L.F., Martínez-Castañón, G.A., Téllez-Déctor, E.J., Niño-Martínez, N., Zavala-Alonso, N.V. and Loyola-Rodríguez, J.P. 2013. Adherence inhibition of *Streptococcus mutans* on dental enamel surface using silver nanoparticles. *Materials science & engineering C*. **33**(4): 2197–2202.
- Faghihi, K. and Shabanian, M. 2011. Thermal and optical properties of silver-polyimide nanocomposite based on diphenyl sulfone moieties in the main chain. *Journal of the Chilean Chemical Society*. **2**: 665–667.

- Fang, Z., Fu, W., Dong, Z., Zhang, X., Gao, B., Guo, D., He, H. and Wang, Y. 2011. Preparation and biocompatibility of electrospun poly(l-lactide-co-ε-caprolactone)/fibrinogen blended nanofibrous scaffolds. *Applied Surface Science*. **257**(9): 4133–4138.
- Ferreri, I., Lopes, V., Calderon V, S., Tavares, C.J., Cavaleiro, A. and Carvalho, S. 2014. Study of the effect of the silver content on the structural and mechanical behaviour of Ag-ZrCN coatings for orthopedic prostheses. *Materials Science and Engineering: C*. **42**: 782–790.
- Fischer, B.E.W., Sterzel, H.J. and Wegner, G. 1973. Investigation of the structure of solution grown crystals of lactide copolymers. *Polymer*. **990**: 980–990.
- Fortunati, E., Latterini, L., Rinaldi, S., Kenny, J.M. and Armentano, I. 2011. PLGA/Ag nanocomposites: *in vitro* degradation study and silver ion release. *Journal of materials science: Materials in medicine*. **22**(12): 2735–2744.
- Frantz, C., Stewart, K.M. and Weaver, V.M. 2010. The extracellular matrix at a glance. *Journal of cell science*. **123**: 4195–4200.
- Freier, T., Kunze, C., Nischan, C., Kramer, S., Sternberg, K., Sass, M., Hopt, U.T. and Schmitz, K.-P. 2002. *In vitro* and *in vivo* degradation studies for development of a biodegradable patch based on poly(3-hydroxybutyrate). *Biomaterials*. **23**(13): 2649–2657.
- Freinkel, R.K. and Woodley, D.T. 2001. *The Biology of the Skin*. 3rd ed. CRC Press. New York: Marcel Dekker.
- Frydrych, M. and Chen, B. 2013. Large three-dimensional poly(glycerol sebacate)-based scaffolds – a freeze-drying preparation approach. *Journal of Materials Chemistry B*. **1**(48): 6650–6661.
- García-Vargas, M., González-Chomón, C., Magariños, B., Concheiro, A., Alvarez-Lorenzo, C. and Bucio, E. 2014. Acrylic polymer-grafted polypropylene sutures for covalent immobilization or reversible adsorption of vancomycin. *International journal of pharmaceutics*. **461**: 286–295.
- Gattazzo, F., Urciuolo, A. and Bonaldo, P. 2014. Extracellular matrix: A dynamic microenvironment for stem cell niche. *Biochimica et Biophysica Acta*. **1840**(8): 2506–2519.
- Gautam, K.S. and Ashok, K.G. 2013. Miscibility Studies of PVC / PMMA Blends in Tetrahydrofuran by Viscosity, Density, refractive Index and Ultrasonic. *Nanosystems: Physics, Chemistry, Mathematics*. **4**(2): 288–293.

- Gautam, S., Chou, C., Dinda, A.K., Potdar, P.D. and Mishra, N.C. 2014. Surface modification of nanofibrous polycaprolactone/gelatin composite scaffold by collagen type I grafting for skin tissue engineering. *Materials Science and Engineering: C*. **34**: 402-409.
- Georgieva, N., Bryaskova, R. and Tzoneva, R. 2012. New Polyvinyl alcohol-based hybrid materials for biomedical application. *Materials Letters*. **88**: 19–22.
- Ghasemi-Mobarakeh, L., Prabhakaran, M.P., Morshed, M., Nasr-Esfahani, M.H. and Ramakrishna, S. 2010. Bio-functionalized PCL nanofibrous scaffolds for nerve tissue engineering. *Materials Science and Engineering: C*. **30**(8): 1129–1136.
- Goissis, G., Marcantonio, E., Marcantônio, R.A., Lia, R.C., Cancian, D.C. and de Carvalho, W.M. 1999. Biocompatibility studies of anionic collagen membranes with different degree of glutaraldehyde cross-linking. *Biomaterials*. **20**(1): 27–34.
- Goonoo, N., Bhaw-Luximon, A., Rodriguez, I.A., Wesner, D., Schönherr, H., Bowlin, G.L. and Jhurry, D. 2014. Poly(ester-ether)s: II. Properties of electrospun nanofibres from polydioxanone and poly(methyl dioxanone) blends and human fibroblast cellular proliferation. *Biomaterials Science*. **2**(3): 339-351.
- Göpferich, A. 1996. Mechanisms of polymer degradation and erosion. *Biomaterials*. **17**(2): 103–14.
- Gorgieva, S. and Kokol, V. 2011. Synthesis and application of new temperature-responsive hydrogels based on carboxymethyl and hydroxyethyl cellulose derivatives for the functional finishing of cotton knitwear. *Carbohydrate Polymers*. **85**(3): 664–673.
- Greve, D.R. and Richards, T.W., 1979. *Fire Door Core*. U.S. Patent No: 868,437.
- Groeber, F., Holeiter, M., Hampel, M., Hinderer, S. and Schenke-Layland, K. 2011. Skin tissue engineering--*in vivo* and *in vitro* applications. *Advanced drug delivery reviews*. **63**: 352–366.
- Guirguis, O.W. and Moselhey, M.T.H. 2012. Thermal and structural studies of poly(vinyl alcohol) and hydroxypropyl cellulose blends. *Natural Sciences*. **4**(1): 57–67.
- Gunasekaran, T., Nigusse, T. and Dhanaraju, M.D. 2011. Silver nanoparticles as real topical bullets for wound healing. *The journal of the American College of Clinical Wound Specialists*. **3**(4): 82–96.
- Habermehl, J., Skopinska, J., Boccafoschi, F., Sionkowska, A., Kaczmarek, H., Laroche, G. and Mantovani, D. 2005. Preparation of ready-to-use, stockable and reconstituted collagen. *Macromolecular bioscience*. **5**(9): 821–828.

- Habibovic, P., Barrère, F., Blitterswijk, C.A., Groot, K. and Layrolle, P. 2004. Biomimetic Hydroxyapatite Coating on Metal Implants. *Journal of the American Ceramic Society*. **85**(3): 517–522.
- Halim, A.S., Khoo, T.L. and Mohd Yussof, S.J. 2010. Biologic and synthetic skin substitutes: An overview. *Indian journal of plastic surgery*. **43**(Suppl): 23–28.
- Harding, K., Kirsner, R., Lee, D., Mulder, G. and Serena, T. 2010. *International Consensus. Acellular matrices for the treatment of wounds*. London: Wounds International.
- He, L., Liao, S., Quan, D., Ma, K., Chan, C., Ramakrishna, S. and Lu, J. 2010. Synergistic effects of electrospun PLLA fiber dimension and pattern on neonatal mouse cerebellum C17.2 stem cells. *Acta biomaterialia*. **6**(8): 2960–2969.
- He, W., Ma, Z., Yong, T., Teo, W.E. and Ramakrishna, S. 2005. Fabrication of collagen-coated biodegradable polymer nanofiber mesh and its potential for endothelial cells growth. *Biomaterials*. **26**(36): 7606–7615.
- He, Y., Zhu, B. and Inoue, Y. 2004. Hydrogen bonds in polymer blends. *Progress in Polymer Science*. **29**(10): 1021–1051.
- Hermansson, L. 2014. *Nanostructural Bioceramics: Advances in Chemically Bonded Ceramics*. 1st edition. Singapore, Pan Stanford Publishing, Pte. Ltd.
- Hermawan, H., Ramdan, D. and Djuansjah, J.R.P. 2011. *Biomedical Engineering - From Theory to Applications*. Europe: InTech.
- Herndon, D.N., Barrow, R.E., Rutan, R.L., Rutan, T.C., Desai, M.H. and Abston, S. 1989. A comparison of conservative versus early excision. Therapies in severely burned patients. *Annals of surgery*. **209**(5): 547–552.
- Holland, B.J. and Hay, J.N. 2001. The thermal degradation of poly(vinyl alcohol). *Polymer*. **42**(16): 6775–6783.
- Horch, R.E., Jeschke, M.G., Spilker, G., Herndon, D.N. and Kopp, J. 2005. Treatment of second degree facial burns with allografts-preliminary results. *Burns*. **31**(5): 597–602.
- Huang, H.H., Ni, X.P., Loy, G.L., Chew, C.H., Tan, K.L., Loh, F.C., Deng, J.F. and Xu, G.Q. 1996. Photochemical formation of silver nanoparticles in poly (N-vinylpyrrolidone). **12**:909–912.
- Huang, Z.-M., Zhang, Y.-Z., Kotaki, M. and Ramakrishna, S. 2003. A review on polymer nanofibers by electrospinning and their applications in nanocomposites. *Composites Science and Technology*. **63**(15): 2223–2253.

- Hutmacher, D.W. 2000. Scaffolds in tissue engineering bone and cartilage. *Biomaterials*, **21**(24): 2529–43.
- Jana, N.R., Sau, T.K. and Pal, T. 1999. Growing Small Silver Particle as Redox Catalyst. *The Journal of Physical Chemistry B*. **103**(1): 115–121.
- Jiang, E.Y. and Rieppo, J. 2006. Enhancing FTIR imaging capabilities with two-dimensional correlation spectroscopy (2DCOS): A study of concentration gradients of collagen and proteoglycans in human patellar cartilage. *Journal of Molecular Structure*. **799**: 196–203.
- Jin, G., Prabhakaran, M.P. and Ramakrishna, S. 2011. Stem cell differentiation to epidermal lineages on electrospun nanofibrous substrates for skin tissue engineering. *Acta biomaterialia*. **7**(8): 3113–3122.
- Joyce, C.W., Joyce, K.M., Mahon, N., Chan, J.C., Sugrue, C.M., Dockery, P., Carroll, S.M. and Kelly, J.L. 2014. A novel barbed suture tie-over dressing for skin grafts: A comparison with traditional techniques. *Journal of plastic, reconstructive & aesthetic surgery*. **67**(9):1237-1241.
- Judith, R., Nithya, M., Rose, C. and Mandal, A.B. 2012. Biopolymer gel matrix as acellular scaffold for enhanced dermal tissue regeneration. *Biologicals: journal of the International Association of Biological Standardization*. **40**(4): 231–239.
- Kamide, K., 2005. *Cellulose and Cellulose Derivatives*. The Netherlands: Elsevier B.V.
- Karp, J.M., Dalton, P.D., Shoichet, M.S. and Cahn, F. 2003. Scaffolds for Tissue Engineering Clinical Use of Porous. *MRS Bulletin*. April: 301–306.
- Kelly, K.L., Coronado, E., Zhao, L.L. and Schatz, G.C. 2003. The optical properties of metal nanoparticles: The influence of size, shape, and dielectric environment. *The Journal of Physical Chemistry B*. **107**(3): 668–677.
- Kfistner, U., Hoffmann, H., Dnges, R. and Ehrler, R. 1996. Interactions between modified hydroxyethyl cellulose (HEC) and surfactants. *Colloids and Surfaces A*. **112**: 209–225.
- Khor, E, 1997. Methods for the treatment of collagenous tissues for bioprotheses. *Biomaterials*. **18**(2): 95–105.
- Ko, C.-L., Tien, Y.-C., Wang, J.-C. and Chen, W.-C. 2012. Characterization of controlled highly porous hyaluronan/gelatin cross-linking sponges for tissue engineering. *Journal of the mechanical behaviour of biomedical materials*. **14**: 227–38.

- Kopeliovich, D. 2012. Subs Tech: Scanning Electron Microscope. (online) http://www.substech.com/dokuwiki/doku.php?id=scanning_electron_microscope (31 May 2012)
- Kühn, K. 1987. *Structure and Function of Collagen Types*. University of Michigan: Academic Press.
- Kumar, A., Negi, Y.S., Bhardwaj, N.K. and Choudhary, V. 2012. Synthesis and characterization of methylcellulose/PVA based porous composite. *Carbohydrate Polymers*. **88**(4): 1364–1372.
- Kumbar, S.G., Nukavarapu, S.P., James, R., Nair, L.S. and Laurencin, C.T. 2008. Electrospun poly(lactic acid-co-glycolic acid) scaffolds for skin tissue engineering. *Biomaterials*. **29**(30): 4100–4107.
- Kwak, W.-G., Oh, M.-H. and Gong, M.-S. 2014. Preparation of silver-coated cotton fabrics using silver carbamate *via* thermal reduction and their properties. *Carbohydrate Polymers*. **115**: 317-324.
- Lahann, J., Klee, D., Thelen, H., Bienert, H., Vorwerk, D. and Höcker, H. 1999. Improvement of haemocompatibility of metallic stents by polymer coating. *Journal of materials science*. **10**(7): 443–448.
- Lambotte, A. 1909. Technique et indication des prothèses dans le traitement des fractures. *Press Med*. **17**: 321-326.
- Lane, W.A. 1895. Some Remarks on the Treatment of Fractures. *British medical journal*. **1**(1790): 861–863.
- Larese, F.F., D'Agostin, F., Crosera, M., Adami, G., Renzi, N., Bovenzi, M. and Maina, G. 2009. Human skin penetration of silver nanoparticles through intact and damaged skin. *Toxicology*. **255**: 33–37.
- Lee, K.Y., Jeong, L., Kang, Y.O., Lee, S.J. and Park, W.H. 2009. Electrospinning of polysaccharides for regenerative medicine. *Advanced Drug Delivery Reviews*. **61**(12): 1020–1032.
- Leukers, B., Gülkan, H., Irsen, S.H., Milz, S., Tille, C., Schieker, M. and Seitz, H. 2005. Hydroxyapatite scaffolds for bone tissue engineering made by 3D printing. *Journal of materials science: Materials in medicine*. **16**(12): 1121–1124.
- Li, F., Zhao, Y. and Song, Y. 2010. *Nanofibers*. Europe: InTechOpen.

- Li, W.-J., Laurencin, C.T., Caterson, E.J., Tuan, R.S. and Ko, F.K. 2002. Electrospun nanofibrous structure: a novel scaffold for tissue engineering. *Journal of biomedical materials research*. **60**(4): .613–621.
- Liao, H., Qi, R., Shen, M., Cao, X., Guo, R., Zhang, Y. and Shi, X. 2011. Improved cellular response on multiwalled carbon nanotube-incorporated electrospun polyvinyl alcohol/chitosan nanofibrous scaffolds. *Colloids and Surfaces B: Biointerfaces*. **84**(2): 528–535.
- Liedermann, K. and Lapc, L. 2000. Dielectric relaxation in hydroxyethyl cellulose. **42**: 369–374.
- Life Technologies, DMEM, high glucose, pyruvate (online). <https://www.lifetechnologies.com/order/catalog/product/11995065> (3 November 2014).
- Van der Linden, H.J., Herber, S., Olthuis, W. and Bergveld, P. 2003. Stimulus-sensitive hydrogels and their applications in chemical (micro)analysis. *The Analyst*. **128**(4): 325–331.
- Liu, H., Li, X., Zhou, G., Fan, H. and Fan, Y. 2011. Electrospun sulfated silk fibroin nanofibrous scaffolds for vascular tissue engineering. *Biomaterials*. **32**(15), 3784–3793.
- Liu, S.Q., 2007. *Bioregenerative Engineering: Principles and Applications*. John Wiley & Sons.Inc.
- Liu, X., Smith, L. a, Hu, J. and Ma, P.X. 2009. Biomimetic nanofibrous gelatin/apatite composite scaffolds for bone tissue engineering. *Biomaterials*. **30**(12): 252–258.
- Liu, Y., Jiang, H., Li, Y. and Zhu, K. 2008. Control of dimensional stability and degradation rate in elctrospun composite scaffolds composed of poly (D,L-lactide-co-glycolide) and poly (ϵ -caprolactone). *Chinese Journal of Polymer Science*. **26**(1): 63-71.
- Liu, Y., Ma, L. and Gao, C. 2012. Facile fabrication of the glutaraldehyde cross-linked collagen/chitosan porous scaffold for skin tissue engineering. *Materials Science and Engineering: C*. **32**(8): 2361–2366.
- Liu, Y., Zheng, Z., Zara, J.N., Hsu, C., Soofer, D.E., Lee, K.S., Siu, R.K., Miller, L.S., Zhang, X., Carpenter, D., Wang, C. and Ting, K. 2012. The antimicrobial and osteoinductive properties of silver nanoparticle/poly(DL-lactic-co-glycolic acid)-coated stainless steel. *Biomaterials*. **33**: 8745-8756.

- Lu, T., Li, Y. and Chen, T. 2013. Techniques for fabrication and construction of three-dimensional scaffolds for tissue engineering. *International journal of nanomedicine*. 8: 337–350.
- Lv, Y., Liu, H., Wang, Z., Liu, S., Hao, L., Sang, Y., Liu, D., Wang, J. and Boughton, R.I. 2009. Silver nanoparticle-decorated porous ceramic composite for water treatment. *Journal of Membrane Science*. **331**: 50–56.
- Ma, L. 2003. Collagen/chitosan porous scaffolds with improved biostability for skin tissue engineering. *Biomaterials*. **24**(26): 4833–4841.
- Ma, P.X., 2008. Biomimetic materials for tissue engineering. *Advanced drug delivery reviews*. **60**(2): 184–198.
- Maceo, A.V. 2011. *Fingerprint Sourcebook :Chapter 2- Anatomy and physiology of adult friction ridge skin*. National Criminal Justice Reference Service, USA.
- MacNeal, R.J. 2014. *MerckManuals: Structure and features of the skin*. Home Health Handbook. New Jersey, USA.
- Macneil, S. 2008. Biomaterials for tissue engineering of skin. *Materials Today*. **11**(5): 26–35.
- Magrez, A., Kasas, S., Salicio, V., Pasquier, N., Seo, J.W., Celio, M., Catsicas, S., Schwaller, B. and Forró, L. 2006. Cellular toxicity of carbon-based nanomaterials. *Nano letters*. **6**(6): 1121–1125.
- Majeed Khan, M.A., Kumar, S., Ahamed, M., Alrokayan, S.A. and Alsalhi, M.S. 2011. Structural and thermal studies of silver nanoparticles and electrical transport study of their thin films. *Nanoscale research letters*. **6**(434): 1-8.
- Malafaya, P.B., Silva, G. a and Reis, R.L. 2007. Natural-origin polymers as carriers and scaffolds for biomolecules and cell delivery in tissue engineering applications. *Advanced drug delivery reviews*. **59**: 207–233.
- Mani, U., Dhanasingh, S., Arunachalam, R., Paul, E., Shanmugam, P., Rose, C. and Mandal, A.B. 2013. A simple and green method for the synthesis of silver nanoparticles using ricinus communis leaf extract. **2**: 221–225.
- Mansur, H.S. and Mansur, A.A.P. 2007. Synchrotron SAXS, XRD and FTIR characterization of nanostructured PVA/TEOS hybrid cross-linked with glutaraldehyde. *Solid State Phenomena*. **121**: 855–858.

- Mansur, H.S., Oréfice, R.L. and Mansur, A.A.P. 2004. Characterization of poly(vinyl alcohol)/poly(ethylene glycol) hydrogels and PVA-derived hybrids by small-angle X-ray scattering and FTIR spectroscopy. *Polymer*. **45**(21): 7193–7202.
- Marsich, E., Bellomo, F., Turco, G., Travan, A., Donati, I. and Paoletti, S. 2013. Nanocomposite scaffolds for bone tissue engineering containing silver nanoparticles: preparation, characterization and biological properties. *Journal of materials science. Materials in medicine*. **24**(7): 1799–1807.
- Mathew, T. V and Kuriakose, S. 2013. Photochemical and antimicrobial properties of silver nanoparticle-encapsulated chitosan functionalized with photoactive groups. *Materials science & engineering C*. **33**(7): 4409–4415.
- Matthews, J.A., Wnek, G.E., Simpson, D.G. and Bowlin, G.L. 2002. Electrospinning of collagen nanofibers. *Biomacromolecules*. **3**(2): 232–238.
- Medtech Insight, Tissue Engineering and Cell Transplantation: U.S. Markets for Skin Replacements and Substitutes (online). <http://www.medtechinsight.com/ReportA426.html> (13 Mei 2014).
- Mei, L., Hu, D., Ma, J., Wang, X., Yang, Y. and Liu, J. 2012. Preparation, characterization and evaluation of chitosan macroporous for potential application in skin tissue engineering. *International journal of biological macromolecules*. **51**(5): 992–997.
- Meryman, H.T. 1976. Historical recollections of freeze-drying. *Developments in biological standardization*: **36**: 29–32.
- Metcalf, A.D. and Ferguson, M.W.J. 2007. Tissue engineering of replacement skin: the crossroads of biomaterials, wound healing, embryonic development, stem cells and regeneration. *Journal of the Royal Society Interface*. **4**(14): 413–437.
- Meyers, M.A., Chen, P.-Y., Lin, A.Y.-M. and Seki, Y. 2008. Biological materials: Structure and mechanical properties. *Progress in Materials Science*. **53**(1): 1–206.
- Miles, C. a, Avery, N.C., Rodin, V. V and Bailey, A.J. 2005. The increase in denaturation temperature following cross-linking of collagen is caused by dehydration of the fibres. *Journal of molecular biology*. **346**(2): 551–556.
- Millington, P.F. and Wilkinson, R. 2009. *Skin*. New York: Cambridge University Press.
- Mohiti-Asli, M., Pourdeyhimi, B. and Lobo, E.G. 2014. Novel, silver-ion-releasing nanofibrous scaffolds exhibit excellent antibacterial efficacy without the use of silver nanoparticles. *Acta biomaterialia*. **10**(5): 2096–104.

- Molladavoodi, S., Gorbet, M., Medley, J. and Kwon, H.J. 2013. Investigation of microstructure, mechanical properties and cellular viability of poly(L-lactic acid) tissue engineering scaffolds prepared by different thermally induced phase separation protocols. *Journal of the mechanical behaviour of biomedical materials*. **17**:186–197.
- Mukherjee, M. and Mahapatra, A. 2009. Catalytic effect of silver nanoparticle on electron transfer reaction: Reduction of $[\text{Co}(\text{NH}_3)_5\text{Cl}](\text{NO}_3)_2$ by iron(II). *Colloids and Surfaces A: Physicochemical and Engineering Aspects*. **350**(1-3): 1–7.
- Mukherjee, S.G., O’Claonadh, N., Casey, A. and Chambers, G. 2012. Comparative *in vitro* cytotoxicity study of silver nanoparticle on two mammalian cell lines. *Toxicology*. **26**(2): 238–51.
- Murasawa, N., Koseki, H., Li, X.-R., Iwata, Y. and Sakamoto, T. 2012. Study on Thermal Behaviour and Risk Assessment of Biomass Fuels. *International Journal of Energy Engineering*. **2**(5): 242–252.
- Naseri, N., Algan, C., Jacobs, V., John, M., Oksman, K. and Mathew, A.P. 2014. Electrospun chitosan-based nanocomposite mats reinforced with chitin nanocrystals for wound dressing. *Carbohydrate polymers*. **109**: 7–15.
- Ninan, N., Muthiah, M., Park, I.-K., Elain, A., Thomas, S. and Grohens, Y. 2013. Pectin/carboxymethyl cellulose/microfibrillated cellulose composite scaffolds for tissue engineering. *Carbohydrate polymers*. **98**(1): 877-885.
- Ning, C.C., Logsetty, S., Ghughare, S. and Liu, S. 2014. Effect of hydrogel grafting, water and surfactant wetting on the adherence of PET wound dressings. *Burns*. **40**(6):1164-1171.
- Nishida, N., Hara, M., Sasabe, H. and Knoll, W. 1996. Thermal desorption spectroscopy of alkanethiol self-assembled monolayer on Au (111). *Japanese Journal of Applied Physics Part I*. **35**(11): 5866-5872.
- Nishida, N., Hara, M., Sasabe, H. and Knoll, W., 1997. Formation and exchange processes of alkanethiol self-assembled monolayer on studied by thermal desorption spectroscopy and scanning tunneling microscopy Au (111). *Japanese Journal of Applied Physics, Part I*. **36**(4A): 2379-2385.
- O’Brien, F.J. 2011. Biomaterials & scaffolds for tissue engineering. *Materials Today*. **14**(3): 88-95.
- O’Brien, F.J., Harley, B. a, Yannas, I. V and Gibson, L.J. 2005. The effect of pore size on cell adhesion in collagen-GAG scaffolds. *Biomaterials*. **26**(4): 433-41.

- Osborne, C.S., Reid, W.H. and Grant, M.H. 1999. Investigation into the biological stability of collagen/chondroitin-6-sulphate gels and their contraction by fibroblasts and keratinocytes: the effect of cross-linking agents and diamines. *Biomaterials*. **20**(3): 28-290.
- Panzavolta, S., Gioffrè, M., Focarete, M.L., Gualandi, C., Foroni, L. and Bigi, A. 2011. Electrospun gelatin nanofibers: optimization of genipin cross-linking to preserve fiber morphology after exposure to water. *Acta biomaterialia*. **7**(4): 1702–1709.
- Park, J.B. and Bronzino, J.D. 2003. *Biomaterials: Principles and Applications*. CRC Press. New York: Marcel Dekker.
- Parvin, F., Rahman, M.A., Islam, J.M.M., Khan, M.A. and Saadat, A.H.M. 2010. Preparation and characterization of starch/PVA blend for biodegradable packaging material. *Advanced Materials Research*. **123-125**: 351–354.
- Paul, R.G. and Bailey, A.J. 2003. Chemical stabilisation of collagen as a biomimetic. *TheScientificWorldJournal*. **3**: 138–55.
- Paur, H.-R., Cassee, F.R., Teeguarden, J., Fissan, H., Diabate, S., Aufderheide, M., Kreyling, W.G., Hänninen, O., Kasper, G., Riediker, M., Rothen-Rutishauser, B. and Schmid, O. 2011. In-vitro cell exposure studies for the assessment of nanoparticle toxicity in the lung - A dialog between aerosol science and biology. *Journal of Aerosol Science*. **42**(10): 668–692.
- Pawar, S. V and Yadav, G.D. 2014. PV /chitosan-glutaraldehyde cross-linked nitrile hydratase as reusable biocatalyst for conversion of nitriles to amides. *Journal of Molecular Catalysis B: Enzymatic*. **101**: 115–121.
- Payne, K.J. and Veis, A. 1988. Fourier transform IR spectroscopy of collagen and gelatin solutions: deconvolution of the amide I band for conformational studies. *Biopolymers*, **27**(11): 1749–60.
- Peña, J., Corrales, T., Izquierdo-Barba, I., Doadrio, A.L. and Vallet-Regí, M., 2006. Long term degradation of poly(ϵ -caprolactone) films in biologically related fluids. *Polymer Degradation and Stability*. **91**(7): 1424-1432.
- Peppas, N.A. and Merrill, E.W, 1976. Differential scanning calorimetry of crystallized PVA hydrogels. *Journal of Applied Polymer Science*. **20**(6): 1457–1465.
- Peppas, N.A. and Merrill, E.W. 1977. Development of semicrystalline poly(vinyl alcohol) hydrogels for biomedical applications. *Journal of Biomedical Materials Research*, **11**(3): 423–434.

- Pereira, R.F. and Bártolo, P.J. 2013. Degradation Behaviour of Biopolymer-based Membranes for Skin Tissue Regeneration. *Procedia Engineering*. **59**: 285–291.
- Peresin, M.S., Habibi, Y., Zoppe, J.O., Pawlak, J.J. and Rojas, O.J. 2010. Nanofiber composites of polyvinyl alcohol and cellulose nanocrystals: manufacture and characterization. *Biomacromolecules*. **11**(3): 674–681.
- PerkinElmer, 2005. *FT-IR Spectroscopy-Attenuated Total Reflectance(ATR)*. USA: PerkinElmer.
- Petsko, G.A. and Ringe, D. 2004. *Protein Structure and Function*. London: NewScience Press and Sinauer Associates and Blackwell Science.
- Pham, Q.P., Sharma, U. and Mikos, A.G. 2006. Electrospinning of polymeric nanofibers for tissue engineering applications: a review. *Tissue engineering*. **12**(5): 1197–1211.
- Pielesz, A. 2014. Temperature-dependent FTIR spectra of collagen and protective effect of partially hydrolysed fucoidan. *Spectrochimica Acta Part A: Molecular and Biomolecular Spectroscopy*. **118**: 287–293.
- Pinto, R.J.B., Marques, P.A.A.P., Neto, C.P., Trindade, T., Daina, S. and Sadocco, P. 2009. Antibacterial activity of nanocomposites of silver and bacterial or vegetable cellulosic fibers. *Acta biomaterialia*. **5**(6): 2279–2289.
- Prabhakar, P.K., Raj, S., Anuradha, P.R., Sawant, S.N. and Doble, M. 2011. Biocompatibility studies on polyaniline and polyaniline-silver nanoparticle coated polyurethane composite. *Colloids and surfaces B:Biointerfaces*. **86**(1): 146–153.
- Prabhakaran, M.P. 2012. *Biomedical Applications of Polymeric Nanofibers*. New York: Springer Science & Business Media.
- Rai, M., Yadav, A. and Gade, A. 2009. Silver nanoparticles as a new generation of antimicrobials. *Biotechnology advances*. **27**(1): 76–83.
- Ramakrishna, S. 2011. *Biomaterials: A Nano Approach*. New York: CRC Press.
- Ramshaw, J.A., 1986. Distribution of type III collagen in bovine skin of various ages. *Connective tissue research*, **14**(4), pp.307–14.
- Ratanavaraporn, J., Rangkupan, R., Jeeratawatchai, H., Kanokpanont, S. and Damrongsakkul, S. 2010. Influences of physical and chemical cross-linking techniques on electrospun type A and B gelatin fiber mats. *International journal of biological macromolecules*, **47**(4): 431–438.

- Raveendran, P., Fu, J. and Wallen, S.L. 2003. Completely “green” synthesis and stabilization of metal nanoparticles. *Journal of the American Chemical Society*. **125**(46):13940–13941.
- Reis, E.F. dos, Campos, F.S., Lage, A.P., Leite, R.C., Heneine, L.G., Vasconcelos, W.L., Lobato, Z.I.P. and Mansur, H.S. 2006. Synthesis and characterization of poly(vinyl alcohol) hydrogels and hybrids for rMPB70 protein adsorption. *Materials Research*. **9**(2): 185–191.
- Reneker, D.H. and Chun, I. 1996. Nanometre diameter fibres of polymer, produced by electrospinning. *Nanotechnology*. **7**(3): 216–223.
- Roohani, M., Habibi, Y., Belgacem, N.M., Ebrahim, G., Karimi, A.N. and Dufresne, A. 2008. Cellulose whiskers reinforced polyvinyl alcohol copolymers nanocomposites. *European Polymer Journal*. **44**(8): 2489–2498.
- Roohani-Esfahani, S.I. and Hala Zreiqat, H., 2012. *Integrated Biomaterials in Tissue Engineering*. Scriviner Publishing LLC.
- Sachlos, E. and Czernuszka, J.T. 2003. Making tissue engineering scaffolds work. Review: the application of solid freeform fabrication technology to the production of tissue engineering scaffolds. *European cells & materials*. **5**: 29–39.
- Sahoo, S., Ang, L.T., Cho-Hong Goh, J. and Toh, S.L., 2010. Bioactive nanofibers for fibroblastic differentiation of mesenchymal precursor cells for ligament/tendon tissue engineering applications. *Differentiation: research in biological diversity*. **79**(2), 102–110.
- Salaam, L.E., Dean, D. and Bray, T.L. 2006. *In vitro* degradation behaviour of biodegradable 4-star micelles. *Polymer*. **47**(1): 310–318.
- Salmoria, G. V., Klauss, P., Paggi, R. a., Kanis, L. a. and Lago, A. 2009. Structure and mechanical properties of cellulose based scaffolds fabricated by selective laser sintering. *Polymer Testing*. **28**(6): 648–652.
- Sangur, R. 2010. Tissue engineering: An Update. *Smile Dental Journal*. **5**(3): 1–6.
- Sankar, D., Chennazhi, K.P., Nair, S. V and Jayakumar, R. 2012. Fabrication of chitin/poly(3-hydroxybutyrate-co-3-hydroxyvalerate) hydrogel scaffold. *Carbohydrate polymers*. **90**(1): 725-729.
- Sannino, A., Esposito, A., De Rosa, A., Cozzolino, A., Ambrosio, L. and Nicolais, L. 2003. Biomedical application of a superabsorbent hydrogel for body water elimination in the

- treatment of edemas. *Journal of biomedical materials research Part A*. **67**(3), 1016–1024.
- Sanpui, P., Murugadoss, A., Prasad, P.V.D., Ghosh, S.S. and Chattopadhyay, A. 2008. The antibacterial properties of a novel chitosan-Ag-nanoparticle composite. *International journal of food microbiology*. **124**(2):142-146.
- Santos, C.F.L., Silva, A.P., Lopes, L., Pires, I. and Correia, I.J. 2012. Design and production of sintered β -tricalcium phosphate 3D scaffolds for bone tissue regeneration. *Materials Science and Engineering: C*. **32**(5): 1293–1298.
- Sarti, B. and Scandola, M. 1995. Viscoelastic and thermal properties of collagen/poly(vinyl alcohol) blends. **16**(10): 785–792.
- Schoof, H., Apel, J., Heschel, I. and Rau, G. 2001. Control of pore structure and size in freeze-dried collagen sponges. *Journal of biomedical materials research*. **58**(4): 352-357.
- Sell, S. a, McClure, M.J., Garg, K., Wolfe, P.S. and Bowlin, G.L. 2009. Electrospinning of collagen/biopolymers for regenerative medicine and cardiovascular tissue engineering. *Advanced drug delivery reviews*. **61**(12): 1007–1019.
- Shalumon, K.T., Binulal, N.S., Selvamurugan, N., Nair, S.V., Menon, D., Furuike, T., Tamura, H. and Jayakumar, R. 2009. Electrospinning of carboxymethyl chitin/poly(vinyl alcohol) nanofibrous scaffolds for tissue engineering applications. *Carbohydrate Polymers*. **77**(4): 863–869.
- Shanmugasundaram, N., Ravichandran, P., Reddy, P.N., Ramamurty, N., Pal, S. and Rao, K.P. 2001. Collagen-chitosan polymeric scaffolds for the *in vitro* culture of human epidermoid carcinoma cells. *Biomaterials*. **22**: 1943–1951.
- Shao, S., Zhou, S., Li, L., Li, J., Luo, C., Wang, J., Li, X. and Weng, J. 2011. Osteoblast function on electrically conductive electrospun PLA/MWCNTs nanofibers. *Biomaterials*. **32**(11): 2821-2833.
- Sharma, V.K., Yngard, R. a and Lin, Y. 2009. Silver nanoparticles: green synthesis and their antimicrobial activities. *Advances in colloid and interface science*. **145**(1-2): 83–96.
- Sherman, W. 1912. Vanadium steel bone plates and screws. *Surg Gynecol Obstet*. **14**: 629-634.
- Shi, Y., Xiong, D. and Zhang, J. 2014. Effect of irradiation dose on mechanical and biotribological properties of PVA/PVP hydrogels as articular cartilage. *Tribology International*. **78**: 60–67.

- Shin, Y.M., Hohman, M.M., Brenner, M.P. and Rutledge, G.C. 2001. Experimental characterization of electrospinning: the electrically forced jet and instabilities. *Polymer*. **42**(25): 09955–09967.
- Shum, A.W.T. and Mak, A.F.T. 2003. Morphological and biomechanical characterization of poly(glycolic acid) scaffolds after *in vitro* degradation. *Polymer Degradation and Stability*. **81**(1): 141–149.
- Shvedova, A.A., Kisin, E.R., Mercer, R., Murray, A.R., Johnson, V.J., Potapovich, A.I., Tyurina, Y.Y., Gorelik, O., Arepalli, S., Schwegler-berry, D., Hubbs, A.F., Antonini, J., Evans, D.E., Ku, B., Ramsey, D., Maynard, A., Kagan, V.E., Castranova, V., Baron, P., Anna, A., Ashley, R., Ann, F. and Cas, V. 2005. Unusual inflammatory and fibrogenic pulmonary responses to single-walled carbon nanotubes in mice. *The American Journal of Physiology - Lung Cellular and Molecular Physiology*. **289**(5): 698–708.
- Siljanovska, G., Blazevska-gilev, J., Fajg, R. and Tomovska, R. 2014. Surface-Enhanced Raman Scattering activity of Ag/graphene /polymer nanocomposite films synthesized by laser ablation. *Thin Solid Films*. **564**: 115–120.
- Silver, F.H. 1987. *Biological materials : structure, mechanical properties, and modeling of soft tissues*. New York : New York University Press.
- Silver, F.H., Kato, Y.P., Ohno, M. and Wasserman, A.J. 1992. Analysis of mammalian connective tissue: relationship between hierarchical structures and mechanical properties. *Journal of long-term effects of medical implants*. **2**(2-3):165–198.
- Sinha Roy, D. and Rohera, B.D. 2002. Comparative evaluation of rate of hydration and matrix erosion of HEC and HPC and study of drug release from their matrices. *European journal of pharmaceutical sciences*. **16**(3): 193–199.
- Sionkowska, A. 2011. Current research on the blends of natural and synthetic polymers as new biomaterials: Review. *Progress in Polymer Science*. **36**(9): 1254–1276.
- Sionkowska, A., Płanecka, A., Kozłowska, J. and Skopińska-Wiśniewska, J. 2009. Photochemical stability of poly(vinyl alcohol) in the presence of collagen. *Polymer Degradation and Stability*. **94**(3): 383-388.
- Sionkowska, A., Skopińska, J. and Wisniewski, M. 2004. Photochemical stability of collagen/poly (vinyl alcohol) blends. *Polymer Degradation and Stability*. **83**(1): 117-125.

- Smith, L.T., Holbrook, K.A. and Byers, P.H. 1982. Structure of the dermal matrix during development and in the adult. *The Journal of investigative dermatology*. **79**(Suppl 1): 93s–104s.
- Song, J., Kang, H., Lee, C., Hwang, S.H. and Jang, J. 2012. Aqueous synthesis of silver nanoparticle embedded cationic polymer nanofibers and their antibacterial activity. *ACS applied materials & interfaces*. **4**(1): 460-465.
- Song, W., Markel, D.C., Wang, S., Shi, T., Mao, G. and Ren, W. 2012. Electrospun polyvinyl alcohol-collagen-hydroxyapatite nanofibers: a biomimetic extracellular matrix for osteoblastic cells. *Nanotechnology*. **23**(1115101): 1-16.
- Sorokulova, I., Watt, J., Olsen, E., Globa, L., Moore, T., Barbaree, J. and Vodyanoy, V., 2012. Natural biopolymer for preservation of microorganisms during sampling and storage. *Journal of microbiological methods*. **88**(1): 140-146.
- Stevens, K.N.J., Crespo-Biel, O., van den Bosch, E.E.M., Dias, A. a, Knetsch, M.L.W., Aldenhoff, Y.B.J., van der Veen, F.H., Maessen, J.G., Stobberingh, E.E. and Koole, L.H. 2009. The relationship between the antimicrobial effect of catheter coatings containing silver nanoparticles and the coagulation of contacting blood. *Biomaterials*. **30**(22): 3682–3690.
- Stoyneva, V., Momekova, D., Kostova, B. and Petrov, P. 2014. Stimuli sensitive super-macroporous cryogels based on photo-crosslinked 2-hydroxyethylcellulose and chitosan. *Carbohydrate polymers*. **99**: 825–30.
- Subia, B., Kundu, J. and Kundu, S.C. 2010. *Tissue engineering*. Europe: InTechOpen.
- Sudhamani, S., Prasad, M. and Udaya Sankar, K. 2003. DSC and FTIR studies on gellan and polyvinyl alcohol (PVA) blend films. *Food Hydrocolloids*, **17**(3): 245–250.
- Sugantha Kumari, V., Khaleel Basha, S. and Sudha, P.N. 2011. Physicochemical and morphological evaluation of chitosan/poly(vinyl alcohol)/methylcellulose chemically cross-linked ternary blends. *Polymer Bulletin*. **68**(5): 1387–1393.
- Suming-Li, H. Garreu, M.V. 1990. Structure-property relationships in the case of the degradation of massive poly(-hydroxy acids) in aqueous media: Part 3 Influence of the morphology of poly (L-/actic acid). *Journal of Materials Sciece: Materials in Medicine*. **1**:198–206.
- Sumitha, M.S., Shalumon, K.T., Sreeja, V.N., Jayakumar, R., Nair, S. V. and Menon, D. 2012. Biocompatible and Antibacterial Nanofibrous Poly(ϵ -caprolactone)-Nanosilver Composite Scaffolds for Tissue Engineering Applications. *Journal of Macromolecular Science Part A*. **49**(2): 131–138.

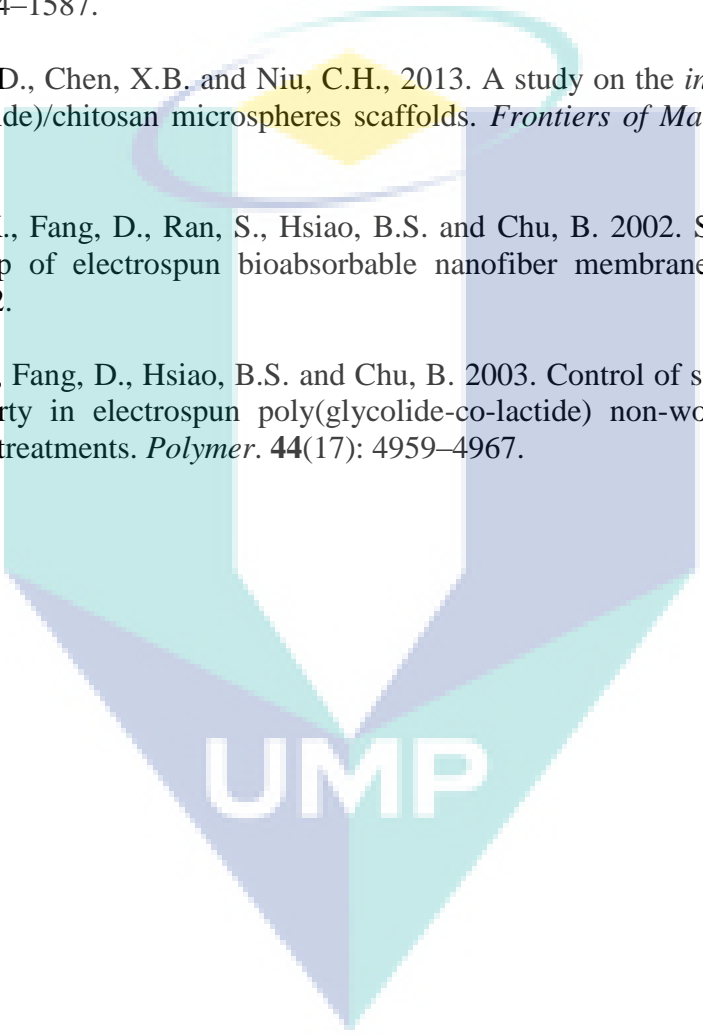
- Sun, W., Sun, D., Wei, Y., Liu, S. and Zhang, S. 2007. Oil-in-water emulsions stabilized by hydrophobically modified hydroxyethyl cellulose: adsorption and thickening effect. *Journal of colloid and interface science*. **311**(1): 228-236.
- Sung, H.W., Hsu, H.L., Shih, C.C. and Lin, D.S. 1996. Cross-linking characteristics of biological tissues fixed with monofunctional or multifunctional epoxy compounds. *Biomaterials*. **17**(14):1405-1410.
- Synder, D.L., Sullivan, N. and Schoelles, K.M. 2012. *Skin substitutes for treating chronic wounds*. Technology Assessment Report. 2012.
- Szymanski, M.S. and Porter, R.A. 2013. Preparation and quality control of silver nanoparticle-antibody conjugate for use in electrochemical immunoassays. *Journal of immunological methods*. **387**(1-2): 262-269.
- Tangsadthakun, C., Kanokpanont, S., Sanchavanakit, N., Banaprasert, T. and Damrongsakkul, S., 2006. Properties of Collagen / Chitosan Scaffolds for Skin Tissue Engineering. *Journal of metals, materials and minerals*. **16**(1): 37-44.
- Tanigami, T., Yano, K., Yamaura, K. and Matsuzawa, S. 1995. Anomalous swelling of poly(vinyl alcohol) film in mixed solvents of dimethylsulfoxide and water. *Polymer*, **36**(15): 2941–2946.
- Tanyolaç, D., Sönmezışık, H., Ozdural, A.R. 2005. A low cost porous polyvinylbutyral membrane for BSA adsorption. *Biochemical Engineering Journal*. **22**: 221–228.
- Taylor, P., Fang, X. and Reneker, D.H. 2006. Physics DNA Fibers by Electrospinning. *Journal of Macromolecular Science , Part B*. **36**(2): 37–41.
- Thakkar, K.N., Mhatre, S.S. and Parikh, R.Y. 2010. Biological synthesis of metallic nanoparticles. *Nanomedicine : nanotechnology, biology, and medicine*. **6**(2): 257-262.
- Tortora, G.J. and Bryan, D. 2012. *Principles of anatomy & physiology*. Hoboken, NJ: Wiley Inc.
- Tripathy, J., Mishra, D.K. and Behari, K. 2009. Graft copolymerization of N-vinylformamide onto sodium carboxymethylcellulose and study of its swelling, metal ion sorption and flocculation behaviour. *Carbohydrate Polymers*. **75**(4): .604-611.
- Trombino, S., Cassano, R., Bloise, E., Muzzalupo, R., Tavano, L. and Picci, N. 2009. Synthesis and antioxidant activity evaluation of a novel cellulose hydrogel containing trans-ferulic acid. *Carbohydrate Polymers*. **75**(1): 184-188.
- UCare: Quality and Management. 2013. *Bioengineered skin substitutes*. New York: Ucare.

- Van der Rest, M. and Garrone, R. 1991. Collagen family of proteins. *FASEB journal*. **5**(13): 2814–23.
- V. Rivas-Orta, R. Antonio-Cruz, A.M. Mendoza-Martínez, Cepeda A.B.M. and Cruz-Gómez C.G. 2008. Hydrogels from poly(acrylic acid)/carboxymethyl cellulose & poly (acrylic acid)/methyl cellulose. *Journal of Materials Online*. **4**: 1-9.
- Vepari, C. and Kaplan, D.L. 2007. Silk as a Biomaterial. *Progress in polymer science*. **32**(8-9): 991-1007.
- Veríssimo, D.M., Leitão, R.F.C., Ribeiro, R. a, Figueiró, S.D., Sombra, A.S.B., Góes, J.C. and Brito, G.A.C., 2010. Polyanionic collagen membranes for guided tissue regeneration: Effect of progressive glutaraldehyde cross-linking on biocompatibility and degradation. *Acta biomaterialia*. **6**(10): 4011- 4018.
- Viet, D., Sarawade, P.B., Jeong, S., Hoon, S., Kim, J., Gyu, Y. and Taik, H. 2013. Effective water disinfection using silver nanoparticle containing silica beads. *Applied Surface Science*. **266**: 280–287.
- Vlierberghe, S. Van, Cnudde, V., Dubruel, P., Masschaele, B., Cosijns, A., Paepe, I. De, Jacobs, P.J.S., Hoorebeke, L. Van, Remon, J.P. and Schacht, E. 2007. Porous gelatin hydrogels: 1. Cryogenic formation and structure analysis. *Biomacromolecules*. **8**(2): 331- 337.
- Vodnik, V. V., Božanić, D.K., Bibić, N., Šaponjić, Z. V. and Nedeljković, J.M., 2008. Optical Properties of Shaped Silver Nanoparticles. *Journal of Nanoscience and Nanotechnology*. **8**(7): 3511-3515.
- Wang, L. and L. Carrier, R. 2011. *Advances in Biomimetics*. Europe: InTechOpen.
- Wang, T.W., Sun, J.S., Wu, H.C., Tsuang, Y.H., Wang, W.H. and Lin, F.H. 2006. The effect of gelatin-chondroitin sulfate-hyaluronic acid skin substitute on wound healing in SCID mice. *Biomaterials*. **27**(33): 5689-5697.
- Watt, F.M., Fujiwara, H. 2011. Cell-Extracellular matrix interactions in normal and diseased skin.
- Williams, D.F. 2006. Definitions in biomaterials. *Proceedings of a Consensus Conference of the European Society for Biomaterials*. Amsterdam:Elsevier.
- Williams, D.F. and Cunningham, J. 1979. *Materials in clinical dentistry*. London:Oxford University Press.

- Wittke, J.H., 2008. Signals. (online). <http://www4.nau.edu/microanalysis/microprobe-sem/signals.html> (10 September 2014)
- Wu, G.M., Lin, S.J. and Yang, C.C. 2006. Preparation and characterization of PVA/PAA membranes for solid polymer electrolytes. *Journal of Membrane Science*. **275**(1-2): 127–133.
- Wu, J., Zheng, Y., Song, W., Luan, J., Wen, X., Wu, Z., Chen, X., Wang, Q. and Guo, S. 2014. In situ synthesis of silver-nanoparticles/bacterial cellulose composites for slow-released antimicrobial wound dressing. *Carbohydrate polymers*. **102**: 762–771.
- Wu, X., Liu, Y., Li, X., Wen, P., Zhang, Y., Long, Y., Wang, X., Guo, Y., Xing, F. and Gao, J. 2010. Preparation of aligned porous gelatin scaffolds by unidirectional freeze-drying method. *Acta biomaterialia*. **6**(3): 1167–1177.
- Xiao, J., Duan, H., Liu, Z., Wu, Z., Lan, Y., Zhang, W., Li, C., Chen, F., Zhou, Q., Wang, X., Huang, J. and Wang, Z., 2011. Construction of the recellularized corneal stroma using porous acellular corneal scaffold. *Biomaterials*. **32**(29): 6962–6971.
- Xu, X., Tan, C., Liu, H., Wang, F., Li, Z., Liu, J. and Ji, J. 2013. Carbon black supported ultra-high loading silver nanoparticle catalyst and its enhanced electrocatalytic activity towards oxygen reduction reaction in alkaline medium. *Journal of Electroanalytical Chemistry*. **696**: 9–14.
- Yang, D., Yu, K., Ai, Y., Zhen, H., Nie, J. and Kennedy, J.F. 2011. The mineralization of electrospun chitosan/poly(vinyl alcohol) nanofibrous membranes. *Carbohydrate Polymers*. **84**(3): 990–996.
- Yang, L., Fitié, C.F.C., van der Werf, K.O., Bennink, M.L., Dijkstra, P.J. and Feijen, J. 2008. Mechanical properties of single electrospun collagen type I fibers. *Biomaterials*. **29**(8): 955–962.
- Yang, S., Leong, K.F., Du, Z. and Chua, C.K. 2001. The design of scaffolds for use in tissue engineering. Part I. Traditional factors. *Tissue engineering*. **7**(6): 679–689.
- Yang, Y., Zhao, Y., Tang, G., Li, H., Yuan, X. and Fan, Y., 2008b. *In vitro* degradation of porous poly(l-lactide-co-glycolide)/ β -tricalcium phosphate (PLGA/ β -TCP) scaffolds under dynamic and static conditions. *Polymer Degradation and Stability*. **93**(10): 1838–1845.
- Yannas, I. V., Lee, E., Orgill, D.P., Skrabut, E.M. and Murphy, G.F. 1989. Synthesis and characterization of a model extracellular matrix that induces partial regeneration of adult mammalian skin. *Proceedings of the National Academy of Sciences of the United States of America*. **86**(3): 933–937.

- Yarin, A.L., Koombhongse, S. and Reneker, D.H. 2001. Bending instability in electrospinning of nanofibers. *Journal of Applied Physics*. **89**(5): 3018.
- Yoon, J., Baek, B. and Lee, Y.S. 2009. *Organic Foaming Plastic Body Having Excellent Thermal Resistance and Durability*. US Patent Application Publication No.: 12/159, 948.
- Zeeman, R., Dijkstra, P.J., van Wachem, P.B., van Luyn, M.J., Hendriks, M., Cahalan, P.T. and Feijen, J. 1999. Successive epoxy and carbodiimide cross-linking of dermal sheep collagen. *Biomaterials*. **20**(10): 921–931.
- Zeleny, J. 1914. The electrical discharge from liquid points, and a hydrostatic method of measuring the electric intensity at their surfaces. *Physical Review*. **3**(2): 69–91.
- Zhang, D., Chen, L., Zang, C., Chen, Y. and Lin, H. 2013. Antibacterial cotton fabric grafted with silver nanoparticles and its excellent laundering durability. *Carbohydrate polymers*. **92**(2): 2088–2094.
- Zhang, H., Nie, H., Li, S., White, C.J.B. and Zhu, L. 2009. Cross-linking of electrospun polyacrylonitrile/hydroxyethyl cellulose composite nanofibers. *Materials Letters*. **63**(13-14): 1199–1202.
- Zhang, K., Melo, M.A.S., Cheng, L., Weir, M.D., Bai, Y. and Xu, H.H.K. 2012. Effect of quaternary ammonium and silver nanoparticle-containing adhesives on dentin bond strength and dental plaque microcosm biofilms. *Dental materials*. **28**(8): 842–852.
- Zhang, K., Yin, A., Huang, C., Wang, C., Mo, X., Al-Deyab, S.S. and El-Newehy, M. 2011. Degradation of electrospun SF/P(LLA-CL) blended nanofibrous scaffolds *in vitro*. *Polymer Degradation and Stability*. **96**(12): 2266–2275.
- Zhang, Y.Z., Venugopal, J., Huang, Z.-M., Lim, C.T. and Ramakrishna, S. 2006. Cross-linking of the electrospun gelatin nanofibers. *Polymer*. **47**(8): 2911–2917.
- Zhang, Z. and Michniak-Kohn, B.B. 2012. Tissue engineered human skin equivalents. *Pharmaceutics*. **4**(1): 26–41.
- Zhao, C., Tan, A., Pastorin, G. and Ho, H.K. 2012. Nanomaterial scaffolds for stem cell proliferation and differentiation in tissue engineering. *Biotechnology advances*. **31**(5): 654–68.
- Zhao, J., Tian, R. and Zhi, J. 2008. Deposition of silver nanoleaf film onto chemical vapor deposited diamond substrate and its application in surface-enhanced Raman scattering. *Thin Solid Films*. **516**(12): 4047–4052.

- Zhbankov, R.G. 1966. *Infrared Spectra of Cellulose and its Derivatives*. New York : Plenum Publishing Corporation.
- Zhong, S.P., Zhang, Y.Z. and Lim, C.T. 2010. Tissue scaffolds for skin wound healing and dermal reconstruction. *Nanomedicine and nanobiotechnology*. **2**(5): 510–525.
- Zhou, W.Y., Guo, B., Liu, M., Liao, R., Rabie, A.B.M. and Jia, D. 2010. Poly(vinyl alcohol)/halloysite nanotubes bionanocomposite films: Properties and *in vitro* osteoblasts and fibroblasts response. *Journal of biomedical materials research, Part A*. **93**(4): 1574–1587.
- Zhu, N., Cooper, D., Chen, X.B. and Niu, C.H., 2013. A study on the *in vitro* degradation of poly(l-lactide)/chitosan microspheres scaffolds. *Frontiers of Materials Science*. **7**(1): 76–82.
- Zong, X., Kim, K., Fang, D., Ran, S., Hsiao, B.S. and Chu, B. 2002. Structure and process relationship of electrospun bioabsorbable nanofiber membranes. *Polymer*. **43**(16): 4403–4412.
- Zong, X., Ran, S., Fang, D., Hsiao, B.S. and Chu, B. 2003. Control of structure, morphology and property in electrospun poly(glycolide-co-lactide) non-woven membranes *via* post-draw treatments. *Polymer*. **44**(17): 4959–4967.

The logo for UMP (Universiti Malaysia Perlis) is a large, stylized shield shape. It is divided into four quadrants: top-left is light blue, top-right is light purple, bottom-left is light blue, and bottom-right is light purple. The letters 'UMP' are written in white, bold, sans-serif font across the bottom center of the shield.

UMP

ACHIEVEMENTS

List of publications

- 1) **Farah Hanani Zulkifli**, Fathima Shahitha Jahir Hussain, Mohammad Syaiful Bahari Abdull Rasad, Mashitah Mohd Yusoff. 2014. *In vitro* degradation study of novel hec/pva/collagen nanofibrous scaffold for skin tissue engineering applications. *Polymer degradation and stability*. **110**: 473-481.
- 2) **Farah Hanani Zulkifli**, Fathima Shahitha Jahir Hussain, Mohammad Syaiful Bahari Abdull Rasad, Mashitah Mohd Yusoff. 2014. Nanostructured materials from hydroxyethyl cellulose for skin tissue engineering. *Carbohydrate Polymers*. **114**:238-245.
- 3) **Farah Hanani Zulkifli**, Fathima Shahitha Jahir Hussain, Mohammad Syaiful Bahari Abdull Rasad, Mashitah Mohd Yusoff. 2014. Improved cellular response of chemically crosslinked collagen incorporated hydroxyethyl cellulose/poly(vinyl) alcohol nanofibers scaffold. *Journal of Biomaterials Application*. **29**:1014-1027.
- 4) **Farah Hanani Zulkifli**, Fathima Shahitha Jahir Hussain, Mashitah Mohd Yusoff, Nurul Nadiah Hamidon, Sugandha Chahal. 2013. Cross-linking effect on electrospun Hydroxyethyl cellulose/poly(vinyl) alcohol nanofibrous scaffolds. *Procedia Engineering*. **53**:689-698.

List of Conferences and Exhibition:

- 1) **Farah Hanani Zulkifli**, Fathima Shahitha Jahir Hussain, Mohammad Syaiful Bahari Abdull Rasad, Mashitah Mohd Yusoff. 2014. Nano-biomaterials from modified cellulose for skin tissue engineering. *Creation, Innovation, Technology and Research Exposition (CITREX)*. Silver award.

- 2) **Farah Hanani Zulkifli**, Fathima Shahitha Jahir Hussain, Mohammad Syaiful Bahari Abdull Rasad, Mashitah Mohd Yusoff. 2013. Scaffolds from chemically modified cellulose nanofibers for skin tissue engineering. *Malaysian Technical Universities Conference on Engineering & Technology (MUCET)*.
- 3) **Farah Hanani Zulkifli**, Fathima Shahitha Jahir Hussain, Mohammad Syaiful Bahari Abdull Rasad, Mashitah Mohd Yusoff. 2013. Electrospun nanofibrous mats of modified cellulose as potential scaffold for skin tissue engineering. *National Conference on Industry-Academia Initiatives on Biotechnology (CIA-Biotech)*.
- 4) Dr. Fathima Shahitha*, Prof. Mashitah Binti Mohd Yusoff, Sugandha Chahal and **Farah Hanani Binti Zulkifli**. 2013. Nanofibrous scaffolds from water soluble polymers for bone growth. *Creation, Innovation, Technology and Research Exposition (CITREX)*. Bronze award.
- 5) Dr. Fathima Shahitha*, Prof. Mashitah Binti Mohd Yusoff, **Farah Hanani Binti Zulkifli** and Sugandha Chahal. 2012. Scaffolds from chemically modified cellulose for bone tissue engineering. *Creation, Innovation, Technology and Research Exposition (CITREX)*. Silver award.
- 6) **Farah Hanani Zulkifli**, Fathima Shahitha Jahir Hussain, Mashitah Mohd Yusoff, Nurul Nadiyah Hamidon, Sugandha Chahal. 2013. Cross-linking effect on electrospun Hydroxyethyl cellulose/poly(vinyl) alcohol nanofibrous scaffolds. *Malaysian Technical Universities Conference on Engineering & Technology (MUCET)*.
- 7) Dr. Fathima Shahitha, Prof. Mashitah Binti Mohd Yusoff, **Farah Hanani Binti Zulkifli** and Sugandha Chahal. 2012. Scaffolds from chemically modified cellulose for bone tissue engineering. *Biomalaysia*. Silver award.

- 8) Dr. Fathima Shahitha, Prof. Mashitah Binti Mohd Yusoff, Dr. Azhari Hamid Nour Abduelrahman and **Farah Hanani binti Zulkifli**. 2011. Anti e-coli membrane by green chemistry approach for healthcare applications. *Biomalaysia*.
- 9) **Farah Hanani Binti Zulkifli**, Dr. Fathima Shahitha and Sugandha Chahal. 2012. Cross-linking effect on electrospun hydroxyethyl cellulose/ poly(vinyl) alcohol nanofibrous scaffolds. *National Conference on Postgraduate Research (NCON-PGR)*.

